



**A Computational Parameter Study for  
Three-Dimensional Shock-Bubble Interactions**

**John Niederhaus**

**September 2007**

**UWFDM-1334**

Ph.D. thesis.

**FUSION TECHNOLOGY INSTITUTE  
UNIVERSITY OF WISCONSIN  
MADISON WISCONSIN**

# **A Computational Parameter Study for Three-Dimensional Shock-Bubble Interactions**

John Niederhaus

Fusion Technology Institute  
University of Wisconsin  
1500 Engineering Drive  
Madison, WI 53706

<http://fti.neep.wisc.edu>

September 2007

UWFDM-1334

Ph.D. thesis.

# **A Computational Parameter Study for Three-Dimensional Shock-Bubble Interactions**

By

**John Henry J. Niederhaus**

A DISSERTATION SUBMITTED IN PARTIAL FULFILLMENT OF THE  
REQUIREMENTS FOR THE DEGREE OF

DOCTOR OF PHILOSOPHY  
(ENGINEERING PHYSICS)

at the

**UNIVERSITY OF WISCONSIN – MADISON**

2007

© Copyright by John Henry J. Niederhaus 2007

All Rights Reserved

# Abstract

The morphology of the multifluid compressible flow associated with a shock-bubble interaction in a gas environment is characterized using a series of three-dimensional multifluid Eulerian simulations. The bubble consists of a spherical gas volume of radius 2.54 cm (128 grid points) which is accelerated by a planar shock wave. Fourteen scenarios are considered: four gas combinations, including Atwood numbers  $-0.8 < A < 0.7$  and Mach numbers  $1.1 < M \leq 5$ . The data are queried at closely-spaced time intervals in order to characterize the temporal evolution of various integral features of shock-bubble interactions, including the mean density, internal energy, mean velocity, dimensions, and circulation associated with the shocked bubble. Scaling arguments based on quantities computed from one-dimensional gasdynamics are found to collapse the trends in many of these quantities successfully for fixed  $A$ , although complex changes in the shock wave refraction pattern introduce effects that preclude successful scaling across the gas combinations. An azimuthal averaging scheme is implemented in order to extract mean and fluctuating density and enstrophy fields, from which the intensity, spatial distribution, and spectral content of these fluctuations are computed for each of the scenarios. The data indicate that a transient turbulent state is achieved only for convergent geometry and  $A > 0.2$ . The action of nonlinear-acoustic effects and vorticity generation is depicted in sequenced visualizations of the density and vorticity fields, and of the azimuthal mean and fluctuating density and enstrophy fields. Effects associated with the inclusion of a thin, dense, film-like cladding on the interface are quantified using an additional series of simulations, showing that the effects are insignificant except in cases with  $|A| < 0.2$ .

# Acknowledgements

The work presented here was entirely made possible by my advisor, Professor Riccardo Bonazza, and by my co-advisor, Jeff Greenough (LLNL), who have guided me with great patience and insight over the past four years. I wish to thank Professor Bonazza for providing the impetus for studying shock-bubble interactions, and for tirelessly reviewing results, posing thoughtful questions and challenges, and providing redirection when necessary. I am also indebted to Jeff Greenough for providing access to the *Raptor* code and to LLNL computing platforms, and for his guidance of this work by identifying aspects of the problem and regions of the parameter space needing further investigation, and new angles from which to approach them. I also wish to thank Jeff for two summers' worth of close personal interaction and training on-site at LLNL, which provided invaluable exposure to tools, methods, and expertise I would not have encountered otherwise.

I have also benefited immensely from close interaction and collaboration with Dr. Jason Oakley, who provided extensive training in many practical aspects of scientific computing. Dr. Oakley guided this work forward by extensive assistance in the development of computational tools, painstaking critique of various research reports and publication drafts, and countless hours spent in thoughtful discussions. The one-dimensional gas-dynamics reconstruction model for the circulation in shock-bubble interactions which appears in this study was devised entirely by Dr. Oakley.

I am further indebted to Dr. Mark Anderson for his guidance and insight during the course of this project, as well as for thoughtful and challenging comments on research results presented in group meetings, reports, and publication drafts.

Experimental shock tube data shown here were derived from experiments performed in the Wisconsin Shock Tube Laboratory by Devesh Ranjan and Brad Motl, with the capable technical oversight and help of Paul Brooks. I am sincerely grateful for the opportunity to work with this group in an experiment-driven environment.

I would like to thank the entire *VisIt* team for their attentive help at various points. Postprocessing for these simulations was done exclusively with the *VisIt* software. I am especially grateful to Hank Childs, who personally helped with the implementation of many *VisIt* functionalities for this work, particularly the DDF feature, without which azimuthal averaging in a Cartesian dataset would have been vastly more difficult.

Thanks also go to each of my thesis committee members for their questions and suggestions, to Professor Leslie Smith for numerous conversations regarding convergence in Euler simulations, to the Livermore Computing staff for help with technical computing issues and access to world-class computing resources, to Aaron Miles for comments and discussions on mixing and dimensional analysis, to Oleg Schilling for insightful comments on several drafts of this dissertation, to Devesh Ranjan for extensive discussions on secondary vortex rings and compressibility effects, to Brad Motl for insights on flow visualization, and to Dr. Silke Haustein for ESWL references.

Thanks also to Mom and Dad for *everything*.

Finally, in fond memory of many glorious Friday lunches on Regent Street in Madison, I sing with Adams' dolphins: "So long (Big Ten Pub), and thanks for all the (cat)fish!"

This work was partially supported by the U.S. Department of Energy Grant No. DE-FG52-06NA26196. This work was also partially performed under the auspices of the U.S. Department of Energy at the University of California, Lawrence Livermore National Laboratory under Contract No. W-7405-ENG-48.

# Contents

<b>Abstract</b>	<b>i</b>
<b>Acknowledgements</b>	<b>ii</b>
<b>Notation and Symbols</b>	<b>xiv</b>
<b>1 Introduction</b>	<b>1</b>
1.1 Scope, Motivation, and Organization . . . . .	3
1.2 Overview of the Physics of Shock-Bubble Interactions . . . . .	9
1.2.1 Nomenclature . . . . .	10
1.2.2 Shock-induced compression . . . . .	10
1.2.3 Nonlinear-acoustic effects . . . . .	15
1.2.4 Vorticity production . . . . .	20
1.3 Overview of Relevant Previous Studies of Shock-Bubble Interactions . . . . .	25
1.3.1 Seminal experimental work . . . . .	25
1.3.2 Recent experimental work . . . . .	27
1.3.3 Two-dimensional numerical simulations . . . . .	28
1.3.4 Three-dimensional numerical simulations . . . . .	30
1.3.5 Two-dimensional parameter studies . . . . .	31
1.3.6 Analytical modeling . . . . .	34
<b>2 Numerical method</b>	<b>40</b>
2.1 Description of Simulation Code . . . . .	40

2.1.1	Equations . . . . .	40
2.1.2	The <i>Raptor</i> code . . . . .	41
2.1.3	Adaptive mesh refinement . . . . .	42
2.1.4	Eulerian Godunov integrator . . . . .	43
2.1.5	Multifluid capturing . . . . .	44
2.1.6	Settings . . . . .	44
2.1.7	Computing facilities . . . . .	45
2.2	Mesh-Sensitivity of Solutions for Shock-Bubble Interaction Problems . .	46
2.2.1	Two-dimensional simulations . . . . .	48
2.2.2	Sensitivity of extracted quantities to mesh spacing . . . . .	53
2.3	Validation of Numerical Method with Theory, Experiments, and Simulations	57
2.3.1	Shock wave interaction with a gas slab: theory . . . . .	58
2.3.2	Shock wave interaction with a spherical bubble: experiments . .	61
2.3.3	Shock wave interaction with a cylindrical bubble: simulations . .	67
2.3.4	Shock wave interaction with a spherical bubble: simulations . .	72
<b>3</b>	<b>Simulation Setup and Results</b>	<b>76</b>
3.1	Setup of Three-Dimensional Parameter Study Simulations . . . . .	77
3.1.1	Coordinate system and geometry . . . . .	77
3.1.2	Boundary conditions . . . . .	78
3.1.3	Initial condition . . . . .	79
3.1.4	Fluid properties . . . . .	80
3.1.5	Ill-posed phenomena and interface smoothing . . . . .	80
3.1.6	Parameter study cases . . . . .	82

3.2	Flow Visualizations and Descriptions . . . . .	84
3.2.1	Shock refraction, reflection, and diffraction . . . . .	86
3.2.2	Vorticity production and bubble deformation . . . . .	92
<b>4</b>	<b>Analysis of Integral Features</b>	<b>96</b>
4.1	Mach Scaling for Integral Flow Features . . . . .	96
4.1.1	Mean bubble-fluid density . . . . .	98
4.1.2	Bubble fluid internal energy . . . . .	104
4.1.3	Mean bubble fluid velocity . . . . .	108
4.1.4	Bubble dimensions . . . . .	111
4.2	Measurements and Models for Circulation . . . . .	117
4.2.1	Definition . . . . .	117
4.2.2	Circulation models based on baroclinic torque . . . . .	120
4.2.3	Circulation model motivated by asymptotics . . . . .	121
4.2.4	Circulation model based on one-dimensional gasdynamics . . . . .	124
4.2.5	Circulation obtained from simulations . . . . .	127
<b>5</b>	<b>Analysis of Complex Flow Features and Turbulent Mixing</b>	<b>135</b>
5.1	Non-Axisymmetric Features and Turbulence . . . . .	136
5.1.1	Background considerations regarding turbulence . . . . .	136
5.1.2	Monotone-integrated large eddy simulation . . . . .	138
5.1.3	Mixing transition and Reynolds number . . . . .	140
5.1.4	Averaging scheme . . . . .	147
5.1.5	Mean and fluctuating flowfields . . . . .	151
5.1.6	Turbulence intensity . . . . .	159

5.1.7	Radial and axial fluctuation profiles . . . . .	164
5.1.8	Fluctuation power spectra . . . . .	172
5.2	Mixing . . . . .	179
5.2.1	Fluctuation intensity . . . . .	181
5.2.2	Mean ambient-fluid volume fraction . . . . .	183
5.2.3	Molecular mixing fraction profile . . . . .	187
5.3	Departure from Axisymmetry . . . . .	192
<b>6</b>	<b>Analysis of Film Effects</b>	<b>195</b>
6.1	Modeled Film Material . . . . .	195
6.2	Flow Visualizations . . . . .	197
6.3	Mean Bubble-Fluid Density . . . . .	203
6.4	Circulation . . . . .	205
<b>7</b>	<b>Discussion and Conclusion</b>	<b>210</b>
7.1	Complex Shock Refraction and Non-Similarity . . . . .	211
7.2	Non-Axisymmetric Effects, Turbulence, and Mixing . . . . .	213
7.3	Modeling and Timescaling Arguments Based on One-Dimensional Gas-dynamics . . . . .	214
7.4	Significance and Application . . . . .	216
7.5	Limitations and Future Work . . . . .	217
7.6	Conclusion . . . . .	219
<b>A</b>	<b>One-Dimensional Gasdynamics Analysis for a Shocked Gas Slab</b>	<b>221</b>
<b>B</b>	<b>Derivation of Compressible Vorticity Transport Equation</b>	<b>229</b>

B.1	Vector Identities . . . . .	229
B.2	Viscous Term . . . . .	230
B.3	Derivation . . . . .	232
B.4	Baroclinic Source Term . . . . .	233
<b>C</b>	<b>Input Files</b>	<b>234</b>
C.1	Inputs . . . . .	234
C.2	Probin . . . . .	241
	<b>Bibliography</b>	<b>245</b>

# List of Figures

1	One-dimensional shock transmission/reflection . . . . .	13
2	One-dimensional shock transmission/reflection in a gas slab . . . . .	15
3	Schematic representation of shock-bubble interaction flowfields . . . . .	17
4	Schematic representation of baroclinic vorticity deposition . . . . .	22
5	Setup for mesh-sensitivity simulations . . . . .	48
6	Mesh-sensitivity study results, air-He, $t = 188 \mu\text{s}$ . . . . .	49
7	Mesh sensitivity study results, air-He, $t = 437 \mu\text{s}$ . . . . .	50
8	Mesh sensitivity study results, air-Kr, $t = 188 \mu\text{s}$ . . . . .	51
9	Mesh sensitivity study results, air-Kr, $t = 437 \mu\text{s}$ . . . . .	52
10	Maximum and mean densities for air-He mesh sensitivity study . . . . .	55
11	Maximum and mean densities for air-Kr mesh sensitivity study . . . . .	55
12	Trends in mean bubble-fluid density for mesh sensitivity study . . . . .	57
13	Pressure and density profiles for a shocked helium slab . . . . .	60
14	Pressure and density profiles for a shocked krypton slab . . . . .	60
15	Experimental/numerical results for air-He, $M=2.95$ . . . . .	63
16	Experimental/numerical results for air-He, $M=2.95$ at late times . . . . .	65
17	Experimental/numerical bubble dimensions for air-He, $M=2.95$ . . . . .	66
18	Simulated flowfield for air-R22, $M=1.22$ shocked cylindrical bubble . . .	69
19	Circulation/baroclinicity for air-R22, $M=1.22$ shocked cylindrical bubble	71
20	Simulated flowfield for air-R12, $M=2.5$ shocked spherical bubble . . . . .	73
21	Vorticity/circulation for air-R12, $M=2.5$ shocked spherical bubble . . . . .	74

22	Parameter study simulation setup . . . . .	78
23	Flowfield evolution for air-He, $M=1.68$ . . . . .	85
24	Flowfield evolution for N <sub>2</sub> -Ar, $M=3.38$ . . . . .	87
25	Flowfield evolution for air-Kr, $M=1.68$ . . . . .	88
26	Flowfield evolution for air-R12, $M=5$ . . . . .	90
27	Three-dimensional rendering for air-R12, $M=5$ . . . . .	94
28	Normalized mean bubble-fluid density . . . . .	101
29	Normalized bubble-fluid internal energy . . . . .	107
30	Normalized mean bubble-fluid velocity . . . . .	110
31	Transverse dimension of the shocked bubble ( $f \geq 0.5$ ) . . . . .	113
32	Streamwise dimension of the shocked bubble ( $f \geq 0.5$ ) . . . . .	114
33	Streamwise dimension of the shocked bubble ( $f \geq 10^{-6}$ ) . . . . .	116
34	Schematic diagram for measuring and modeling circulation . . . . .	118
35	Circulation, air-He, $M = 1.2, 3.0$ . . . . .	128
36	Circulation, N <sub>2</sub> -Ar, $M = 1.33, 3.38$ . . . . .	129
37	Circulation, air-Kr, $M = 1.2, 3.0$ . . . . .	131
38	Circulation, air-R12, $M = 1.14, 5.0$ . . . . .	131
39	Baroclinic source term and Laplacian of density . . . . .	132
40	Ratio of modeled to computed circulation . . . . .	134
41	Late-time density and vorticity fields for air-Kr and air-R12 . . . . .	141
42	Late-time density and vorticity fields for air-He and N <sub>2</sub> -Ar . . . . .	142
43	Grid-scale Reynolds number . . . . .	144
44	Physical Reynolds number . . . . .	145

45	Azimuthal averaging . . . . .	148
46	Azimuthally averaged fields for air-He, $M=1.68$ . . . . .	151
47	Fluctuating fields for air-He, $M=1.68$ . . . . .	152
48	Azimuthally averaged fields for N <sub>2</sub> -Ar, $M=3.38$ . . . . .	153
49	Fluctuating fields for N <sub>2</sub> -Ar, $M=3.38$ . . . . .	153
50	Azimuthally averaged fields for air-Kr, $M=1.68$ . . . . .	154
51	Fluctuating fields for air-Kr, $M=1.68$ . . . . .	155
52	Azimuthally averaged fields for air-R12, $M=5$ . . . . .	156
53	Fluctuating fields for air-R12, $M=5$ . . . . .	157
54	Volume-averaged density fluctuations . . . . .	160
55	Volume-averaged enstrophy fluctuations . . . . .	161
56	Radial and axial profiles of initial-condition density fluctuations . . . . .	165
57	Radial profiles of density fluctuations . . . . .	166
58	Axial profiles of density fluctuations . . . . .	167
59	Radial profiles of enstrophy fluctuations . . . . .	169
60	Axial profiles of enstrophy fluctuations . . . . .	170
61	Power spectra for initial-condition density fluctuations . . . . .	173
62	Radial power spectra of density fluctuations . . . . .	175
63	Axial power spectra of density fluctuations . . . . .	176
64	Radial power spectra of enstrophy fluctuations . . . . .	177
65	Axial power spectra of enstrophy fluctuations . . . . .	178
66	Volume-averaged bubble-fluid volume fraction fluctuations . . . . .	182
67	Time-dependent mean ambient-fluid volume fraction . . . . .	185
68	Turbulent mixing for air-R12, $M=2.5$ and $M=5$ . . . . .	188

69	Molecular mixing fraction profiles . . . . .	190
70	Time-dependent decomposed enstrophy . . . . .	193
71	Flowfield evolution for air-He, $M=1.68$ with film material . . . . .	198
72	Flowfield evolution for N <sub>2</sub> -Ar, $M=3.38$ with film material . . . . .	199
73	Flowfield evolution for air-Kr, $M=1.68$ with film material . . . . .	201
74	Flowfield evolution for air-R12, $M=5$ with film material . . . . .	202
75	Normalized mean bubble fluid density for simulations with film . . . . .	204
76	Circulation, air-He, $M = 1.68$ , with and without film material . . . . .	205
77	Circulation, N <sub>2</sub> -Ar, $M = 3.38$ , with and without film material. . . . .	206
78	Circulation, air-Kr, $M = 1.68$ , with and without film material. . . . .	207
79	Circulation, air-R12, $M = 5$ , with and without film material. . . . .	207
80	One-dimensional shock transmission/reflection in a gas slab . . . . .	222

# List of Tables

1	Theoretical pressure and density in shocked gas slab . . . . .	59
2	Properties of fluids appearing in the simulations . . . . .	81
3	Overview of parameter study scenarios . . . . .	83
4	Computed and modeled values of circulation . . . . .	132
5	Dynamic viscosities . . . . .	144
6	Postshock kinematic viscosities . . . . .	147
7	Estimated Reynolds numbers for parameter study scenarios . . . . .	148

# Notation and Symbols

## Latin symbols

$A$	Atwood number
$A_f$	Atwood number associated with film material
$\mathbf{A}$	Area vector
$B$	Baroclinic torque
$D$	Space occupied by the computational domain
$D/Dt$	Total derivative
$E_I$	Internal energy carried by bubble fluid
$F(U)$	Flux of $U$ in $x$ -direction
$G(U)$	Flux of $U$ in $y$ -direction
$H(U)$	Flux of $U$ in $z$ -direction
$K$	Artificial viscous flux scaling factor
$L$	Computational domain length
$M$	Mach number
$\mathcal{M}$	Molecular mass
$N$	Number of grid points spanning the computational domain

$P$	Closed path of integration
$Q$	Threshold for density-gradient-based refinement
$R$	Initial bubble radius
$\mathcal{R}$	Acoustic impedance
$\mathfrak{R}$	Gas constant
$\delta\mathcal{R}$	Acoustic impedance mismatch
$R_V$	Vortex ring major radius
$\delta R_f$	Thickness of film layer
$Re$	Reynolds number
$Re_\Delta$	“Effective” or grid-scale Reynolds number for Eulerian simulations
$Re_\nu$	Physical Reynolds number based on circulation and viscosity
$S$	Surface enclosed by $P$
$T$	Temperature
$U$	Vector of conserved variables
$\mathbf{U}$	Velocity vector
$V_\perp$	Velocity component normal to boundary
$V_\parallel$	Velocity component tangential to boundary
$\mathcal{V}$	Volume

$\mathcal{V}^*$	Total weighted volume of bubble
$\mathcal{V}_0$	Initial bubble volume
$d\mathcal{V}$	Differential volume element
$W$	Shock wave speed
$W^*$	Propagation speed of the faster of the incident and transmitted shock waves
$\tilde{W}$	Propagation speed $W^*$ , corrected for slowing due to diffraction for $\chi > 2.0$
$W_i$	Propagation speed of incident shock wave
$W_t$	Propagation speed of shock wave transmitted into bubble
$c$	Sound speed
$e$	Total energy per unit mass
$f$	Volume fraction of bubble fluid
$h$	Enthalpy
$k$	Index of azimuthal section
$k_r$	Radial wavenumber
$k_y$	Axial wavenumber
$\ell$	Characteristic length scale
$m_f$	Total mass of bubble film material
$\hat{n}$	Unit normal vector

$p$	Pressure
$r$	Radial coordinate
$\mathbf{r}$	Position vector
$\mathbf{r}_{xz}$	Axisymmetric ( $x$ - $z$ -plane) radial coordinate vector
$\mathbf{r}_c$	Position of bubble center
$\Delta r$	$r$ -dimension of shocked-bubble region
$\mathbf{s}$	Path vector
$t$	Time (relative to initial shock impact)
$t^*$	Time of shock wave passage
$u$	Scalar $x$ -velocity
$\Delta y$	$y$ -dimension of shocked-bubble region
$u'_1$	Flow speed of shocked ambient gas, in lab frame
$v$	Scalar $y$ -velocity
$\langle v \rangle$	Volume-averaged $y$ -velocity of bubble
$v_V$	Vortex ring translational velocity
$y_c$	$y$ -coordinate of bubble center
$w$	Scalar $z$ -velocity

## Greek symbols

$\Gamma$	Circulation
$\Gamma_0$	Net or total circulation (equivalent to $\Gamma$ )
$\Gamma_-$	Negative component of circulation
$\Gamma_+$	Positive component of circulation
$\bar{\Gamma}$	Azimuthal mean circulation
$\tilde{\Gamma}$	Fluctuating circulation with respect to azimuthal mean
$\hat{\Gamma}$	Circulation at the instant of shock passage
$\Delta$	Computational cell size on finest AMR level
$\Delta_c$	Computational cell size on coarsest AMR level
$\Phi$	Placeholder scalar function
$\Omega$	Enstrophy
$\Omega_0$	Characteristic enstrophy scale
$\beta$	Inertia coefficient for solid bodies in accelerating flows
$\gamma$	Ratio of specific heats
$\theta$	Azimuthal coordinate
$\hat{\theta}$	Azimuthal unit vector
$\theta_Y$	Youngs' [111] molecular mixing fraction

$\nu$	Kinematic viscosity
$\nu^*$	Characteristic kinematic viscosity
$\zeta$	Mean ambient-fluid volume fraction in bubble region
$\rho'$	Density
$\langle \rho \rangle$	Mean (volume-averaged) bubble gas density
$\rho^*$	Normalized mean bubble gas density
$\rho_1$	Unshocked ambient gas density
$\rho_2$	Unshocked bubble gas density
$\rho'_1$	Shocked ambient gas density
$\rho'_1$	Shocked bubble gas density
$\rho_f$	Film material density
$\Delta\rho$	Laplacian of density field
$\delta\rho$	Maximum fractional density difference
$\sigma$	Ratio of shocked bubble gas density to twice-shocked ambient gas density
$\tau$	Dimensionless time
$\phi$	Shock wave angle of incidence relative to unshocked interface
$\phi_c$	Critical angle for irregular shock refraction
$\chi$	Initial density ratio of bubble gas relative to ambient gas

$\omega$	Vorticity vector
$\omega$	Scalar vorticity
$\langle \omega \rangle$	Radially-averaged scalar vorticity
$\nabla$	Gradient operator

### Subscripts

1	Ambient fluid
2	Bubble fluid
$i$	Incident shock wave
$r$	Reflected shock wave
$t$	Transmitted shock wave

### Diacritical marks

'	Singly shocked fluid
"	Twice shocked fluid
'''	Three-times shocked fluid

- Azimuthally averaged field (two-dimensional)
- $\sim$  R.m.s. fluctuating field (two-dimensional)
- $\checkmark$  Full fluctuating field (three-dimensional)
- $\langle \checkmark \rangle$  Volume-averaged fluctuation intensity (scalar quantity)
- $\tilde{\sim}$  Axially averaged r.m.s. fluctuating field (one-dimensional)
- $\equiv$  Radially averaged r.m.s. fluctuating field (one-dimensional)
- $\approx$  Power spectrum for radially averaged profile
- $\approx^c$  Power spectrum for axially averaged profiles

# Chapter 1

## Introduction

Since the publication of Rudinger and Somers' 1960 paper on shock-bubble interactions [95], it has been well known that the acceleration of a density inhomogeneity by means of a shock wave gives rise to distinctive fluid motions that are absent under isentropic acceleration. These motions drastically alter the shape of the inhomogeneity and result in the formation of characteristic vortices and, often, of regions of intense mixing. Further, the shape and propagation pattern of the shock wave simultaneously undergoes significant transformations.

In its simplest configuration – that of a planar shock wave propagating in a medium which is uniform except for a single spherical or cylindrical density inhomogeneity – this problem can be considered as a prototype to a larger class of problems: shock-accelerated inhomogeneous flows, in which a shock wave propagates in a medium characterized by a distribution of inhomogeneities in density, temperature, or other state variables. Such flows are found in systems at wide-ranging energetic and spatial scales where shock waves encounter various types of inhomogeneities. The motion and evolution of the fluid interfaces, the surrounding medium, the shock wave, or the inhomogeneities themselves resulting from the interaction introduces effects that are of great concern in many engineering designs and physical descriptions of natural processes.

In interstellar and intergalactic media, shock and blast waves associated with relativistic jets, supernovae, interstellar winds, and spiral density waves interact with gaseous clouds of various temperatures and densities, resulting in significant disruption to the evolution of interstellar and intergalactic media as clouds are destroyed under shock acceleration [52, 91, 48, 44]. A particularly striking example of an apparent shock-cloud interaction is seen in the *Chandra* x-ray images of the bright eastern knot of the Puppis A supernova remnant [48]. In terrestrial atmospheric contexts, sonic boom signatures associated with supersonic flight have been shown to be strongly affected by the interaction of the pressure pulse with temperature and density inhomogeneities in the atmosphere, which act as converging or diverging lenses, and distort the pulse by nonlinear-acoustic diffraction and focusing [24, 81, 66]. Shock-accelerated inhomogeneous flows are also found in supersonic combustion engines, where compressible turbulent mixing of the fuel and the oxidizer is shown to be strongly enhanced by the interaction of a shock wave with the flame [67, 110]. Shock-flame interactions have been observed extensively in laboratory environments, and very well-resolved schlieren images showing the destruction of a spherical flame bubble by a shock wave can be found in Ref. [94].

Shock-accelerated inhomogeneous flows also arise in shock-mitigation and energy-transfer schemes where foams and bubbly liquids are used to redistribute the impulse of shock waves as they interact with void regions in the medium of propagation [4, 18, 25]. In many of these schemes, bubble collapse and jetting phenomena are of foremost concern. These are also of great concern in extracorporeal shock wave lithotripsy, which is a standard treatment for renal stones, employing high-amplitude ultrasound pulses to destroy stones by focussed pressure waves and cavitation erosion [21, 26, 30]. The interaction of the lithotripter pulses with gas voids results in their deformation and

collapse, often with very strong subsequent jetting and pressure redistribution effects [32, 16, 50].

Finally, viewed as a growing density-interface perturbation excited by impulsive acceleration, the shock-bubble interaction has been noted [42] as a finite-mass, high interface-curvature analog to the Richtmyer-Meshkov instability [92, 71], which is of particular importance in the physics of inertial confinement fusion (ICF) [65].

## 1.1 Scope, Motivation, and Organization

What Rudinger and Somers (1960) first formally observed, and what is of concern in hydrodynamic instabilities in ICF implosions, is shock-induced compressible turbulent mixing. This is a powerful and effective means of mixing two fluids initially separated by an interface or by a set of interfaces. In the context of ICF, it leads to the intermingling of fuel and non-fuel materials, which can severely degrade the energy yield from fusion. In other contexts, however, mixing introduced by shock waves can be desirable, as in the case of supersonic combustion. In all contexts within which it is found, compressible turbulent mixing is the ultimate outcome of three fundamental sets of coupled hydrodynamic processes that operate simultaneously in shock-accelerated inhomogeneous flows: (1) shock-induced compression and heating; (2) shock reflection, refraction, and diffraction (or “nonlinear-acoustic” effects); and (3) vorticity production. Dramatic effects result from the interaction of these mechanisms, and include complex fields of secondary shocks and rarefactions, shock focusing, jetting, prominent and long-lived vortices, and regions of intense turbulent mixing.

In shock-bubble interactions, each of these processes is particularly strong when compared to similar effects seen in Richtmyer-Meshkov instabilities and other shock-contact interactions. This is because the bubble is an isolated body, and because its surface includes all possible inclinations to the incoming shock wave. The isolated, discrete nature of a bubble implies that all of the interior fluid is relatively near to the interface, and is therefore subjected to the deformation and vortical effects generated there. The closed geometry of the interface implies that on the bubble equator, the interface is normal to the incoming shock wave, and therefore is subject to the strongest shock-refraction effects and shock-induced vorticity deposition. Shock-bubble interactions therefore provide a configuration where shock-induced vorticity generation, interface deformation, and mixing are uniquely intense, although because of the discrete nature of the bubble, the volume where the effects are strongest is relatively small (in comparison to Richtmyer-Meshkov instabilities). Interest in the problem thus stems primarily from the intensity and localization of such effects, which can produce distinctive, transient hydrodynamic effects that are of great interest in the various applications described above.

In the present study, our purpose is threefold. First, the extensive database of two-dimensional simulations for shock-bubble interactions [79, 52, 113, 69, 34] is extended further, here, to three spatial dimensions. Such a study has long been recommended by researchers in the field [109, 52, 113] as a means of characterizing the response of the shocked-bubble flow to perturbations which break the symmetry of the initial condition, and the growth of turbulence-like disordered and chaotic features in the mixing region that develops as a result. Only within the past ten years has the capability arisen to simulate these flows computationally in three spatial dimensions at acceptable resolution and over realistic temporal scales.

For shock wave interactions with spherical bubbles, when axisymmetry is relaxed, Widnall-type [108] azimuthal vortex instability modes are free to grow on the vortex ring produced in the shock-bubble interaction, leading to the deterioration of the dominant vortical features and the growth of turbulence-like features in the flow. Although the initial seeds for the growth of these features cannot always be characterized experimentally, it is well known that microscopic asymmetries in initial interfaces, as well as molecular fluctuations, initially grow exponentially by Rayleigh-Taylor, Richtmyer-Meshkov, and Kelvin-Helmholtz instabilities during shock acceleration, so that a very wide range of length scales develops in the flow. Similarly, in numerical initial conditions, perturbations from symmetry are introduced by discretization errors and the projection of round features onto square meshes [53].

Some recent three-dimensional studies have indicated that this growth is crucial to the proper representation of the large-scale behavior of the flow [51, 93]. It is anticipated that the simulations performed here will provide a suitable database for investigating and parameterizing the growth of these features. In order to realize this expectation, a robust technique based on azimuthal averaging is defined here for characterizing high-Reynolds-number fluctuations arising in computed shock-bubble-interaction flowfields. This technique is employed to generate a turbulence-like description for shock-bubble interactions, including averaged and fluctuating fields, turbulence intensity profiles and temporal trends, and Fourier spectra.

The second and more immediate purpose of the current study is to produce a unified set of simulations that spans a significant portion of the parameter space of previous work on this problem, in order to facilitate the evaluation and continued development of analytical models and scaling laws for various features of shock-bubble interactions.

The data are therefore queried at closely-spaced time intervals in order to characterize time-dependent integral features of shock-bubble interactions and correlate the observed phenomenologies across the parameter space. These features include the spatial extents, translation speed, mean density, internal energy, circulation, and mixedness of the shocked bubble. This information is used to evaluate existing models and scaling laws, or to establish the conditions under which they may be regarded as reliable.

Thirdly, the parameter study is extended further to investigate an issue that has arisen in experimental investigations [86, 87], namely the effect of the thin liquid film layer typically present in experimental initial conditions. It is currently unclear whether such a film is capable of generating some features that have been observed in experiments, including secondary vortex rings and upstream and downstream jets. Effects associated with the inclusion of a thin, dense cladding on the bubble surface will be quantified and parameterized, with a view toward clarifying the mechanism for effects observed in experiments, and identifying the regions of the parameter space where they may be expected to be significant.

The scope of the present study is limited to the spherical-bubble scenario, and we place particular emphasis on the configuration where the bubble fluid has higher density than the ambient medium. Also, our focus is on thermodynamic environments that are accessible to mechanical, gas-phase shock tubes operating from atmospheric pressure. In comparison with laser- or x-ray-driven shock tubes and two-phase or liquid-phase experimental platforms, mechanical shock tubes provide both the most uniform and well-controlled planar shock waves, as well as the opportunity to take advantage of optical diagnostics which are not available in laser- or x-ray-driven shock tubes, and are less effective in two-phase environments. Thus, we confine our attention to Mach

numbers  $M \leq 5$ , and Atwood number magnitudes  $|A| \leq 0.8$ . For simplicity, multi-bubble and complex or non-spherical scenarios are also excluded. Further, because of the nature of planar-laser-based flow diagnostics used in recent shock tube experiments for shock-bubble interactions, which typically rely on flow tracers in the bubble gas, our focus here lies with the evolution of the bubble itself rather than the ambient medium and shock waves, though these aspects of the flowfield are included in the analysis when necessary.

Significant effort is also devoted to characterizing the reliability of the numerical method used here. If the results of the simulations presented here are to be used confidently to advance our understanding of shock-bubble interactions, such characterization is necessary in order to establish the correctness of the algorithms used in the simulations. To this end, verification of the convergence properties and mesh-sensitivity of solutions presented here are evaluated, and detailed comparison is made between computed solutions for various test problems and the results of theoretical, experimental, and previous numerical work. However, the comparison of experimental and numerical results for the specific shock-bubble interaction scenarios considered as part of the parameter study is beyond the scope of this work. For that reason, many of the details of experimental environments are absent from these simulations, including shock tube side and end walls. Since these scenarios have been chosen specifically for their links to experimental work, such comparisons in future work may take advantage of the results presented here.

Progress on these three primary objectives for the current study, within the scope just described, will contribute to the continued advancement of our understanding of various issues that are significant in the larger field of shock-contact interactions and

shock-accelerated inhomogeneous flows. The most important of these issues is the evaluation of numerical methods, and particularly of implicit large eddy simulation techniques for simulating flows with compressible turbulent mixing. The work described here constitutes a large body of data that may be compared to experimental results and theoretical predictions in order to determine whether confidence in such methods is well-founded. Other issues include the significance of three-dimensional effects such as vortex stretching, the conditions under which turbulent effects become important or cease to be important, the usefulness of scaling arguments based on shock wave speeds and shocked flow speeds, and the changes to such flows caused by interface-forming materials such as soap film.

The organization of this dissertation is as follows. In the remainder of Chapter 1, a general discussion of the physics of shock-bubble interactions is given, and the historical background and current understanding of this problem is discussed, based on experimental, numerical, and theoretical work in the literature. Chapter 2 provides a description of the numerical method (called *Raptor*) used in the simulations presented here, and of verification and validation tests performed in the context of shock-bubble interactions. The parameter study simulations are outlined in Chapter 3, with a detailed qualitative description of the computed solutions. In Chapter 4, the time-evolution of various integral features of the flowfields is presented, and comparison is made to analytical models and scaling laws for these quantities. Chapter 5 examines the more complex aspects of shock-bubble interactions appearing in these three-dimensional simulations, including non-axisymmetric features, turbulence, and mixing. The effects of the presence of a soap film layer on the bubble surface are characterized in Chapter 6 using a series of additional simulations. Finally, in Chapter 7, we provide a summary of the results of

this study, and their significance and limitations.

## 1.2 Overview of the Physics of Shock-Bubble Interactions

A shock-bubble interaction is the unsteady flow associated with the passage of a shock wave across a discrete inhomogeneity in an otherwise uniform medium. Here, we consider shock-bubble interactions in the specific context of a gaseous environment, a well-defined spherical interface, a planar incident shock wave, and a uniform isothermal inhomogeneity consisting of a foreign gas species with a thin interfacial transition layer. This is a dramatic simplification of the environments where shock-bubble interactions are typically found in nature and engineering applications, because we neglect all effects associated with incident shock wave curvature, incident wave thickness and pressure decay, interface diffusion thickness, complex interface geometries, radiative energy transfer, ionization, molecular dissociation, phase changes, chemical and nuclear reactions, and electric and magnetic fields. The physics that emerge under these simplifications are purely hydrodynamic, dominated by three coupled, simultaneous processes: (1) shock-induced compression and heating; (2) nonlinear-acoustic effects including shock reflection, refraction, and diffraction; and (3) vorticity production. Each of these processes constitutes a fundamental component of the phenomenology of shock-bubble interactions, which is summarized below.

### 1.2.1 Nomenclature

Before describing these processes in detail, we note that the following nomenclature is used here. The two fluids are indicated by subscripts 1 and 2, where fluid 1 is the ambient fluid and fluid 2 is the bubble fluid. Fluid properties including the molecular mass  $\mathcal{M}$  and ratio of specific heats  $\gamma$  are defined for each fluid. The speed of a shock wave is represented by  $W$ , its Mach number by  $M$ , and the incident and transmitted shock waves by subscripts  $i$  and  $t$ , respectively. Thus,  $W_i$  represents the incident shock wave speed (in the ambient fluid), and  $W_t$  the transmitted shock wave speed (in the bubble fluid). Flow variables are identified using a subscript 1 or 2 to indicate the fluid being described, and primes are used to indicate the number of shock or rarefaction waves that have passed over the fluid. These variables include pressure  $p$ , density  $\rho$ , and streamwise scalar velocity  $v$ . Hence,  $\rho_1$  and  $\rho_2$  represent the pre-shock density of the ambient and bubble fluids, respectively, and  $\rho'_1$  and  $\rho'_2$  represent the densities after the passage of the first shock wave. The ambient gamma-law sound speed can then be written as  $c_1 = \sqrt{\gamma_1 p_1 / \rho_1}$ , the incident Mach number as  $M = W_i/c_1$ , an Atwood number as  $A = (\rho_2 - \rho_1)/(\rho_2 + \rho_1)$ , and an initial density ratio as  $\chi = \rho_2/\rho_1$ . Finally,  $f$  represents the bubble fluid volume fraction field and  $\mathbf{U}$  the velocity vector field.

### 1.2.2 Shock-induced compression

The most fundamental effect of shock wave passage over a bubble is the sudden jump in pressure, density, and total energy. For a normal shock wave propagating in the  $+x$ -direction at constant speed  $W$  into a homogeneous stagnant gas, the change in the state of the fluid across the shock wave can be obtained directly from the laws of conservation

of mass, momentum, and energy. If we consider a reference frame moving with the shock wave, and define  $\rho$  ( $\rho'$ ),  $u$  ( $u'$ ),  $p$  ( $p'$ ),  $T$  ( $T'$ ), and  $h$  ( $h'$ ) to be the density, velocity, pressure, temperature, and enthalpy of the fluid ahead of (behind) the shock front, then conservation of mass, momentum, and energy requires:

$$\rho W = \rho' (W - u') \quad (1.1)$$

$$p + \rho W^2 = p' + \rho' (W - u')^2 \quad (1.2)$$

$$h + \frac{W^2}{2} = h' + \frac{(W - u')^2}{2}, \quad (1.3)$$

where we have assumed there is no heat addition or removal at the boundary (*i.e.*, the flow is adiabatic), and no external forces or viscous stresses are present. For a calorically perfect gas with a specific heat ratio  $\gamma$ , we have

$$h = e + \frac{p}{\rho} = \frac{\gamma \mathfrak{R} T}{\mathcal{M}(\gamma - 1)}, \quad (1.4)$$

where  $\mathfrak{R}$  is the universal gas constant. Formulae can then be derived, which give, explicitly,  $\rho'$ ,  $T'$ ,  $u'$ , and  $W$  for a given pressure ratio  $p'/p$  and initial conditions  $\rho$ ,  $u$ ,  $p$ , and  $T$  [1, 55, 64]. These formulae are described in detail in Appendix A.

The system given by Eqs. 1.1-1.3 can be extended to the situation where a normal shock wave propagates across a planar gaseous interface (also described in Appendix A) by enforcing mechanical equilibrium at the interface, *i.e.*, by requiring that the interface remain stationary with respect to the gas on both sides of it at all times. Thus, the pressure and normal velocity are both required to remain continuous at the interface throughout shock passage. These requirements are referred to as dynamic and kinematic matching conditions, and can be written as

$$\left. \frac{\partial p}{\partial x} \right|_{x=d} = 0 \quad (1.5)$$

$$\left. \frac{\partial u}{\partial x} \right|_{x=d} = 0, \quad (1.6)$$

where  $x = d$  is the interface location.

Upon shock wave impact on the interface, these conditions may be satisfied by postulating the appearance of a reflected wave and a transmitted wave in the system. The nature of these waves depends on the sign of the change in acoustic impedance across the interface. The acoustic impedance  $\mathcal{R} = \rho c$  is a measure of the stiffness of the material, in the sense that the motion of a fluid in response to a pressure impulse  $\delta p$  is given by  $\delta u = \delta p / \mathcal{R}$  [106]. (The acoustic impedance  $\mathcal{R}$  is unrelated to the gas constant  $\mathfrak{R}$ , and the symbol  $\mathcal{R}$  is used in reference to the analogy with ohmic resistance.) The change in acoustic impedance is referred to as “impedance mismatch,”  $\delta\mathcal{R} = \mathcal{R}_2 - \mathcal{R}_1$ . If  $\delta\mathcal{R} < 0$ , then the shock wave increases in speed after transmission, and the initial gas must expand in order to maintain mechanical equilibrium at the interface. Thus, the reflection is a rarefaction wave. Conversely, if  $\delta\mathcal{R} > 0$ , then the shock wave decreases in speed after transmission, and the initial gas must contract in order to maintain mechanical equilibrium at the interface. In that case, the reflection is a shock wave.

The transmitted wave, however, is always a shock wave [55]. This is true regardless of the shape of the interface or the orientation of the interface to the shock. Thus, in shock-bubble interactions, the immediate effect of shock impact on the bubble is the sudden increase of the density, pressure, and total energy of the bubble gas corresponding to the transmitted shock wave strength, regardless of the sign of  $\delta\mathcal{R}$ . The magnitude of the increase can be estimated by neglecting, for the moment, the curvature of the

interface, and examining shock passage over the bubble surface at the nearest tangent point, where curvature is minimal, using a one-dimensional description.

For one-dimensional shock passage over a single discontinuous interface between two gases, the post-shock flow properties are piecewise-constant functions of the  $x$ -coordinate, except within a small region occupied by the wave front itself. For shock waves, the streamwise dimension of this region is on the order of the molecular mean free path of the gas, and may be regarded as vanishingly small. For rarefaction waves, this region has finite thickness, and the fluid properties vary continuously with  $x$  in this region. These regions are shown in Fig. 1, for the case of  $\mathcal{R}_2 > \mathcal{R}_1$ , where the reflected wave is a shock wave.

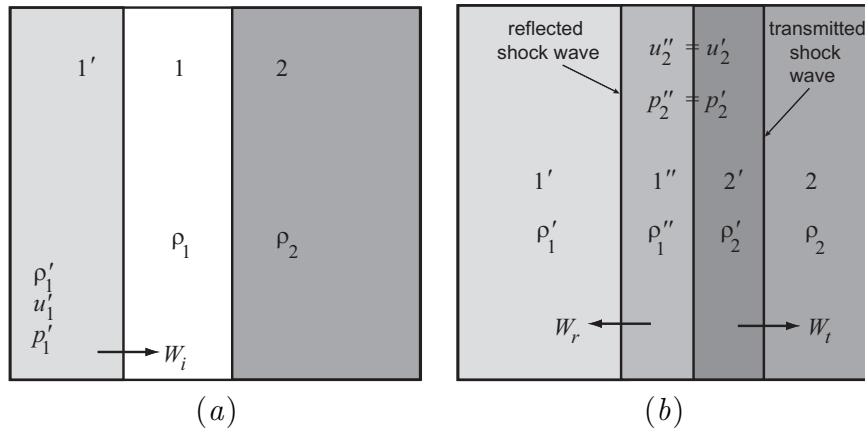


Figure 1: Schematic diagram of one-dimensional shock transmission and reflection at a discontinuous interface where  $\mathcal{R}_2 > \mathcal{R}_1$ : (a), pre-shock; (b), post-shock.

The shocked interface system then consists of five regions: region 1 is the unshocked upstream gas, region 2 is the unshocked downstream gas, region 1' is the shocked upstream gas, region 2' is the downstream gas that has interacted with the transmitted shock wave, and region 1'' is the upstream gas that has interacted both with the initial

incident shock wave and with the shock or rarefaction wave reflected from the interface. If the initial, unshocked conditions and incident shock strength are known, the flow properties in each of the other four regions can be computed by iteratively solving an algebraic system of equations derived from Eqs. 1.1-1.3 for each wavefront and Eqs. 1.5-1.6 for the interface (with a gamma-law equation of state for each fluid).

This system can be extended to the case of a one-dimensional gas slab by adding a second interface to the problem, where the gas behind the second interface has the same composition as the initial gas. Then the system based on Eqs. 1.1-1.3 can be solved for each shock wave by enforcing Eqs. 1.5-1.6 at both interfaces. By recursively computing changes in fluid properties at each shock-interface interaction, the solution can be built up to include fluid properties in each of the regions shown on the  $x$ - $t$  plots in Fig. 2, except those regions occupied by rarefaction waves. A complete system of equations that describes the transmission of a shock wave over a gas slab, up through two internal reflections, is given in Appendix A.

In this way, the state of a gas slab subjected to acceleration by a planar shock wave may be tracked analytically through the interaction of each wave with each interface. This provides a very simple analogy for shock-bubble interactions, where the effects of interface curvature and shock wave refraction are neglected. Using this type of simulation, important parameters of the post-shock flow may be estimated *a priori* from the initial shock strength and the thermodynamic state of the bubble and ambient fluids. This approach has been used by Giordano and Burtschell (2006) [34] to predict the change in the volume of a bubble due to interaction with a shock wave, via the change in the bubble fluid density in the one-dimensional approximation.

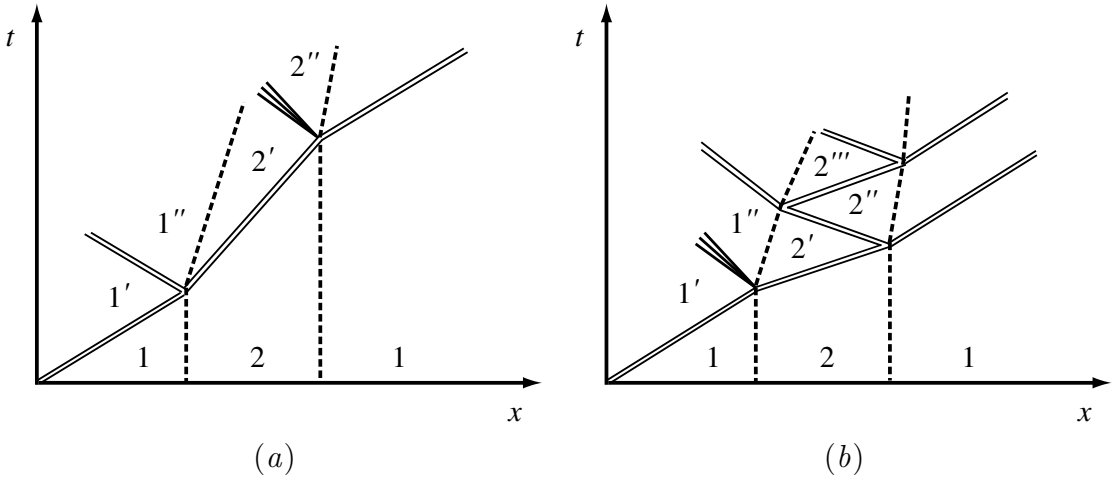


Figure 2: Schematic diagram of 1D shock transmission and reflection in a one-dimensional gas slab: (a),  $\mathcal{R}_2 > \mathcal{R}_1$ ; (b),  $\mathcal{R}_2 < \mathcal{R}_1$ . Solid double lines indicate shock waves, dashed lines indicate fluid interfaces, and triple diverging solid lines indicate rarefaction waves.

### 1.2.3 Nonlinear-acoustic effects

The curvature of the interface introduces two strong effects that intensify (and often irregularize) the shock-induced compression, heating, and acceleration expected from the one-dimensional-gasdynamics analysis given above: (1) nonlinear-acoustic effects, which produce additional shock and rarefaction waves in the flowfield, and (2) vorticity production, which introduces transverse and rotational motion, and severely deforms the bubble interface.

“Nonlinear-acoustic effects” refers to the refraction, reflection, and diffraction of the incident shock wave by the bubble. These effects were first highlighted and thoroughly documented for shock-bubble interactions by Haas and Sturtevant (1987) [42]. Because of the acoustic impedance mismatch at the interface, the bubble acts like a converging or diverging lens. For impedance mismatch  $\delta\mathcal{R} < 0$ , the transmitted shock wave develops

convex curvature due to refraction, running ahead of the exterior, unrefracted shock wave. This situation is therefore referred to as “divergent geometry.” Conversely, for  $\delta\mathcal{R} > 0$ , the transmitted shock wave develops a concave curvature and falls behind the unrefracted shock wave, and this situation is called “convergent geometry.”

These two scenarios are depicted schematically in Fig. 3. “Refraction” refers to this change in shock wave shape due to the impedance mismatch and the curvature of the interface, seen in both the convergent and divergent scenarios in Fig. 3. If we let  $\phi$  denote the local angle of incidence between the shock front and the interface on which it is incident, then for small  $\phi$ , the incident, reflected, and transmitted portions of the shock wave must all meet at a single point on the interface. For  $\phi > \phi_c$ , where  $\phi_c$  is called the “critical angle,” the refraction pattern becomes “irregular” in the divergent case, meaning that different portions of the shock wave no longer meet at a single point, but one runs ahead of the other, and secondary shock waves or Mach reflections are generated, which connect them [46, 47]. Specifically, a precursor shock wave connects the incident (unrefracted) shock wave to the transmitted wave, and a Mach stem develops outside the bubble between the incident shock wave and the bubble surface. These three discontinuities meet at a “triple point,” just outside the bubble. These features of the irregular shock refraction pattern are shown in Fig. 3(a). The critical angle for irregular refraction decreases with increasing  $M$  and decreasing (negative)  $\delta\mathcal{R}$ , and is generally much less than  $\pi/2$  [99]. Therefore, we expect to observe irregular refraction, and thus secondary features such as Mach stems and precursor shock waves, in many shock-bubble interactions in divergent geometry, since the angle of incidence varies between zero and  $\pi$  during shock passage.

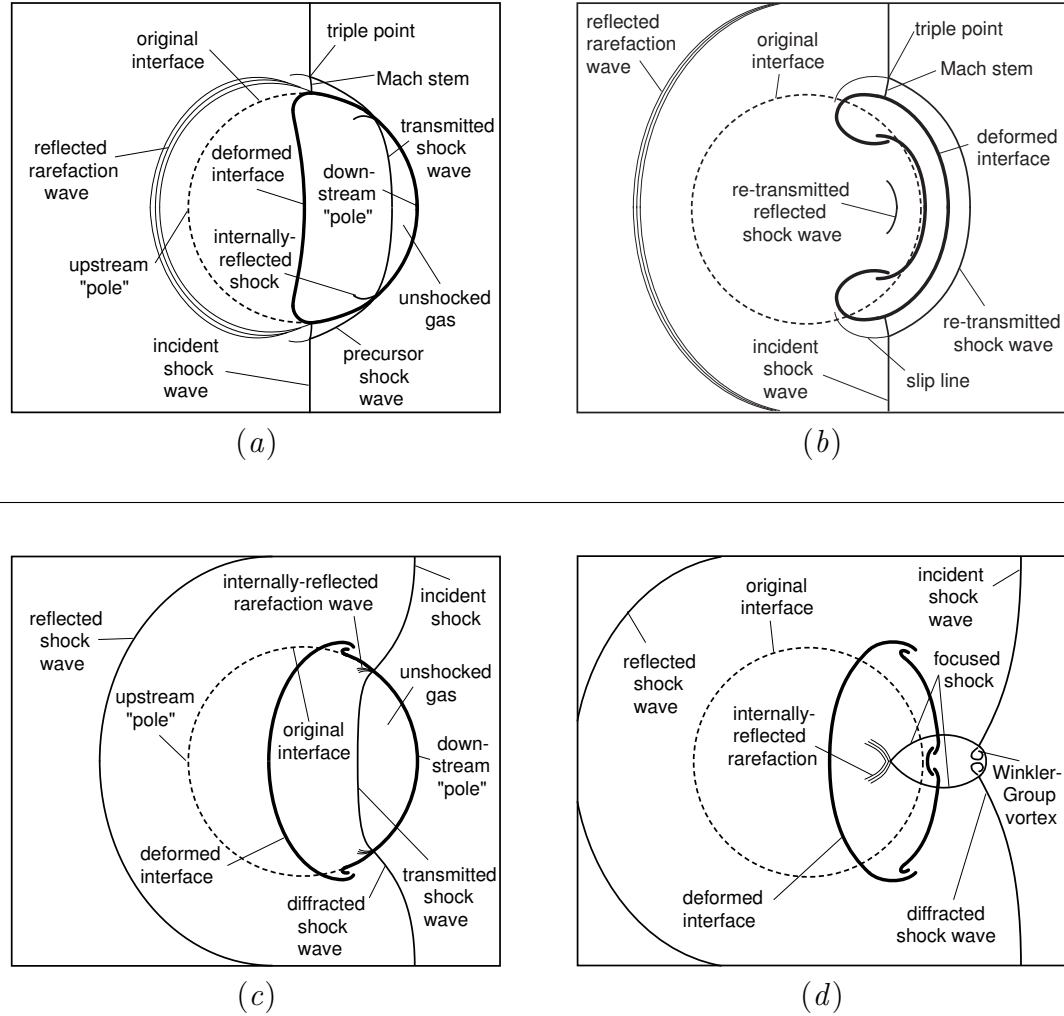


Figure 3: Representative, schematic view of shock-bubble interaction flowfield and shock refraction patterns. Divergent ( $\delta\mathcal{R} < 0$ ) scenario: (a) during initial shock wave transit, and (b) shortly after initial shock wave transit. Convergent ( $\delta\mathcal{R} > 0$ ) scenario: (c) during initial shock wave transit, and (d) shortly after initial shock wave transit. Incident shock wave propagation is left-to-right.

The divergent scenario is also characterized by the appearance of an upstream-directed reflected rarefaction wave in the ambient gas, and by the generation of an internally-reflected shock wave upon impact of the transmitted shock wave at the downstream bubble surface. In divergent geometry, all internally-reflected waves are shock waves, as shown in Fig. 2. In this scenario, also, because of the formation of irregular shock refraction patterns, a slip surface can be traced in the flowfield along the path traveled by the triple point.

In convergent geometry ( $\delta\mathcal{R} > 0$ ), other dramatic effects associated with shock refraction dominate, particularly at high Mach number and high impedance mismatch. These include, most importantly, for  $M \gg 1$  and/or  $\delta\mathcal{R} \gg 0$ , shock diffraction and focusing. If the impedance mismatch is high enough, portions of the shock wave front sweeping around the bubble periphery are diffracted [42, 84], meaning that for  $\phi > \pi/2$  they are turned toward the axis so that the surface of discontinuity remains nearly normal to the interface, as shown in Fig. 3(c). These diffracted shock waves may then converge with each other and with the transmitted shock wave at the downstream pole, resulting in a short-lived period of very high energy densities and a strong, localized pulse in pressure at the downstream pole. This effect is referred to as shock focusing. The reconvergence of diffracted shock waves, shown in Fig. 3(d) can lead to the interaction of additional discontinuities with the bubble, which propagate in the lateral and upstream directions. The effects of shock diffraction and focusing together can amount to a reshock phenomenon of the type described in the Richtmyer-Meshkov literature [17, 58, 100].

The convergent scenario  $\delta\mathcal{R} > 0$  is also characterized by the appearance of an internally-reflected rarefaction wave arising at the downstream bubble surface after

impact of the transmitted shock wave. This rarefaction wave can cause a violent re-expansion of the bubble after the initial compression, for large  $M$ , which follows very shortly after the strong compression associated with shock focusing and the reconvergence of diffracted shock waves. Thus, for convergent geometry, the bubble may be subjected to strong alternating compression and expansion phases shortly after the initial shock transit. Many of these effects are absent, however, for low  $M$  and low  $\delta\mathcal{R}$ . The internally-reflected waves, along with the discontinuities associated with irregular shock refraction, shock diffraction, and shock focusing – which arise after the passage of the initial planar shock wave – we refer to collectively as “secondary” waves. These play a significant role in the late-time development of the flowfield.

Because the geometry of this problem leads to the development of deformation patterns and shear layers with many features similar to those found in Rayleigh-Taylor, Richtmyer-Meshkov, and Kelvin-Helmholtz instabilities, the Atwood number  $A$  is used henceforth rather than the impedance mismatch  $\delta\mathcal{R}$ , to indicate the expected sense and relative magnitude of effects associated with the density contrast at the interface. Although the convergent/divergent orientation of shock refraction patterns is controlled by  $\delta\mathcal{R}$ , shock refraction only takes place during the initial phases of this flow. After several shock-passage times, the flow is dominated by vortical motion, interface deformation, and turbulent mixing. These processes are more aptly described using  $A$ . It is important to note, however, that shock-bubble interactions will exhibit a divergent, refraction pattern in the nonuniform- $\gamma$  case for  $\delta\mathcal{R} < 0$ , even if  $A > 0$ , and *vice versa*. It is therefore possible for externally reflected shock waves to appear in some cases with  $A < 0$ , if the change in the ratio of specific heats  $\gamma$  offsets the change in density. Conversely, externally reflected rarefaction waves may develop for  $A > 0$ . However, unusual

cases such as these do not appear in the present study. For the scenarios considered here,  $A < 0$  implies  $\delta\mathcal{R} < 0$  and divergent refraction, and  $A > 0$  implies  $\delta\mathcal{R} > 0$  and convergent refraction.

### 1.2.4 Vorticity production

As this field of shock waves (including the “primary” incident shock wave, along with the “secondary” refracted, reflected, diffracted, and focused waves) passes over the bubble, vorticity is produced in the flow. Defining the vorticity  $\boldsymbol{\omega} \equiv \nabla \times \mathbf{U}$ , the production and transport of vorticity is described using the vorticity transport equation,

$$\frac{D\boldsymbol{\omega}}{Dt} - (\boldsymbol{\omega} \cdot \nabla) \mathbf{U} + \boldsymbol{\omega} (\nabla \cdot \mathbf{U}) = \frac{1}{\rho^2} (\nabla \rho \times \nabla p) + \nu \nabla^2 \boldsymbol{\omega}, \quad (1.7)$$

This transport equation for  $\boldsymbol{\omega}$  is obtained by taking the curl of the momentum equation for compressible flow, and is derived from the momentum equation in Appendix B. The physical interpretation of the terms appearing in the equation is as follows.

The second and third terms on the left arise from the convective term in the momentum equation ( $(\mathbf{U} \cdot \nabla) \mathbf{U}$ ). Although they appear here on the left-hand side, they may both be viewed in effect as source terms. The second term is  $(\boldsymbol{\omega} \cdot \nabla) \mathbf{U}$  and represents “vortex stretching,” or the straining of vortex lines (lines everywhere parallel to  $\boldsymbol{\omega}$ ) by gradients in the velocity field. That is, the contraction of a vortex line decreases its vorticity, and the stretching of a vortex line increases its vorticity, by the conservation of angular momentum. Also, the turning of vortex lines by the velocity field can intensify or diminish the vorticity. The third term on the left is  $\boldsymbol{\omega} (\nabla \cdot \mathbf{U})$ , and represents vortex “compression” found in regions of converging or diverging flow ( $\nabla \cdot \mathbf{U} \neq 0$ ).

On the right-hand side, two terms appear, representing vorticity sinks and sources.

Appearing last is the viscous term  $\nu \nabla^2 \boldsymbol{\omega}$ , which represents the dissipation of vorticity by viscous stresses. Dissipative effects can be neglected here because of the low physical viscosities of the fluids considered ( $\mu \sim 10^{-5}$  Pa·s), and the short timescales ( $t \sim 10^{-3}$  s) over which the flow evolution is studied. In the absence of viscous effects, then, the only remaining term on the right in Eq. 1.7 is the baroclinic source term,  $\frac{1}{\rho^2} (\nabla \rho \times \nabla p)$ . This arises from the  $-\nabla p / \rho$  term in the momentum equation. Although this term vanishes in the case of constant-density flows, in compressible flows with density inhomogeneities, vorticity grows locally by baroclinicity wherever the density and pressure gradients are misaligned.

In flows with  $\boldsymbol{\omega} = 0$  everywhere initially, the vortex stretching and compression terms are identically zero. In the absence of viscous effects, then, the vorticity equation can be rewritten for these cases at time zero as

$$\left. \frac{D\boldsymbol{\omega}}{Dt} \right|_{t=0} = (\nabla \rho \times \nabla p) / \rho^2, \quad (1.8)$$

and baroclinicity is thus the origin of all rotational motion that appears in the flowfield. This baroclinic vorticity generation is responsible for the development of instabilities in accelerated inhomogeneous flows including Richtmyer-Meshkov and Rayleigh-Taylor instabilities, and of various instabilities in stratified oceanic and atmospheric flows [70, 2].

On the basis of the vorticity equation, we therefore expect vorticity to grow locally on the fluid interface during passage of a planar shock wave over a spherical bubble. As shown in the schematic diagram in Fig. 4, an upstream-directed pressure gradient is provided by the shock wave. Through the baroclinic mechanism, this pressure gradient interacts with the radially-directed density gradient associated with the curved material interface, inducing the appearance of vorticity on the bubble surface as shown in Fig. 4.

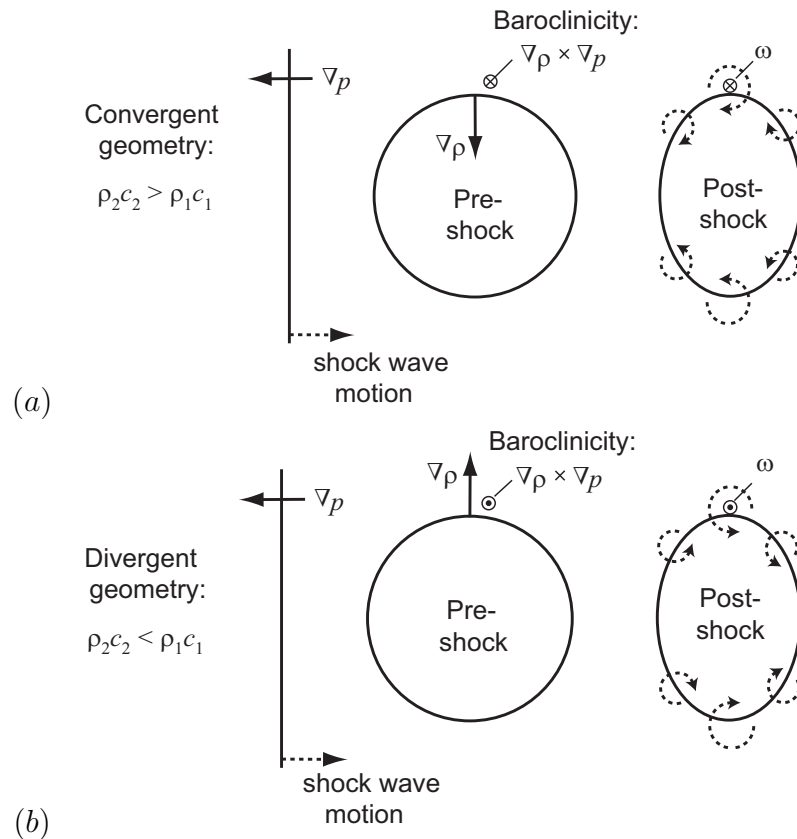


Figure 4: Representative, schematic view of the arrangement of vectors in baroclinic vorticity deposition during and after initial shock transit in shock-bubble interactions in (a) convergent and (b) divergent geometry.

The direction of rotation is determined by the orientation of the density gradient at the bubble surface, and the local magnitude of vorticity growth is determined by the misalignment of  $\nabla p$  and  $\nabla \rho$ . The maximum misalignment is at the bubble equator, where  $\phi = \pi$ , and the maximum vorticity magnitude is therefore generated at this location. This drives the formation of a primary vortex ring near the bubble equator, whose vorticity vector is perpendicular to both the direction of shock wave motion and the radial vector, thus following the azimuthal direction. This primary vortex ring is the dominant feature in the resulting flow, and strongly deforms the interface during and after the passage of the initial shock wave.

Baroclinicity associated with the interaction of the initial planar shock wave with the spherical fluid interface is thus the fundamental mechanism of vorticity production in shock-bubble interactions. However, it should be noted that the total derivative in Eq. 1.7 implies the action of vorticity advection by the velocity field, which is responsible for the redistribution of the baroclinically generated vorticity in the flowfield: *i.e.*, the rolling up of the bubble surface into vortex rings, and the development of Kelvin-Helmholtz vortices in the flowfield in some cases.

Further, after the passage of the initial shock wave, three additional effects lead to further intensification and redistribution of vorticity in the flow. These include (1) baroclinic vorticity generation by secondary shock and rarefaction waves passing over or near the deforming fluid interface [113], (2) baroclinic vorticity generation by centrifugal pressure gradients and density gradients associated with well-developed vortices (“vortex-accelerated vorticity deposition”) [78], and (3) the three-dimensional transport of vorticity by the  $(\boldsymbol{\omega} \cdot \nabla) \mathbf{U}$  vortex stretching mechanism of Eq. 1.7. The strength of

these three mechanisms varies widely with the incident shock wave Mach number, initial Atwood number, and acoustic impedance mismatch. When the magnitude of these effects is great, they can significantly alter the behavior of the flow, and strongly distort and complicate the evolution of the fluid interface, leading, often, to the growth of features including secondary vortex rings, opposite-signed vorticity, and jetting. We refer to these mechanisms collectively as “secondary” vorticity generation, and to (1) and (2) as secondary baroclinic vorticity generation.

As for mechanism (3), it is important to note that the mechanism denoted by  $(\boldsymbol{\omega} \cdot \nabla) \mathbf{U}$  is absent in plane flow [76, 82, 101], and in flows that are uniform in the third dimension. This is apparent from the observation that in two-dimensional flows,  $\mathbf{U}$  can have no variation in the direction of  $\boldsymbol{\omega}$ . Hence, we observe that three-dimensional effects are absent in shock-bubble interactions that have perfect symmetry in the azimuthal direction. Such a symmetric configuration is possible only in theory, since even in the most isolated physical environments, thermal noise is sufficient to introduce non-axisymmetric components to the velocity field, which may operate on the vorticity field via the vortex stretching mechanism. Further, in most natural and engineered environments where shock-bubble interactions are found, non-axisymmetric features in the initial condition can be quite significant, so that three-dimensional treatment is necessary. Widnall *et al.* (1974) [108] showed, for the incompressible, laminar case, that non-axisymmetric perturbations can grow nonlinearly to produce significant azimuthal modal structure on vortex rings.

Thus, the underlying physics of the shock-bubble interaction involve sets of intense, simultaneous, and coupled processes, including shock-induced compression, nonlinear-acoustic effects, and vorticity generation. This yields a parameter space that is very

difficult to characterize, as effects due to one process or another may accumulate non-linearly to generate distinctive behavior in one region of the parameter space that is not seen in other regions. This complexity has inspired a great number of experimental and numerical investigations, outlined below in Sec. 1.3.

## 1.3 Overview of Relevant Previous Studies of Shock-Bubble Interactions

### 1.3.1 Seminal experimental work

Shock-bubble interactions were first investigated in detail in the work of Rudinger and Somers (1960) [95], who were interested in quantifying the response of flow-tracer bubbles to acceleration, with and without shock waves. Using a spark discharge to generate a roughly cylindrical column of heated, low-density gas across a shock tube either before or after passage of a shock wave, they showed clearly that the response of the cylindrical bubble was radically different when acceleration was accompanied by the passage of a shock wave over the bubble. The relative velocity, shape, and volume of the shocked bubble was drastically changed with respect to the shock-free case. Rudinger and Somers verified that these effects were due to vortical instabilities excited during shock wave passage over the spark column, and they introduced a simple model for the relative velocity of the shocked bubble. Very well-resolved schlieren images of shock wave propagation over a roughly spherical flame bubble from the experimental work of Rudinger (1958) [94] were also presented in figure 7, giving further confirmation of this conclusion and evidence of the formation of a vortex ring.

Since that time, a rich database of literature has developed related to the subject of shock-bubble interactions, particularly within the last twenty years. In their seminal paper of 1987, Haas and Sturtevant [42] reported on experiments performed in a horizontal shock tube, subjecting cylindrical and spherical bubbles to acceleration by planar shock waves, in both convergent-geometry (air-R22) and divergent-geometry (air-helium) cases. By analogy to geometrical acoustics, they constructed a detailed description of the refraction, reflection, and diffraction processes to which the initial shock wave is subjected during its interaction with a bubble of circular cross section, and the consequent patterns of secondary shock wave development. The configuration of rays and wavefronts in shock-bubble interactions (for cylindrical bubbles) computed using geometrical acoustics was presented by Haas and Sturtevant in figures 1-4.

Haas and Sturtevant also produced very highly-resolved shadowgraph images of the post-shock evolution of the shocked bubbles, for the divergent and convergent scenarios, at Mach numbers  $M \leq 1.25$ . These distinctive images, found in figures 8-14 of the 1987 paper, exhibited the development of complex shock refraction and diffraction patterns in shock-bubble interactions as expected from geometrical acoustics calculations, and depicted the deformation of the bubble and the development of vortical features and mixing regions. Haas and Sturtevant used the theory of Kelvin for the translational motion of vortex rings [54] to compute the total circulation associated with these vortical features in the spherical-bubble scenarios. More detailed results and analysis from this work can be found in the dissertation of J. F. Haas [41].

### 1.3.2 Recent experimental work

A number of experimental studies for shock-bubble interactions have appeared more recently, beginning with the work of Layes *et al.* (2003,2005) [60, 61], in which high-speed shadowgraph photography was used to capture the interaction of shock waves at  $M \leq 1.25$  in air with spherical soap bubbles filled with krypton, nitrogen, or helium. Layes *et al.* produced further qualitative characterization of the flow evolution for shock-bubble interactions, and showed that for each of the cases they studied, at late times, the streamwise dimension of the bubble grew at a constant rate and the shocked bubble moved at a constant translational speed. More extensive analysis of the experimental results, as well as data for  $M \leq 1.68$  can be found in the dissertation of G. Layes [59], and in the work of Giordano and Burtschell (2006) [34] and Layes and LeMétayer (2007) [62].

Experimental results have appeared recently in the work of Ranjan *et al.* (2005) [86] for shock-bubble interactions at higher Mach numbers than was studied by Haas and Sturtevant or Layes *et al.* Ranjan *et al.* (2005) have studied the case of a soap bubble filled with argon, accelerated by a  $M = 2.88$  shock wave in nitrogen, using planar laser diagnostics to capture the flowfield development on a section near the bubble midplane. Further, Ranjan *et al.* (2007) [87] have used similar diagnostic techniques to study the case of a helium-filled bubble, accelerated by a  $M = 2.95$  shock wave. In both cases, the shocked bubble was found to reach a constant translational velocity at late times, as reported by Layes *et al.*, but distinct secondary vortex rings were observed to form at later times as well, which had not been observed previously in experimental results for lower Mach numbers. These long-lived secondary vortex rings can be seen clearly in the planar-laser-illuminated images found in Fig. 2 of the 2005 paper, and in Fig. 4 of

the 2007 paper.

Several studies of shock-bubble interactions in the context of laser-driven shock-tube experiments have also appeared recently. Klein *et al.* (2003) [51] studied the case of a solid copper sphere embedded in a low-density foam medium, accelerated by a shock wave at  $M \approx 10$  driven by x-ray ablation of the foam material. They found that the late-time development of the shocked sphere showed structural characteristics that could be accounted for by the action of three-dimensional Widnall-type azimuthal instabilities. Also, Hansen *et al.* (2007) [43] studied a similar case using a solid aluminum sphere embedded in a foam medium, with an ablatively-driven shock wave. Using improved flow diagnostics they also found Widnall instabilities to be significant in the development of the shocked sphere, and proposed a model to describe the stripping of mass from the sphere by the shock wave and post-shock flow. These three-dimensional structure development and mass-stripping effects are clearly visible in the x-ray radiographs shown in Fig. 3 of the 2007 paper.

### 1.3.3 Two-dimensional numerical simulations

A number of very thorough two-dimensional numerical investigations of particular instances of shock-bubble interactions have also appeared in the literature. Picone and Boris (1988) [79] were the first to simulate the experiments of Haas and Sturtevant. Although their two-dimensional simulations only achieved a grid resolution of less than 50 cells per bubble radius ( $R_{50}$ ), they captured the development of the vortical features observed by Haas and Sturtevant. They devised a model for the circulation in shock-bubble interactions (see also Ref. [80]); however, this model consistently overpredicted the circulation. Later, Quirk and Karni (1996) [84] used an adaptive mesh refinement code

to simulate the Haas and Sturtevant cylindrical-bubble experiments, in both convergent and divergent geometry, with 446 cells per bubble radius ( $R_{446}$ ). These simulations successfully resolved many of the fine details of the complex, highly vortical flowfield and the pattern of refracted, reflected, and diffracted shock waves observed and described by Haas and Sturtevant. Direct comparison between experimental and simulated flowfields is shown in the color plots in figures 7 and 8 of Quirk and Karni.

Several other computational studies focused on particular aspects of shock-bubble interactions. Winkler *et al.* (1987) [109] simulated the interaction of a  $M = 2$  shock wave with a spherical bubble of a relatively dense gas to highlight the observed development of a supersonic vortex ring downstream from the bubble in the post-shock flow. Cowperthwaite (1989) [20] produced low-resolution ( $R_{20}$ ) simulations for air-freon-12 and helium-freon-12 shock-bubble interactions, demonstrating agreement with simple models for the post-shock density and velocity of the bubble. Zabusky and Zeng (1998) [113] produced a compelling analysis of the specific case of a spherical bubble of refrigerant gas R12 accelerated by shock waves of various strengths, demonstrating, in particular, the crucial importance of secondary shock waves and opposite-signed vorticity in the ultimate development of the shocked bubble. The development of secondary vortical features and opposite-signed vorticity over time was depicted strikingly by Zabusky and Zeng in plots of the  $r$ -integrated vorticity from simulated flowfield, shown in figures 12 and 16 of the 1998 paper. More recently, Marquina and Mulet (2003) [69] produced simulations of the Haas and Sturtevant helium cylinder experiments, with very high spatial resolution (890 grid points per bubble radius), showing the growth of distinctive “turbulent” features resulting from the shock-bubble interaction. Giordano and Burtschell (2006) [34] simulated the experiments of Layes *et al.* (2003, 2005) [60, 61] with spherical

helium, nitrogen, and krypton bubbles in air, contrasting the development of spherical and cylindrical bubbles, and successfully employing a simple model based on 1D gas dynamics to predict the total bubble volume at late times in the shock-bubble interaction.

### 1.3.4 Three-dimensional numerical simulations

As computational resources have improved dramatically over the past two decades, the capability has arisen to simulate shock-bubble interactions numerically in three spatial dimensions at adequate grid resolution. Since certain fundamental aspects of the flowfield evolution in shock-bubble interactions, particularly at high Mach numbers and Atwood numbers, are inherently three-dimensional, such simulations have proven meaningful. However, the scope of numerical work on three-dimensional shock-bubble interactions has been limited. Results from the first fully three-dimensional simulations for shock-bubble interactions were presented by Stone and Norman (1992) [102]. Their simulations were performed at a modest spatial resolution of  $R_{60}$  and indicated that vortex rings forming in shock-bubble interactions within astrophysical contexts at  $M \sim 10$  are unstable in three dimensions, and tend to disintegrate into fragments at late times. Fig. 2 in the 1992 paper shows three-dimensionally rendered images of the vorticity distribution in these high- $M$  shock-bubble interactions.

More recently, the work of Klein *et al.* (2003) [51] included a three-dimensional adaptive mesh refinement simulation for the interaction of a  $M \sim 10$  shock wave with a solid copper sphere in a low-density foam medium. This simulation showed that an azimuthal bending-mode instability similar to the Widnall instability for incompressible flows [108] acts to break up the primary vortex ring generated in the shock-bubble interaction. This azimuthal redistribution of the sphere mass accounted for features of

the experimental data that could not be fully explained by two-dimensional simulations. This is depicted clearly in Fig. 19 of the 2003 paper, which shows a three-dimensionally-rendered image of the “multimode fluted” azimuthal structure appearing on the shocked sphere at late times. Three-dimensional simulations have thus shown useful results in various studies for shock-bubble interactions, but a more comprehensive study of shock-bubble interactions in three spatial dimensions is needed in order to extend the basis by which such three-dimensional mechanisms in shock-bubble interactions across a wide range of Mach numbers and Atwood numbers are understood.

### 1.3.5 Two-dimensional parameter studies

Such a broad-scoped approach to the problem of shock-bubble interactions has been used in a number of studies based on two-dimensional numerical simulations. In the work of Klein, McKee, and Colella (1994) [52] (henceforward, “KMC94”), an extensive series of two-dimensional simulations was carried out for shock-bubble interactions in astrophysical contexts, for initial density ratios  $3 \leq \chi \leq 400$ , and Mach numbers  $10 \leq M \leq 1000$ . KMC94 provided a thorough analysis of many aspects of the shocked bubble across this parameter space, including the mean pressure and density, dimensions, velocity, velocity dispersion, circulation, and fragmentation. They performed this analysis on the basis of timescaling arguments and simple theoretical models which allowed them to examine the dependence of these properties on the initial density ratio  $\chi$  and the Mach number  $M$ . Although the models and scaling arguments were not applied and compared to the numerical results consistently for each of the scenarios considered in the study of KMC94, they showed significant evidence for Mach scaling of the flowfield within this parameter space. Plots of the density contours from their simulations for  $M = 10$  and

$M = 1000$  shock-bubble interactions at  $\chi = 10$ , given in Fig. 2 in the 1994 paper, clearly show the strong qualitative similarity of the flowfield for Mach numbers varying over a very large range.

The work of KMC94 was performed in the high- $M$  region of the parameter space. For  $M \geq 10$ , KMC94 expected the flow evolution to be independent of  $M$ , because their formulations of the shock jump conditions for pressure and density (Eqs. 4.1 and 4.2 in KMC94) approach an asymptote for  $M \rightarrow \infty$ , and because of the Mach-scaling properties of the Euler equations [96]. In other parametric studies, the shocked bubble evolution has been studied for  $M < 10$ , where the Mach scaling hypothesis may not hold. These include the two-dimensional numerical work of Samtaney and Zabusky (1994) [99], Bagabir and Drikakis (2001) [3], and Levy *et al.* (2003) [63], as well as the three-dimensional numerical work described in this dissertation.

Samtaney and Zabusky (1994) [99] (henceforward, “SZ94”) produced a comprehensive analysis of shock-contact interactions in various geometries, including planar-inclined, sinusoidal, and circular interfaces. They devised scaling laws for the rate of circulation deposition during shock wave passage over these interfaces, based on shock polar analysis, and performed two-dimensional Eulerian simulations using a second-order Godunov code for a wide range of Mach numbers and density ratios, to compare to these scaling laws. For circular interfaces, these simulations spanned Mach numbers  $1.05 \leq M \leq 2.0$  and density ratios  $2.6 \leq \chi \leq 33.0$ . The analysis of SZ94 was limited primarily to the circulation, but their results for temporal trends in the circulation showed fairly consistent agreement among these simulations to the models they proposed, indicating that Mach scaling based on shock polar analysis is possible even at these low Mach numbers, for the circulation.

The studies of KMC94 and SZ94 were both limited, however, to convergent shock-refraction geometry:  $\chi > 1$  or  $A > 0$ . Bagabir and Drikakis (2001) [3] studied the case of a cylindrical helium bubble in air, accelerated by shock waves at Mach numbers  $1.22 \leq M \leq 6$ ; Levy *et al.* (2003) [63] considered spherical helium and SF<sub>6</sub> bubbles in air for  $1.5 \leq M \leq 3$ . The simulations of Bagabir and Drikakis were performed using a single-fluid Eulerian Godunov code with spatial resolution of  $R_{56}$ . The results show that even on a dimensionless timescale based on the Mach number  $M$  and ambient-fluid sound speed  $c_1$ , the flow evolution shows unique qualitative features at each Mach number within this regime, although the dimensions of the shocked bubble at a fixed post-shock time appear to reach an asymptotic limit for  $M \geq 2.5$ . The usefulness of these findings is limited by the modest spatial resolution used in this study, which leads to the growth of Richtmyer-Meshkov instabilities on the downstream bubble surface. Further, the details of the bubble compression, the circulation, and other quantifiable features are not fully analyzed. In the work of Levy *et al.*, an interface-tracking two-dimensional ALE code was used to simulate shock-bubble interactions, showing that for  $M < 2$ , the vortex ring velocity follows a Mach-number scaling based on the circulation scaling law of Samtaney and Zabusky (1994) [99]. However, the application of the scaling law was limited to a single gas combination, and the circulation itself was not presented.

It is anticipated that the results presented here from the current parameter study for shock-bubble interactions will build upon the work described in these studies in several ways. Most importantly, the current simulations are carried out in three dimensions, with spatial resolution ( $R_{128}$ ) adequate to capture the significant details of the flowfield. Further, the simulations employ a multifluid capturing algorithm that allows each fluid to be assigned a unique value of  $\gamma$ . Finally, although it is limited to thermodynamic and

hydrodynamic regimes accessible to mechanical shock tubes ( $M \leq 5$  and  $|A| \leq 0.8$ ) the scope of the study includes both convergent and divergent shock-refraction geometries, with diagnostics for quantitative analysis of many of the integral features of the flowfield.

### 1.3.6 Analytical modeling

This quantitative analysis across a broad parameter space makes the present study useful as a tool for the evaluation of analytical models that have emerged for various aspects of a bubble's response to impulsive acceleration by a shock wave. Many different types of models appear in the literature for quantities that may be computed from simulations or measured in experiments. Klein, McKee, and Colella (1994) [52] in particular, have generated simple models for a variety of features of the flowfield; however, typical experimental diagnostics do not provide access to many of these features, which include the velocity dispersion, the mean pressure in the bubble, and others. Here, our focus is primarily on quantities that are directly or indirectly measurable in shock tube experiments. These include models for the translational vortex velocity and for the circulation.

Rudinger and Somers [95] proposed the first model for the translational velocity  $v_V$  of the vortex ring produced in the interaction of a shock wave with a spherical bubble. They used the analysis of Taylor (1953) for a vortex ring produced by impulsive motion of a submerged body [105]. This model is written as

$$\frac{v_V}{u'_1} = \left( 1 + \beta \frac{1 - \sigma}{\sigma + \frac{1}{2}} \right), \quad (1.9)$$

where  $\beta = 0.436$  is the inertia coefficient for spheres in Taylor's theory, and  $\sigma = \rho'_2/\rho'_1$  is the post-shock bubble-to-ambient density ratio. The Rudinger-Somers vortex-ring

velocity model is simple and useful; for fixed  $\sigma$ , it yields a normalized velocity  $v_V/u'_1$  that is invariant in  $M$ . Because of the uncertainty in the effective shape of the bubbles in the experiments of Rudinger and Somers, they found that the measured vortex velocities fell between those predicted using Eq. 1.9 with the value of  $\beta$  corresponding to spheres and cylinders.

This vortex velocity is also the subject of an approximation proposed by Picone and Boris [79], which incorporates baroclinic vorticity generation (and thus allows  $v_V/u'_1$  to vary with  $M$  for fixed gas combinations). Picone and Boris used this approximation to set the parameters for adaptive gridding in Eulerian simulations for shock-bubble interactions, but did not comment on the effectiveness of the model in comparison to experimental or numerical results. Though intended to capture the motion of the entire shocked bubble, the approximation is useful as a model of the motion of the vortex itself. In the formulation of Picone and Boris, the translation speed is obtained from the circulation  $\Gamma$  associated with the vortex as

$$v_V = u'_1 + \frac{\Gamma}{4\pi R_V}, \quad (1.10)$$

where  $R_V$  denotes the major radius of the vortex ring. The circulation  $\Gamma$  is defined as the path integral of the velocity, on a closed path  $P$  encircling the vortex,

$$\Gamma \equiv \int_P \mathbf{U} \cdot d\mathbf{s}. \quad (1.11)$$

This can be rewritten using Stokes' theorem as an area integral of vorticity,

$$\Gamma = \int_S \boldsymbol{\omega} \cdot d\mathbf{A}, \quad (1.12)$$

where  $S$  is the surface bounded by  $P$ . Picone and Boris also proposed a model for the circulation, based on an integral of the baroclinic vorticity production over the time of shock transit across the bubble, assuming negligible change in the shape of the shock wave and the bubble. The model is described in greater detail by Picone *et al.* (1985) [80], and can be written in our notation as

$$\Gamma_{\text{PB}} = 2u'_1 \left(1 - \frac{u'_1}{2W_i}\right) R \ln \left(\frac{\rho_1}{\rho_2}\right). \quad (1.13)$$

Substituting this circulation into Eq. 1.10, and reformulating the result as a normalized vortex velocity, we obtain

$$\frac{v_V}{u'_1} = 1 + \frac{R}{2\pi R_V} \left(1 - \frac{u'_1}{2W_i}\right) \ln \left(\frac{\rho_1}{\rho_2}\right). \quad (1.14)$$

A much wider variety of models appears in the literature for the circulation in shock-bubble interactions. The circulation is defined above in Eqs. 1.11-1.12, and can be regarded as a measure of the total intensity of rotational motion in the plane in which the integral is evaluated. The model of Picone and Boris (1988) [79] given in Eq. 4.20 was the first devised specifically for shock-bubble interactions. But the approach was perhaps over-simplified, as Picone and Boris compared the model predictions to their simulation results and found that the model generally overestimated the magnitude of the circulation, for cylindrical and spherical bubble in both convergent and divergent shock-refraction geometry.

Six years later, Yang, Kubota, and Zukoski (1994) [110] produced a model for the circulation in shock-bubble interactions. They used an approach similar to that used by Picone and Boris involving integrating the baroclinic vorticity production during shock passage, taking advantage of some simplifying assumptions. Their model can be written

using our nomenclature as

$$\Gamma_{\text{YKZ}} = \frac{4R}{W_i} \frac{p'_1 - p_1}{\rho'_1} \left( \frac{\rho_2 - \rho_1}{\rho_2 + \rho_1} \right) = \frac{4R}{W_i} \frac{p'_1 - p_1}{\rho'_1} A. \quad (1.15)$$

Yang, Kubota, and Zukoski presented results from two-dimensional simulations for the interaction of a shock wave with a cylindrical bubble of helium in an air environment, at Mach numbers  $M = 1.05 \leq M \leq 2.0$  (several scenarios with larger density ratios  $\chi < 1$  were also simulated). The simulations used an Eulerian flux-corrected-transport method, and a spatial resolution of  $R_{20}$ . The results showed that the model predicted the circulation obtained from simulations to within about 15% error, while the model of Picone and Boris was again found to overestimate the circulation consistently.

A model for the circulation that was both more general and more successful was provided at the same time in the work of Samtaney and Zabusky (1994) [99]. Their circulation model was derived from scaling arguments based on shock-polar analysis [46, 47], which can capture baroclinic vorticity deposition along with the bulk compression and local interface deformation induced by shock passage, without making use of the simplifying assumptions of the Picone-Boris or Yang-Kubota-Zukoski models. In our nomenclature, the circulation model of Samtaney and Zabusky for circular interfaces is written as

$$\Gamma_{\text{SZ}} = \left(1 + \frac{\pi}{2}\right) \left(\frac{2}{1 + \gamma}\right) \left(1 - \chi^{-\frac{1}{2}}\right) (1 + M^{-1} + 2M^{-2}) (M - 1) R c_1. \quad (1.16)$$

Samtaney and Zabusky demonstrated that the model had the appropriate asymptotic behavior, and they showed the effectiveness of this model in predicting the circulation across a wide parameter space, for the convergent-refraction-geometry regime, using

results from the two-dimensional simulations described in their 1994 paper. Samtaney *et al.* (1998) [98] also provided an extension of this model to divergent geometry for planar-inclined interfaces, but this extension has not yet been shown to be effective for circular interfaces. The more general formula for circulation deposition in shock-contact interactions on which this model is based has been implemented in a number of different geometries, and it has also appeared in the context of a more general discussion of the Richtmyer-Meshkov instability and related flows [112].

Aside from direct analytical modeling for the translational velocity and circulation associated with the shock-accelerated bubble, theoretical tools based on gasdynamics and dimensional analysis are also useful. Using the procedure outlined in Sec. 1.2.2, based on iterative solutions to the one-dimensional gasdynamics equations (Eqs. 1.1-1.3 for each wavefront and Eqs. 1.5-1.6 for each interface), the state of the bubble fluid after shock wave passage in the one-dimensional approximation may be directly computed. This method may also be extended to obtain the state of the bubble fluid after the passage of any number of internally reflected shock waves, or after a single internally reflected rarefaction wave. Such an approach was used by Giordano and Burtschell (2006) [34] to obtain the mean density of the bubble fluid after the initial shock transient. The results compared favorably with both two-dimensional numerical simulations and experimental measurements from the data of Layes (2005) [59]. Quantities obtained from one-dimensional gasdynamics can also be used to reconstruct the post-shock velocity field, from which an estimate of the circulation may be obtained; this type of approach for the circulation is discussed in more detail in Sec. 4.2.4.

Finally, dimensional analysis appears nearly universally in the literature on shock-bubble interactions and, more generally, in shock-contact interactions. Since these flows

appear on physical length scales ranging from  $10^{-6}$  m [17] to  $10^{16}$  m [44], timescaling arguments based on the fundamental dimensional parameters driving the flow are necessary. Such an approach should allow one to view the evolution of flow parameters from these widely different length scales on a common timescale. The most common approach is to construct normalized time using the Mach number  $M$ , the initial bubble radius  $R$ , the ambient sound speed  $c_1$ , and the physical time  $t$  as  $tMc_1/R$ , which represents dimensionless time. This could also be written as  $tW_i/R$ , and has been used in numerous studies of shock-bubble interactions [3]. Klein, McKee, and Colella (1994) [52] proposed an alternative timescaling based on the “cloud-crushing time,” which is the time required for the transmitted shock wave to move over a distance equal to  $R$  in the bubble fluid. In our notation, the dimensionless time based on such a scaling would be  $tW_t/R$ . (They also proposed a number of other relevant timescales, which are specific to certain quantities measured from their simulations.) In some cases, the post-shock flow speed  $u'_1$  has also been used to construct a dimensionless timescale as  $tu'_1/R$  or  $tu'_1/2R$  [49]. In all of these cases, the timescale is based on a characteristic velocity, which is typically computed using one-dimensional gasdynamics. This is the approach for timescaling that is followed in the present study.

# Chapter 2

## Numerical method

In this study, we take advantage of modern computing techniques and resources to investigate shock bubble interactions over the parameter space  $-0.8 < A < 0.7$  and  $1.1 < M \leq 5.0$ , in fully three-dimensional numerical simulations. This is done by means of a higher-order Godunov scheme for integrating the Euler equations on an adaptive mesh, implemented in a code called *Raptor*.

### 2.1 Description of Simulation Code

#### 2.1.1 Equations

Governing equations are obtained by considering the unsteady compressible flow of a single ideal fluid. If we neglect viscous effects (*i.e.*, restrict ourselves to short timescales), the flow is described by the three-dimensional compressible Euler equations. These can be formulated as a hyperbolic system of conservation laws which, in 3D Cartesian space and in the absence of body forces, takes the form

$$\frac{\partial U}{\partial t} + \frac{\partial F(U)}{\partial x} + \frac{\partial G(U)}{\partial y} + \frac{\partial H(U)}{\partial z} = 0, \quad (2.1)$$

where the conserved variables are  $U = (\rho, \rho u, \rho v, \rho w, \rho e)^T$ , and the fluxes are

$$F(U) = \begin{pmatrix} \rho u \\ \rho u^2 + p \\ \rho uv \\ \rho uw \\ \rho ue + up \end{pmatrix}, \quad G(U) = \begin{pmatrix} \rho v \\ \rho vu \\ \rho v^2 + p \\ \rho vw \\ \rho ve + vp \end{pmatrix}, \quad H(U) = \begin{pmatrix} \rho w \\ \rhowu \\ \rho wv \\ \rho w^2 + p \\ \rho we + wp \end{pmatrix} \quad (2.2)$$

In this system,  $t$ ,  $x$ ,  $y$ , and  $z$  are the time and space coordinates, and  $u$ ,  $v$ ,  $w$ ,  $\rho$ ,  $p$ , and  $e$  represent the  $x$ -,  $y$ -,  $z$ -velocity, density, pressure, and total energy per unit mass, respectively. In the perfect-gas idealization, the system is closed by introducing an explicit gamma-law equation of state,

$$p = (\gamma - 1) \rho \left[ e - \frac{1}{2} (u^2 + v^2 + w^2) \right], \quad (2.3)$$

where  $\gamma$  is the ratio of specific heats and appears as a fluid property.

### 2.1.2 The *Raptor* code

Our purpose in the current work is to explore the parameter space of the shock-bubble interaction in three spatial dimensions. A second-order, piecewise linear Eulerian Godunov code with adaptive mesh refinement (AMR), named *Raptor*, is chosen for this purpose, particularly for its excellent scalability on parallel computing platforms. This code is based on the single-fluid compressible hydrodynamics code using block-structured AMR which was developed originally by the Center for Computational Sciences and Engineering at the Lawrence Berkeley National Laboratory, and is currently under development at the Lawrence Livermore National Laboratory. The scheme is a conservative finite-difference method; hence, mass, momentum, and energy are all conserved. It is

second-order accurate in space and time for smooth flow, and captures shock waves with minimal numerical dissipation and overshoot. Further, application of the scheme in simulations for shock-accelerated gas flows, *e.g.*, by Henderson *et al.* (1991) [47], has resulted in very good agreement with experiments.

The code is implemented in a hybrid C++/Fortran framework, where the infrastructure necessary for managing the AMR grid hierarchy and parallelization are implemented in C++ and the numerical integration kernels are implemented in Fortran, as described by Crutchfield and Welcome (1993) [22]. The current parallelization strategy for data distribution and load balancing are described by Rendleman *et al.* (2000) [90], and the performance of the code on approximately 64,000 processors of the IBM BlueGene/L machine is described by Greenough *et al.* (2005) [37].

### 2.1.3 Adaptive mesh refinement

The integration kernel is embedded within the block-structured AMR framework of Berger and Oliger (1984) [9] in order to maximize resolution for fixed computational cost. This framework breaks the domain into a number of three-dimensional rectangular (“block-structured”) grids, synchronizes the integration of Eq. 2.1 on each grid, and maintains a nested hierarchy of higher-resolution subdomains whose distribution is updated dynamically during the simulation to enhance spatial resolution and accuracy in regions of interest. The AMR technique has been used extensively in shock hydrodynamics computations (see Henderson *et al.*, 1991 [47]; Klein, McKee, and Colella, 1994 [52]; and Baltrusaitis *et al.* (1996) [5]), and its implementation has been discussed in detail by Berger and Colella (1989) [8] and Bell *et al.* (1994) [6].

### 2.1.4 Eulerian Godunov integrator

To summarize the scheme as implemented for the current study, numerical integration of the hyperbolic system in Eq. 2.1 is accomplished using an operator-split, second-order Godunov method, which has been described in detail by Pember *et al.* (1996) [77]. The basic kernel is the piecewise linear method (PLM) of Colella (1985) [12], which is based on a higher-order extension of Godunov’s method first proposed by van Leer (1979) [107] – the MUSCL algorithm. In its one-dimensional form, cell-centered, cell-averaged initial data  $u(x_i, t_n)$  are interpolated using a piecewise-continuous linear profile, to obtain cell-edge values at the half-timestep,  $u(x_{i\pm 1/2}, t_{n+1/2})$ . The profile slope is determined by a fourth-order finite difference approximation, with constraints added to maintain monotonicity, which provides a profile that is steeper than that obtained by a standard fourth-order approximation. The resulting left and right states for the half-timestep at each cell interface are then input to an approximate Riemann solver.

The solver is based on the ideas given in Bell *et al.* (1989) [7], whereby one considers the cumulative effect of state changes across waves, and in Collela and Glaz (1985) [13] whereby, to second order, rarefaction waves can be approximated as shock waves. The output from the Riemann solver, the so-called “Godunov state,” is then used to compute the fluxes. The solution at the next timestep  $u(x_i, t_{n+1})$  is then obtained by explicit conservative differencing, with timestep size determined previously by the CFL condition; the CFL number in these simulations is set to 0.8. (By adopting a recursive time advancement approach, the solution is advanced on each AMR level using that level’s appropriate CFL number.) The scheme is extended to two and three dimensions by Strang splitting (see Strang, 1968 [103]), following the approach given by Bell *et al.* [6], which yields second-order accuracy after the complete permutation cycle. Symmetry

preservation tests of the three-dimensional integrator, not included here, have been performed by running two-dimensional shock-contact interaction problems that are uniform in the third dimension of the domain. Results from  $x$ - $y$ ,  $y$ - $z$  and  $x$ - $z$  orientations are found to be identical to the level of round-off error.

### 2.1.5 Multifluid capturing

The single-fluid algorithm is generalized to treat multiple species by adopting a volume-of-fluid (VOF) multifluid approach following Colella *et al.* (1996) [14], and more recently Miller and Puckett (1996) [73], which allows multiple fluids with distinct equations of state for each material. In its original form, the VOF method tracks the material interface by performing a local interface reconstruction. The multifluid capturing method used in this study solves the same system of partial differential equations using the same numerical scheme as given in the above two references, but forgoes the local interface reconstruction, in favor of simple fluid volume advection (see Greenough *et al.*, 1995 [36]). Regions of mixed fluid develop in the vicinity of fluid interfaces, but since individual species densities and energies are separately evolved, the mixing is not excessive when compared to other approaches given in Secs. 2.3.3 and 2.3.4.

### 2.1.6 Settings

Two adjustments of settings for the scheme are applied specifically for the current study, including, first, the addition of a very weak effective artificial viscosity. As described by Colella and Woodward (1984) [15], in some regions of converging flow, particularly near strong shock waves, oscillations can arise in this scheme which require the introduction of dissipative damping. An explicit diffusive flux is thus added to the numerical fluxes in

regions where  $-\nabla \cdot \vec{V}$  is sufficiently large, yielding an effective artificial viscosity similar to the form used by Lapidus (1966) [56]. The magnitude of this term is set to  $K = 0.1$ , in the notation of Colella and Woodward (1984) [15], but only for scenarios with  $M > 2$ .

Secondly, a dual AMR refinement criterion is specified, based on both the bubble fluid volume fraction and the local magnitude of the density gradient. All cells with a nonzero bubble fluid volume fraction are automatically tagged for refinement, as well as all cells with  $|\delta\rho| > Q$ , where  $|\delta\rho|$  is the maximum fractional density difference across all interfaces for a cell,  $|\delta\rho| = 2(\rho_{i+1} - \rho_i)/(\rho_{i+1} + \rho_i)$ , and  $Q = \max(0.9d, 0.1)$ , where  $d$  is the fractional density difference across the initial shock wave. This density-gradient criterion is used here to ensure high resolution for secondary shock waves which may leave and re-enter the bubble; it is removed after the initial shock wave has moved sufficiently far downstream from the bubble region.

It should be noted that these refinement criteria were selected in order to keep the calculation cost to an absolute minimum, in view of the overall cost of the study. For single-case studies with a greater margin for computational cost, the threshold  $Q$  for density-gradient refinement should be set to a much lower value (*e.g.*,  $Q = 0.05$ ) to ensure complete refinement of all discontinuities in the solution, although this will dramatically increase the cost.

### 2.1.7 Computing facilities

All of the simulations comprising this parameter study were performed at the Lawrence Livermore National Laboratory. Each of the simulations was performed using one or more partitions on the BlueGene/L (BGL) machine. This is a 1024-node cluster with two 700-MHz Intel Xeon processors and 512 MB of memory per node. For scenarios

simulated in this study with  $-0.8 < A < 0.2$ , 128 nodes supplied sufficient memory for the simulation, but for  $A > 0.2$ , the simulations typically demanded more memory than is supplied on the 128-node partitions, so 512-node partitions were used instead. On a 512-node partition, the simulations typically ran at 0.5 coarse-grid timesteps per minute; on the 128-node partitions, they ran at 0.25 coarse-grid timesteps per minute, provided that memory constraints were not prohibitive. Thus, full parallel scaleup was not achieved on the 512-node partitions. However, this is due only to relaxed constraints on grid sizes specified in the user input, which reduced the number of grids, so that the optimum distribution of grids over available processors was not achieved. In future simulations, grid-size constraints in the user input should be adjusted appropriately for the partition size being used for each simulation. Here, optimal overall throughput was achieved on the 128-node partitions, running multiple jobs simultaneously, on 128 nodes each. Using the full machine (1024 nodes), the simulations also typically ran at approximately 1 coarse-grid timestep per minute. The full duration of each of the simulations included here is about 550 coarse-grid timesteps.

## 2.2 Mesh-Sensitivity of Solutions for Shock-Bubble Interaction Problems

An issue of crucial importance in Eulerian simulations for shock-accelerated flows is the sensitivity of the solution to the computational mesh. That is, solutions to the discretized representation of the hyperbolic system of PDE's in Eq. 2.1 may not possess all of the properties of the solutions to the system of PDE's if certain features are under-resolved: *i.e.*, if the computational mesh is too coarse. Thus, one must establish the

minimum mesh spacing for which features of the solution may be regarded as fully resolved; schemes for which such a condition exists are convergent schemes. Convergence means that as the mesh spacing is decreased, the solution to the discretized system of equations approaches the solution to the system of PDE's with the same initial and boundary conditions. By Lax's equivalence theorem, stability is the necessary and sufficient condition for a consistent scheme to be convergent, so long as the problem in consideration is well-posed [104].

However, Samtaney and Pullin (1996) [97] have shown in detail that initial value problems for the Euler equations involving shock-contact interactions exhibit many features indicating that such problems are ill-posed, and convergence of the solution at fixed time is not observed in Eulerian simulations for many of these problems. This is particularly true in the absence of surface tension on fluid interfaces, and in the case of contact surfaces that are not aligned to the mesh. Therefore, in the present simulations for shock-bubble interactions, which exclude surface tension and project a circular interface onto a Cartesian mesh, convergence to a pointwise grid-independent solution cannot be expected.

Further, Greenough and Rider (2004) [38] have remarked that even though the Eulerian Godunov method described in Sec. 2.1.4 has second-order accuracy in space and time for regions of smooth flow, in the neighborhood of flow discontinuities, the accuracy reduces to first order. Thus, convergence rates computed from solutions involving shock waves and discontinuities may not reflect the accuracy of the underlying scheme. Greenough and Rider have also observed that for multi-dimensional shock-accelerated flows where no analytic or resolved solution exists, it is unclear how convergence rates could be computed or meaningfully interpreted.

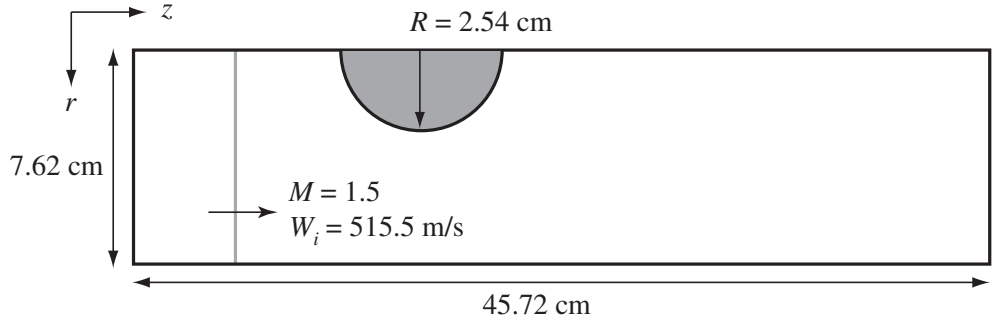


Figure 5: Schematic overview of initial condition used for two-dimensional grid sensitivity study simulations.

Therefore, in order to assess whether solutions computed using *Raptor* for shock-bubble interactions can be regarded as well-resolved, a mesh-sensitivity study is carried out. Normed errors and convergence rates are not computed, in light of the above discussion. Instead, we examine the solution qualitatively at fixed time, and extract various quantities from the dataset to determine under what conditions and for which aspects of the flowfield the simulations may be considered to have sufficient spatial resolution.

### 2.2.1 Two-dimensional simulations

In order to perform such a mesh-sensitivity study, two-dimensional simulations for shock-bubble interactions at varying spatial resolutions are carried out using *Raptor*. These are set up on a rectangular mesh in  $r$ - $z$  symmetry as shown in Fig. 5. A spherical bubble of radius  $R = 2.54$  cm is embedded in an air environment ( $\gamma = 1.399$ ) at atmospheric temperature and pressure, and a  $M = 1.5$  shock wave approaches the bubble from the left. Two scenarios are considered in these simulations: a helium bubble ( $\gamma_2 = 1.667$ ,

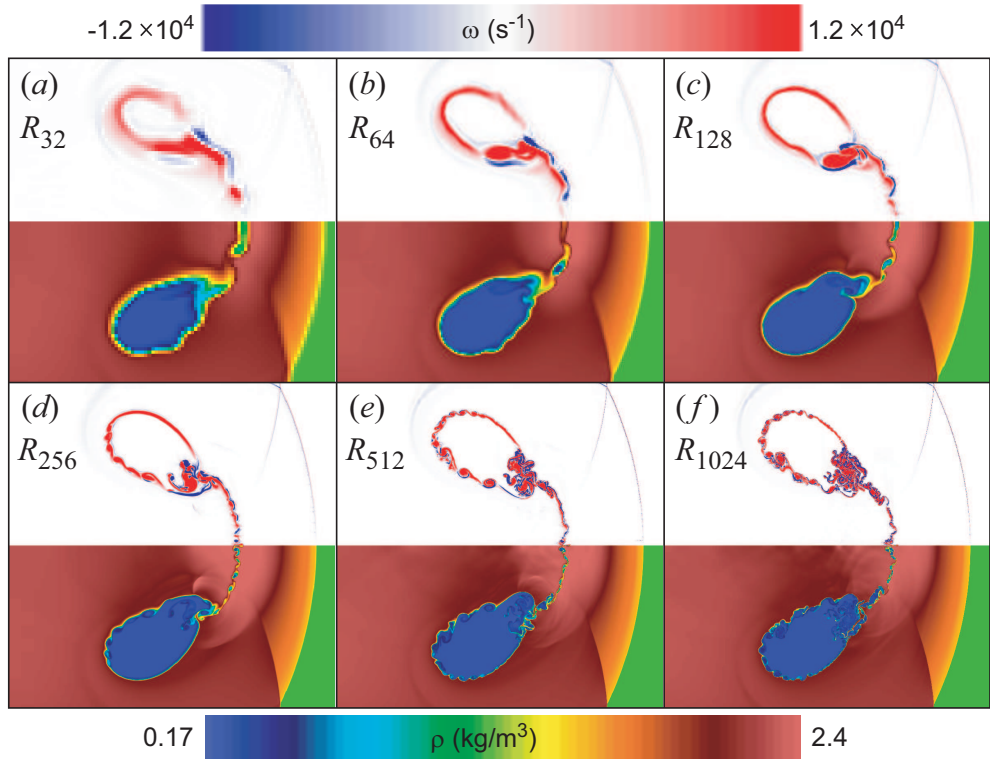


Figure 6: Vorticity (top) and density (bottom) from two-dimensional mesh-sensitivity-study simulations for air-He,  $M = 1.5$ , at  $t = 188 \mu\text{s}$ : (a)  $R_{32}$ , (b)  $R_{64}$ , (c)  $R_{128}$ , (d)  $R_{256}$ , (e)  $R_{512}$ , (f)  $R_{1024}$ . Shock wave motion is left-to-right.

$A = -0.757$ ) and a krypton bubble ( $\gamma_2 = 1.672$ ,  $A = 0.486$ ), using experimentally-measured ratios of specific heats [35]. In both cases, the bubble is initialized with a smooth interfacial transition layer, defined using a Gaussian density profile; the thickness of this layer is  $R/64$ , or 0.04 cm. AMR settings are configured to ensure that all bubble fluid and all density discontinuities with  $|\delta\rho| > 0.05$  are captured on the highest AMR level.

Six simulations are carried out for each scenario, with increasingly fine mesh spacing on the highest AMR level:  $R_{32}$ ,  $R_{64}$ ,  $R_{128}$ ,  $R_{256}$ ,  $R_{512}$ , and  $R_{1024}$ . In the  $R_{1024}$  simulation, a total of four levels of AMR grids are included, and the mesh spacing on the finest level

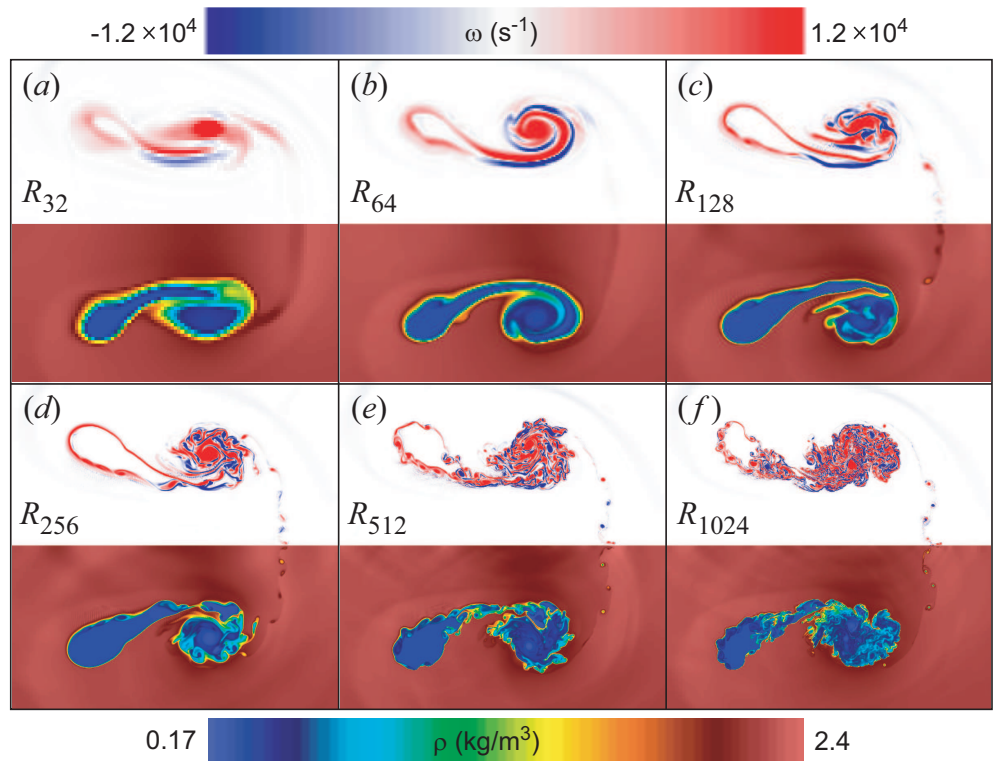


Figure 7: Vorticity (top) and density (bottom) from two-dimensional mesh-sensitivity-study simulations for air-He,  $M = 1.5$ , at  $t = 437 \mu\text{s}$ : (a)  $R_{32}$ , (b)  $R_{64}$ , (c)  $R_{128}$ , (d)  $R_{256}$ , (e)  $R_{512}$ , (f)  $R_{1024}$ . Shock wave motion is left-to-right.

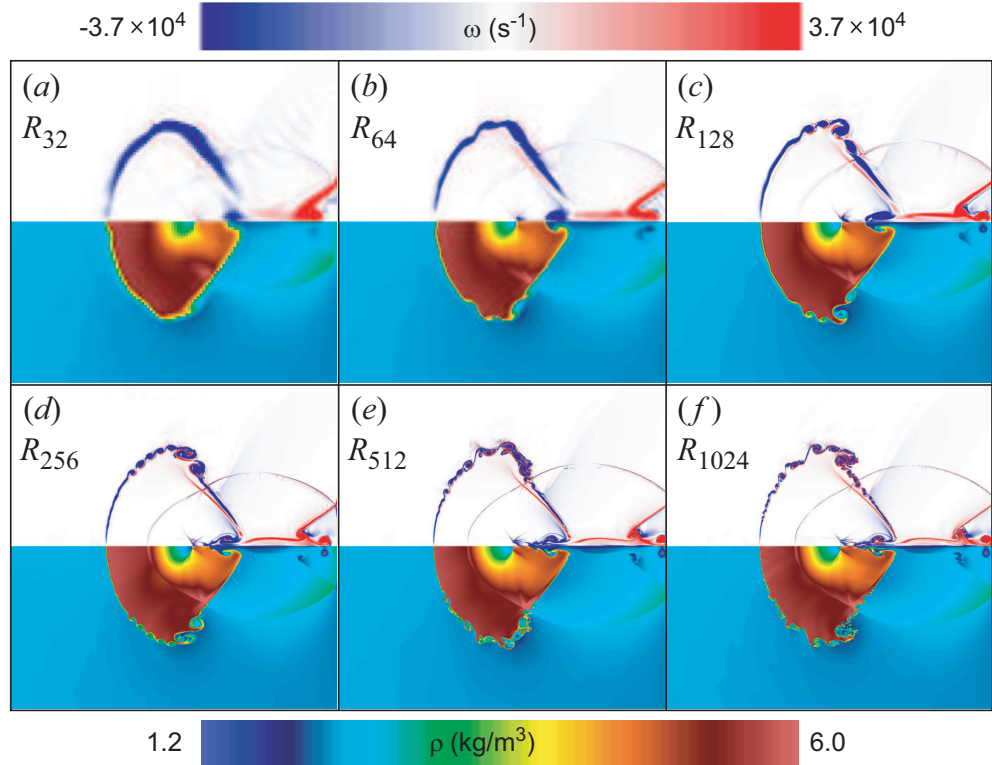


Figure 8: Vorticity (top) and density (bottom) from two-dimensional mesh-sensitivity-study simulations for air-Kr,  $M = 1.5$ , at  $t = 188 \mu\text{s}$ : (a)  $R_{32}$ , (b)  $R_{64}$ , (c)  $R_{128}$ , (d)  $R_{256}$ , (e)  $R_{512}$ , (f)  $R_{1024}$ . Shock wave motion is left-to-right.

is  $\Delta = 25 \mu\text{m}$ . In the two most highly-resolved simulations for each scenario, the CFL number is reduced from 0.8 to 0.4 to maintain the stability of the simulation during shock wave impact on and transit over the bubble.

The computed density and vorticity fields from these simulations are shown in Figs. 6-9. In these figures, the density field is reflected about the axis of symmetry. The vorticity  $\omega = \nabla \times \mathbf{U}$  in these simulations has only a single component – normal to the  $r$ - $z$  plane – and can thus be regarded as a scalar quantity  $\omega$ , which is plotted here. Incident shock wave motion in these plots is left-to-right.

By inspection of Figs. 6-9, we see that for early times in the simulations (Figs. 6 and

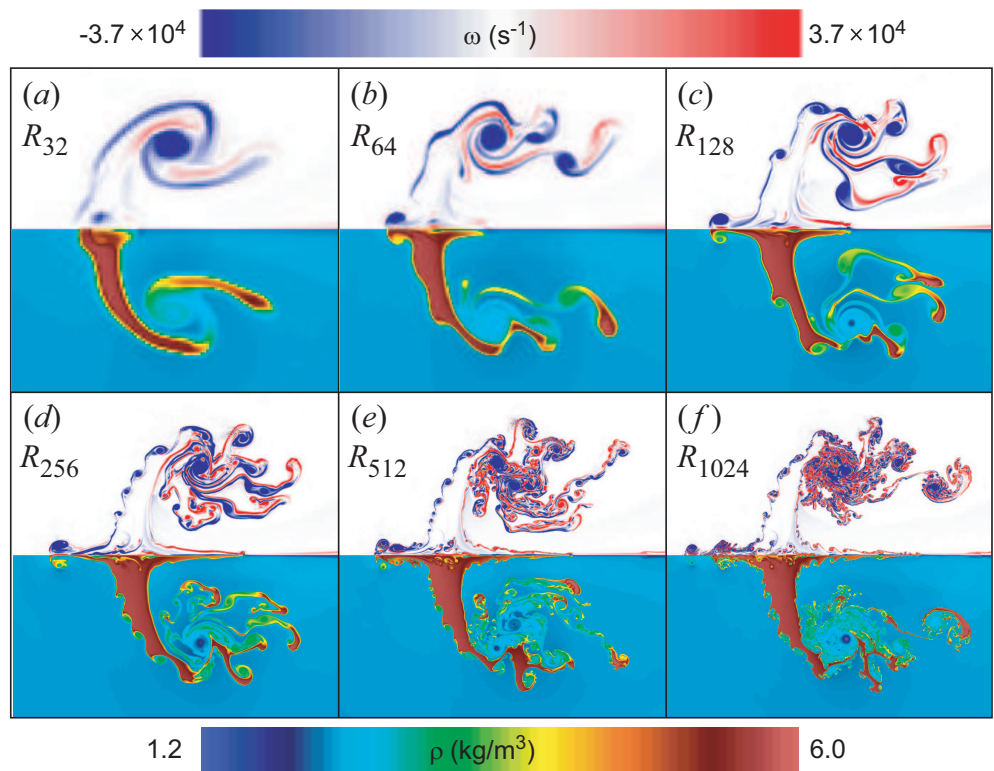


Figure 9: Vorticity (top) and density (bottom) from two-dimensional mesh-sensitivity-study simulations for air-Kr,  $M = 1.5$ , at  $t = 437 \mu s$ : (a)  $R_{32}$ , (b)  $R_{64}$ , (c)  $R_{128}$ , (d)  $R_{256}$ , (e)  $R_{512}$ , (f)  $R_{1024}$ . Shock wave motion is left-to-right.

8), the computed flowfields show remarkable similarity over a very large range in the mesh spacing. The shock refraction pattern generally remains unaltered as the spatial resolution changes, and the large-scale features of the flow, including deformation of the interface and vortex ring development, are also unaltered. However, the small-scale details of the flowfield show significant changes. Kelvin-Helmholtz rollups forming on the bubble surface in Figs. 6(*d-f*) and 8(*d-f*) clearly exhibit periodicity that is dependent on the mesh spacing. We speculate that the mesh spacing sets a lower limit on the wavelength of the vortical perturbations that lead to the development of Kelvin-Helmholtz instabilities on the interface.

At later times in the simulations, as shown in Figs. 7 and 9, these mesh-sensitivity effects at the small scales become much more pronounced. Although integral-scale lengths such as the axial and radial extents of the mixing region and the primary vortex ring diameter do not vary with changes in the mesh spacing, the number and size of secondary eddies in the flow is highly dependent on the spatial resolution of the simulation. At low resolution, a diffuse mixing region forms around a smoothly deforming interface, while at high resolution, the mixing region is very thin, and is wrapped and contorted around a complex field of eddies. We also note that in the late-time flowfield for the air-krypton scenario in Fig. 9, the scale length defined by the distance traveled by the upstream jet observed on-axis in these simulations is also dependent on the mesh spatial resolution of the simulation.

### 2.2.2 Sensitivity of extracted quantities to mesh spacing

The computed solutions, when compared with each other or with experimental images on a pointwise basis, thus exhibit a lack of convergence at fixed time with respect to

the mesh spacing. However, we may gain further insight into the precise nature and extent of the mesh-dependent properties of these Eulerian simulations by examining the variation in integral quantities and norms computed from the simulation datasets.

Noting that some quantities of interest in simulations such as these are linked to extrema in the datasets (*i.e.*, to maxima and minima), while others are linked to integrated or mean quantities, we first examine the mesh-sensitivity at fixed time for maximum values of the density field and for the mean density in the bubble-fluid region. The maximum density  $\rho_{\max}$  is obtained by simply extracting the maximum value of  $\rho$  in the entire domain. The mean bubble-fluid density  $\langle \rho \rangle$  is obtained by evaluating the expression

$$\langle \rho(t) \rangle = \frac{\iint_D \rho f \pi r dr dz}{\iint_D f \pi r dr dz}, \quad (2.4)$$

where  $D$  represents the entire domain area. The variation in  $\rho_{\max}$  and  $\langle \rho \rangle$  with the spatial resolution  $R/\Delta$  is plotted for the air-helium and air-krypton shock-bubble interaction scenarios in Figs. 10 and 11.

The data shown in Figs. 10(*a*) and 11(*a*) indicate that the maximum density  $\rho_{\max}$  in the flowfield continues to vary with the spatial resolution even at very large values of  $R/\Delta$ . Maxima and minima for other flow variables not shown here, including the pressure and the axial velocity, indicate similar behavior. Due to the lack of pointwise convergence at fixed time, quantities obtained using an  $L_\infty$  norm show strong sensitivity to the mesh spacing. The mean bubble-fluid density  $\langle \rho \rangle$ , however, shown in Figs. 10(*b*) and 11(*b*), shows behavior that indicates convergence to a nearly grid-independent value for  $R/\Delta > 500$ . In the air-krypton case shown in Fig. 11(*b*), this value is very close to the value of the bubble-fluid density  $\rho_2''$  predicted from the one-dimensional gasdynamics

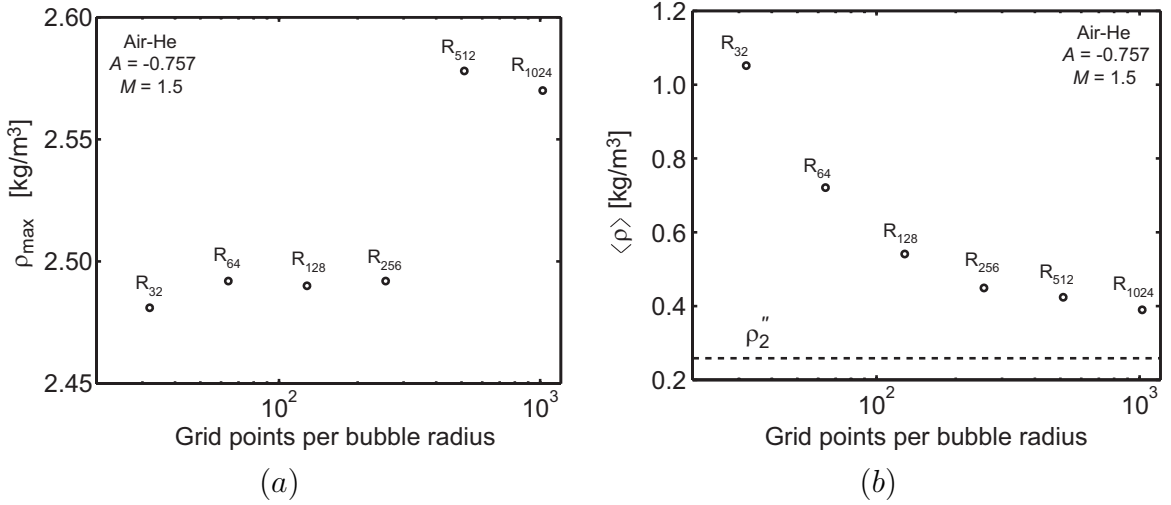


Figure 10: Normed quantities from the computed density field at  $t = 137 \mu\text{s}$  in an air-He,  $M = 1.5$  shock-bubble interaction: (a) maximum density in the flowfield; (b) mean bubble-fluid density, computed using Eq. 2.4. The data are plotted as a function of the spatial resolution, given in grid points per bubble radius.

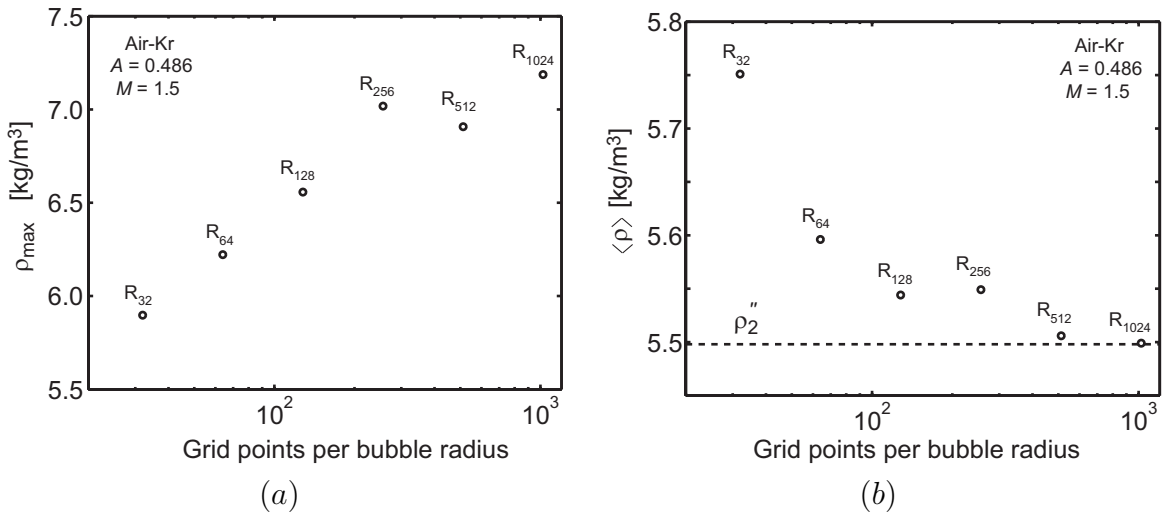


Figure 11: Normed quantities from the computed density field at  $t = 137 \mu\text{s}$  in an air-Kr,  $M = 1.5$  shock-bubble interaction: (a) maximum density in the flowfield; (b) mean bubble-fluid density, computed using Eq. 2.4. The data are plotted as a function of the spatial resolution, given in grid points per bubble radius.

analysis for shocked gas slabs outlined in Sec. 1.2.2 and in Appendix A. The deviation of the mean bubble-fluid density from the one-dimensional-gasdynamics prediction for the air-helium scenario is discussed below in Sec. 4.1.1. We conclude from these results that integrated or mean quantities are much more likely to give a grid-independent result than maximum or minimum quantities, which are more sensitive to local effects in the computed solution.

As an additional indication of the convergence of mean quantities, temporal trends in the mean bubble-fluid density  $\langle \rho \rangle$  are shown in Fig. 12 for the air-helium and air-krypton scenarios at each of the six mesh spacings listed above. The mean density  $\langle \rho \rangle$  is normalized to the one-dimensional gasdynamics prediction  $\rho_2''$  using the expression

$$\rho^*(t) = \frac{\langle \rho(t) \rangle - \rho_2}{\rho_2'' - \rho_2}, \quad (2.5)$$

so that the normalized mean bubble-fluid density  $\rho^*$  is zero at time zero, and approaches unity as  $\langle \rho \rangle \rightarrow \rho_2''$ . In Fig. 12, we see that trends in this normalized quantity can be regarded as effectively independent of the mesh spacing for  $R/\Delta > 100$ . At higher spatial resolution, the trends are nearly identical. This indicates that although the solution is locally and pointwise nonconvergent, some aspects of the computed flowfields, particularly certain integrated and mean quantities, do reach a converged grid-independent state.

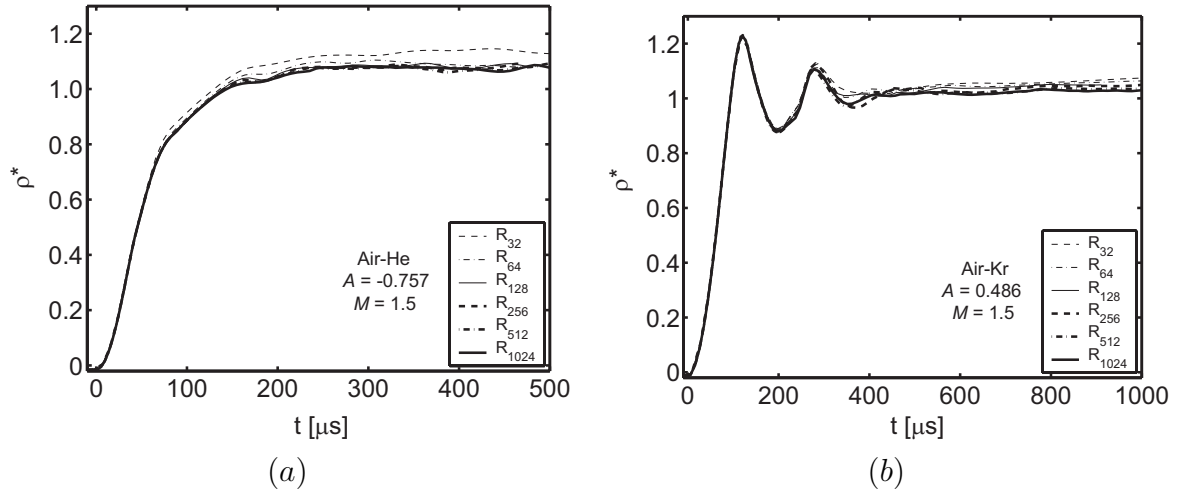


Figure 12: Temporal trends in the normalized mean bubble-fluid density, obtained using Eq. 2.5, for (a) air-helium and (b) air-krypton shock-bubble interaction simulations at  $M = 1.5$ .

## 2.3 Validation of Numerical Method with Theory, Experiments, and Simulations

Apart from the numerical issues of convergence and mesh sensitivity, a fundamental concern is the accuracy with which a numerical method that solves the discretized forms of the conservation laws can represent physical reality, or capture the essential properties of the true solution to the conservation laws. To address this issue, we present simulations for four problems involving shock-accelerated inhomogeneous flows, and compare the results of these simulations to one-dimensional gasdynamics theory, shock tube experiments, and other simulations drawn from well-known points of reference in the literature. The problems simulated here include (1) the interaction of a shock wave with a gas slab, with comparison to one-dimensional gasdynamics theory; (2) the interaction of a shock wave with a spherical helium bubble, with comparison to shock tube experimental data;

(3) the interaction of a shock wave with a cylindrical bubble of refrigerant gas R22, with comparison to the simulations of Quirk and Karni (1996) [84] and experiments of Haas and Sturtevant (1987) [42]; and (4) the interaction of a shock wave with a spherical bubble of refrigerant gas R12, with comparison to the simulations of Zabusky and Zeng (1998) [113].

### 2.3.1 Shock wave interaction with a gas slab: theory

As discussed in Sec. 1.2.2, the conservation equations for mass, momentum, and energy (Eqs. 1.1-1.3), together with dynamic and kinematic matching conditions evaluated at fluid interfaces (Eqs. 1.6-1.6), can be used to construct an algebraic system of equations that describes the interaction of a planar shock wave with a gas slab, given appropriate initial data and gamma-law equations of state. This system of equations is given in Appendix A, and can be solved iteratively to yield the state of the slab and ambient fluids after each interaction with the incident, transmitted, or internally or externally reflected shock waves. The solution to this system yields a set of fluid states that are constant and uniform between each discontinuity in the  $x$ - $t$ -space described by a shock or rarefaction wave. This is not the case only in the region occupied by rarefaction waves.

For the two test scenarios considered in Sec. 2.2, a one-dimensional analog is constructed, using the same physical gas properties and dimensions, but replacing the spherical bubble with a planar gas slab. The system given in Appendix A is solved iteratively in order to find (1) the pressure  $p'_2$  and density  $\rho'_2$  in the gas slab after the passage of the initial transmitted shock wave, and (2) the pressure  $p''_2$  and density  $\rho''_2$  in the gas slab after the passage of the internally reflected wave, which is a shock wave in the

	$p_2$ [kPa]	$p'_2$	$p''_2$	$\rho_2$ [kg/m <sup>3</sup> ]	$\rho'_2$	$\rho''_2$
Air-He	101.3	172.4	213.0	0.166	0.228	0.259
Air-Kr	101.3	315.8	233.5	3.485	6.581	5.489

Table 1: Pressure and density in a shocked slab of helium or krypton in air initially at atmospheric conditions, during interaction of a  $M = 1.5$  shock wave with the slab: computed using one-dimensional gasdynamics. Pressure units are kPa and density units are kg/m<sup>3</sup>.

air-helium case and a rarefaction wave in the air-krypton case. A *Raptor* simulation is performed for each case, using the same AMR setup as the  $R_{128}$  simulations from the mesh-sensitivity study described in Sec. 2.2. (The slab half-thickness is spanned by 128 cells on the highest AMR level.) In this way, we may verify both that the Eulerian simulation properly captures the transmission and reflection of the shock wave as predicted by gasdynamics theory, and that, with the  $R_{128}$  mesh spacing, the higher-order Godunov integrator embedded in *Raptor* properly resolves discontinuities with minimal development of numerical overshoot or Gibbs (oscillatory) phenomena.

The density and pressure in the gas slab during transmission of a  $M = 1.5$  shock wave across the slab, computed using one-dimensional gasdynamics, are shown in Table 1. We note that in convergent geometry,  $p''_2 < p'_2$  and  $\rho''_2 < \rho'_2$ , because the internally reflected wave is a rarefaction wave; the opposite is true in divergent geometry, because the internally reflected wave is a shock wave. The values computed from one-dimensional gasdynamics are then compared to the pressure and density profiles extracted at selected times from the *Raptor* simulations in Figs. 13-14.

The simulation results shown in Fig. 13-14 indicate the highly reliable shock-capturing capability of the *Raptor* scheme. In both the air-helium and air-krypton scenarios, the

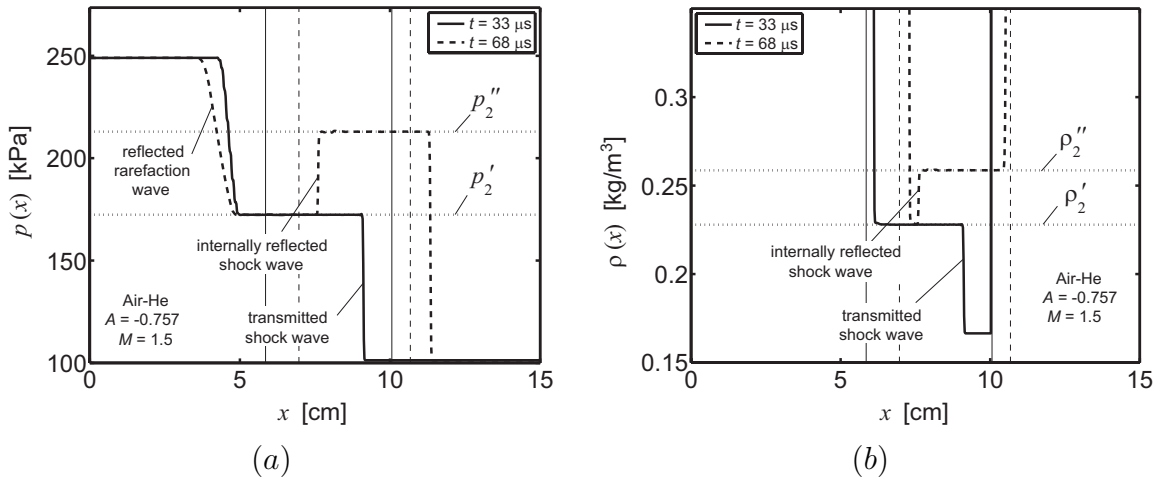


Figure 13: Profiles in (a) pressure and (b) density obtained from *Raptor* simulations for a helium slab in air shocked at  $M = 1.5$ . The bounds of the bubble region are marked by vertical lines, and horizontal dotted lines indicate the predictions of one-dimensional gasdynamics theory for the pressure and density in the slab.

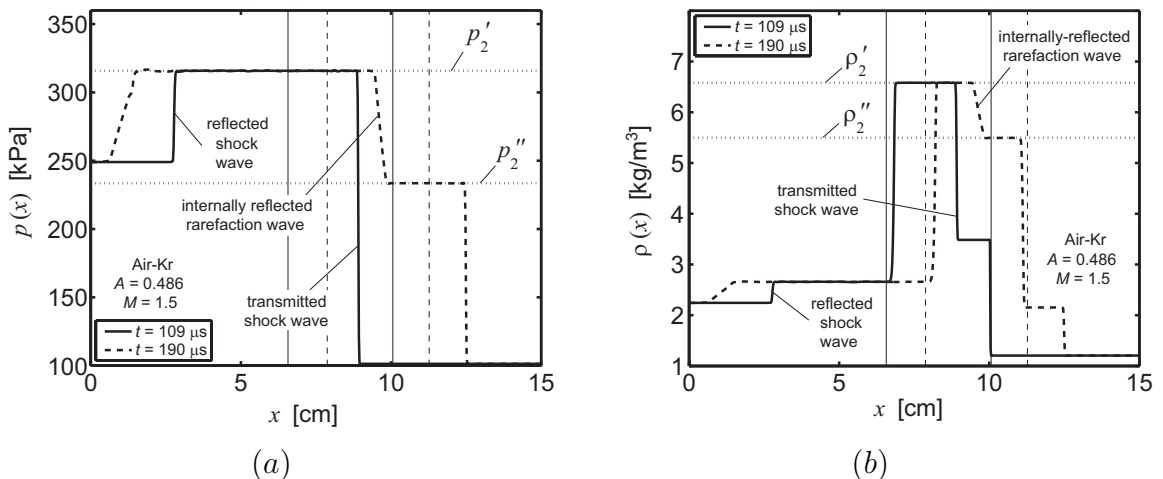


Figure 14: Profiles in (a) pressure and (b) density obtained from *Raptor* simulations for a krypton slab in air shocked at  $M = 1.5$ . The bounds of the bubble region are marked by vertical lines, and horizontal dotted lines indicate the predictions of one-dimensional gasdynamics theory for the pressure and density in the slab.

pressure and density of the gas in the slab change nearly exactly as the one-dimensional gasdynamics theory predicts, during the passage, first, of the transmitted shock wave, and, second, of the internally reflected shock or rarefaction wave. This indicates that the implementation of the discretized Euler equations in the numerical method, within the context of the multifluid-capturing algorithm, accurately captures the shock transmission and reflection properties of the system of conservation laws. Further, we observe in Figs. 13-14 that with the AMR settings configured to achieve a spatial resolution equivalent to  $R_{128}$  in shock-bubble interactions, very little spurious oscillatory behavior or overshoot is observed near the discontinuities in either the pressure or density profiles. This indicates that monotonicity constraints and upwinding are properly implemented in the scheme so that shock waves and contact surfaces can be well resolved in the solution.

### 2.3.2 Shock wave interaction with a spherical bubble: experiments

Validation for *Raptor* is also provided by experimental data from shock tube experiments for shock-bubble interactions. Ranjan *et al.* (2007) [87] have performed experiments in a vertical shock tube, subjecting a spherical soap bubble filled with helium to acceleration by a  $M = 2.95$  shock wave, in a nitrogen environment initially at atmospheric temperature and pressure. Flow visualization is provided by planar laser illumination and Mie scattering from atomized soap film particles entrained in the post-shock flow. At very late times, Ranjan *et al.* observe the development of large, distinct secondary and tertiary vortex rings at the upstream end of the shocked bubble, rotating in the opposite sense to the primary vortex ring. Ranjan *et al.* also report the translational velocity and estimated circulation associated with the shocked bubble, obtained from

the experimental flow visualizations. In related work at the Wisconsin Shock Tube Laboratory, these experiments have been extended to lower Mach numbers,  $M = 1.45, 2.08$ , and the results have been compared in detail to numerical simulations by Ranjan *et al.* (2007) [88].

These experiments are simulated here using *Raptor* on a three-dimensional Cartesian mesh at a spatial resolution of  $R_{100}$  on the finest AMR level. A single quadrant of the flowfield is included in the simulation. The bubble is initialized as a spherical volume of radius  $R = 1.905$  cm, with no soap film or surface tension effects included. Visualizations of the flowfields from both simulations and experiments are shown for the  $M = 2.95$  scenario in Fig. 15, and at late times for all three scenarios ( $M = 1.45, 2.08, 2.95$ ) in Fig. 16. Numerical images show a slice through the dataset, oriented at a 30-degree angle to the boundary. The density field is plotted, with an overlaid contour indicating the isosurface of  $f = 10^{-6}$ ; the component of the vorticity normal to the slice plane is plotted alongside the density as a reflection. The transverse width of the field of view is 8 cm in the experimental and numerical images, and the initial shock wave motion is downward.

In Fig. 15, we observe that the patterns of deformation undergone by the bubble in simulations bear strong similarities to those seen in experiments. The images are labeled using a dimensionless time based on the transmitted shock wave speed  $W_t$ . The bubble is initially compressed axially during the transit of the initial shock wave, seen in Fig. 15(a). Vorticity generated by the baroclinic term appearing in Eq. 1.7 causes the upstream surface of the bubble to deform and “cave in” toward the downstream surface [87], as seen in Fig. 15(b-c). The caving-in portion of the upstream surface impinges on the downstream surface, and the vortex layer generated on the bubble surface during

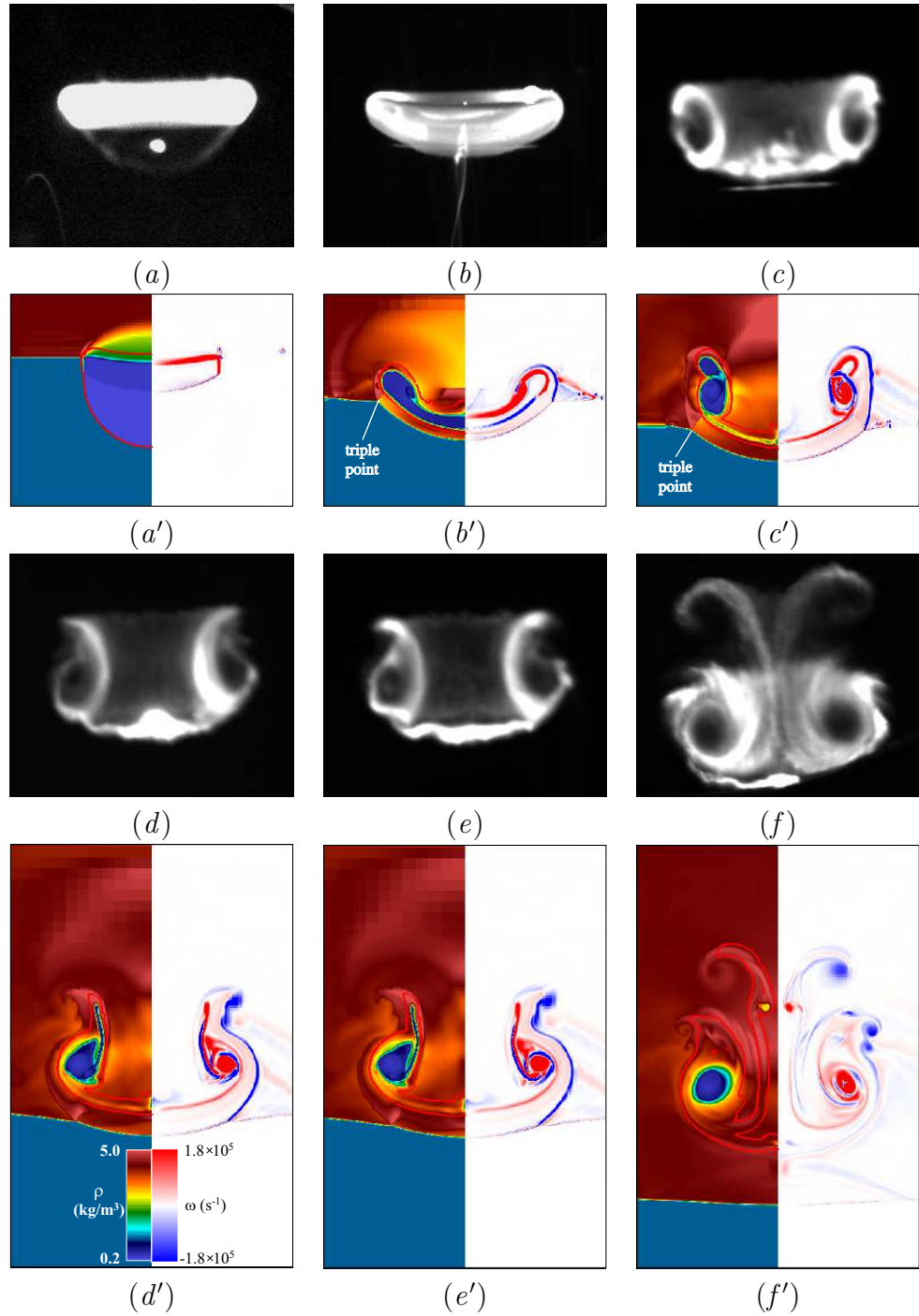


Figure 15: Flowfield evolution for  $M = 2.95$ , air-He shock-bubble interaction. Numerical images show (on the left) the total density with the isosurface of  $f = 10^{-6}$  plotted in red, and (on the right) vorticity magnitude. Dimensionless times  $tW_t/R$  are (a) 1.3, (a') 1.3, (b) 4.0, (b') 4.1, (c) 7.7, (c') 7.7, (d) 11.4, (d') 11.5, (e) 11.6, (e') 11.8, (f) 23.8, (f') 23.6. The width of the field of view in each image is 8 cm.

shock passage rolls up and draws the bubble fluid into a characteristic primary vortex ring, as seen at the downstream end of the bubble in Fig. 15(*d*). This “caving-in” or inversion process, observed in both experiments and simulations here, is a well-known feature of divergent-geometry shock-bubble interactions, as observed in Refs. [42], [60], [87] and [88]. The correspondence between experimental and numerical results continues to intermediate times, where we see, in Fig. 15(*f-f'*), the emergence of upstream vortical features on the bubble, rotating in the opposite sense to the primary vortex ring.

The growth of this secondary vortex ring becomes even more pronounced as time goes on. In Fig. 16, for  $tW_t/R > 60$ , we see that the secondary vortex ring is a coherent flow feature that persists to late times. Fig. 16 shows the simulated and experimental flowfields at very late times for the three scenarios: (*a*)  $M = 1.45$ , (*b*)  $M = 2.08$ , and (*c*)  $M = 2.95$ . We observe that the secondary vortex ring (SVR) appears in both the  $M = 2.95$  and  $M = 2.08$  scenarios at late times. Further, a tertiary vortex ring (TVR) develops in the  $M = 2.95$  scenario, as well. However, both experiments and simulations show that for  $M < 2$ , a distinct secondary vortex ring rotating oppositely to the primary vortex ring (PVR) never appears, even at the very late times ( $tW_t/R > 100$ ) shown in Fig. 16(*a-a'*). Overall, we note a remarkable resemblance between the experimental and numerical visualizations of the shocked-bubble flowfield. The correspondence between the experimental and numerical results improves with increased Mach number due to the better flow-tracing properties of atomized soap film particles generated by stronger shock waves.

Finally, we compare the streamwise dimension  $S$  and lateral dimension  $L$  of the shocked-bubble region, obtained from experiments and simulations. These data indicate the initial compression of the bubble by the shock wave, and the subsequent growth of the

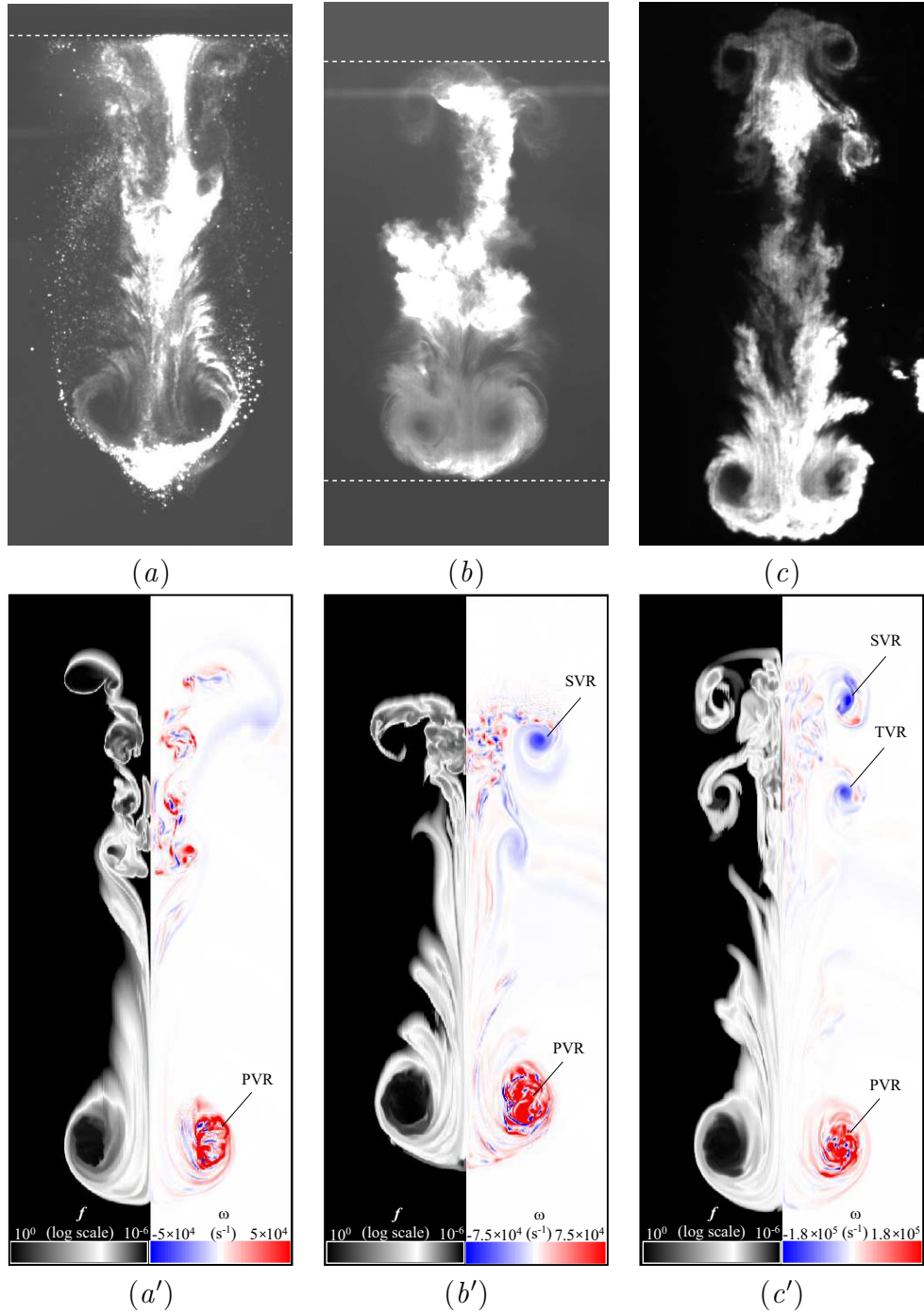


Figure 16: Late-time flowfield visualizations for  $M = 2.95$ , air-He shock-bubble interaction. Numerical images show (on the left) the helium volume fraction  $f$  on a logarithmic gray scale peaked at  $f = 10^{-4}$ , and (on the right) vorticity magnitude  $\omega$ . Dimensionless times  $tW_t/R$  are (a) 105.8, (a') 105.8, (b) 63.4, (b') 63.5, (c) 69.5, (c') 63.5. The width of the field of view in each image is 8 cm, and dotted lines indicate cropping locations.

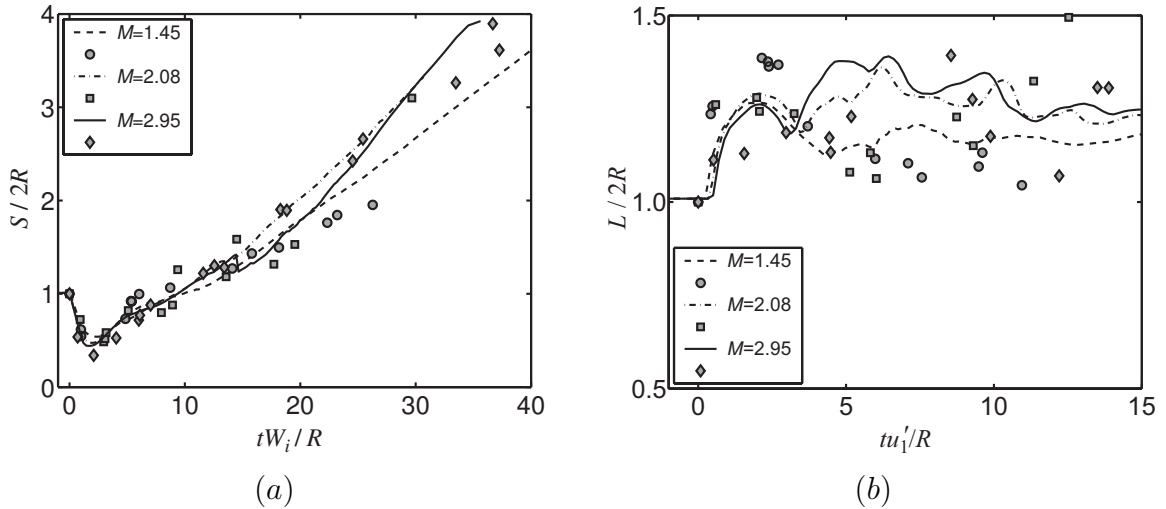


Figure 17: Temporal evolution of shocked bubble dimensions from experiments and simulations for a spherical helium bubble: (a) streamwise dimension, and (b) lateral dimension. The dimensionless timescale is based on the incident shock wave speed  $W_i$  or the post-shock ambient flow speed  $u'_1$ . Symbols represent experimental data; lines represent simulation results.

mixing region under the action of vortical effects initiated by shock wave passage over the bubble. The streamwise and lateral extents are plotted on dimensionless timescales for each of the three scenarios in Fig. 17. The spatial extents are obtained from simulation data by taking the average of fifteen azimuthal samples of the extrema of the  $f = 0.1$  contour; they are obtained from experimental data by recording the extrema of the region with a Mie-scattered signal that is greater than background. (Error bars are not included in these data, because the uncertainty in the experimental data originates primarily in the repeatability of the experiment, not in measurement error.) We observe that the *Raptor* simulations capture the evolution in the streamwise dimension of the bubble with good accuracy, although the agreement deteriorates at later times. For the lateral dimension of the bubble shown in Fig. 17(b), comparison of experimental and

numerical data indicates much stronger lateral growth at early times for  $M = 1.45$  than is found in simulations, although the early-time agreement is improved for higher Mach numbers. At late times, the experimental data do not show a clear trend, but, like the numerical results, indicate that the diameter of the shocked bubble does not exceed  $3R$  for  $tu'_1/R \leq 15$ .

Overall, we find that simulations for shock-bubble interactions using *Raptor* exhibit remarkable agreement with the results of shock tube experiments for these particular scenarios. This lends further support to the claim that *Raptor* may be used with confidence to simulate shock-bubble interactions.

### 2.3.3 Shock wave interaction with a cylindrical bubble: simulations

Two further test problems are considered here for validation of the numerical method. These are drawn from well-known points of reference in the literature: one problem studied by Quirk and Karni (1996) [84] (henceforward, QK96), and the other by Zabusky and Zeng (1998) [113] (henceforward, ZZ98).

In the first of these test problems, the shock-bubble interaction is considered for a cylindrical bubble of initial radius  $R = 2.5$  cm, containing refrigerant gas R22 (molar mass  $\mathcal{M} = 91.4$  g/mole, ratio of specific heats  $\gamma = 1.249$ ), accelerated by a planar shock wave of strength  $M = 1.22$  in air, as studied experimentally by Haas and Sturtevant (1987) [42]. QK96 integrated the Euler equations for this problem on a two-dimensional Cartesian mesh using a “nearly conservative primitive-variable” shock-capturing scheme within a two-level AMR implementation, at an effective grid resolution of  $R_{446}$  (446 grid cells in a distance equal to  $R$ ). The same initial and boundary conditions, AMR setup

and fluid properties are used here – except that a smoothed initial bubble surface is created – and the Euler equations are integrated using the *Raptor* scheme described in Sec. 2.1. In this “smoothed” setup, a subgrid VOF model (described in more detail in Sec. 3.1.5) is used to smooth corners protruding from the curved bubble surface.

Plots of the vorticity magnitude  $\omega = |\nabla \times \mathbf{U}|$  and the density gradient magnitude  $|\nabla \rho| = \sqrt{(\partial \rho / \partial x)^2 + (\partial \rho / \partial y)^2}$  from these simulations are shown in figure 18, which can be compared to the images shown in figure 7(a,c,d,e,g,h) of QK96, and to the experimental shadowgraphs in figure 11(a,c,d,e,g,h) of Haas and Sturtevant (1987) [42]. The flow visualizations in Fig. 18 demonstrate a qualitative level of agreement with the results of QK96, for many of the features highlighted in that work, including the “folding” of the transmitted shock wave seen in Fig. 18(b) ( $t = 142 \mu\text{s}$ ), and the two-pronged axial jet arising due to shock focusing, visible just right of center in Fig. 18(d-f). The wave patterns associated with shock focusing and the convergence of diffracted and reflected shock waves observed both in Haas and Sturtevant’s experiments and by QK96 at  $t = 187 \mu\text{s}$  and  $t = 247 \mu\text{s}$  are clearly resolved in the current simulations, as shown in Fig. 18(c,d). Further, the behavior of the total velocity circulation over time, computed as  $\Gamma(t) = \int \omega(x, y, t) dA$ , is shown in Fig. 19(a), and corresponds closely to the data shown in figure 15(a) of QK96, with a peak circulation of  $6.1 \text{ m}^2/\text{s}$  and a distinct drop in total circulation after shock passage, near  $t = 188 \mu\text{s}$ .

However, QK96 have noted that the initial development of vortical features on the surface of the bubble during shock passage has some grid-dependent properties. The growth of such grid-dependent features in Eulerian simulations for shock-contact initial-value problems has been characterized explicitly by Samtaney and Pullin (1996) [97] as a manifestation of the non-convergence of Euler simulations. The effect of these features is

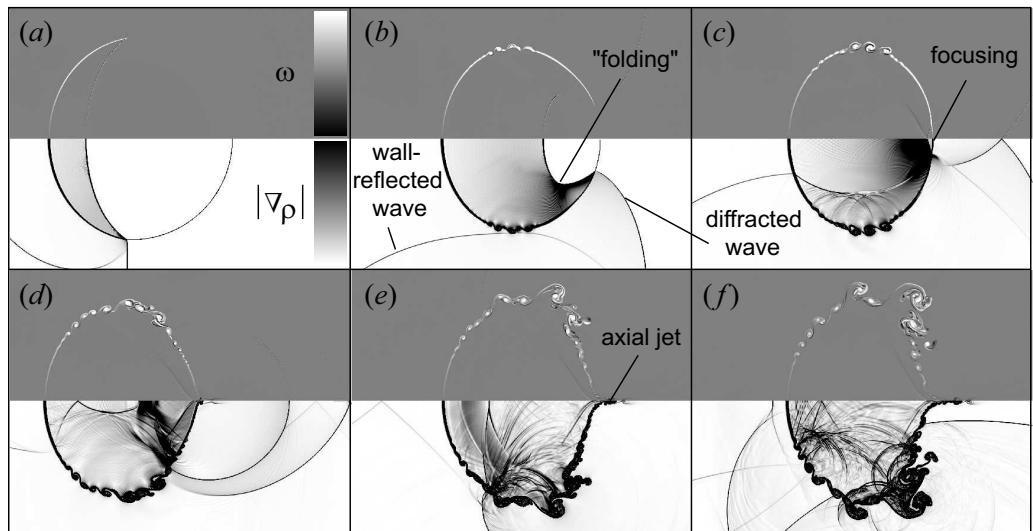


Figure 18: Vorticity magnitude (top) and density gradient magnitude (bottom) in the interaction of a  $M = 1.22$  shock wave with a cylindrical R22 bubble of radius 2.5 cm, after [84], simulated in two dimensions with *Raptor* at 446 grid points per bubble radius. Shock wave propagation is left-to-right. Times relative to initial shock wave impact: (a) 51  $\mu\text{s}$ , (b) 142  $\mu\text{s}$ , (c) 189  $\mu\text{s}$ , (d) 247  $\mu\text{s}$ , (e) 341  $\mu\text{s}$ , (f) 412  $\mu\text{s}$ .

particularly significant in the simulations described by QK96, because of the discontinuous nature of the initial bubble surface. That is, the interfacial layer effectively has zero thickness, and the volume fraction  $f$  of the bubble-interior gas is everywhere either zero or one in the initial condition. Corrugations are therefore present on the surface, due to the discretized projection of the curved interface onto the rectangular grid. This discretization sets a cutoff wavelength for the development of the Kelvin-Helmholtz rollups observed on the interface in Fig. 18, which results in the non-convergence of simulations for this flow using different methods and grid sizes. The “smoothed” setup has been introduced in order to minimize these effects, while keeping the density gradient at the bubble boundary as large as possible.

The simulations shown in Fig. 18 are repeated with an “unsmoothed” definition of the initial bubble surface in which the subgrid smoothing is removed. The resulting post-shock growth of the positive and negative components of the circulation is enhanced up to roughly 10% by  $t = 100 \mu\text{s}$  in the “unsmoothed” case, relative to the “smoothed” case, as shown in Fig. 19(a). The total circulation is unchanged, however, indicating that this is a more appropriate quantity for comparison between methods and initial data than the components of the circulation. The additional rotation manifested in the components of the circulation appears visibly as vortices on the interface in the “unsmoothed” case, and is introduced by the same baroclinic mechanism that is responsible for the large-scale vortical growth:

$$B(t) \equiv \left( \frac{d\Gamma}{dt} \right)_b = \int \frac{1}{\rho^2} (\nabla \rho \times \nabla p) \cdot d\mathbf{A}. \quad (2.6)$$

The total area-integrated baroclinic torque  $B(t)$ , along with its positive and negative components, is plotted against time in Fig. 19(b), showing that, although the net

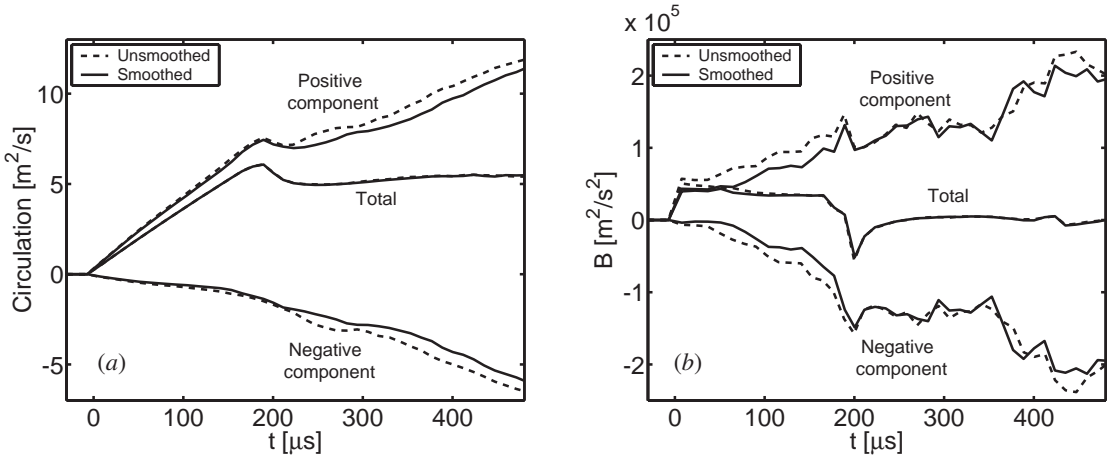


Figure 19: Decomposed (a) circulation  $\Gamma$  and (b) area-integrated baroclinic torque  $B$  versus time, for the interaction of a  $M = 1.22$  shock wave with a cylindrical bubble of R22, with bubble surfaces “unsmoothed” and discontinuous, or “smoothed” by use of a subgrid VOF technique.

or “total” values of  $B(t)$  are unchanged, the positive and negative components of  $B$  are both enhanced by as much as 40% during shock passage over the bubble in the “unsmoothed” case, relative to the “smoothed” case. (For example, at  $t = 65 \mu\text{s}$ , the positive component of baroclinic torque for the “unsmoothed” case is  $0.72 \times 10^5 \text{ m}^2/\text{s}^2$ , while for the “smoothed” case, it is only  $0.46 \times 10^5 \text{ m}^2/\text{s}^2$ .) Angular momentum added by this additional local torque accumulates over time, resulting in the enhanced magnitudes of the circulation components seen at late times in Fig. 19(a). The additional local baroclinic torque due to corners on the initial interface can have either sign, and thus adds nothing to the net integrated torque. However, the components of the local torque are significantly enhanced, resulting in the development of spurious vortices.

### 2.3.4 Shock wave interaction with a spherical bubble: simulations

A second two-dimensional test problem for the shock-bubble interaction involves a spherical bubble of refrigerant gas R12 ( $\mathcal{M}=120.9$  g/mole,  $\gamma=1.141$ ) accelerated by a  $M = 2.5$  planar shock wave. This scenario was simulated by Zabusky and Zeng (1998) [113] – “ZZ98” – on a uniform two-dimensional rectangular grid in  $r$ - $z$  symmetry about the direction of shock wave motion, at a spatial resolution of  $R_{55}$ , using a second-order upwind TVD scheme. The flow is simulated with *Raptor*, using the same boundary and initial conditions and fluid properties given by ZZ98 (including a “smoothed” initial bubble surface), except that the geometry is scaled to a bubble radius of  $R = 1$  cm here. In Fig. 20, the vorticity magnitude and density fields resulting from the *Raptor* simulation are plotted, showing the generation of opposite-signed vorticity and the emergence of secondary vortical features at late times, as seen in figure 13 of ZZ98. In particular, at  $t = 93$   $\mu\text{s}$  (Fig. 20f), one should note the formation of a distinct secondary vortex ring on the upstream bubble surface, a small axial jet and vortex ring on the downstream surface, and regions of opposite-signed vorticity within the primary vortex ring, as observed by ZZ98. Very good qualitative agreement between the two methods is also evident, by comparison to ZZ98.

These phenomena are depicted clearly in the plot of  $r$ -integrated vorticity in Fig. 21(a), in which figure 16(a) of ZZ98 is reproduced using the current results. The radially-averaged vorticity

$$\langle \omega \rangle = \frac{\int_0^{r_{\max}} \|\boldsymbol{\omega}\| dr}{r_{\max}} \quad (2.7)$$

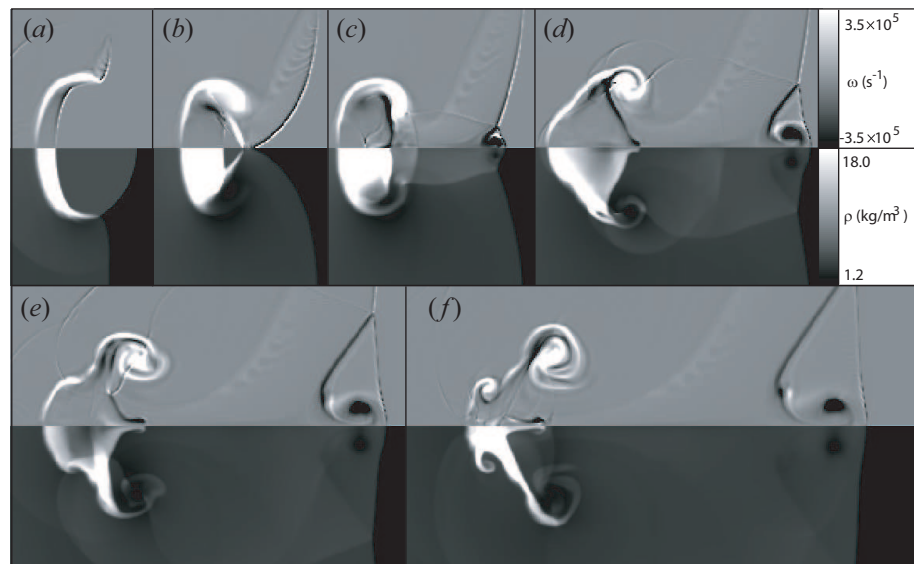


Figure 20: Vorticity magnitude (top) and density (bottom) plots for the interaction of a  $M = 2.5$  shock wave with a spherical R12 bubble of radius 1 cm (after [113]), simulated with *Raptor* in two dimensions ( $r$ - $z$  symmetry) with 55 grid points per bubble radius. Shock wave propagation is left-to-right. Times relative to shock wave impact: (a) 19  $\mu$ s, (b) 34  $\mu$ s, (c) 45  $\mu$ s, (d) 60  $\mu$ s, (e) 76  $\mu$ s, (f) 93  $\mu$ s.

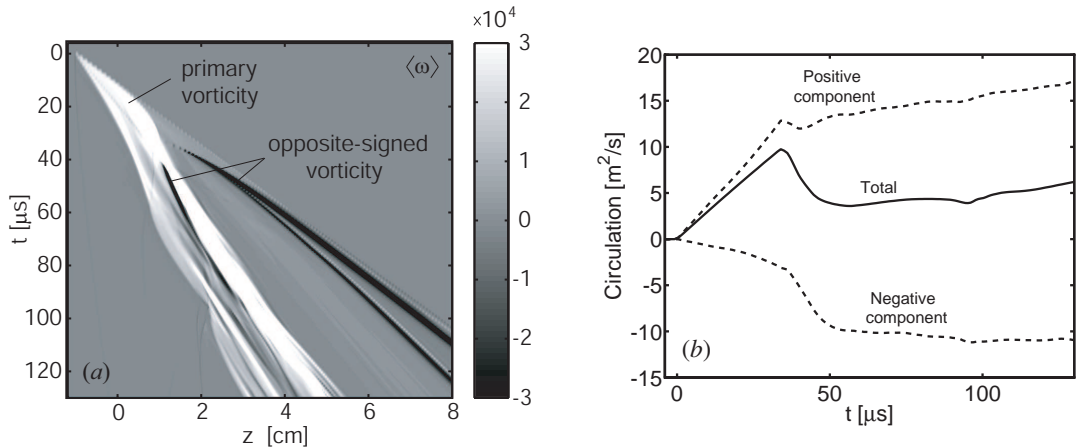


Figure 21: Integrated vortical behavior for a  $M = 2.5$ , air-R12 shock-bubble interaction: (a) space-time plot of the  $r$ -integrated vorticity  $\langle \omega \rangle$ , after figure 16(a) of [113], and (b) decomposed circulation in the domain versus time. Opposite-signed vorticity (black) begins to appear in (a) when the transmitted shock wave reflects from the downstream bubble surface, resulting in the downturn in circulation seen in (b) after  $t = 34$  μs.

is plotted on the  $z$ - $t$  coordinate axes, with time progressing in the downward direction. The prominent white streak represents primary (positive) vorticity generated during initial shock passage. Black streaks appear within the white when the transmitted shock wave reaches  $z = R$  (where the origin is at the bubble center), due to opposite-signed vorticity generated by reflected shock waves originating at that time. A prominent black streak runs ahead of the primary white structure, which represents the strong opposite-signed vorticity associated with the Winkler-Group supersonic vortex ring (see Winkler *et al.* (1987) [109]) trailing behind the shock wave after re-transmission into the ambient gas, first visible in Fig. 20(c) and depicted schematically in Fig. 3.

The circulation, integrated over the entire computational domain, and decomposed into its positive and negative components, is plotted over time in Fig. 21(b), which can be compared to figure 17(c) in ZZ98. The total circulation has a peak at shock passage

near  $t = 34 \mu\text{s}$ , followed by a very strong decrease to less than half the peak value. This abrupt decrease is caused by the deposition of opposite-signed vorticity by reflected shocks, and is vividly documented by ZZ98. The plots in both Fig. 21(a) and Fig. 21(b) demonstrate a high degree of quantitative agreement between the results of ZZ98 and results generated using *Raptor*.

# Chapter 3

## Simulation Setup and Results

The multidimensional, multifluid Eulerian Godunov AMR code *Raptor*, whose construction and performance is described in Chapter 2, is used here to study shock-bubble interactions using a series of three-dimensional simulations across a parameter space delimited by  $-0.8 < A < 0.7$  and  $1.14 \leq M \leq 5$ . The extension from two-dimensional to three-dimensional treatment in this study is motivated by two observations: first, that the shock-bubble interaction exhibits features that are fundamentally turbulent (see Haas and Sturtevant, 1987 [42]); and, second, that the behavior of two-dimensional and three-dimensional turbulence is fundamentally different, due to the absence of the vortex-stretching mechanism in two-dimensional symmetry (see Pope, 2000 [82]). Further, the presence of non-axisymmetric perturbations in the initial bubble geometry has been experimentally observed [51, 43] to initiate azimuthal vortex ring instabilities of the type described for incompressible flows by Widnall *et al.* (1974) [108]. These significant non-axisymmetric and turbulent effects arise because of the transport of mass, momentum and energy in the azimuthal direction, and lead to a late-time flow field characterized by disorderly motion and well-developed mixing regions, rather than by the well-defined, coherent vortex dipoles and vortex projectiles observed in the two-dimensional simulations of Zabusky and Zeng (1998) [113] and others.

## 3.1 Setup of Three-Dimensional Parameter Study Simulations

### 3.1.1 Coordinate system and geometry

Three-dimensional simulations for the parameter study are set up using a Cartesian mesh subtending a quadrant of a typical shock tube flow field, including a quarter-spherical bubble of radius  $R$ , as shown in Fig. 22. (The growth of azimuthal mode numbers less than four is thus excluded, and the computational effort here is devoted to the behavior of shorter-wavelength perturbations.) A coordinate system is defined whose  $y$ -axis is coincident with the shock tube long axis in the direction of shock wave motion, and whose  $x$ - and  $z$ -axes run in the transverse directions. The incident shock wave and freestream flow move in the  $+y$ -direction. The domain represents a physical space of dimensions  $4R \times L_y \times 4R$ , where  $4R = 10.16$  cm, and  $L_y$  is variable and selected to be large enough to accommodate the motion of the shocked bubble through the times of interest. An alternate coordinate system can be used to describe this space by defining an  $x$ - $z$ -plane radial coordinate  $\mathbf{r}_{xz} = (x, 0, z)$  and an azimuthal unit vector  $\hat{\theta} = \hat{y} \times \mathbf{r}_{xz}/|\mathbf{r}_{xz}|$ .

In the present simulations, the base grid resolution is  $32 \times N_y \times 32$ , where  $N_y = L_y/\Delta_c$  and  $\Delta_c$  is the (uniform) coarse-grid cell size. Two levels of AMR are superposed on the coarse grid, with a refinement ratio of 4 each. This gives a mesh resolution on the finest AMR level of  $\Delta = 198$   $\mu\text{m}$ , which effectively corresponds to  $R_{128}$ . AMR settings are chosen to require maximum refinement in all regions having a nonzero bubble fluid volume fraction, and near any strong density gradients. Thus, the entire bubble

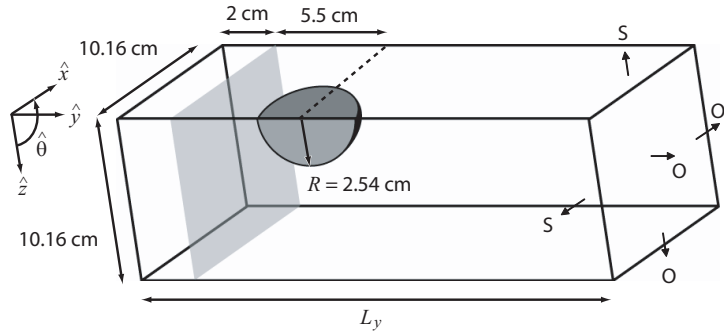


Figure 22: Schematic representation of initial and boundary conditions. Boundaries are symmetric (indicated by “S”) or outflow (“O”). The shock wave and freestream flow move in the  $+y$ -direction.

region is captured with maximum resolution and accuracy, and the primary shock wave is captured at maximum resolution and accuracy from the initialization of the problem until refinement of density gradients is turned off after the shock wave has moved to a distance of at least  $7R$  downstream from the bubble. In many cases, however, density-gradient refinement is enforced for twice that duration or more, to allow for replanarization of the shock front, particularly at high  $M$  and high  $A$ . Refinement of nonzero bubble fluid concentrations remains active throughout the entire simulation.

### 3.1.2 Boundary conditions

Symmetry boundary conditions are imposed on the two interior bounding surfaces parallel to the freestream flow ( $-\hat{x}$  and  $-\hat{z}$ ), indicated by “S” in Fig. 22. For a surface defined by outward normal vector  $\hat{n}$ , and velocity components parallel and perpendicular to the surface,  $V_{\parallel}$  and  $V_{\perp}$  respectively, the symmetry condition requires

$$V_{\perp} = 0 \quad , \quad (3.1)$$

$$\partial V_{||}/\partial \hat{n} = 0 \quad , \quad (3.2)$$

$$\partial \rho / \partial \hat{n} = 0 \quad , \quad (3.3)$$

$$\partial e / \partial \hat{n} = 0, \quad (3.4)$$

Outflow conditions are enforced on the four other bounding surfaces: two exterior surfaces parallel to the freestream flow ( $+\hat{x}$  and  $+\hat{z}$ ), and two bounding surfaces normal to the mean flow ( $-\hat{y}$  and  $+\hat{y}$ ), denoted by “O” in figure 22. The outflow condition applies a zeroth-order extrapolation to the boundary: *i.e.*, the outermost plane of data is copied into the boundary, so that gradients across the boundary are zero. Shock reflections are then minimized, though not eliminated completely for flows with strong shock waves. Contamination of the solution by reflections in these cases is prevented by using adaptive gridding to keep the boundary as far from the region of interest as possible.

### 3.1.3 Initial condition

In the initial condition, a planar shock wave approaches a spherical bubble of specified test gas. Three regions are defined in the initial condition: a bubble-interior region and shocked and unshocked regions of the ambient gas. The bubble region is a quarter-spherical volume of radius  $R = 2.54$  cm, centered on the  $y$ -axis, as shown in Fig. 22. The remainder of the domain is filled with the ambient gas. A perfect discontinuity in the flow variables, representing a planar shock wave of specified strength propagating in the exterior fluid, is initially located 2.96 cm from the upstream surface of the bubble

region, and approaches the bubble in the  $+\hat{y}$  direction.

The bubble interior gas and unshocked exterior gas regions are initialized at an ambient atmospheric pressure  $p_1 = 101.3$  kPa and temperature  $T_1 = 293$  K. The bubble and unshocked exterior gas are initially assumed to be at rest and in thermal and mechanical equilibrium, and any buoyant motion of the bubble is neglected here.

### 3.1.4 Fluid properties

An experimentally-measured ratio of specific heats  $\gamma$  for each gas is obtained from JANAF data [35], using the initial, unshocked pressure and temperature. Each fluid defined in the initial condition retains this fixed value of  $\gamma$  throughout the entire simulation (thus there are two distinct  $\gamma$  values). The bubble interior gases used in this study include helium, argon, krypton and dichlorodifluoromethane (refrigerant gas freon-12; henceforward, “R12”); the ambient gases used are air and nitrogen. (Nitrogen is used as the ambient gas in three scenarios in order to coincide with the work of Ranjan *et al.*, 2005 [86].) The fixed fluid properties and initial densities and sound speeds for all of the gases used in the present parameter study can be found in table 2. Post-shock properties of the ambient gases used in the initialization are computed using the laws of one-dimensional gasdynamics [64].

### 3.1.5 Ill-posed phenomena and interface smoothing

Using these initial data, then, the hyperbolic system in Eq. 2.1 is solved numerically as an initial-value problem. Samtaney and Pullin (1996) [97] have thoroughly examined the issue of convergence for solutions of the compressible Euler equations, and shown that

Gas	$\mathcal{M}$	$\gamma$	$c$	$\rho$
	[g/mole]		[m/s]	[kg/m <sup>3</sup> ]
He	4.003	1.667	1007.2	0.167
N <sub>2</sub>	28.013	1.399	348.8	1.165
Air	28.967	1.399	343.0	1.205
Ar	39.948	1.670	319.1	1.661
Kr	83.804	1.672	220.5	3.485
R12	120.91	1.143	151.8	5.028

Table 2: Initial properties of fluids in the current simulations. The initial pressure and temperature in the system are  $1.013 \times 10^5$  Pa and 300 K, respectively.

such simulations exhibit many ill-posed phenomena, the most significant of which is non-convergence of the solution at fixed time, with respect to the spatial-temporal resolution. This is a significant issue in Eulerian simulations for shock-accelerated inhomogeneous flows, particularly in the absence of surface tension on fluid interfaces, and on rectangular grids. The solution does not always vary continuously with the initial data: interface features associated with projection onto a rectangular grid introduce grid-dependent features to shock refraction and vortex formation patterns, as discussed in Sec. 2.3.3. The problem studied here may therefore be considered ill-posed, and in this sense, some small-scale features of the simulated flowfields may be suspect. However, the Eulerian AMR simulations discussed here represent the optimal computational effort for which solutions at this local resolution can be obtained in the context of a parameter study.

The effects of ill-posed phenomena in the results are minimized here by smoothing the initial bubble surface while maintaining its large density gradient. A subgrid VOF technique (mentioned in Sec. 2.3.3) is used to ensure that the interfacial transition layer has a small but finite thickness. In this technique, each cell spanning the surface  $(x^2 + (y - y_c)^2 + z^2)^{\frac{1}{2}} = R$  is first divided uniformly into 1000 subcells (ten in each

direction), where  $y_c$  is the  $y$ -coordinate of the bubble center. Each subcell is regarded as interior to the bubble if the bubble radius  $R$  exceeds the distance of the subcell center to the bubble center. The appropriate bubble fluid volume fraction for the parent cell is then determined by the number of interior subcells it subtends. This suppresses the appearance of corners on the bubble surface and produces a smoothed initial interface, with a maximum interfacial layer thickness of two grid cells, or  $R/64$ . Therefore, the effective perturbation on the initial bubble interface due to the grid has an amplitude on the order of  $\Delta_f/10$  (19.8  $\mu\text{m}$ , thus subgrid), and a minimum wavelength on the order of  $\Delta_f$  (198  $\mu\text{m}$ ). (The spectral content of this effective perturbation can be found in Sec. 5.1.8, Fig. 61.)

### 3.1.6 Parameter study cases

Fourteen shock-bubble-interaction scenarios, including four different gas combinations, are considered here. An overview of the parameter study scenarios is given in Table 3, showing the Mach number  $M$  of the incident shock wave, the Atwood number  $A$  and initial density ratio  $\chi = \rho_2/\rho_1$  at the unshocked interface, and relevant velocities for each scenario, computed from one-dimensional gasdynamics. These simulations and the results are also described in detail in Ref. [74]. (Sample input files for the *Raptor* simulations are given in Appendix C.) Scenarios are selected to coincide with previous experimental or computational work on this subject [60, 61, 59, 62, 86, 87, 113]. Although this produces a nonuniform sampling of the parameter space, the results may be referenced directly to previous work using only spatial scaling arguments if necessary.

Case no.	Gas combination	$M$	$A$	$\chi$	$W_i$ [m/s]	$u'_1$ [m/s]	$W_t$ [m/s]
1	Air/He	1.20	-0.757	0.138	411.6	104.8	1112
2		1.50			514.5	238.3	1259
3		1.68			576.2	310.2	1344
4		3.00			1029	762.5	1958
5	N <sub>2</sub> /Ar	1.33	0.176	1.426	463.9	168.1	432.3
6		2.88			1005	736.5	981.2
7		3.38			1179	896.8	1159
8	Air/Kr	1.20	0.486	2.892	411.6	104.8	275.4
9		1.50			514.5	238.3	361.7
10		1.68			576.2	310.2	414.8
11		3.00			1029	762.5	811.4
12	Air/R12	1.14	0.613	4.173	391.0	75.15	182.4
13		2.50			857.5	600.5	499.3
14		5.00			1715	1373	1080

Table 3: Parameter study overview, including the incident shock Mach number  $M$ , the Atwood number  $A$  and density ratio  $\chi$  at the unshocked interface, and lab-frame speeds  $W_i$ ,  $u'_1$  and  $W_t$  of the incident shock wave, shocked ambient gas and transmitted shock wave, respectively.

## 3.2 Flow Visualizations and Descriptions

With this setup, simulations are carried out for each of the fourteen cases outlined in Sec. 3.1 and Table 3, using the Raptor code described in Chapter 2. Data files are generated and stored after every fifth coarse-grid timestep. The solution in each case is carried out to about  $\tau = 25$  (roughly 500 coarse-grid time steps, for these simulations), where  $\tau$  is a dimensionless timescale normalized to the bubble radius traversal time for whichever wave is fastest: the initial shock wave, or the shock wave transmitted across the equivalent one-dimensional interface between the ambient and bubble gases. Thus, for  $A < 0$ , the transmitted shock wave is the fastest-moving shock wave in the system, and the dimensionless timescale  $\tau$  is given by  $\tau = tW_t/R$ . This timescale can be computed in general as  $\tau = tW^*/R$ , where

$$W^* = \begin{cases} W_i, & A \geq 0 \\ W_t, & A < 0 \end{cases}, \quad (3.5)$$

Under this timescaling, in the absence of shock diffraction, the moment of shock passage (arrival of the *first* shock wave at the downstream bubble pole) corresponds to  $\tau = 2$  for all scenarios. At shock passage, the initial stage of baroclinic vorticity deposition ceases, and opposite-signed vorticity appears as reflected shock and rarefaction waves traverse the bubble, moving in the upstream direction.

Figures 23-26 show the development of the shocked bubble to  $\tau = 25$ , for four scenarios from the present simulations. In these representative plots, a slice is taken through the three-dimensional data at an angle of  $\theta = \pi/6$  to the  $x = 0$  plane. The total density  $\rho$  and vorticity magnitude  $\omega = \boldsymbol{\omega} \cdot \hat{\boldsymbol{\theta}}$  on the slice are plotted, where  $\hat{\boldsymbol{\theta}} = \hat{\mathbf{y}} \times \hat{\mathbf{r}} = (\cos(\theta), 0, -\sin(\theta))$ , and  $\hat{\boldsymbol{\theta}}$  is directed normally out of the page on the top, and into the

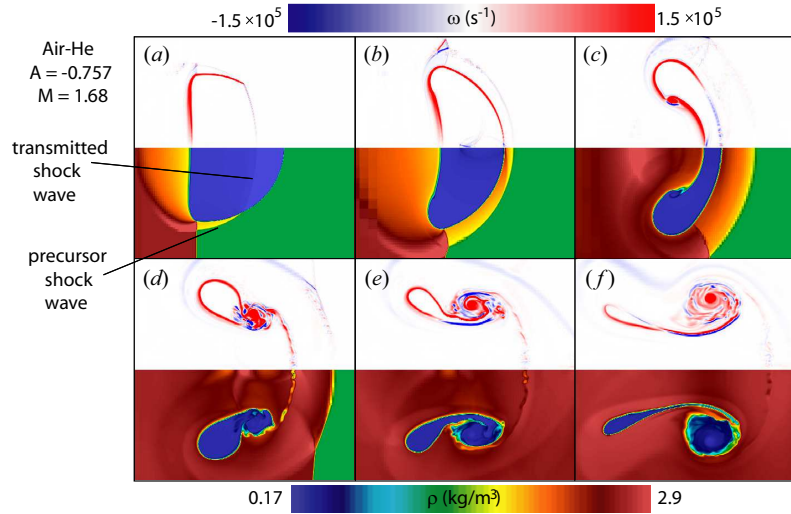


Figure 23: Density (bottom) and vorticity magnitude (top) on the  $\theta = \pi/6$  plane for the  $M = 1.68$  air-He scenario ( $A = -0.757$ ): (a)  $\tau = 1.4$ , (b)  $\tau = 2.6$ , (c)  $\tau = 5.2$ , (d)  $\tau = 9.9$ , (e)  $\tau = 15.0$ , (f)  $\tau = 24.9$ . The density color palette is shown at bottom, and vorticity is plotted on a symmetric color palette centered on white, shown at top. Note that  $\tau = tW_t/R$  here. Incident shock wave propagation is left-to-right.

page on the bottom. The scenarios are arranged in figures 23-26 in order of increasing Atwood number. Individual frames are labeled by the dimensionless time  $\tau$ , as given in the figure captions.

In these simulations, we consider the shock-bubble interaction within an idealized shock-tube environment. Thus, the incident shock wave is assumed to have negligible curvature, thickness and pressure decay, and the effects of radiation, conduction, phase changes, ionization, electric and magnetic fields and chemical and nuclear reactions (which are significant in many environments where shock-bubble interactions take place) are all neglected. The physical mechanisms that remain are purely hydrodynamic, and are dominated by three nonlinearly coupled, simultaneous processes: (1)

shock-induced compression and heating; (2) nonlinear-acoustic phenomena; and (3) vorticity production and transport.

The first of these can be clearly understood in terms of the Rankine-Hugoniot conditions, which characterize irreversible changes across surfaces of discontinuity in a gas. The second and third types of processes are much more difficult to characterize, because they involve the highly nonlinear effects of the curved density interface at the bubble surface. This curvature leads to the “scattering” of the incident shock wave into reflected, refracted, diffracted and transmitted waves, collectively referred to as “nonlinear-acoustic effects.” It also leads to the creation of a field of strong, coupled vortices in the flow as the incident and scattered shock waves interact with the deforming density interface, via the baroclinic source term in Eq. 1.7. These two types of processes are clearly visualized in Figs. 23-26, and described in Secs. 3.2.1 and 3.2.2

### **3.2.1 Shock refraction, reflection, and diffraction**

Examining the wave patterns seen in Figs. 23-26, we note that the variety of refraction, reflection, and diffraction patterns indicates the breadth of this parameter space. In the air-He ( $A = -0.757$ ) scenario shown in Fig. 23, it is apparent that the interaction has reached the irregular refraction regime as early as  $\tau = 1$ . Because of the very large negative Atwood number, which reflects the drop in acoustic impedance across the interface, the transmitted shock wave, visible in Fig. 23(a), has distinctly convex curvature. Further, because of the small critical angle at this  $A$ , a precursor shock wave and Mach stem form outside the bubble, while the transmitted shock wave runs far ahead of the incident shock wave inside the bubble (Fig. 23a). The bubble thus acts like a strongly divergent lens, refracting the shock front away from the axis. Also, we

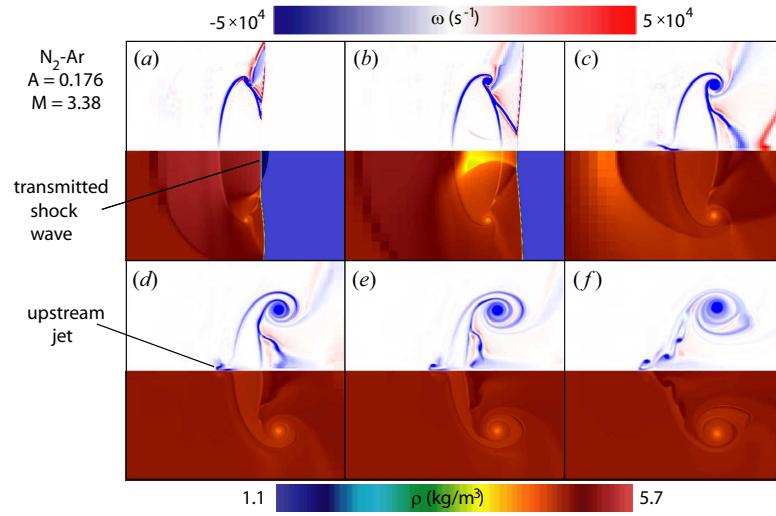


Figure 24: Density (bottom) and vorticity magnitude (top) on the  $\theta = \pi/6$  plane for the  $M = 3.38$   $N_2\text{-Ar}$  scenario ( $A=0.176$ ): (a)  $\tau = 1.6$ , (b)  $\tau = 2.6$ , (c)  $\tau = 5.0$ , (d)  $\tau = 10.0$ , (e)  $\tau = 15.0$ , (f)  $\tau = 24.9$ . The density color palette is shown at bottom, and vorticity is plotted on a symmetric color palette centered on white, shown at top. Note that  $\tau = tW_i/R$  here. Incident shock wave propagation is left-to-right.

see that positive vorticity is generated on the surface of the bubble as the transmitted shock wave passes, long before the passage of the incident shock wave.

In the nitrogen-argon ( $A = 0.176$ ) scenario shown in Fig. 24, the refractive effect is very weak, due to a small magnitude of  $A$  (see Table 3). Thus, the transmitted shock wave has only very subtle concave curvature, even at  $M = 3.38$ . In this case, the angle of inclination between the unshocked bubble interface and the incident shock wave only reaches normality at the midpoint of shock wave transit across the bubble, and becomes nearly tangential again at the downstream surface; no shock-diffraction or shock-focusing behavior is observed.

In the air-krypton ( $A = 0.486$ ) and air-R12 ( $A = 0.613$ ) scenarios in Figs. 25 and 26, however, the refractive effect is quite strong. The formation of a collapsing shock

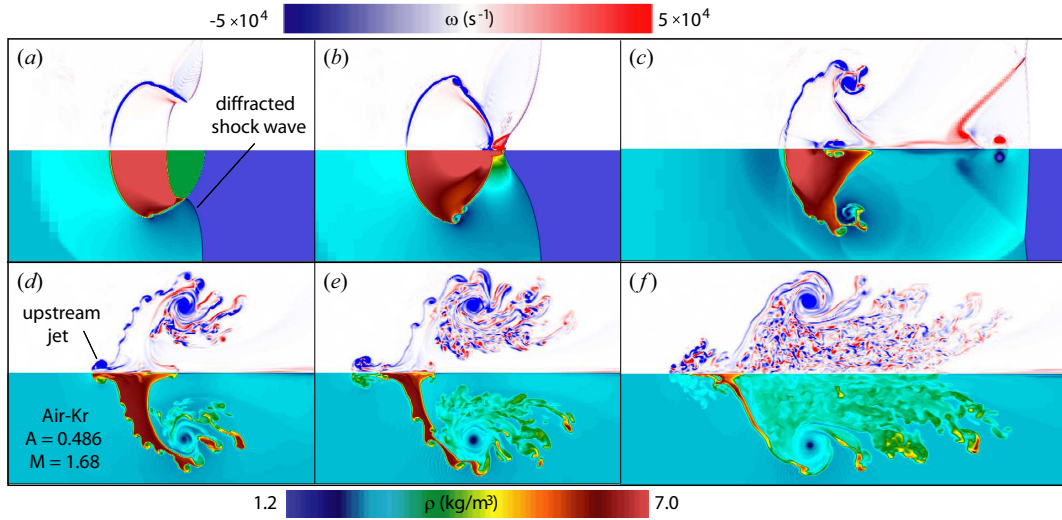


Figure 25: Density (bottom) and vorticity magnitude (top) on the  $\theta = \pi/6$  plane for the  $M = 1.68$  air-Kr scenario ( $A=0.486$ ): (a)  $\tau = 1.6$ , (b)  $\tau = 2.6$ , (c)  $\tau = 5.0$ , (d)  $\tau = 10.2$ , (e)  $\tau = 14.9$ , (f)  $\tau = 25.0$ . The density color palette is shown at bottom, and vorticity is plotted on a symmetric color palette centered on white, shown at top. Note that  $\tau = tW_i/R$  here. Incident shock wave propagation is left-to-right.

cavity of the type described by ZZ98 [113] is clearly resolved in the simulations, as the transmitted shock wave becomes strongly concave, and undergoes focusing. The bubble, in these cases, acts like a strongly convergent lens, refracting the shock wave toward the axis.

Diffracted shock waves become particularly important in the strongly convergent cases. Diffracted shock waves, shown schematically in Fig. 3(c-d), are the portions of the incident shock wave which are distorted as they sweep around the periphery of the bubble, without encountering the density interface directly. Unlike in the weakly convergent nitrogen-argon scenario, in the strongly convergent cases (air-krypton and air-R12), the diffracted shock wave remains nearly normal to the bubble surface at the point where it contacts the interface, while sweeping around from the equator to the

downstream pole, where focusing occurs. This “near-normality” behavior, observed in simulations previously by Samtaney and Zabusky (1994) [99], dramatically changes the shape of the primary shock front as it moves downstream from the vicinity of the bubble, and effectively slows the progress of vorticity deposition, as the diffracted shock wave must travel a distance equal to  $(1 + \pi/2)R$  to reach the downstream pole, rather than just  $2R$ . Thus, the diffracted shock waves do not reconverge on the downstream pole until approximately  $\tau \approx 2.57$ , rather than 2.0, as shown in Figs. 25(*b*) and 26(*b*).

Further, because the diffracted shock waves maintain normality to the bubble surface, shock waves diffracted around opposing limbs of the bubble collide with each other when they reach the downstream pole, as depicted schematically in Fig. 3(*d*). This collision, compounded with the focusing of the transmitted shock wave, produces an intense pressure jump and initiates additional periods of baroclinic vorticity deposition as the resulting shock waves subsequently traverse the bubble in the lateral and upstream directions. Shock waves moving laterally across the bubble after such a collision are visible as curved, light blue fronts moving across a darker blue background in Fig. 26(*c-d*). The effects of these secondary shock waves, such as dramatic changes in the bulk density of the bubble, are known to be present as late as  $\tau = 12$  (see Sec. 4.1.1 and Fig. 39).

Another noticeable result of the intense nonlinear acoustic effects in the high- $A$  shock-bubble interaction is the formation of a Winkler-Group vortex, following just behind the shock wave after re-transmission into the ambient gas, seen in Figs. 25(*c*) and 26(*c*) [109]. This opposite-signed vortex ring is also responsible for the prominent black streak seen in figure 21(*a*), running ahead of the shocked bubble region.

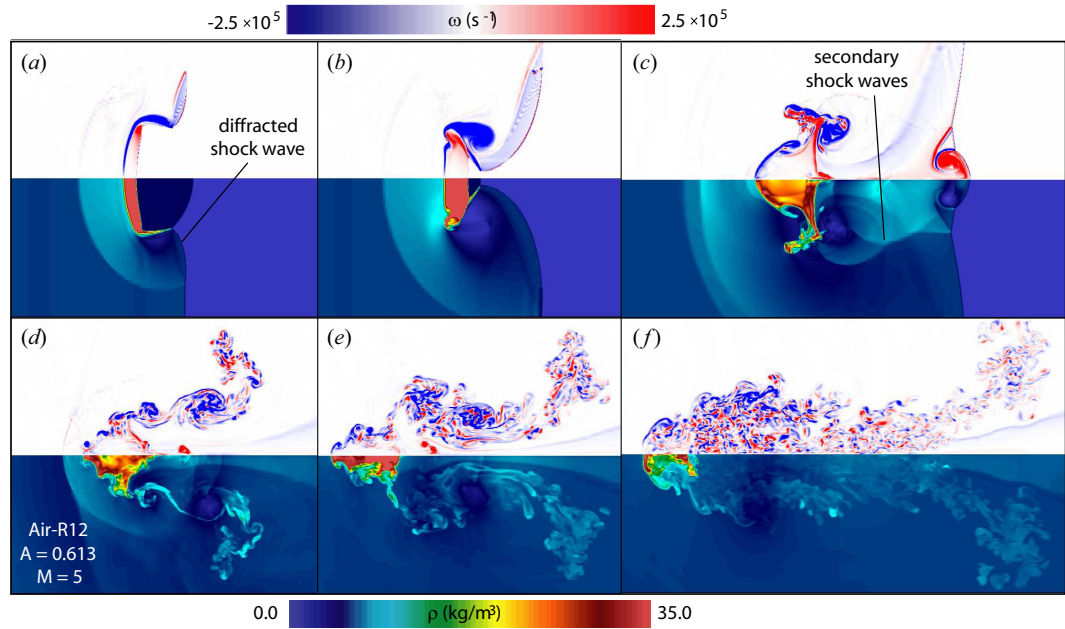


Figure 26: Density (bottom) and vorticity magnitude (top) on the  $\theta = \pi/6$  plane for the  $M = 5.0$  air-R12 scenario ( $A=0.613$ ): (a)  $\tau = 1.5$ , (b)  $\tau = 2.5$ , (c)  $\tau = 5.0$ , (d)  $\tau = 10.1$ , (e)  $\tau = 15.0$ , (f)  $\tau = 25.0$ . The density color palette is shown at bottom, and vorticity is plotted on a symmetric color palette centered on white, shown at top. Note that  $\tau = tW_i/R$  here. Incident shock wave propagation is left-to-right.

In all of the convergent-geometry cases ( $A > 0$ ), reflected and/or diffracted (“secondary”) waves reverberate through the bubble after  $\tau = 2$ . This is due to the nature of nonlinear-acoustic effects in  $A > 0$  scenarios: shock waves leaving the bubble must produce reflected rarefaction waves in the bubble gas, while, simultaneously, diffraction and focusing processes produce secondary shock waves into the bubble region. Thus, even in the weakly convergent nitrogen-argon scenario, a rarefaction and shock wave successively pass through the bubble moving upstream after  $\tau = 2$ , visible as a shock-bounded yellow region in Fig. 24(b). These are generated by the interaction of the transmitted shock wave with the downstream interface, and by convergence of the diffracted shock waves. In the  $M = 3.38$  and  $M = 2.88$  scenarios, this results in a very small secondary upstream jet and vortex ring, visible at  $\tau \geq 10$  in Fig. 24(d-f), though the effect is suppressed in the  $M = 1.33$  case. This secondary upstream-directed wave may be partially responsible for secondary jets and vortices observed experimentally by Ranjan *et al.* (2005) [86], though the effect may be magnified by the presence of soap film material in shock tube experiments.

It is also worth noting that inward-directed rarefactions of substantial strength typically do not arise in the convergent-geometry cases unless the Mach number is sufficiently high; only the outward-directed spherical rarefaction wave appears, generated by the initial impact of the incident shock wave on the upstream bubble surface. More importantly, inward-directed rarefaction waves do not arise at all in the divergent-geometry cases, at any Mach number. Thus, the bulk density of the bubble fluid may decrease after initial shock passage in convergent geometry, but not in most divergent-geometry scenarios. (This is shown quantitatively in Sec. 4.1.1.)

### 3.2.2 Vorticity production and bubble deformation

This complex field of shock and rarefaction waves produces a similarly complex vorticity field and interface-deformation pattern in the bubble region. One of the most dramatic ways in which the bubble deforms is by the formation of prominent axial jets. An axial jet of some form arises in all of the heavy-bubble cases, except the nitrogen-argon,  $M = 1.33$  case. In the other nitrogen-argon scenarios, a very weak upstream jet forms at very late times on the upstream bubble pole due to reflections. The air-krypton and air-R12 scenarios show both upstream and downstream jetting, due to shock focusing and strong reflections, with a particularly strong downstream jet forming in the air-R12,  $M = 1.14$  case due to shock focusing. Upstream jetting in the air-krypton,  $M = 1.5$  scenario is also seen in the experiments and simulations of [62]. In the high- $M$  air-krypton and air-R12 scenarios here, downstream jets are suppressed by the rapid formation of a large primary vortex ring, and upstream jetting is more prevalent, visible particularly in Fig. 25(*d-f*).

In almost every case in the parameter study, a distinguishable vortex ring core forms in the flow by  $\tau = 15$ , or much sooner in some cases. This is the expected behavior, according to the standard description based on baroclinic vorticity deposition. In some cases, particularly nitrogen-argon,  $M = 2.88, 3.38$ , this vortex core is the only visible feature in the vorticity field at late times. This is true, for the nitrogen-argon case in particular, because the different compressibilities of the ambient and bubble gases result in a decrease of the Atwood number during shock passage. As can be seen in Fig. 24(*c-f*), the post-shock density contrast between bubble and ambient gases at  $M = 3.38$  is very small, and this results in very little additional vorticity generation after the passage of the initial shock wave. In most of the other scenarios, however, where the density contrast is increased by shock passage, the vorticity field continues to increase

in complexity at intermediate and late times, due to a number of effects, including the growth of Kelvin-Helmholtz instabilities on the interface, and the action of the “vortex-accelerated vorticity deposition” mechanism described by [78]. Further, the circulation associated with vortices in the flow can also grow, due to the passage of secondary shock and rarefaction waves described in Sec. 1.2.3 and the associated baroclinic vorticity generation. (This is examined quantitatively in Sec. 4.2.)

In fact, in many cases, the vortical growth *after* initial shock passage is more dramatic and complex than the growth initiated directly by the primary incident shock wave. In this sense, the shock-bubble interaction at high  $A$  is analogous to Richtmyer-Meshkov growth after reshock [17, 58, 100], since secondary shock waves interacting with the deformed interface greatly complicate the evolution of the interface and the vorticity field.

In the high-Mach-number air-R12 cases, the vorticity field becomes so complex that the primary vortex core becomes almost indistinguishable at late times, due to the combined intensity of the effects described above (see Figs. 26*f* and 27*f*), and due to the azimuthal transport of vorticity. The vigorous secondary vorticity generation and transport eventually leads to the development of an amorphous distribution of intense and disorderly vortical perturbations, with characteristics that we speculate might be best described loosely as “chaotic” or “turbulent.” Associated with the intense field of vortical fluctuations and disorderly motion is a region of intense mixing. The shocked bubble is effectively reduced to a small core of compressed fluid, trailing behind a complex plume-like structure exhibiting well-developed mixing, as seen in Fig. 26(*e-f*). These results indicate a much more amorphous and chaotic flowfield at late times than is seen in the results from two-dimensional simulations shown in figure 14 in ZZ98, or in the

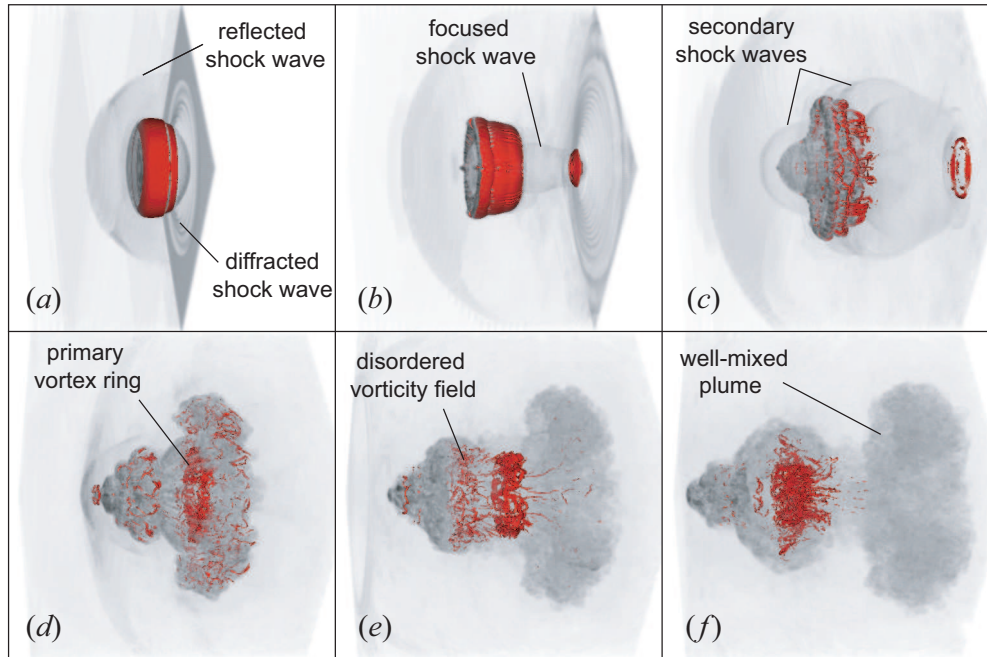


Figure 27: Three-dimensionally-rendered plot of the Laplacian of the density field ( $\Delta\rho$ ) in line-of-sight attenuated gray, with an isosurface of vorticity magnitude  $\|\omega\|=10^{-6} \text{ s}^{-1}$  plotted in opaque red for the  $M = 5.0$  air-R12 scenario ( $A=0.613$ ): (a)  $\tau = 1.5$ , (b)  $\tau = 3.9$ , (c)  $\tau = 5.7$ , (d)  $\tau = 9.9$ , (e)  $\tau = 13.7$ , (f)  $\tau = 18.3$ . Note that  $\tau = tW_i/R$  here. Incident shock wave propagation is left-to-right.

results for the  $M = 2.5$  two-dimensional test problem shown here in Fig. 20. The two-dimensional simulations show a late-time flowfield dominated by large, distinct vortex rings and vortex projectiles, while the three-dimensional simulations capture the complex and often disordered morphology of a turbulent flowfield resulting from the transport of mass, momentum and energy in all three spatial dimensions.

As a clearer illustration of these distinctive effects arising due to the strength of nonlinear-acoustic effects at high Atwood number, a time-sequenced three-dimensional rendering of the density and vorticity fields for the air-R12,  $M = 5$  scenario is included in Fig. 27. In these images, the development of a complex field of secondary shock waves

is evident, which strongly influences the late-time evolution of the flowfield. These secondary waves arise as a result of strong nonlinear-acoustic effects including shock refraction, diffraction, and focusing. The subsequent development of the flowfield is strongly coupled to the propagation of these secondary waves across the bubble by baroclinic vorticity production. The secondary shock waves seen propagating in the lateral and upstream directions in Fig. 27(*c-d*) transit the deforming bubble and visibly enhance the complexity of the evolving vorticity field. At late times, then, the vorticity field, visible as red filaments and blobs in Fig. 27(*d-f*) takes on a disordered, seemingly chaotic character.

# Chapter 4

## Analysis of Integral Features

In order to evaluate the performance of the analytical models mentioned in Sec. 1.3.6 across this parameter space for shock-bubble interactions, and to deepen the understanding of the phenomena described in Sec. 3.2, a number of integral diagnostics are applied to the data generated in these 14 simulations. Each of these quantities is obtained by an integral or norm over the computed solution, and provides a characterization of a different aspect of the flow evolution in shock-bubble interactions. The measured values and temporal trends are compared to analytical models and scaling laws. First, several quantities are measured and analyzed in terms of the predictions of one-dimensional gasdynamics, which provides a means of Mach-number scaling for this flow, in many cases. Second, the circulation associated with the shocked bubble are measured and compared with the analytical models discussed in Sec. 1.3.6.

### 4.1 Mach Scaling for Integral Flow Features

In shock-accelerated inhomogeneous flows, which evolve in natural and engineered systems on a vast range of spatial and temporal scales, we are particularly interested in identifying descriptions in which two such systems behave identically. We expect that such descriptions are possible, because of the similarity properties of the Euler equations. These properties and the conditions under which they exist have been discussed

in detail by Ryutov *et al.* (1999) [96]. In particular, they note that the Euler equations for a polytropic gas are invariant under certain linear transformations of the spatial coordinate, the density, or the pressure, and that the relationships between the coefficients in these transformations yield the following identity for systems *A* and *B*,

$$\tilde{v}_A \sqrt{\frac{\tilde{\rho}_A}{\tilde{p}_A}} = \tilde{v}_B \sqrt{\frac{\tilde{\rho}_B}{\tilde{p}_B}}, \quad (4.1)$$

where  $\tilde{v}_{A,B}$ ,  $\tilde{\rho}_{A,B}$ , and  $\tilde{p}_{A,B}$  are characteristic velocities, densities, and pressures for systems *A* and *B*. Since the quantity  $\tilde{v} (\tilde{\rho}/\tilde{p})^{\frac{1}{2}}$  is similar to a Mach number, it is anticipated that scaling with a characteristic Mach number in shock-accelerated flows is possible. Ryutov *et al.* note that in flows that are driven by strong shock waves, then, only the initial density distribution and time dependence of the shock driving makes each system unique.

In shock-accelerated inhomogeneous flows, however, such self-similar scaling is not necessarily possible, because the ratio of specific heats  $\gamma$  is not uniform in space. In the case of shock-bubble interactions, further, the initial density distribution is geometrically identical, but dramatically different between systems in terms of the magnitude of the density gradient. These differences lead ultimately to differences also in the time dependence of the shock driving for the system. As the Atwood number changes, the shock refraction patterns also change dramatically, so that the acceleration experienced by the bubble is also quite different. At high Atwood number, the bubble is accelerated not only by the initial shock wave, but by a series of complex secondary waves.

Therefore, rather than seeking a simple scaling in  $M$  for shock-bubble interactions, we resort to the one-dimensional gasdynamics analysis outlined in Sec. 1.3.6 and Appendix A, which incorporates the initial contrast in  $\gamma$  and  $\rho$  in the analysis of shock passage

over a discrete inhomogeneity. Thus, Mach-scaling is possible, but the dependence on  $M$  is indirect, and is obtained by evaluation of the laws of one-dimensional gasdynamics. This one-dimensional-gasdynamics-based analysis is used (1) to provide characteristic velocities for the construction of timescales and (2) to predict the late-time state of the bubble fluid in the absence of two-dimensional effects associated with interface curvature. The quantities measured here from the computed datasets and subjected to this analysis include the mean density, internal energy, and velocity of the bubble fluid, as well as the streamwise and lateral dimensions of the bubble region.

#### 4.1.1 Mean bubble-fluid density

The response of the bubble to the compressive effects of interaction with the initial shock wave and the subsequent scattered shock and rarefaction waves is characterized by tracking the mean density of the bubble fluid. Giordano and Burtschell (2006) [34] have demonstrated how one-dimensional gasdynamics can be used to predict the final mean density of the bubble fluid at late times after shock passage with good accuracy. In their description, the passage of a shock wave across the bubble is modeled using the known evolution of gas properties during the passage of a shock wave across a discrete slab inhomogeneity in a gas medium. (This is the same procedure described in Sec. 1.3.6 and Appendix A.) At each encounter between a wave and an interface, properties of the resulting transmitted and reflected waves are computed from the initial conditions by iteratively solving a system of equations derived from one-dimensional gasdynamics. By tracking the density changes in the slab through the passage of a sufficient number of these transmitted and reflected waves, one arrives at a “final” bulk density for the slab. Such a methodology can be appropriate only until a rarefaction wave has passed

through the slab, at which point the dimension of the slab and the thickness of the rarefaction wave dictate subsequent behavior. In the convergent geometry, a reflected rarefaction wave is produced when the shock interacts with the downstream interface, and, consequently, only the first two shock reflection/transmission events may be tracked. However, in divergent geometry, only shock waves are reflected back into the slab, and any desired number of events may be tracked.

In this one-dimensional model, a final density  $\rho_2''$  is computed after the transit of two waves: (1) the initial transmitted shock wave and (2) the internally-reflected shock wave or rarefaction wave. Giordano and Burtschell have compared experimental and computational results to this model by regarding  $\rho_2''$  as the final average density of bubble fluid and invoking conservation of mass, so that  $\mathcal{V}_f/\mathcal{V}_0 = \rho_2/\rho_2''$ , where  $\rho_2$  is the (unshocked) density at which the bubble fluid is initialized,  $\mathcal{V}_f$  is the final or asymptotic bubble volume, and  $\mathcal{V}_0$  is the initial, unshocked bubble volume. The resulting ratios of final to initial volume  $\mathcal{V}_f/\mathcal{V}_0$  were then compared to volume ratios obtained from both two-dimensional axisymmetric simulations and shock tube experiments, for one air-helium case and one air-krypton case. The volume they measured from simulations is a “species volume,” or a weighted sum of partial volumes in each cell, written in integral form as

$$\mathcal{V}^*(t) = \int_D f(x, y, z, t) d\mathcal{V}, \quad (4.2)$$

where  $\mathcal{V}^*(t)$  is the total weighted volume of the bubble fluid,  $f(x, y, z, t)$  is the local volume fraction of bubble fluid, and  $D$  is the entire computational domain. By measuring the weighted volume rather than the total volume of the  $f > 0$  region, the effects of shock compression are not conflated with the effects of mixing. The computational

results shown by Giordano and Burtschell (2006) [34] indicate that the total weighted volume is abruptly driven downward during initial shock passage, then, for convergent geometry, oscillates briefly as secondary reflected and diffracted shock waves pass over the bubble and, finally, approaches an asymptotic value very near to that predicted by the one-dimensional model.

Here, we examine the same effect in terms of the mean bubble fluid density  $\langle \rho \rangle$  rather than the volume. In this way, the result may be compared directly to the density predicted from one-dimensional gasdynamics. The time-dependent mean bubble fluid density is obtained from simulations as

$$\langle \rho(t) \rangle = \frac{\pi R^3 \rho_2}{3 \int_D f(x, y, z, t) dV}, \quad (4.3)$$

where  $R$  is the initial bubble radius and  $\rho_2$  is the initial (unshocked) density of the bubble fluid. The mass of the quarter-spherical bubble is  $\pi R^3 \rho_2 / 3$ , and Eq. 4.3 is obtained by invoking conservation of mass. In order to compare our computational results to the one-dimensional model, measured trends  $\langle \rho(t) \rangle$  from simulations are normalized to the one-dimensional model as

$$\rho^*(t) = \frac{\langle \rho(t) \rangle - \rho_2}{\rho''_2 - \rho_2}. \quad (4.4)$$

Under this normalization,  $\langle \rho(0) \rangle = 0$  by construction, and  $\langle \rho(t) \rangle = 1$  represents the one-dimensional-gasdynamics limit. Thus, for a successful model prediction,  $\langle \rho(t) \rangle \rightarrow 1$  as  $t \rightarrow \infty$ .

The time-dependent mean bubble-fluid density is plotted with this one-dimensional-gasdynamics normalization on the dimensionless timescale  $tW^*/R$  for all 14 scenarios in Fig. 28. In these plots, the compression history of the shocked bubble collapses nearly

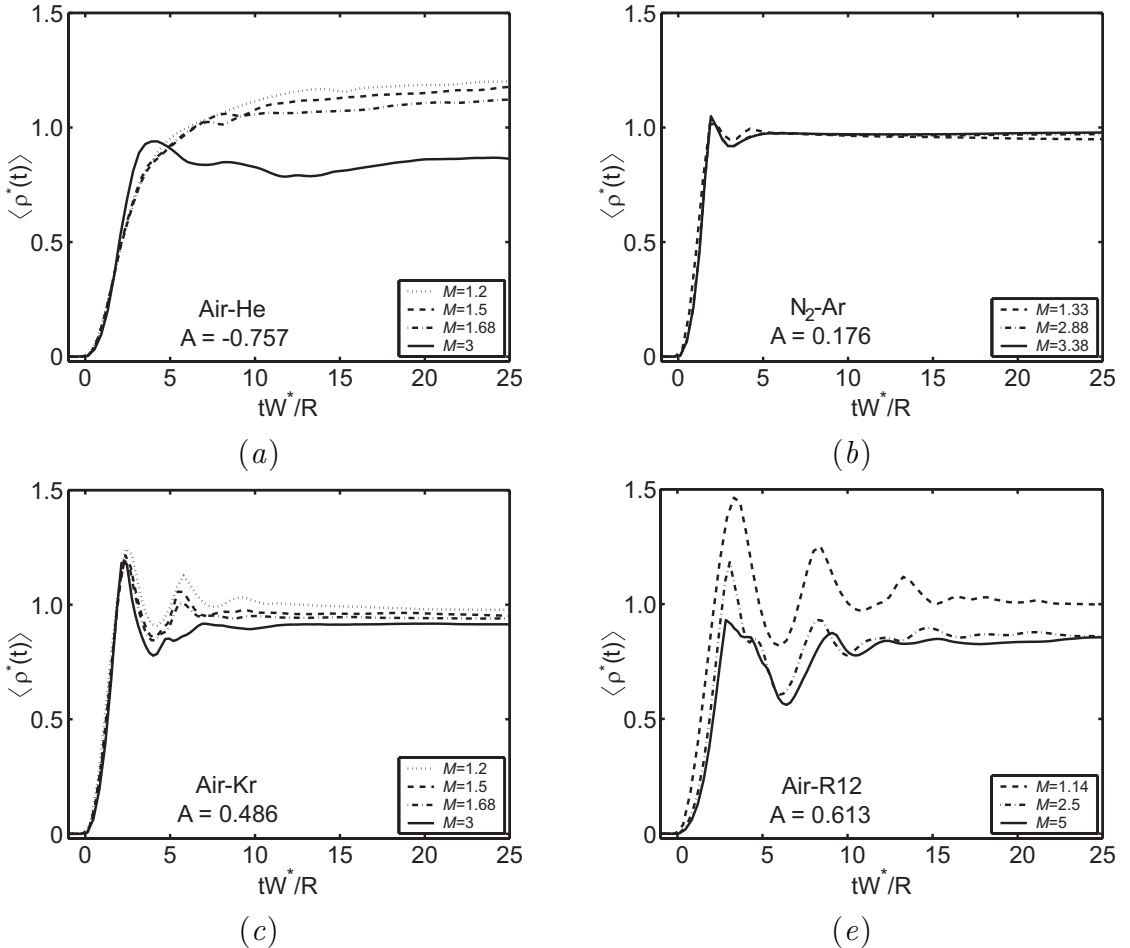


Figure 28: Plots over dimensionless time of the mean bubble fluid density obtained from three-dimensional simulations, normalized to the density obtained from the one-dimensional gasdynamics model, using Eq. 4.4: (a) Air-He, (b) N<sub>2</sub>-Ar, (c) Air-Kr and (d) Air-R12.

to a single trend within each gas pairing, except for the unusual behavior in the air-He,  $M = 3$  scenario. For the convergent-geometry scenarios (Fig. 28*b-d*), the compression ratio of the bubble fluid oscillates about the one-dimensional-gasdynamics limit for a short time after initial shock passage, as secondary shock waves and rarefaction waves reverberate through the bubble region. The compression ratio initially increases due to the transit of the primary shock wave, then decreases as a reflected expansion wave moves across the bubble, then increases due to shock focusing. Oscillations continue as shock waves introduce compression phases, and rarefaction waves introduce decompression phases. (Such oscillations in the mean density were also observed in the numerical results of Cowperthwaite (1989) [20].)

The strength and duration of these oscillations in the heavy-bubble scenarios increase more strongly with  $A$  than with  $M$ . This is because the strength of secondary shock waves and the complexity of the refraction pattern drastically increase as the refractive power of the bubble increases. As the intensity of secondary shock waves grows, the length of time  $t_s$  during which  $\langle \rho \rangle$  continues to oscillate about unity also increases. For the nitrogen-argon cases, this time is only roughly  $t_s = 5R/W^*$ , while in the air-krypton and air-R12 cases, it increases to  $11R/W^*$  and  $15R/W^*$ , respectively.

No such oscillations are apparent in the divergent-geometry cases, for  $M < 3$  (Fig. 28*a*). In these cases, the mean bubble-fluid density increases nearly monotonically. This is a manifestation of the absence of rarefaction waves from the bubble gas during the transit of primary and secondary waves. In the divergent-geometry cases, all internally reflected waves are shock waves, and no decompression phases are observed in the compression trends. This is not the case in the  $M = 3$  scenario, however. The mean density suddenly drops shortly after the initial shock transit. This indicates that at high Mach number,

intensified nonlinear-acoustic effects give rise to waves in the air-He scenarios that are not present for  $M < 2$ , which allow the bubble gas to expand. This also suggests that the upstream, trailing helium lobes or “rings” which persist to late time for  $M < 1.3$  (see Layes *et al.*, 2005 [61]) but are diminished dramatically for  $M \approx 3$  (see Ranjan *et al.*, 2007 [88]) play a significant role in the coupling of the bubble gas bulk compression to the transit of the primary shock wave and the field of secondary waves.

The collapse of these data to a nearly self-similar trend is particularly remarkable in the nitrogen-argon and air-krypton cases (Fig. 28*b,c*). For these scenarios, the one-dimensional gasdynamics prediction is accurate to within less than 7% for late times ( $tW^*/R > 10$ ), across a very broad range of Mach numbers. The bubble mean density thus appears to equilibrate to a value very near that predicted by the one-dimensional theory, suggesting that refractive effects are significant only during the initial transient phase for these cases. For the two gas pairs with highest magnitude of  $A$ , however, *i.e.*, air-helium and air-R12 (Fig. 28*a,d*), the model is less accurate, and its accuracy deteriorates with increased Mach number. (It is important to note here that in checks of the mass-conservation property of the numerical method, the bubble-fluid mass is found to change by no more than 0.25% in all of the simulations included in the present study.)

Although the timescale shown here is based on  $W^*$ , a number of other timescales were tested, but none showed the collapse seen in Fig. 28, where oscillations in  $\langle\rho\rangle$  for  $A > 0$  are in phase within each gas combination. However, it is clear that with this timescaling, oscillations in the normalized mean density have differing periods at different Atwood numbers, since secondary shock waves acting on the bubble fluid density have speeds that depend not only on  $M$  but also on  $A$ . This dependence is highly nonlinear, and a small change in  $A$  can introduce a significant change in the shock refraction, reflection

and diffraction pattern. The problem thus has a fundamentally different character at each value of  $A$ . For fixed  $A$ , however, Fig. 28 shows that the timescales for bubble fluid compression are set by shock wave speeds, and the Mach number can thus be scaled out, particularly for the initial transient phase.

### 4.1.2 Bubble fluid internal energy

The energetic response of the bubble to interaction with a shock wave is characterized by measuring the internal energy of the bubble fluid as a function of time from the computed datasets. The multifluid capturing algorithm incorporated in the *Raptor* code maintains the partial density  $(\rho f)_i$  and partial energy density  $(\rho f e)_i$ , for each fluid  $i$  in the simulation, as conserved variables, where  $f$  represents the volume fraction for fluid  $i$  and  $e$  represents the total energy per unit mass for fluid  $i$ . Hence, the energy associated with each fluid is easily obtained from computed datasets. The partial density  $(\rho f)_i$  is the density fluid  $i$  would have in a certain mesh cell if it filled the entire cell (if  $f_i = 1$ ). The partial energy density  $(\rho f e)_i$  is the energy density fluid  $i$  would have in a certain mesh cell if it filled the entire cell. For a two-fluid simulation, we have as identities that

$$\rho = (\rho f)_1 + (\rho f)_2 \quad (4.5)$$

and

$$\rho e = (\rho f e)_1 + (\rho f e)_2. \quad (4.6)$$

As an aside, we note that the mass fraction  $g_i$  for fluid  $i$  can then be computed as

$$g_i = \frac{(\rho f)_i}{\rho}. \quad (4.7)$$

Although the internal energy for the bubble fluid could be obtained from the partial pressure of the bubble fluid using the mass fraction, partial pressures for each fluid are not maintained explicitly in the scheme. Therefore, we obtain the internal energy by subtracting the kinetic energy from the total energy. The integrated internal energy  $E_I$  carried by the bubble fluid is therefore obtained as

$$E_I(t) = \int_D (\rho f e)_2 dV - \int_D \frac{1}{2} (\rho f)_2 \|\mathbf{U}\|^2 dV. \quad (4.8)$$

The internal energy carried by a gas slab subjected to acceleration by a shock wave of known strength can be computed using the one-dimensional gasdynamics approach outlined in Sec. 1.2.2 and described in detail in Appendix A. The internal energy of some mass  $m$  of a calorically perfect gas is obtained from the temperature as

$$E_I = mc_v T, \quad (4.9)$$

where  $c_v$  is the specific heat at constant volume. Therefore, to obtain the internal energy for a mass equivalent to a quarter-spherical bubble of radius  $R$ , with initial density  $\rho_2$ , after passage of the initial shock wave and the internally reflected wave, we let  $m = \rho_2 \pi R^3 / 3$  and write

$$E''_I = \frac{\rho_2 \pi R^3}{3} c_v T''_2. \quad (4.10)$$

For a calorically perfect gas with gas constant  $\mathfrak{R}_2$ , ratio of specific heats  $\gamma_2$ , and molecular mass  $\mathcal{M}_2$ , we may write

$$c_v = \frac{\mathfrak{R}_2}{\gamma_2 - 1} = \frac{\mathfrak{R}}{\mathcal{M}_2(\gamma_2 - 1)}, \quad (4.11)$$

where  $\mathfrak{R}$  is the universal gas constant. Then the internal energy is

$$E''_I = \frac{\rho_2 \pi R^3}{3} \frac{\mathfrak{R}}{\mathcal{M}_2(\gamma_2 - 1)} T''_2. \quad (4.12)$$

This quantity represents the internal energy we expect to be carried by the inhomogeneity after the passage of the initial shock wave and the internally reflected wave, by the one-dimensional gasdynamics approximation. (In SI units, this quantity would have units of Joules.)

Plots of the bubble-fluid internal energy  $E_I$ , normalized to the one-dimensional-gasdynamics prediction  $E''_I$  are shown in Fig. 29. Trends in the internal energy for the 14 scenarios show remarkable similarity to the trends in the normalized density. The internal energy undergoes a sharp increase during the passage of the initial shock wave, but equilibrates to a value very near to that predicted by the one-dimensional gasdynamics model at late times. For the convergent-geometry scenarios ( $A > 0$ ), the energy oscillates about the one-dimensional gasdynamics prediction briefly after shock passage. The intensity and duration of these oscillations grows dramatically with increasing Atwood number. In the divergent-geometry scenarios, however ( $A < 0$ ), the internal energy increases much more smoothly; the increase is nearly monotonic for  $M < 3$ . This is the same behavior as observed in the trends of the normalized mean bubble fluid density shown in Fig. 28.

The difference between the trends in the convergent and divergent scenarios can be attributed to the difference in shock refraction patterns. In divergent geometry, secondary shock and rarefaction waves are directed away from the axis and away from

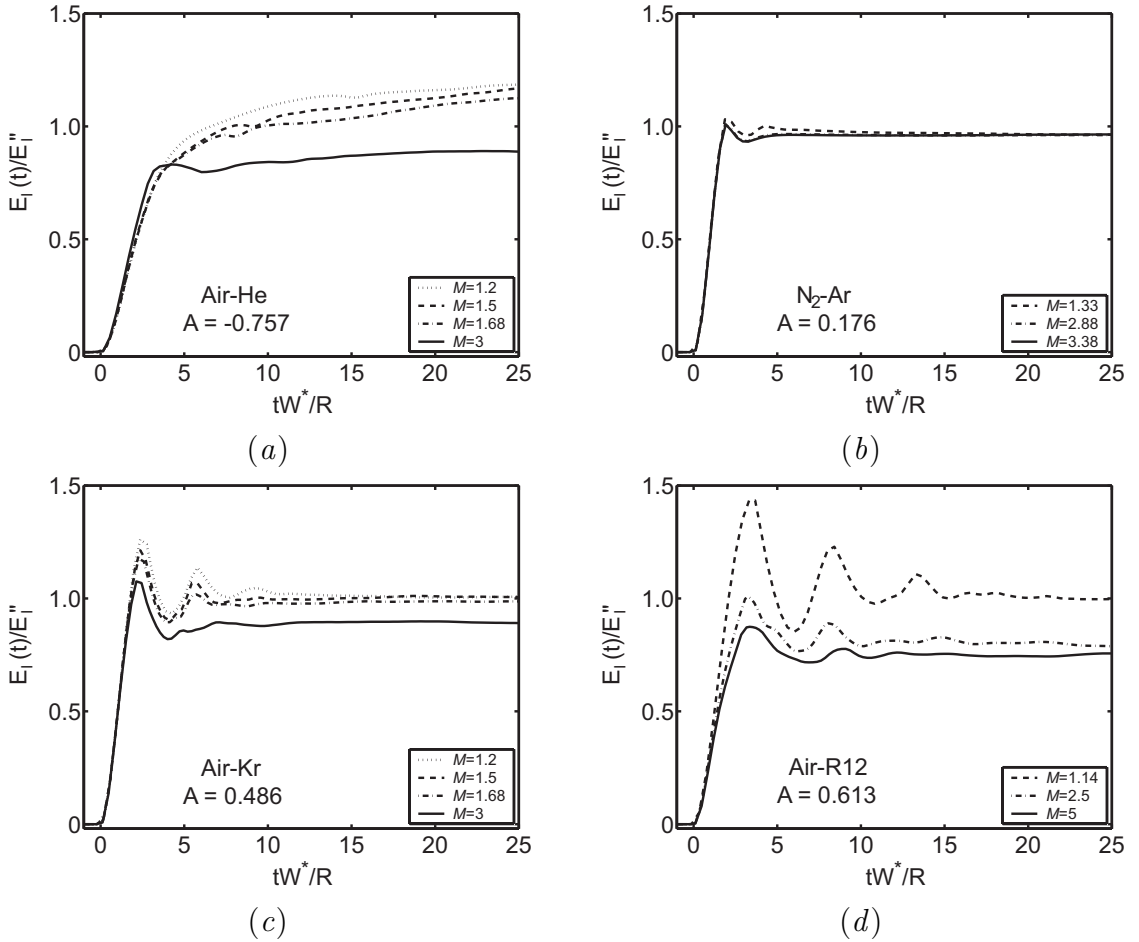


Figure 29: Plots over dimensionless time of the shocked-bubble internal energy  $E^I$  obtained from three-dimensional simulations using Eq. 4.8. Internal energy values are normalized to the one-dimensional-gasdynamics prediction,  $E_I''$ : (a) Air-He, (b) N<sub>2</sub>-Ar, (c) Air-Kr and (d) Air-R12.

the homogeneity, so that strong variations in the mean density or internal energy of the bubble fluid do not appear after the passage of the initial shock wave, except at high Mach number ( $M > 2$ ). In convergent geometry, however, secondary waves are directed toward the axis, and often interact with the bubble fluid simultaneously as they retransit the inhomogeneity. This results in strong secondary oscillations in the density and internal energy. Thus, the refractive nature of the shock wave's interaction with the bubble results in very different patterns of both compression and energy accumulation in the bubble fluid for convergent and divergent geometries.

Further, although a change in the sign of  $A$  causes dramatic changes in the evolution of the flowfield, even a small change in the magnitude of  $A$  strongly alters the development of the flowfield, as seen in Figs. 28 and 29. Thus, we may consider the shock-bubble interaction to be unique problem at each Atwood number [74]. Nevertheless, in both the density and internal energy trends shown in Figs. 28 and 29, we see that the analytical approach based on one-dimensional gasdynamics allows us to predict the state of the fluid in the inhomogeneity at late times, for any Atwood number, after the passage of the initial shock wave and secondary shock and rarefaction waves.

#### 4.1.3 Mean bubble fluid velocity

The one-dimensional gasdynamics approach is also useful in predicting other integral properties of the bubble gas after the transit of the primary shock wave and the series of secondary waves. The same analysis can be used to obtain, first, the streamwise velocity  $V'$  in the slab inhomogeneity after the passage of the initial transmitted shock and, second, the streamwise velocity  $V''$  in the inhomogeneity after the passage of the internally reflected wave. Comparison of these modeled velocities to the volume-averaged

bubble  $y$ -velocity  $\langle v(t) \rangle$  obtained from simulations shows that the bubble velocity at late time is bounded by  $V'$  and  $V''$ .

The mean bubble  $y$ -velocity is computed from simulations as

$$\langle v(t) \rangle = \frac{3}{\pi R^3 \rho_2} \int_D \rho_b f v dV, \quad (4.13)$$

where  $\rho_b$  is the local partial density of bubble fluid,  $f$  is the bubble fluid volume fraction,  $v$  is the local  $y$ -velocity and  $\pi R^3 \rho_2 / 3$  is the total mass of the quarter-spherical bubble. Mean bubble velocities obtained using Eq. 4.13 are normalized as  $\langle v(t) \rangle / V''$  and plotted on a dimensionless timescale for each scenario in Fig. 30. Also indicated on each plot at the right margin is the ratio  $V'/V''$ , which varies only slightly with  $M$  for fixed  $A$ . Note that for divergent-geometry,  $V'' < V'$ , because the internally-reflected wave is a shock wave; however, for convergent-geometry, the internal reflection is a rarefaction wave, so  $V'' > V'$ .

The dimensionless timescale chosen for the plots of the mean bubble velocity in Fig. 30 is  $tW_t/R$ . The timescale is thus based on the transmitted wave speed, rather than  $W_i$  or  $W^*$ ; this timescale yields the best collapse of the velocity data during the initial transient ( $tW_t/R < 2$ ). This confirms that timescales for bubble fluid acceleration during shock transit are set by the transmitted shock wave speed. At late times, the bubble fluid mean velocity equilibrates to a value bounded by  $V'$  and  $V''$ . In all convergent-geometry scenarios, we observe that  $V'/V'' < \langle v(t) \rangle < 1$  for  $t \rightarrow \infty$ . In the divergent-geometry cases,  $1 < \langle v(t) \rangle < V'/V''$  for  $t \rightarrow \infty$ . Thus, the one-dimensional gasdynamics analysis provides a useful tool for predicting the final bubble fluid velocity.

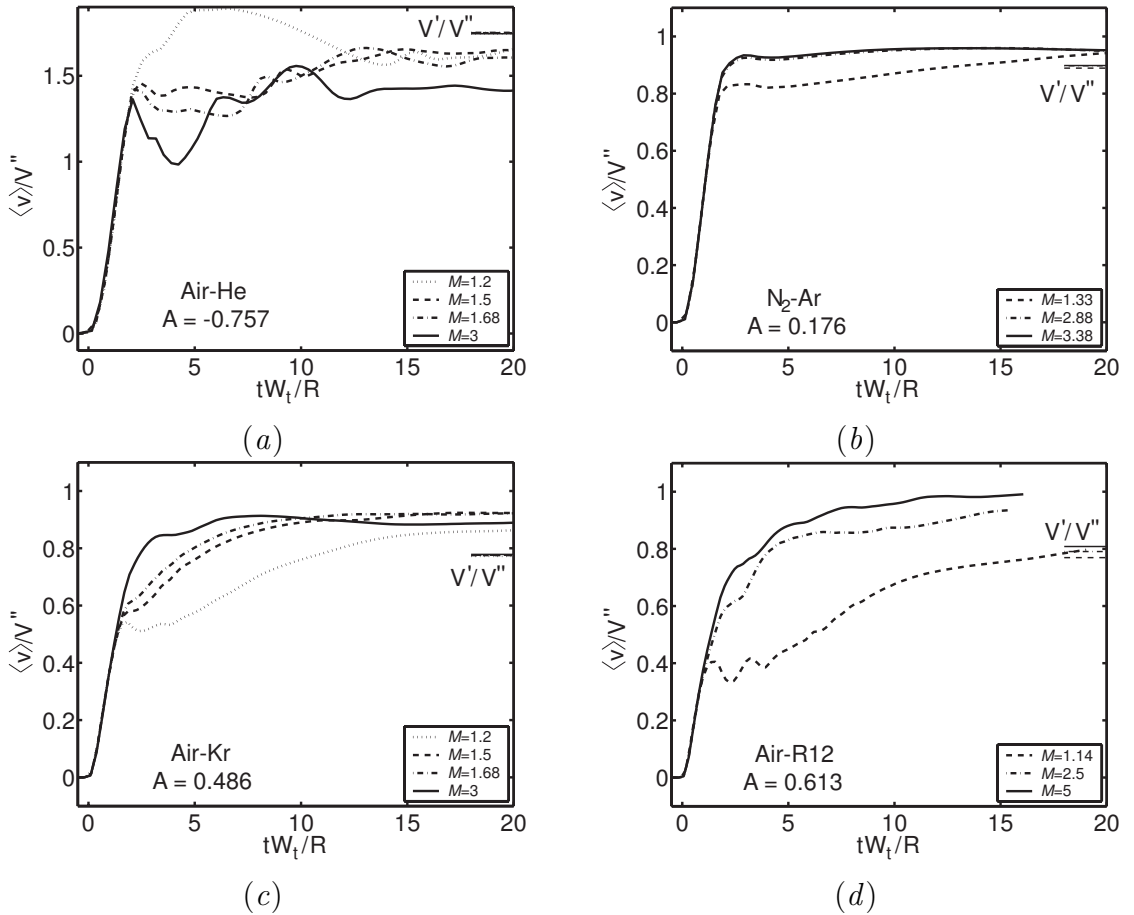


Figure 30: Plots over dimensionless time of the shocked-bubble mean velocity  $\langle v \rangle$  obtained from three-dimensional simulations. Velocities are normalized to the  $y$ -velocity  $V''$  obtained from the one-dimensional gasdynamics analysis: (a) Air-He, (b)  $N_2$ -Ar, (c) Air-Kr and (d) Air-R12. Line segments at the right margin indicate the ratio  $V'/V''$ .

#### 4.1.4 Bubble dimensions

Although no analytical model exists for them, the quantities most readily obtained from experimental data for shock-bubble interactions are the dimensions of the bubble region, *i.e.*, the maximum streamwise and transverse extents of the region with a bubble-gas concentration larger than some threshold value. This diagnostic yields information related to the deformation of the bubble by the transit of shock waves and the action of vortices formed in the flow. Hansen *et al.* (2007) [43] have also regarded the streamwise dimension of the shocked bubble as an indication of the extent of mixing of the bubble fluid into the ambient medium. Here, we measure the streamwise and transverse dimensions of the shocked bubble in order to determine whether trends in the dimensions may also be scaled in time for fixed  $A$  as we have seen that other quantities may scale.

For the present three-dimensional, quarter-symmetry simulations, therefore, a procedure is defined for performing measurements using a series of 48 sample planes at incremented azimuthal ( $\theta$ ) locations,

$$\theta_k = \frac{k-1}{47} \frac{\pi}{2}, \quad k = 1, \dots, 48. \quad (4.14)$$

For each of the 48 azimuthal locations, a planar section is extracted from the dataset, whose normal vector is tangent to  $\hat{\theta}_k = (\cos(\theta_k), 0, -\sin(\theta_k))$ . On each section, integral diagnostics are measured and stored for every timestep. This is carried out for each of the 48 sample sections, over the time-duration of each simulation, for each of the 14 scenarios studied here. Thus, for azimuthal locations  $k = 1, \dots, 48$ , we obtain  $\phi_k(t)$ , where  $\phi_k$  is an integral quantity computed over the  $k$ -th azimuthal slice in the dataset. Then an azimuthally-averaged value of  $\phi$  is obtained by taking the mean:

$$\bar{\phi}(t) = \frac{1}{48} \sum_{k=1}^{48} \phi_k(t). \quad (4.15)$$

In the current datasets, the bubble dimensions are obtained on each of the 48 sections described above, by isolating all cells where the volume fraction of bubble gas  $f$  is equal to or greater than 0.5, and recording the maximum radial coordinate  $R_k(t)$  and minimum and maximum axial coordinates  $y_{min,k}(t)$  and  $y_{max,k}(t)$  occupied by the isolated data. After azimuthal averaging, we compute the mean lateral dimension as  $2\Delta r = 2\bar{R}(t)$  and the mean streamwise dimension as  $\Delta y = \bar{y}_{max}(t) - \bar{y}_{min}(t)$  for all timesteps  $t = t_n$ ,  $n = 1, \dots, N$ . These dimensions are plotted for 12 of the 14 scenarios in Figs. 31 and 32, using the dimensionless timescale  $tW^*/R$ .

From the plots shown in Figs. 31 and 32, we see that very different trends in the spatial extents can result from only small changes in the incident Mach number. This is due to the sensitivity of this diagnostic to local features of the flow, such as secondary vortex rings, which can be advected to the extremity of the bubble region, and thus suddenly increase or decrease its apparent dimensions. Such effects can be observed in Fig. 32, where sudden downward jumps result from the intermingling of bubble and ambient fluid in the head of the helium region, seen in Fig. 23(d-e) at  $\tau = 15$ . However, the initial compression of the bubble due to shock wave impact is visible in the streamwise dimension plot (Fig. 32) for every case, as a strong decrease in the streamwise dimension, which passes through a minimum between  $tW^*/R = 2$  and  $tW^*/R = 5$ . Simultaneously, a brief decrease in the lateral dimension of the bubble region is discernible as well in Fig. 31(b-d). The strength and duration of this lateral compression increases with the initial density ratio  $\chi$ , and the lateral compression ends when vortex rings that have formed on the bubble equator begin to move bubble fluid radially outward.

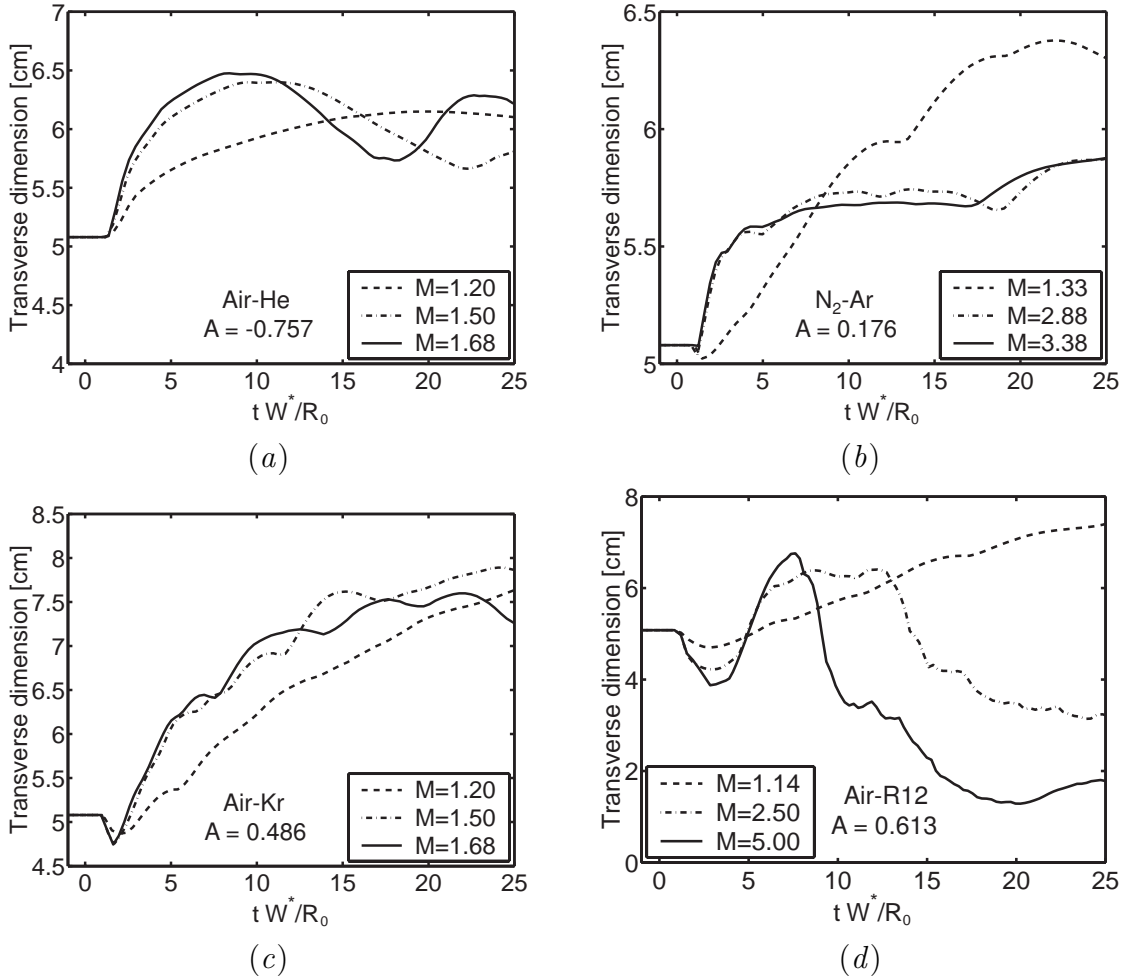


Figure 31: Plots of the  $\theta$ -averaged transverse (radial) dimension of the bubble region,  $2\Delta r(t)$ , measured using a threshold of  $f \geq 0.5$ , on the dimensionless timescale  $tW^*/R$ , where  $W^*$  is given by Eq. 3.5. Gas combinations: (a) air-He, (b) N<sub>2</sub>-Ar, (c) air-Kr, (d) air-R12.

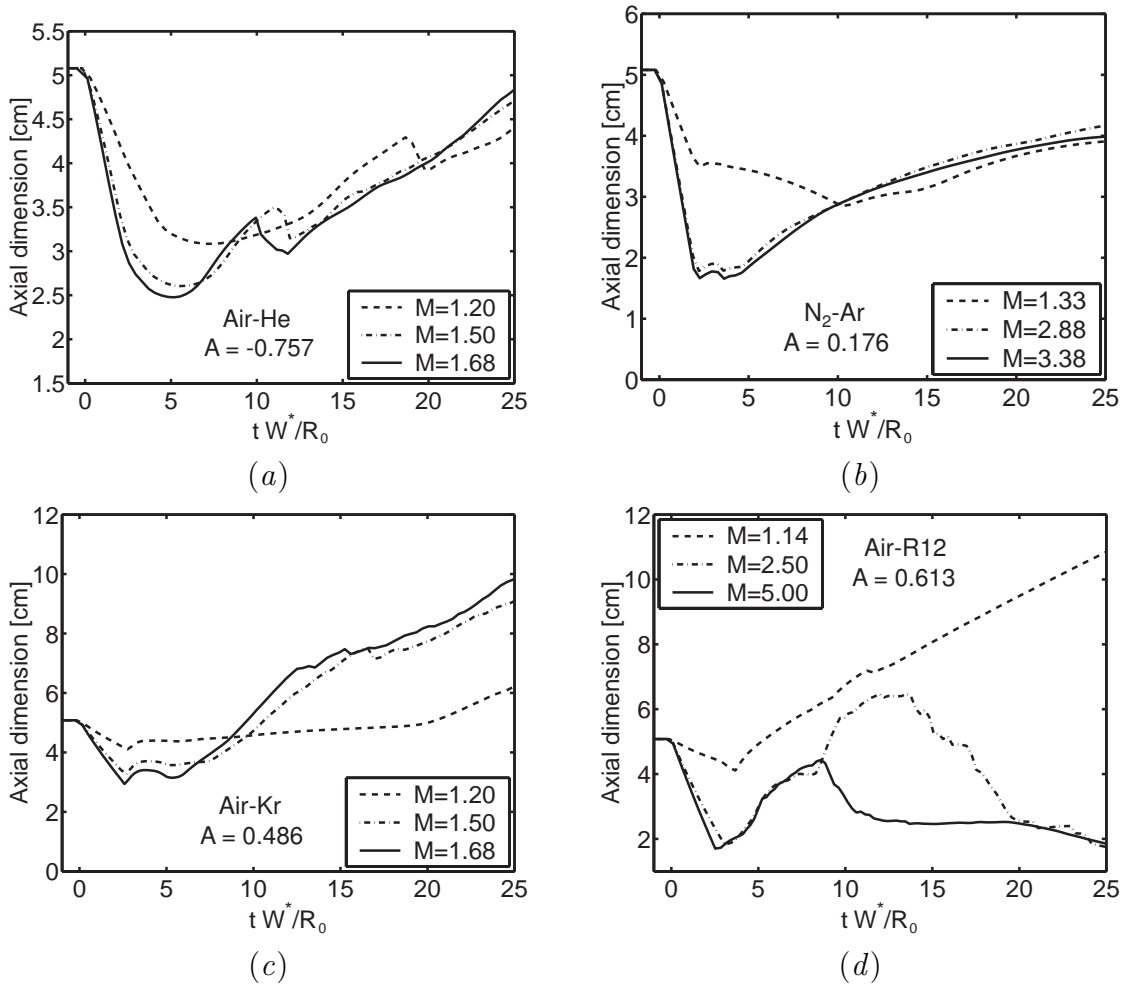


Figure 32: Plots of the  $\theta$ -averaged axial dimension of the bubble region,  $\Delta y(t)$  measured using a threshold of  $f \geq 0.5$ , on the dimensionless timescale  $tW^*/R$ , where  $W^*$  is given by Eq. 3.5. Gas combinations: (a) air-He, (b) N<sub>2</sub>-Ar, (c) air-Kr, (d) air-R12.

It can also be observed that the transverse bubble dimension curves do not, in general, collapse to a single trend, except at early times and higher Mach numbers. Trends in the streamwise bubble dimension show some tendency to collapse under this scaling, although in the lower Mach number cases, again, they appear to deviate. Also, the air-R12 scenarios for  $M = 2.5, 5.0$  indicate a dramatic drop at later times in both the radial and axial dimension of the bubble region to levels even below the initial values, which is not seen in any other scenarios. This is due to the regions of intense mixing that develop in these high- $M$ , high- $\chi$  cases. As this intense mixing proceeds, the volume fraction of bubble fluid,  $f$ , drops below 0.5 over a large portion of the shocked-bubble region, which consequently falls outside the  $f = 0.5$  contour, reducing the apparent dimensions of the bubble region to the dimensions of the tiny core of dense fluid left behind at late times (see Fig. 26e-f).

In order to provide a clearer measurement of axial elongation of the bubble, the streamwise dimension of the bubble-fluid region is measured again by finding the maximum and minimum  $y$ -coordinate inside the  $f \geq 10^{-6}$  region, rather than merely the  $f \geq 0.5$  region. In this measurement, for brevity, we forgo the sectioning and azimuthal averaging technique used for the data shown in Fig. 32, and record the axial distance  $\Delta y_m$  between the global extrema of the bubble-fluid region. These data are shown in Fig. 33. The trends in the absolute axial dimension of the bubble-fluid region, measured for  $f \geq 10^{-6}$ , show that although the bubble dimension generally follows a roughly self-similar trend (compression followed by re-expansion driven by vortical motion and mixing), the trends show very different features under varying Mach number, as seen also in Figs. 31-32. However, we do observe that with a threshold of  $f \geq 10^{-6}$  rather than  $f \geq 0.5$ , the continued late-time growth of the bubble region in the high- $M$  air-R12

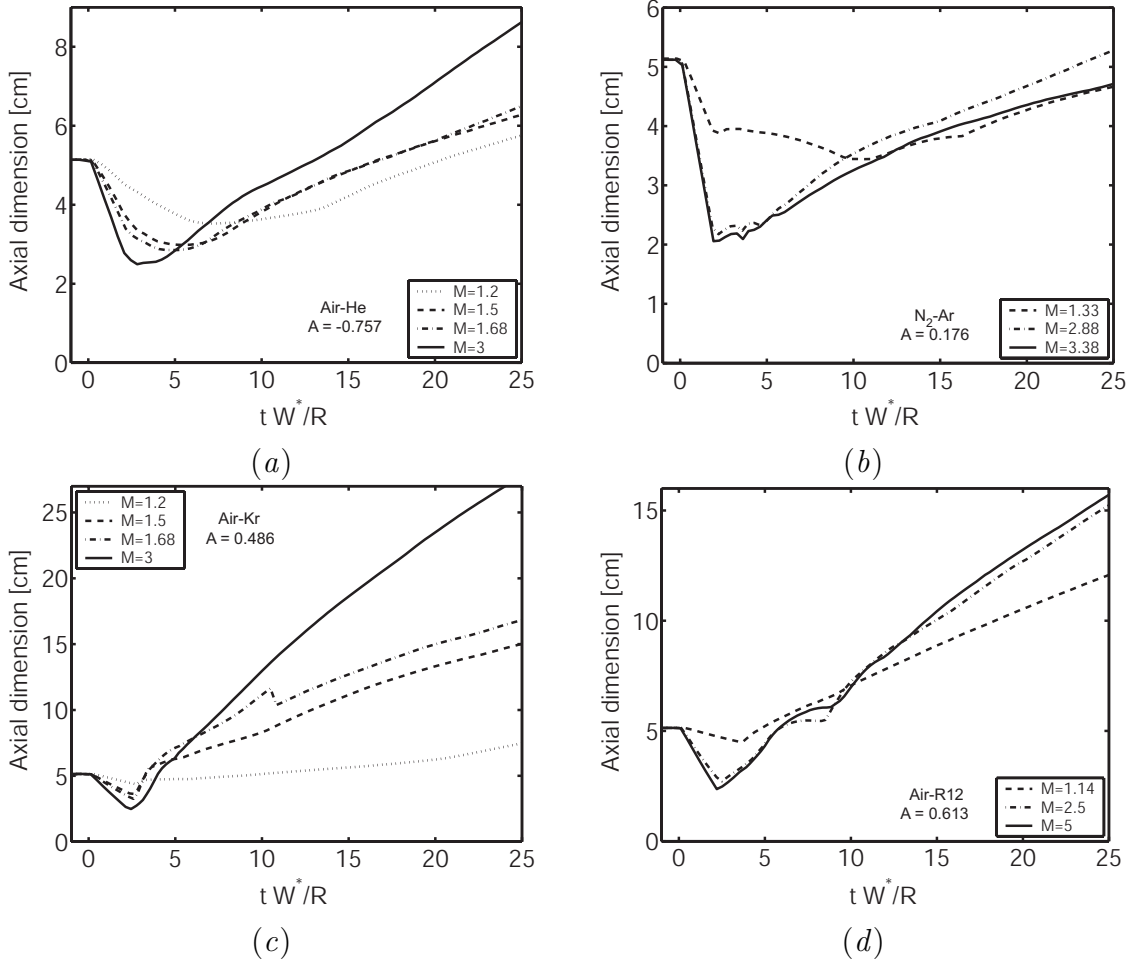


Figure 33: Plots of the absolute axial dimension of the bubble region, measured using a threshold of  $f \geq 10^{-6}$ , on the dimensionless timescale  $tW^*/R$ , where  $W^*$  is given by Eqn. 3.5. Gas combinations: (a) air-He, (b) N<sub>2</sub>-Ar, (c) air-Kr, (d) air-R12.

cases is captured much more effectively.

We also note that the minimum axial dimension reached by the bubble during shock passage varies consistently with the Mach number. In general, for the convergent-geometry scenarios, the minimum axial dimension reached by the shocked bubble, to less than 5% error, is  $D(1 - 0.13W_i/(W_i - u'_1))$ ; for the divergent-geometry scenarios, the minimum axial dimension is roughly  $D(1 - 0.20W_i/(W_i - u'_1))$ . This suggests that the factor  $(W_i - u'_1)/W_i$ , which also appears in Richtmyer's simple formula for the compression of a sinusoid perturbation subjected to shock acceleration [92], may provide a useful scaling factor for trends in the dimensions of shocked bubbles. Such an analysis is excluded here for brevity.

## 4.2 Measurements and Models for Circulation

### 4.2.1 Definition

Another method by which shock-bubble interactions have commonly been understood and modeled is by means of the circulation – that is, the circulation of the velocity field about a path  $P$  enclosing a diametral half-plane in the flowfield. One leg of  $P$  lies on the axis of symmetry (the  $y$ -axis, here), and the opposite leg lies on a parallel line outside the region of nonzero vorticity, as shown in Fig. 34. An axisymmetric coordinate system is defined whose origin lies at the farthest upstream extent of the reflected shock (point “A”).

For the path  $P$ , the circulation is defined as

$$\Gamma = \oint_P \mathbf{U} \cdot d\mathbf{s} \quad (4.16)$$

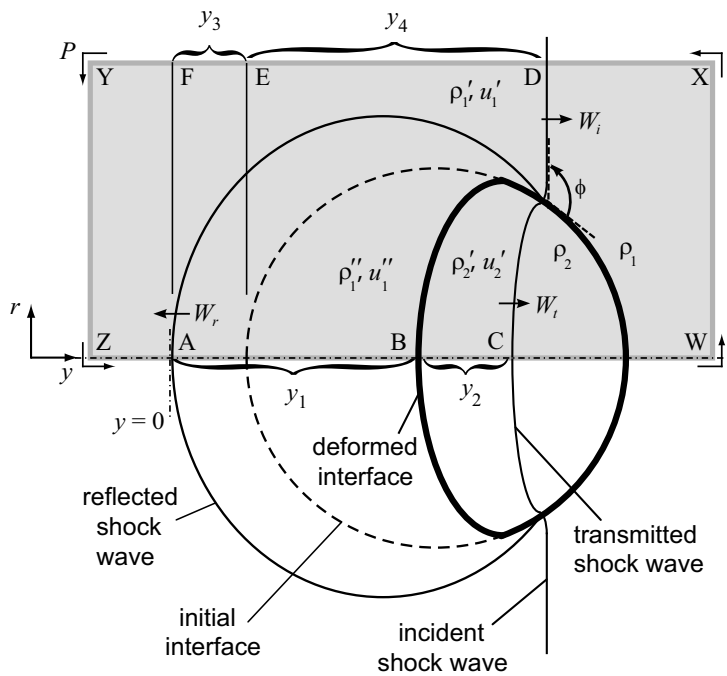


Figure 34: Schematic diagram of the convergent-geometry shock-bubble interaction for  $t < 2R/W_t$ , showing notation used in computing and modeling the circulation in the flow.

which, by Stokes' theorem, is equivalent to the area integral of vorticity:

$$\Gamma = \int_S \boldsymbol{\omega} \cdot d\mathbf{A}, \quad (4.17)$$

where  $S$  is the area bounded by  $P$ .

The circulation quantifies the net strength of the vortex rings generated by the shock-bubble interaction. For this reason, it has been the subject of a number of analytical models with various conceptual bases. Four models are considered here, and compared to the results of the present simulations, including the formulations of Picone and Boris (1988) [79] (henceforward, “PB”), Yang *et al.* (1994) [110] (henceforward, “YKZ”), Samtaney and Zabusky (1994) [99] (henceforward, “SZ”), and a new model proposed in Ref. [75].

Each of these models predicts the total circulation present in the flow at the instant of shock passage. This is the moment at which the fastest shock wave in the system reaches the downstream pole of the bubble and reflected waves are generated. For the air-helium scenarios, this instant corresponds to  $tW_t/R = 2.0$ . For the nitrogen-argon cases, it is given by  $tW_i/R = 2.0$ . However, in the air-krypton and air-R12 cases, the instant of first shock passage is delayed due to the curvature of the diffracted shock wave. That is, because of the large refractive power of the bubble (large  $A$ ), the portion of the shock front in contact with the bubble surface remains normal to the interface after it has moved downstream of the bubble equator. Defining  $\phi$  to be the angle between the plane of the unperturbed shock front and the tangent plane to the bubble surface at the point of contact with the shock, the shock wave must traverse a distance  $\pi R/2$  for  $\phi \geq \pi/2$ , rather than merely  $R$ , before reaching the downstream ( $\phi = \pi$ ) surface of the bubble. Thus, the progress of the shock wave across the distance  $2R$  is effectively slowed

by a factor of  $2/(1 + \pi/2)$  in these scenarios. Therefore, we construct an “effective” shock wave speed  $\tilde{W}$  for timescaling, to account for this effect:

$$\tilde{W} = \begin{cases} W_t, & A < 0 \\ W_i, & 0 \leq A \leq 0.2 \\ 2W_i/(1 + \pi/2), & A > 0.2 \end{cases}. \quad (4.18)$$

The circulation at the instant of first shock passage is then defined as

$$\hat{\Gamma} = \Gamma|_{t=2R/\tilde{W}}, \quad (4.19)$$

and corresponds to the circulation at the “end of phase (iii),” in the terminology of Samtaney and Zabusky (1994) [99]. Only a timescale based on  $\tilde{W}$  will place the circulation at shock passage  $\hat{\Gamma}$  at the same dimensionless time for every scenario.

#### 4.2.2 Circulation models based on baroclinic torque

To obtain the total circulation at shock passage, in the PB and YKZ models, the baroclinic source term in the vorticity equation (Eq. 1.7) is integrated over the half-plane and over the time during which the shock wave initially passes over the bubble, with some simplifying assumptions. The two models assume that both the shape of the bubble and the density ratio relative to its surroundings do not change significantly during initial shock passage, and that the shock front proceeds in linear fashion across the bubble with no changes in its shape or speed. Vorticity production is then decoupled from shock refraction and diffraction, so that the density gradient and pressure gradient components of the baroclinic source term can be evaluated using parameters from the one-dimensional shocked gas slab analog, such as the incident shock wave speed  $W_i$ , the shocked ambient

flow speed  $u'_1$ , and the density of the shocked ambient gas  $\rho'_1$ . Of the scenarios included in the current study, only in the nitrogen-argon,  $M = 1.33$  case are these criteria nearly met. However, the formulae can be regarded as first-order estimates of the circulation resulting from only the passage of the initial shock, neglecting the higher-order effects associated with shock refraction, focusing, diffraction, and reflections. The PB model (see Picone *et al.*, 1985 [80] and Picone and Boris, 1988 [79]), in our notation, is given by

$$\Gamma_{\text{PB}} = 2u'_1 \left(1 - \frac{u'_1}{2W_i}\right) R \ln \left(\frac{\rho_1}{\rho_2}\right), \quad (4.20)$$

and the YKZ model (see Yang, *et al.*, 1994 [110] by

$$\Gamma_{\text{YKZ}} = \frac{4R}{W_i} \frac{p'_1 - p_1}{\rho'_1} \left(\frac{\rho_2 - \rho_1}{\rho_2 + \rho_1}\right) = \frac{4R}{W_i} \frac{p'_1 - p_1}{\rho'_1} A. \quad (4.21)$$

### 4.2.3 Circulation model motivated by asymptotics

An entirely different approach is taken in the SZ model [99, 113], which captures shock refraction effects by including scaling arguments derived from shock polar analysis (see Henderson, 1966 [45] and Henderson, 1989 [46]) and from numerical simulations of shock wave interactions with planar interfaces across a broad parameter space. An “asymptotically-motivated” analysis in Samtaney and Zabusky (1994) [99] yields a general first-order-accurate scaling law for the rate of circulation deposition per unit unshocked interface length, for an interface of arbitrary shape. For the fast/slow configuration ( $c_1 > c_2$ ), and unit ambient unshocked density and pressure (and thus sound speed  $\gamma^{\frac{1}{2}}$ ), their formulation is given as

$$\frac{d\Gamma_1}{ds} = \frac{2\gamma^{\frac{1}{2}}}{\gamma + 1} \left(1 - \chi^{-\frac{1}{2}}\right) \sin \phi (1 + M^{-1} + 2M^{-2}) (M - 1), \quad (4.22)$$

where  $s$  is a path length along the interface,  $\chi = \rho_2/\rho_1$ ,  $\phi$  is the local inclination of the unshocked interface relative to the unperturbed incident shock front (labeled in Fig. 34) and  $\gamma$  is a characteristic ratio of specific heats for the flow, *e.g.*,  $\gamma = (\gamma_2 + \gamma_1)/2$ .

This formula is an approximation to the exact expression for the circulation associated with regular refraction of a shock wave at a planar interface, given by Samtaney and Zabusky (1994) [99] (SZ) as equation 2.11. The scaling law in Eq. 4.22 possesses a number of desirable properties. First, the  $\sin \phi$  factor ensures that  $d\Gamma/ds$  has the same sign and periodicity as  $\nabla \rho \times \nabla p$ . Also, the circulation deposition scales linearly with  $M$  for large  $M$ , asymptotes to zero for  $M \rightarrow 1$  and is independent of  $\chi$  for large  $\chi$ . This formula has been used, with success, to predict the circulation on sinusoidal, circular and elliptical interfaces accelerated by shock waves of various strengths [99, 113, 112, 89].

The use of this scaling law here, however, is presented with two qualifiers. First, in this form, it is only applicable for fast/slow refraction scenarios ( $c_1 > c_2$ ), and thus can only be applied to convergent-geometry shock-bubble interactions in the present study. An extension of the theory to the slow/fast configuration, for shocked planar inclined gas interfaces, has been derived and validated using Eulerian simulations by Samtaney *et al.* (1998) [98]. (Values computed using this extension, adapted for circular interfaces, are shown here in Table 4.) Second, for planar inclined gas interfaces, SZ have computed the circulation using both the exact expression and the scaling law shown here (Eq. 4.22), for a series of inclination angles  $\phi$ , Mach numbers  $M$ , and density ratios  $\chi$  (plotted in figure 15 of SZ). SZ regard the scaling law as valid only in the parameter space subregion where the difference between the two is less than 10%, and shock refraction

does not become irregular. Since most of the scenarios considered here fall in the region of irregular refraction even at  $\phi = \pi/3$ , we proceed with the scaling law formulation (Eq. 4.22) only as a means of estimating the circulation.

To obtain the circulation in the shocked bubble, SZ integrate Eq. 4.22 along a half-circumference of the bubble (from  $\phi = 0$  to  $\phi = \pi$ ). (The result is identical for both spherical and cylindrical bubbles.) The formula is modified for  $\phi > \pi/2$  to account for diffraction of the shock wave propagating around the bubble interface, by invoking a “near-normality” hypothesis. This takes into account the empirical observation that the diffracted shock wave maintains its front at 90-degree angles to the unshocked bubble surface, in the case of  $A > 0.2$  where shock wave curvature is significant. Thus, the substitution  $\sin\phi = 1$  is made in the second half of the integral, for  $\pi/2 < \phi \leq \pi$ . In the case of  $0 < A < 0.2$ , we observe that the near-normality hypothesis does not hold, and this substitution is therefore not made. This yields the following formula for the circulation:

$$\Gamma_{\text{SZ}} = \begin{cases} \left(\frac{4}{1+\gamma}\right) \left(1 - \chi^{-\frac{1}{2}}\right) (1 + M^{-1} + 2M^{-2}) (M - 1) R c_1, & 0 < A < 0.2 \\ \left(1 + \frac{\pi}{2}\right) \left(\frac{2}{1+\gamma}\right) \left(1 - \chi^{-\frac{1}{2}}\right) (1 + M^{-1} + 2M^{-2}) (M - 1) R c_1, & A \geq 0.2 \end{cases}, \quad (4.23)$$

where the dimensionless scaling law (equation 5.15 of SZ) has been multiplied by the ratio  $c_1/\gamma^{\frac{1}{2}}$ , in order to obtain the circulation in physical units. ZZ98 have used this formula (for  $A > 0.2$ ) to predict the circulation present in the shocked bubble flow, simulated using a two-dimensional Godunov code, just after passage of the initial shock wave, for the air-R12 scenario at  $M = 1.14, 1.5, 2.5, 5.0$ . Levy *et al.* (2003) [63] also

employed the SZ scaling law in their derivation of a model for the velocity of a shocked-bubble vortex ring. It should be noted, however, that the formula appearing in both of these studies (given as equation 26 in ZZ98) contains an incorrect additional factor of  $\gamma^{\frac{1}{2}}$ , and the intended form is that shown here in (4.23).

The scaling law in Eq. 4.22, which is the basis of this formula, is derived by SZ as a first-order approximation to the circulation per unit length. A third-order-accurate correction to this scaling law is proposed in Appendix A.2 of SZ. After integrating around the bubble and incorporating this third-order extension in the scaling law (following equation 5.11 of SZ), a third-order-accurate version of the SZ model (henceforward, “SZ3”) is then written as

$$\Gamma_{\text{SZ3}} = \Gamma_{\text{SZ}} + \frac{1}{\gamma^{\frac{1}{2}}} \left( \frac{2}{3} + \frac{\pi}{2} \right) \Gamma'_3 R c_1, \quad (4.24)$$

where the form of  $\Gamma'_3$  is given in Appendix A.2 of SZ. The inclusion of the third-order-accurate extension introduces a change of more than 10% only in the nitrogen-argon,  $M = 2.88, 3.38$  and air-krypton,  $M = 1.2$  cases, but the results presented in Sec. 4.2.5 generally show better accuracy with respect to computed values when this third-order correction is included. The values computed using the first-order- and third-order-accurate formulations are shown here in Table 4.

#### 4.2.4 Circulation model based on one-dimensional gasdynamics

A third approach to modeling the circulation has been proposed by Oakley [75], in which the velocity field at shock passage is reconstructed using one-dimensional gasdynamics

parameters and fits to computational data across the parameter space, and the circulation is computed using line integrals over this reconstructed field. Consider the velocity field  $\mathbf{U}$  at the instant of shock passage. The circulation associated with this field can be obtained by integrating the velocity along a path  $P$  identical to that shown enclosing the gray area in Fig. 34, except that at shock passage, the points C and D on the path are advanced downstream to locations near the line  $y = 2R$ . Using this path of integration, the circulation can be computed exactly as

$$\Gamma = \int_A^B \mathbf{U} \cdot \hat{\mathbf{y}} dy + \int_B^C \mathbf{U} \cdot \hat{\mathbf{y}} dy + \int_D^E \mathbf{U} \cdot \hat{\mathbf{y}} dy + \int_E^F \mathbf{U} \cdot \hat{\mathbf{y}} dy, \quad (4.25)$$

where it is noted that there is no contribution to the integral along the path  $P$  from the line segments  $\overline{CW}$ ,  $\overline{WX}$ ,  $\overline{XD}$  and  $\overline{YZ}$ ; and that the contributions from the line segments  $\overline{FY}$  and  $\overline{ZA}$  cancel. Let the path of integration be arranged such that the line segment  $\overline{DF}$  lies in a region where  $\mathbf{U} = u'_1 \hat{\mathbf{y}}$ , and the line segment  $\overline{AC}$  lies on the axis of symmetry, where  $\mathbf{U} \cdot \hat{\mathbf{r}} = 0$ . Then the expression in Eq. 4.25 becomes

$$\Gamma = \int_A^B v_{AB}(y) dy + \int_B^C v_{BC}(y) dy - u'_1 (y_3 + y_4) \quad (4.26)$$

where the axial velocities  $v_{AB}(y)$  and  $v_{BC}(y)$  and the distances  $y_3$  and  $y_4$  must be modeled. By solving the one-dimensional gasdynamics equations iteratively for the transmission of a normal shock wave into a slab of gas whose properties are known, we may obtain the reflected shock wave strength  $M_r$  and speed  $W_r$ , the speed of the transmitted shock wave  $W_t$  and the particle speed behind the transmitted shock wave  $u'_2$ . Two-dimensional simulations within the present parameter space suggest, further, that the on-axis gas velocity in the region between the interface ( $y = y_1$ ) and the spherical reflected shock wave ( $y = 0$ ) may be modeled as

$$v_{AB}(y) = -u'_1 + (u'_1 - u'_2) \left( \frac{y}{R} \right)^2, \quad (4.27)$$

where the coordinate system in Fig. 34 has been chosen such that the origin is fixed to the on-axis location of the reflected shock wave, and  $u'_2$  is the post-shock velocity in fluid 2. The  $y^2$  term ensures that the reconstructed velocity behind the reflected shock wave varies non-linearly in  $y$  as we would expect for a spherical expanding wave; this formulation has been obtained by fits to two-dimensional simulation results.

If we also substitute  $u'_2$  for  $v_{BC}$  in Eq. 4.26 (*i.e.*, neglect the on-axis effects of shock refraction and focusing), and evaluate the remaining line integrals, we obtain an estimate of the circulation based on the one-dimensional gasdynamics reconstruction,

$$\Gamma_R = u'_1 y_1 + \frac{1}{3} R (u'_1 - u'_2) \left( \frac{-y_1}{R} \right)^3 + u'_2 y_2 - u'_1 (W_i t^* + y_3), \quad (4.28)$$

where the lengths of the line segments  $y_1$ ,  $y_2$ ,  $y_3$ , and  $y_4$  are also obtained from one-dimensional gasdynamics as

$$\begin{aligned} y_1 &= \frac{1}{\sqrt{M_r}} (u'_2 + W_r) t^*, \\ y_2 &= (W_t - u'_2) t^*, \\ y_3 &= \frac{W_r t^*}{\sqrt{M_r}}, \\ y_4 &= W_i t^*, \\ t^* &= \frac{2R}{\tilde{W}}. \end{aligned} \quad (4.29)$$

All velocity quantities are obtained from one-dimensional gasdynamics, and the segment length reduction factor,  $1/\sqrt{M_r}$  appearing in Eq. 4.29 is a scaling factor which accounts for the curvature and time-dependent weakening of the reflected spherical shock wave. It is determined empirically from numerical simulations for the shock-bubble interaction,

by a method similar to that by which scaling factors in the model of Samtaney and Zabusky (1994) [99] were obtained. Although the four terms appearing in Eq. 4.28 all have the same order of magnitude and partially offset each other for the present scenarios, the fourth term – associated with the on-axis velocity induced by the incident shock wave – is the dominant term in nearly all of the simulations shown here. Further, we note that although  $\Gamma_R \rightarrow 0$  for  $M \rightarrow 1$ , the model has no asymptote for  $M \rightarrow \infty$ . In this sense, the model should only be regarded as a useful estimate for the circulation within the parameter space of the present study, since it has not been shown to have consistent asymptotic behavior in the same sense as the SZ model.

#### 4.2.5 Circulation obtained from simulations

To compare the results of the current simulations with these models, a procedure is defined for measuring the velocity circulation from three-dimensional data, based on the technique described in Sec. 4.1.4 involving a series of 48 planar sections. The circulation is measured as a function of the azimuthal coordinate  $\theta$ , by evaluating the integral in Eq. 4.17 over each section to obtain the net circulation  $\Gamma_0(\theta_k, t)$ , where  $\omega = \boldsymbol{\omega} \cdot \hat{\theta}_k$  is substituted for  $\boldsymbol{\omega}$  in the integrand. The positive component of the circulation  $\Gamma_+(\theta_k, t)$  and negative component of circulation  $\Gamma_-(\theta_k, t)$  are obtained by only including  $\omega > 0$  and  $\omega < 0$ , respectively, in the integral. For the convergent-geometry scenarios included in this study, vorticity deposition by the initial shock wave produces “negative” rotation in the sense that  $\omega = \boldsymbol{\omega} \cdot \hat{\theta} < 0$ , and in the air-He cases, “positive” rotation ( $\boldsymbol{\omega} \cdot \hat{\theta} > 0$ ) is produced by the initial shock wave. This we call “primary” circulation, corresponding to  $\Gamma_-(\theta, t)$  for the convergent-geometry scenarios (nitrogen-argon, air-krypton and air-R12), and  $\Gamma_+(\theta, t)$  for the light-bubble scenarios (air-helium).

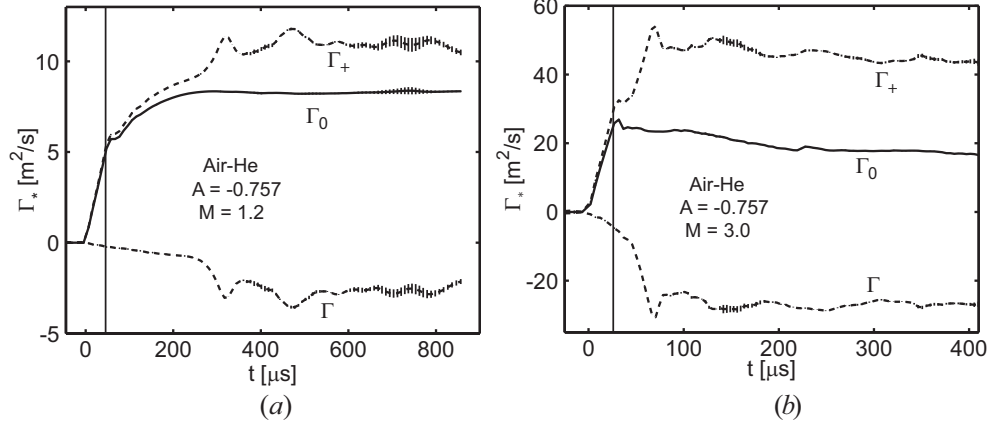


Figure 35: Decomposed circulation  $\Gamma_*$  versus time, for two air-He scenarios: (a)  $M = 1.2$ , and (b)  $M = 3.0$ . Vertical bars indicate r.m.s. azimuthal fluctuations  $\tilde{\Gamma}_*$  and a solid vertical line indicates the time of shock passage,  $t^* = 2R/\tilde{W}$ .

Azimuthally averaged values of the positive, negative and net circulation in the bubble region are obtained as

$$\bar{\Gamma}_*(t) = \frac{2}{\pi} \int_0^{\pi/2} \Gamma_*(\theta, t) d\theta \approx \frac{1}{48} \sum_{k=1}^{48} \Gamma_*(\theta_k, t), \quad (4.30)$$

where  $* \in \{+, -, 0\}$ . Further, r.m.s. fluctuations  $\tilde{\Gamma}_*(t)$  with respect to the azimuthal mean are computed by taking the variance of the 48  $\theta$ -samples:

$$\tilde{\Gamma}_*(t) = \frac{2}{\pi} \sqrt{\int_0^{\pi/2} [\Gamma_*(\theta, t) - \bar{\Gamma}_*(t)]^2 d\theta} \approx \frac{1}{48} \sqrt{\sum_{k=1}^{48} [\Gamma_*(\theta_k, t) - \bar{\Gamma}_*(t)]^2}. \quad (4.31)$$

Plots of  $\bar{\Gamma}_*(t)$  are given in Figs. 35-38 for the highest and lowest Mach number scenarios for each gas pairing included in this study. The time of shock passage,  $t^* \equiv 2R/\tilde{W}$  is indicated on each plot by a solid vertical line. The r.m.s. azimuthal fluctuations in circulation,  $\pm \tilde{\Gamma}_*(t)$ , are plotted as error bars on each curve. These error bars indicate the magnitude of azimuthal-mode fluctuations in the vortex strength, suggesting the growth

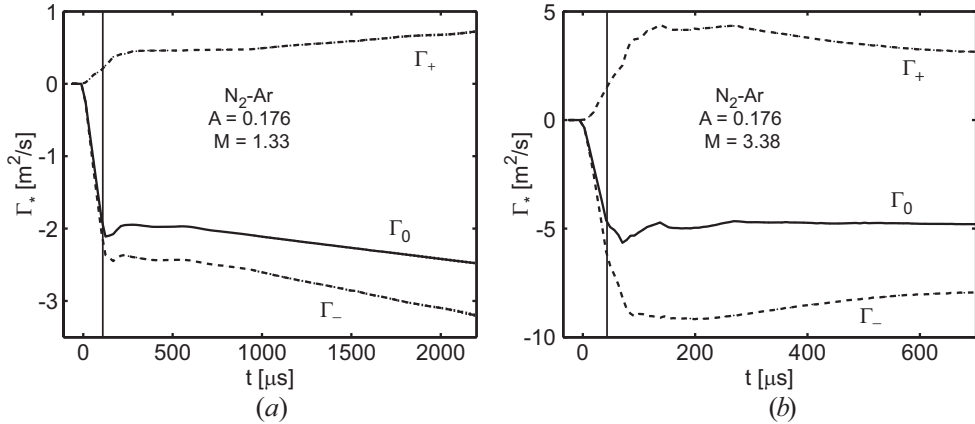


Figure 36: Decomposed circulation  $\Gamma_*$  versus time, for two  $N_2\text{-Ar}$  scenarios: (a)  $M = 1.33$ , and (b)  $M = 3.38$ . Vertical bars indicate r.m.s. azimuthal fluctuations  $\tilde{\Gamma}_*$  and a solid vertical line indicates the time of shock passage,  $t^* = 2R/\tilde{W}$ .

of vortex bending and stretching modes in the vorticity field generated by the shock-bubble interaction. (Note that azimuthal fluctuations in the nitrogen-argon scenarios are so small that the error bars are not visible in the plot shown in Fig. 36.)

The trends in the  $\theta$ -averaged circulation show the abrupt initial shock-driven increase in primary and total circulation, followed by a “plateau” in the total circulation. The initial rise in  $\Gamma_0$  always ends near  $t = t^*$ ; however, the “plateau” in the total circulation does not always begin at shock passage, but later in many cases, after a period characterized by small-amplitude oscillations. Vorticity generation continues in the positive and negative components at intermediate and late times due to two effects. First, vortex-accelerated vorticity deposition (VAVD) is significant: strong vortices deposited in the flow introduce centripetal accelerations which contribute to further vortical growth. This mechanism is described in detail for Richtmyer-Meshkov instabilities by Peng *et al.* (2003) [78], who report that the components of the circulation continue to grow even at very late times in Richtmyer-Meshkov instabilities. Second, vorticity

generation continues due to the reverberating scattered and diffracted shock waves and reflected rarefaction waves discussed in Secs. 1.2.3 and 4.1.1, and highlighted in Fig. 28. Such secondary compressions and expansions generate vorticity baroclinically on the interface as they traverse the deformed bubble, causing the total circulation to continue to change in time.

The significance of these two effects is shown clearly in Fig. 39, where the magnitude of the instantaneous baroclinic source term  $(\nabla\rho \times \nabla p)/\rho^2$  and the magnitude of the Laplacian of the density field  $|\Delta\rho|$  are plotted on the  $\theta = \pi/6$  section, for  $t = 5.0R/W^* = 74.1 \mu\text{s}$  and  $t = 8.35R/W^* = 123.7 \mu\text{s}$  in the air-R12,  $M = 5$  scenario. A number of secondary shock waves are seen traversing the bubble region, and regions of continuing positive and negative baroclinic generation are visible. This is a striking example of secondary vorticity generation after the passage of the initial shock. After such secondary waves have passed out of the bubble region, indicated by  $\langle\rho\rangle \rightarrow 1$  in figure 28, the components of the circulation continue to grow, by the VAVD mechanism of Peng *et al.* [78]

The fact that  $\Gamma_+$  and  $\Gamma_-$  continue to grow while  $\Gamma_0$  remains constant at these later times indicates that the spatial distribution of vorticity decays from one dominated by a few large-scale vortices to one characterized by an increasingly large number of smaller and smaller vortex dipoles shed from the larger vortices. Such an evolution of the vorticity field is evident in the vorticity plots in Figs. 23-26. (It is important to note however, that mesh sensitivity studies have indicated that the components of the circulation ( $\Gamma_+$  and  $\Gamma_-$ ) are strongly sensitive to the computational mesh spacing.)

For comparison with the PB, YKZ, SZ3, and one-dimensional gasdynamics-based circulation models, the circulation at the instant of shock passage is extracted from

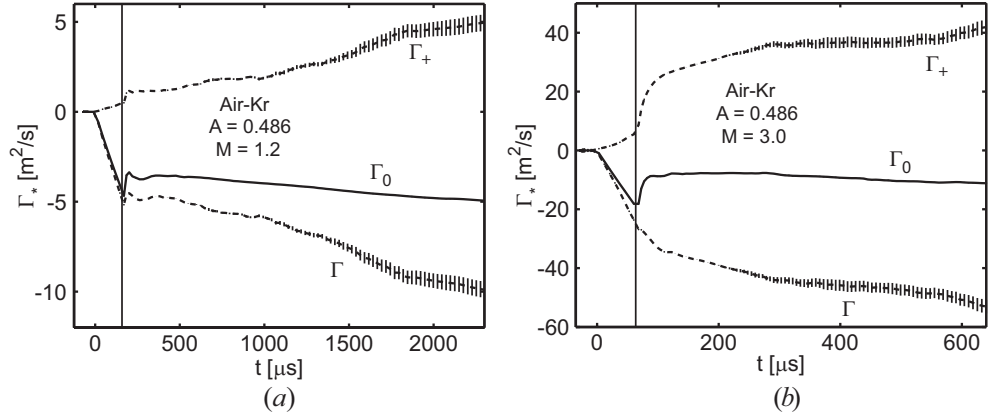


Figure 37: Decomposed circulation  $\Gamma_*$  versus time, for two air-Kr scenarios: (a)  $M = 1.2$ , and (b)  $M = 3.0$ . Vertical bars indicate r.m.s. azimuthal fluctuations  $\tilde{\Gamma}_*$  and a solid vertical line indicates the time of shock passage,  $t^* = 2R/\tilde{W}$ .

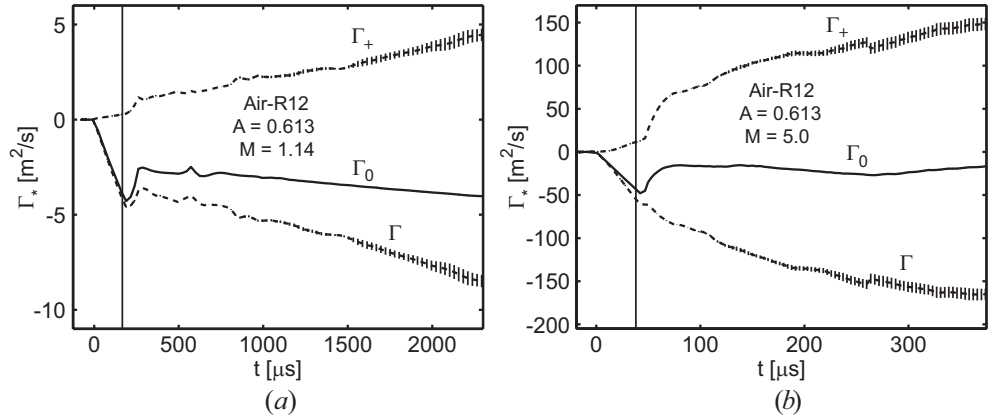


Figure 38: Decomposed circulation  $\Gamma_*$  versus time, for two air-R12 scenarios: (a)  $M = 1.14$ , and (b)  $M = 5$ . Vertical bars indicate r.m.s. azimuthal fluctuations  $\tilde{\Gamma}_*$  and a solid vertical line indicates the time of shock passage,  $t^* = 2R/\tilde{W}$ .

Scenario no.	Gases	$M$	$\hat{\Gamma}_0$ [m <sup>2</sup> /s]	$\Gamma_{PB}$ [m <sup>2</sup> /s]	$\Gamma_{YKZ}$ [m <sup>2</sup> /s]	$\Gamma_{SZ}$ [m <sup>2</sup> /s]	$\Gamma_{SZ3}$ [m <sup>2</sup> /s]	$\Gamma_{1D}$ [m <sup>2</sup> /s]
1	Air-He	1.20	4.98	9.20	5.98	21.05	-6.93	5.47
2		1.50	10.09	18.41	9.84	31.25	11.42	11.53
3		1.68	12.50	22.79	11.04	34.93	24.04	14.50
4		3.00	24.93	48.26	15.25	44.85	77.89	31.24
5	N <sub>2</sub> -Ar	1.33	-1.95	-2.48	-1.91	-2.16	-1.99	-1.98
6		2.88	-4.25	-8.41	-3.50	-6.79	-5.09	-3.88
7		3.38	-4.68	-10.01	-3.82	-7.96	-5.23	-4.29
8		Air-Kr	-4.38	-4.93	-3.84	-4.69	-4.08	-5.85
9	Air-R12	1.50	-8.56	-9.88	-6.32	-9.30	-9.12	-9.63
10		1.68	-10.39	-12.23	-7.09	-11.40	-11.45	-11.05
11		3.00	-18.16	-25.90	-9.79	-22.64	-22.19	-18.74
12		1.14	-3.89	-4.93	-3.82	-4.82	-4.05	-5.33
13		2.50	-22.06	-28.32	-11.22	-25.97	-25.43	-21.89
14		5.00	-43.28	-59.75	-17.10	-51.55	-48.95	-43.73

Table 4: Computed and modeled values of primary circulation at the instant of first shock passage ( $t\tilde{W}/R = 2$ ) for each of the 14 scenarios and each of the models described in Secs. 4.2.2-4.2.4.

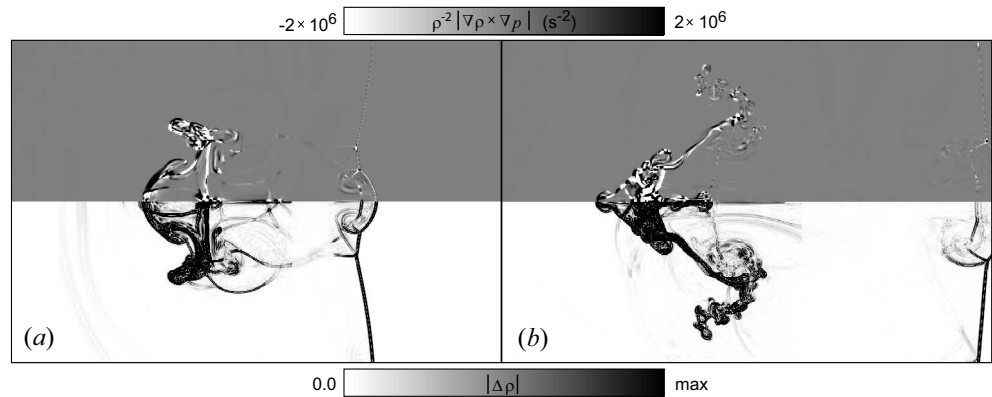


Figure 39: Magnitude of the baroclinic source term  $\rho^{-2} \nabla \rho \times \nabla p$  (top) and magnitude of the Laplacian of the total density field  $|\Delta \rho|$  on the  $\theta = \pi/6$  slice plane, for (a)  $t = 5.0R/W^* = 74.1 \mu\text{s}$  and (b)  $t = 8.35R/W^* = 123.7 \mu\text{s}$  in the air-R12,  $M = 5$  scenario. Incident shock wave propagation is left-to-right.

these data. The ratios of computed to modeled values of the primary net circulation at shock passage  $\hat{\Gamma}_0$  are shown in Fig. 40, and the computed and modeled values themselves are given in Table 4. The data indicate that of the four models, the SZ3 model and our proposed one-dimensional reconstruction (“R”) model, in general, yield the best results across the parameter space. The SZ3 model prediction, for  $A > 0$ , has a maximum error of 22% and an average error of 10%. The one-dimensional reconstruction model gives a maximum error of 37%, and an average error of 10% across the entire parameter space, including  $A < 0$ . In general, both models tend to overpredict the circulation slightly, though the agreement between these two models and the computed values is quite good for  $A > 0$ , and between the “R” model and the computed values for  $A < 0$ . As for the other circulation models, the YKZ model performs reliably for  $A < 0.2$ , including the air-He and N<sub>2</sub>-Ar scenarios, although it exhibits excessive sensitivity to the Mach number for fixed  $A$ . The PB model performs well at high density contrasts,  $A > 0.2$ , but overpredicts the circulation by a factor of approximately two for  $A < 0$ , as has been noted in the papers of both PB and YKZ.

Overall, the results shown in Table 4 and Fig. 40 suggest that a complete and consistent predictive model for the shocked-bubble circulation does not yet exist. The SZ3 and R models provide very good estimates in general, but in sporadic cases they strongly over- or underestimate the values measured from the current simulations, and the SZ3 model is unreliable for  $A < 0$ . Though the R model shows good agreement with computed values within the parameter space of this study, its asymptotic properties are unknown, and its consistency can therefore not be guaranteed. Further, the two simpler models, the PB and YKZ models, which are explicitly stated to be valid only in the case of weak shock waves and small density ratios, appear to perform well in a number of

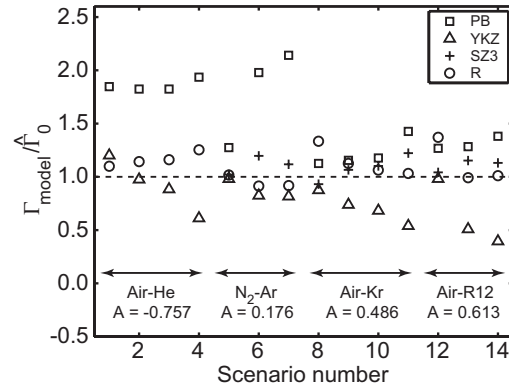


Figure 40: The ratio of modeled circulation to computed circulation at shock passage,  $\Gamma_{model}/\hat{\Gamma}$ , for each of the 14 scenarios included in this study, and all four circulation models described above. See Table 4 for scenario numbers.

cases with a high  $A$  magnitude and high  $M$ . This analysis has been performed also with circulation values measured from simulations only in regions with  $f > 0$  (*i.e.*, in the bubble fluid only), with a similar outcome. However, it is remarkable that, both in the circulation and the bubble compression and mean velocity metrics, analytical models for the shock-bubble interaction with close linkages to one-dimensional gasdynamics have performed well.

# Chapter 5

## Analysis of Complex Flow Features and Turbulent Mixing

In Chapter 4, we saw that many features of shock-bubble interaction flowfields can be characterized and modeled very effectively using approaches that treat the problem as two-dimensional or even one-dimensional, even though the problem as it has been formulated here is only quasi-two-dimensional. That is, the numerical mesh imposes a small-amplitude, high-wave-number density perturbation such that the initial condition is not uniform in the third dimension (the  $\hat{\theta}$  direction). However, the initial condition is homogeneous in the  $\hat{\theta}$  direction, in the sense that the moments of  $\rho(\theta)$  do not vary with  $\theta$ . Thus, the problem has an inherent three-dimensional component, but many of the bulk, integral properties of the flowfield (such as the mean density and velocity of the shocked bubble) are invariant because the problem is quasi-two-dimensional.

The three-dimensional nature of the problem becomes apparent in more complex features of the flowfield that have direct linkages to dissipation and vorticity dynamics at the smallest scales. The most important of these are the mixing of the two fluids, and the deformation of the interface. Through the action of three-dimensional instabilities, the deformation of the interface and the development of the mixing region takes on an

entirely different character in three-dimensional shock-bubble interactions, if the conditions are favorable for transition to turbulence. A primary purpose of the current study is to determine what these conditions are, and characterize the nature and significance of non-axisymmetric effects in three-dimensional Eulerian simulations for shock-bubble interactions. We do this using a series of statistical diagnostics applied to the computed data. First, we establish a means of performing averages over the flowfields to obtain fluctuating quantities and their overall intensities and statistical properties. Second, we apply several metrics to measure mixing directly from the computed flowfields, taking into account the three-dimensional nature of the mixing-region development. Finally, we characterize the significance of three-dimensional effects directly by comparison with corresponding two-dimensional simulations, and by examining the components of the enstrophy in the flowfield.

## 5.1 Non-Axisymmetric Features and Turbulence

### 5.1.1 Background considerations regarding turbulence

Although the flowfields associated with shock-bubble interactions have often been described in terms of turbulence and turbulent mixing [42, 113, 29, 43], some clarification is needed as to what constitutes “turbulence” in these flows, whether these flows can accurately be described as “turbulent,” and what effects we might expect due to turbulence-like features that are present. For the purposes of this study, we describe turbulence as a disordered state that arises in the fluid, which is characterized by seemingly chaotic rotational and dissipative motion, random spatial and temporal fluctuations in the flow variables, enhanced transport and mixing phenomena, a wide range of length

scales, and nonlinear energy transfer from large (driving) scales to small (dissipative) scales via the inherently three-dimensional phenomenon of vortex stretching.

The transition to a turbulent state in a nonstationary flow requires (1) a sufficiently high Reynolds number, (2) a seed perturbation on which the nonlinear energy transfer mechanisms may act, and (3) time for the wide range of length scales to develop [72].

The Reynolds number appearing in condition (1) is defined as

$$Re = \frac{U^* \delta^*}{\nu}, \quad (5.1)$$

where  $U^*$  and  $\delta^*$  represent characteristic velocity and length scales, respectively, and  $\nu$  represents the kinematic viscosity of the fluid. Dimotakis (2000) [27] has observed that in turbulent flows at a certain critical Reynolds number, a transition to a state of enhanced molecular mixing can occur. Above this mixing-transition  $Re$  (which is beyond the threshold for transition from laminar to turbulent flow), an abrupt increase in disorganized three-dimensionality can be observed, which results in a markedly more well-mixed state in the flow. Dimotakis observes that the Reynolds-number threshold for this mixing transition is approximately  $Re = 2 \times 10^4$ . This has subsequently been commonly regarded as the threshold at which turbulent effects become significant in Rayleigh-Taylor and Richtmyer-Meshkov mixing [85, 17].

The consequences of the development of fully three-dimensional turbulence in shock-bubble interactions are similar to those associated with three-dimensional turbulence in Rayleigh-Taylor and Richtmyer-Meshkov instabilities. In general, these consequences include (1) the deterioration of large coherent structures in the flowfield (such as spike/bubble features and vortex projectiles) into smaller, more diffuse regions of disordered motion, and (2) a distinctly higher rate of approach to a state where two initially separated fluids

are very thoroughly mixed to a molecular level. Such effects are inherently driven by three-dimensional mechanisms, and three-dimensional treatment is required to capture them [11]. In two dimensions, a turbulent state may develop, but an inverse cascade of energy is established, which allows coherent structures to grow rather than deteriorate [72, 100].

Turbulence that develops in shock-contact interactions is also fundamentally distinct from classical shear-flow turbulence, and from Rayleigh-Taylor turbulence, in that it is highly transient. That is, the driver for the development of vorticity in the flow is baroclinicity associated with the initial shock wave and secondary shock and rarefaction waves passing over the interface. After these waves have left the vicinity of the interface, turbulent fluctuations are left to decay. Moreover, vorticity is deposited only in a relatively small volume in the flowfield where  $\nabla\rho \times \nabla p \neq 0$ , and the vorticity magnitude in shock bubble interactions is very strongly peaked at the bubble equator where  $\phi = \pi/2$ . Thus, turbulent effects are not only transient but also strongly localized in shock-bubble interactions. Nevertheless, in this study we postulate that the consequences of the development of three-dimensional turbulence in shock-bubble interactions are significant, and employ a number of diagnostics to characterize turbulent effects as observed in Eulerian simulations.

### 5.1.2 Monotone-integrated large eddy simulation

A fundamental problem in employing numerical methods to simulate compressible turbulent mixing is that turbulent flows are multi-scale by nature, and the dissipation that occurs at the smallest scales is a mechanism that cannot be neglected. Therefore, the numerical scheme must encompass macroscopic effects at the largest scales while also

capturing microscopic effects at scales that are orders of magnitude smaller than the largest scales [82]. This can be done by directly solving the Navier-Stokes equations, but the computational cost involved in capturing the high- $Re$  effects is immense, making the problem intractable except for very modest Reynolds numbers, even with the most powerful computing facilities. Alternatives to direct numerical simulation (DNS) are provided by solving a set of equations that result from either (1) averaging over time, space, or an ensemble of equivalent flows (the Reynolds-averaged Navier-Stokes or RANS approach), or (2) applying a spatial filter to the problem so that the fluid motion is separated into large and small scales (the large eddy simulation or LES approach), with the equations being solved for the former, and a subgrid-scale model being employed for the latter. In both cases, some empirical or semi-empirical input is required to relate the subgrid (unresolved) behavior to the mean or large-scale flow and provide closure to the problem.

An alternative to the RANS and LES methodologies is the monotone-integrated LES or “MILES” approach, which has been described in detail by Boris *et al.* (1992) [10], Fureby and Grinstein (2002) [33] and Drikakis *et al.* (2005) [29]. This approach is also known as “implicit large eddy simulation” or ILES [40], and relies on implicit numerical dissipation inherent to the numerical method to emulate the dissipative flow features in the high-wavenumber end of the spectrum, rather than incorporating an explicit LES filter, subgrid-scale model, or eddy viscosity model. In this way, a computationally simpler and more economical scheme is constructed, which also avoids the complexities and errors associated with such explicit filters and models [29]. Further, it has been pointed out that, when employed with an appropriate “high-resolution” (second-order or better) shock-capturing method, the MILES/ILES approach possesses characteristics that

implicitly mimic many of the explicit turbulence modeling techniques used in conventional LES methods [28, ?, 57, 100]. The MILES and ILES techniques have been used successfully in modeling accelerated inhomogeneous flows using high-resolution Eulerian methods by Youngs (1991) [111], Latini *et al.* (2007) [58], Schilling *et al.* (2007) [100] and others.

In the present study, we employ an Eulerian numerical method (*Raptor*) that falls in the category of “high-resolution” schemes outlined by Drikakis *et al.* (2005) [29], as described in Sec. 2.1. The approach in *Raptor* is MILES, and this makes *Raptor* an ideal choice for performing the simulations in the present study, since it yields optimum efficiency in the use of computing resources, while also capturing the unsteady, three-dimensional, high-Reynolds-number effects inherent to turbulent mixing.

### 5.1.3 Mixing transition and Reynolds number

By inspection of Figs. 23-27, it is qualitatively apparent that turbulence-like effects are present in some of the flows simulated here. In the high- $A$ , air-Kr and air-R12 cases in particular (Figs. 25-26), we note several characteristics that are typically attributed to turbulent flowfields. The density and vorticity fields from Figs. 25(f) and 26(f) are reproduced here in Fig. 41 in order to show these more clearly. In these plots we note that a wide range of length scales becomes evident in the flowfield, regions of very thorough mixing develop, and a disordered and apparently chaotic state arises, which is particularly noticeable in the vorticity fields. Further, although it cannot be seen in the two-dimensional plots shown in Fig. 41, there is significant variability in the  $\theta$ -direction in these datasets, indicating the three-dimensionality inherent to the simulated flowfield. We also observe that these effects are generally found for the scenarios at each Mach

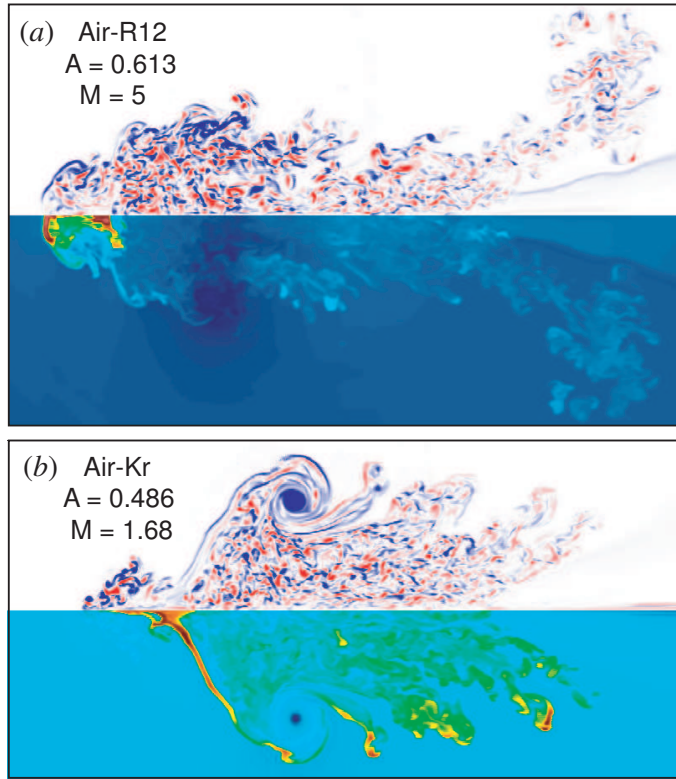


Figure 41: Late time ( $\tau \approx 25$ ) vorticity (top) and density (bottom) fields from (a) the air-R12,  $M = 5$  scenario, and (b) the air-Kr,  $M = 1.68$  scenario, showing evidence of turbulence effects in the flowfield. Incident shock wave propagation is left-to-right.

number in both of these gas combinations.

However, it is not clear whether these features can be described in terms of turbulence, strictly speaking, in light of two observations. First, these simulations are inviscid, and the dissipative mechanism necessary for fully-developed turbulence to exist is therefore absent, except as introduced by numerical dissipation. Second, the dissipation that is introduced by the numerical method acts on the grid scale, which, even on the finest AMR level, under-resolves the physical dissipative scale.

Turbulence-like features are notably absent in a number of the simulations included

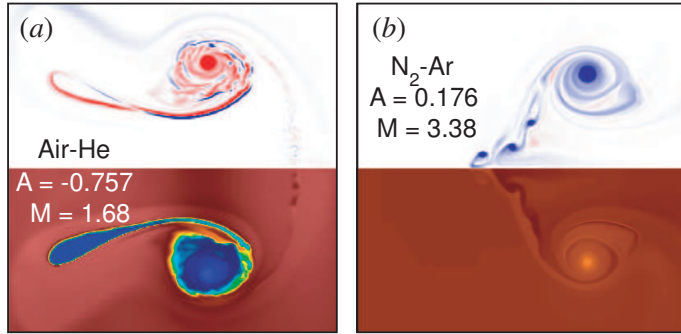


Figure 42: Late time ( $\tau \approx 25$ ) vorticity (top) and density (bottom) fields from (a) the air-He,  $M = 1.68$  scenario, and (b) the N<sub>2</sub>-Ar,  $M = 3.38$  scenario, indicating the absence of strong turbulence effects in the flowfield. Incident shock wave propagation is left-to-right.

in this study. In particular, we see much longer-lived coherent structures and distinctly less thorough mixing in the air-helium and nitrogen-argon scenarios shown in Figs. 23–24, even at high  $M$ . The density and vorticity fields from  $\tau = 25$  are reproduced here in Fig. 42, where we note that the flowfields even at late times are still dominated by the primary vortex ring, with very little mixing between the bubble and ambient fluid evident in these plots. Similar effects are seen at other Mach numbers for these two gas combinations. Thus we are led to conclude that a mixing transition of the type described by Miles *et al.* (2005) [72] as “weak” occurs in the present simulations for shock-bubble interactions between approximately  $A = 0.2$  and  $A = 0.4$ . The term “weak” is used in order to distinguish this transition from the Dimotakis mixing transition which leads to fully-developed turbulence.

To characterize this weak mixing transition in terms of Reynolds numbers, we first define an “effective” or grid-scale Reynolds number for these simulations, following Miles *et al.* (2005) [72],

$$Re_{\Delta} = \left( \frac{\ell}{\Delta} \right)^{4/3}, \quad (5.2)$$

where  $\ell$  is a characteristic length scale. Although the simulations are inviscid, we compute  $Re_{\Delta}$  as an indication of the range of length scales present in the computed flowfield, which may be regarded as an “effective” Reynolds number. Taking the characteristic length scale to be the maximum streamwise dimension of the shocked bubble,  $\ell = \Delta y(t)$ , we obtain time-dependent effective Reynolds numbers shown in Fig. 43. These Reynolds numbers indicate a clear difference between the air-helium/nitrogen-argon cases and the air-krypton/air-R12 cases. For the former,  $Re_{\Delta}$  generally remains smaller than 3000 for the times of interest; for the latter, on the other hand,  $Re_{\Delta}$  generally grows to become larger than 3000 for later times. This suggests that  $Re_{\Delta} = 3000$  could be regarded as a threshold for the weak mixing transition in these simulations. However, we also note from these results that  $Re_{\Delta}$  remains very modest, and is nearly one order of magnitude smaller than the mixing-transition  $Re$  identified by Dimotakis (2000) [27] of  $2 \times 10^4$ .

The true physical Reynolds number associated with shock-bubble interactions at the conditions of the present simulations can be estimated by reformulating the Reynolds number in terms of the circulation  $\Gamma$ , as

$$Re_{\nu} = \frac{\Gamma^*}{\nu^*}, \quad (5.3)$$

where  $\Gamma^*$  is a characteristic circulation for the flow, and  $\nu^*$  is a characteristic kinematic viscosity. If we take  $\Gamma^*$  to be the total circulation in the flowfield obtained from simulations using Eq. 4.17, and take  $\nu^*$  to be the average of the two fluids’ kinematic viscosities,  $\nu^* = \bar{\nu} = (\nu_1 + \nu_2)/2$ , then we obtain time-dependent physical Reynolds numbers shown in Fig. 44.

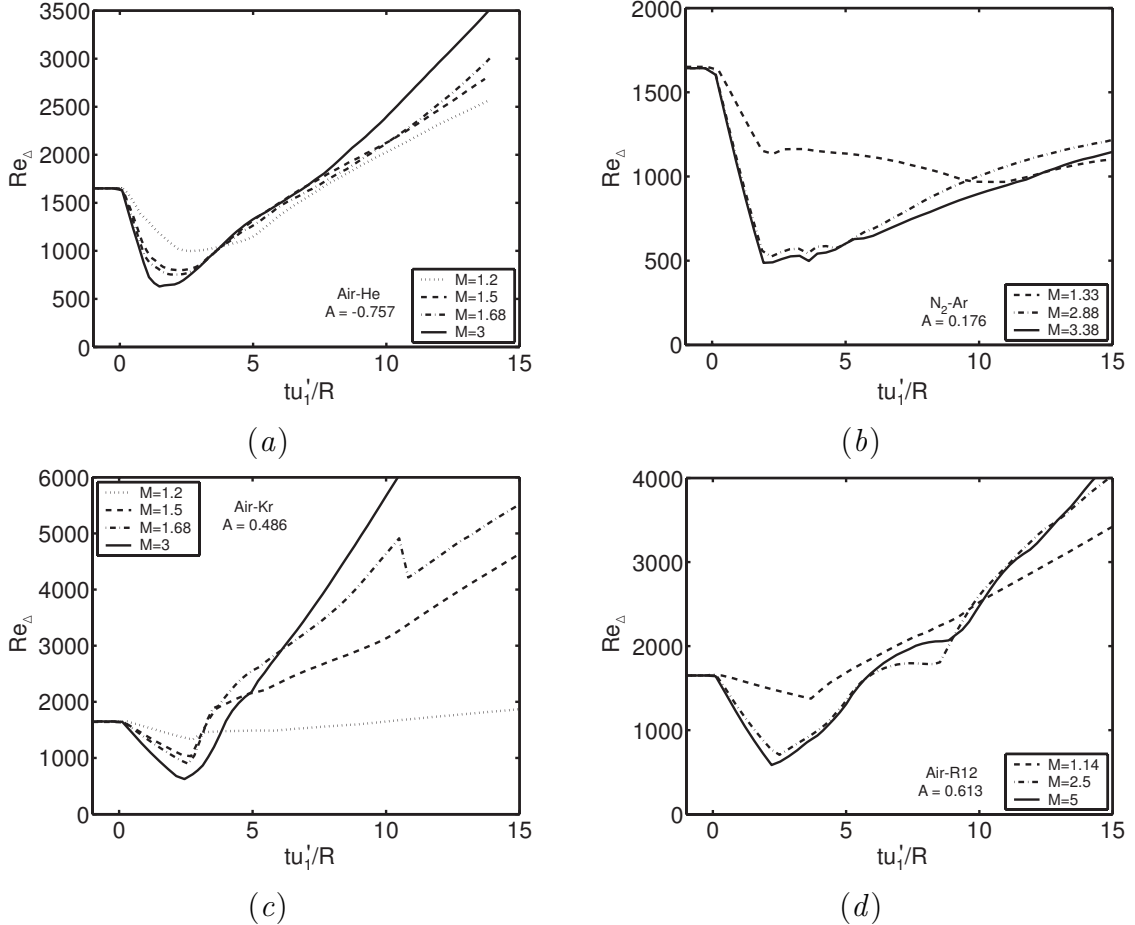


Figure 43: Plots of the grid-scale Reynolds number  $Re_{\Delta}$  obtained using Eq. 5.2: (a) air-He, (b) N<sub>2</sub>-Ar, (c) air-Kr, (d) air-R12.

Gas	$\mu$ [Pa.s]
He	$2.321 \times 10^{-5}$
N <sub>2</sub>	$2.100 \times 10^{-5}$
Air	$2.186 \times 10^{-5}$
Ar	$2.737 \times 10^{-5}$
Kr	$3.093 \times 10^{-5}$
R12	$1.546 \times 10^{-5}$

Table 5: Dynamic viscosities for gases in the present simulations, obtained from JANAF data [35] for atmospheric conditions.

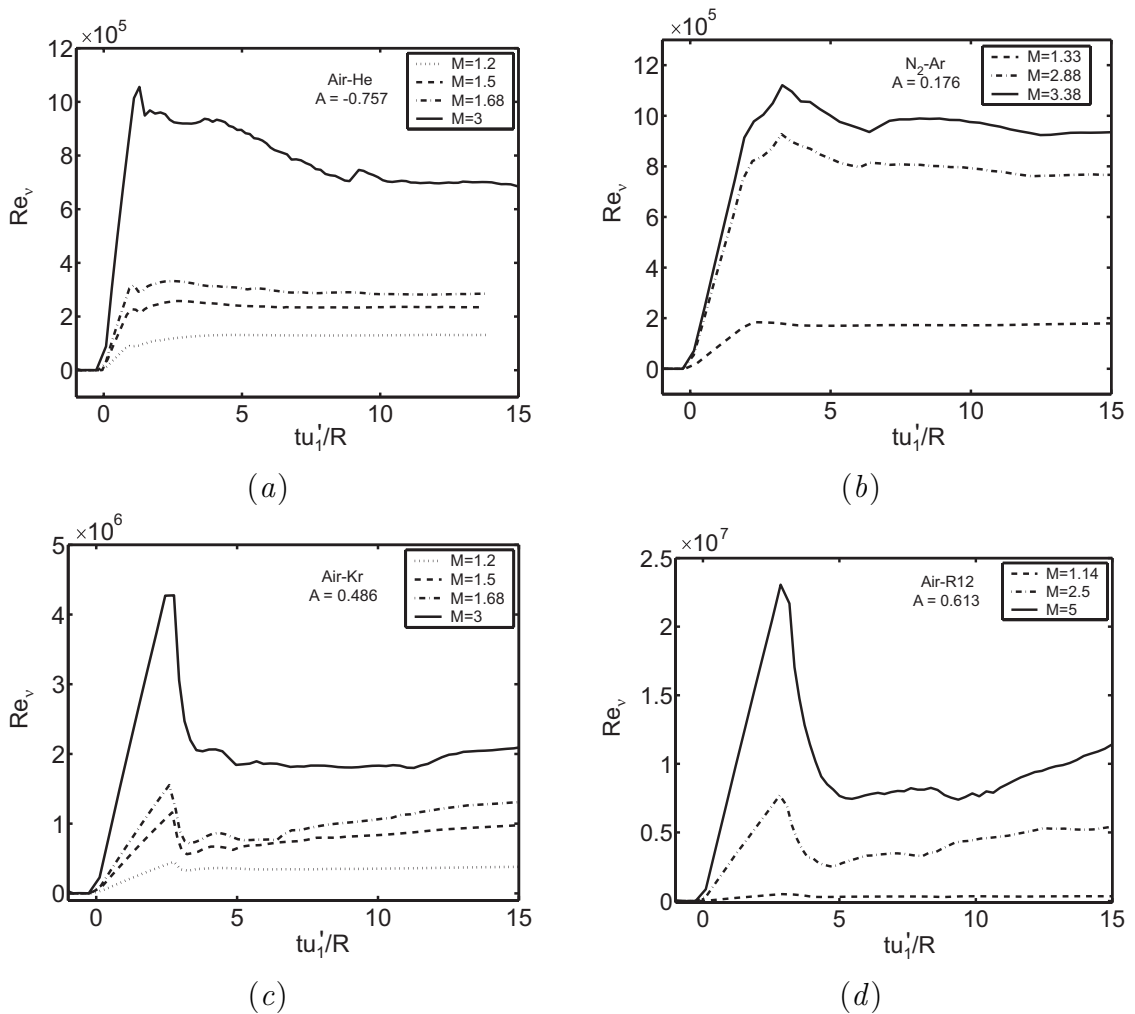


Figure 44: Plots of the physical Reynolds number  $Re_\nu$  obtained using Eq. 5.3: (a) air-He, (b) N<sub>2</sub>-Ar, (c) air-Kr, (d) air-R12.

The dynamic and kinematic viscosities used to compute these Reynolds numbers are shown in Tables 5 and 6. Post-shock kinematic viscosities are obtained by taking the ratio of the dynamic viscosity  $\mu$  at atmospheric conditions [35] to the post-shock density of the bubble fluid  $\rho'$  computed from one-dimensional gasdynamics:

$$\nu_1 = \frac{\mu_1}{\rho'_1} \quad (5.4)$$

$$\nu_2 = \frac{\mu_2}{\rho'_2} \quad (5.5)$$

$$\bar{\nu} = \frac{\nu_1 + \nu_2}{2} \quad (5.6)$$

The physical Reynolds numbers shown in Fig. 44 then represent the  $Re$  we expect for the experimental counterpart to the simulations in this study. We observe in Fig. 44 that  $Re_\nu$  is larger than  $Re_\Delta$  for these simulations by 2-3 orders of magnitude. Further, we note that at late times ( $tu'_1/R \geq 10$ ),  $Re_\nu \geq 10^6$  for the air-krypton and air-R12 cases, in general, while  $Re_\nu < 10^6$  for the air-helium and nitrogen-argon cases. However, in all cases, the Reynolds number computed in this way exceeds the Dimotakis mixing-transition Reynolds number by at least one order of magnitude in the immediate post-shock phase. The Reynolds numbers obtained by both of the methods are shown also in Table 7, including the maximum  $Re$  over the course of the shocked-bubble evolution, and  $Re$  at  $tu'_1/R = 10$ .

Overall, then, we conclude that (1) these simulations under-resolve the smallest-scale turbulent flow features, as is indicated by  $Re_\Delta \ll Re_\nu$ ; and (2) we observe the Reynolds numbers associated with the weak mixing transition in the simulations to be  $Re_\Delta = 3000$  and  $Re_\nu = 10^6$ . The fact that we observe turbulence-like effects at Reynolds numbers exceeding these thresholds, and that the physical Reynolds numbers  $Re_\nu$  are so high,

Scenario no.	Gases	$M$	$\nu_1$ [m <sup>2</sup> /s]	$\nu_2$ [m <sup>2</sup> /s]	$\bar{\nu}$ [m <sup>2</sup> /s]
1	Air-He	1.20	$1.353 \times 10^{-5}$	$1.137 \times 10^{-4}$	$6.362 \times 10^{-5}$
2		1.50	$9.742 \times 10^{-6}$	$8.975 \times 10^{-5}$	$4.975 \times 10^{-5}$
3		1.68	$8.379 \times 10^{-6}$	$7.990 \times 10^{-5}$	$4.414 \times 10^{-5}$
4		3.00	$4.699 \times 10^{-6}$	$4.624 \times 10^{-5}$	$2.547 \times 10^{-5}$
5	N <sub>2</sub> -Ar	1.33	$1.149 \times 10^{-5}$	$1.142 \times 10^{-5}$	$1.146 \times 10^{-5}$
6		2.88	$4.810 \times 10^{-6}$	$6.151 \times 10^{-6}$	$5.480 \times 10^{-6}$
7		3.38	$4.314 \times 10^{-6}$	$5.774 \times 10^{-6}$	$5.044 \times 10^{-6}$
8		1.20	$1.353 \times 10^{-5}$	$7.104 \times 10^{-6}$	$1.032 \times 10^{-5}$
9	Air-Kr	1.50	$9.742 \times 10^{-6}$	$5.626 \times 10^{-6}$	$7.684 \times 10^{-6}$
10		1.68	$8.379 \times 10^{-6}$	$5.104 \times 10^{-6}$	$6.741 \times 10^{-6}$
11		3.00	$4.699 \times 10^{-6}$	$3.801 \times 10^{-6}$	$4.250 \times 10^{-5}$
12		1.14	$1.466 \times 10^{-5}$	$2.426 \times 10^{-6}$	$8.543 \times 10^{-6}$
13	Air-R12	2.50	$5.439 \times 10^{-6}$	$8.223 \times 10^{-7}$	$3.131 \times 10^{-6}$
14		5.00	$3.623 \times 10^{-6}$	$5.377 \times 10^{-7}$	$2.081 \times 10^{-6}$

Table 6: Post-shock kinematic viscosities for each gas, and mean post-shock kinematic viscosities for each gas combination, obtained using Eqs. 5.4-5.6.

indicate together that turbulent effects are significant in shock-bubble interactions, and such effects should be more thoroughly characterized.

### 5.1.4 Averaging scheme

In order to characterize non-axisymmetric and turbulent effects in the present three-dimensional simulations for shock-bubble interactions, an averaging scheme for isolating mean and fluctuating fields is needed. Since the only homogeneous direction in this problem is the azimuthal ( $\hat{\theta}$ ) direction, azimuthal averaging is the basis of the technique used here to obtain mean quantities. This azimuthal averaging scheme is shown schematically in Fig. 45.

The flowfield variables  $\Phi$  are stored as functions of  $x$ ,  $y$ , and  $z$ . An axisymmetric

Scenario no.	Gases	$M$	$Re_\Delta$	$Re_\Delta$	$Re_\nu$	$Re_\nu$
			Maximum	$tu'_1/R = 10$	Maximum	$tu'_1/R = 10$
1	Air-He	1.20	2574	2019	$1.317 \times 10^5$	$1.299 \times 10^5$
2		1.50	2791	2128	$2.578 \times 10^5$	$2.347 \times 10^5$
3		1.68	3004	2117	$3.302 \times 10^5$	$2.833 \times 10^5$
4		3.00	4428	2370	$1.056 \times 10^6$	$7.193 \times 10^5$
5	N <sub>2</sub> -Ar	1.33	1924	969	$2.161 \times 10^5$	$1.720 \times 10^5$
6		2.88	2223	1003	$9.274 \times 10^5$	$7.924 \times 10^5$
7		3.38	1768	896	$1.121 \times 10^6$	$9.755 \times 10^5$
8	Air-Kr	1.20	4494	1654	$4.883 \times 10^5$	$3.540 \times 10^5$
9		1.50	8637	3111	$1.193 \times 10^6$	$8.337 \times 10^5$
10		1.68	9316	4728	$1.553 \times 10^6$	$1.072 \times 10^6$
11		3.00	16163	5695	$4.275 \times 10^6$	$1.831 \times 10^6$
12	Air-R12	1.14	7836	2526	$5.059 \times 10^5$	$3.480 \times 10^5$
13		2.50	7448	2576	$7.702 \times 10^6$	$4.455 \times 10^6$
14		5.00	7484	2541	$2.306 \times 10^7$	$7.632 \times 10^6$

Table 7: Reynolds numbers for shock-bubble interaction simulations, including the grid-scale Reynolds number  $Re_\Delta$  (Eq. 5.2) and the physical Reynolds number  $Re_\nu$  (Eq. 5.3). The maximum value and the value at  $tu'_1/R = 10$  are both shown.

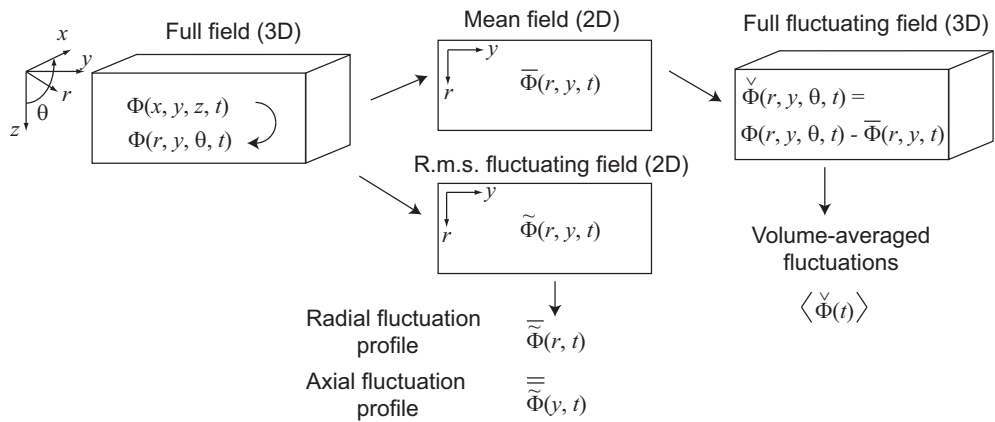


Figure 45: Schematic view of azimuthal averaging procedure.

coordinate system is defined using  $r = (x, 0, y)$  and  $\theta = \tan^{-1}(x/z)$ . Following Kuhl (1996) [53], the two-dimensional azimuthally averaged field  $\bar{\Phi}(r, y, t)$  is then obtained as

$$\bar{\Phi}(r, y, t) = \frac{2}{\pi} \int_0^{\pi/2} \Phi(r, y, \theta, t) d\theta. \quad (5.7)$$

(This procedure for computing azimuthal mean and fluctuating quantities was used by Kuhl (1996) [53] to characterize mixing in simulations for the detonation of a spherical charge of high explosive material.)

In practice, the averaging operation in Eq. 5.7 is carried out by assigning every cell in the three-dimensional mesh to one of an array of bins by their  $r$  and  $y$  coordinates, and then taking the arithmetic mean over the members of each bin. It is important to note that this yields the azimuthal average only in the case of uniform mesh spacing. Also, this yields a mean field free of aliasing errors only in the case where the spacing of each averaging bin is equal to the spacing of the cells in the computational mesh. Hence, two measures must be taken to ensure that this averaging operation produces the most meaningful results: (1) the solution stored on lower-resolution AMR “patches” must be resampled to a mesh with uniform spacing  $\Delta$  (where  $\Delta$  is the spacing of the highest-level mesh cells) and (2) the bin spacing must be set equal to  $\Delta$ .

Using the mean field  $\bar{\Phi}$  obtained using the binning/averaging procedure just described, the two-dimensional r.m.s. fluctuating field  $\tilde{\Phi}(r, y, t)$  is then obtained as

$$\tilde{\Phi}(r, y, t) = \sqrt{\frac{2}{\pi} \int_0^{\pi/2} [\Phi(r, y, \theta, t) - \bar{\Phi}(r, y, t)]^2 d\theta}. \quad (5.8)$$

The full three-dimensional fluctuating field is then found by subtracting the two-dimensional mean field from the full three-dimensional field as

$$\check{\Phi}(r, y, \theta, t) = \Phi(r, y, \theta, t) - \bar{\Phi}(r, y, t). \quad (5.9)$$

The operation denoted by Eq. 5.9 requires a more complex data-handling algorithm, which maintains the association between cells in the full three-dimensional field and the appropriate elements in the two-dimensional mean field, so that the subtraction may be performed correctly. After the subtraction has been performed, an overall r.m.s. measure of the intensity of non-axisymmetric fluctuations in the bubble fluid can then be obtained by a volume average over the three-dimensional fluctuating field:

$$\langle \check{\Phi}(t) \rangle = \sqrt{\frac{\iiint_B [\check{\Phi}(r, y, \theta, t)]^2 dV}{\iiint_B dV}}, \quad (5.10)$$

where  $dV$  denotes a differential volume element and  $B$  represents the bubble fluid region (the region where  $f \neq 0$ ).

Finally, radial and axial profiles of fluctuating quantities are obtained by averages over the two-dimensional field of r.m.s. fluctuations as

$$\tilde{\bar{\Phi}}(r, t) = \frac{1}{L_y} \int_0^{L_y} \tilde{\Phi}(r, y) dy \quad (5.11)$$

and

$$\bar{\tilde{\Phi}}(y, t) = \frac{1}{L_r} \int_0^{L_r} \tilde{\Phi}(r, y) dr, \quad (5.12)$$

where  $L_r$  and  $L_y$  are the radial and axial extents of the region over which averaging has been carried out.

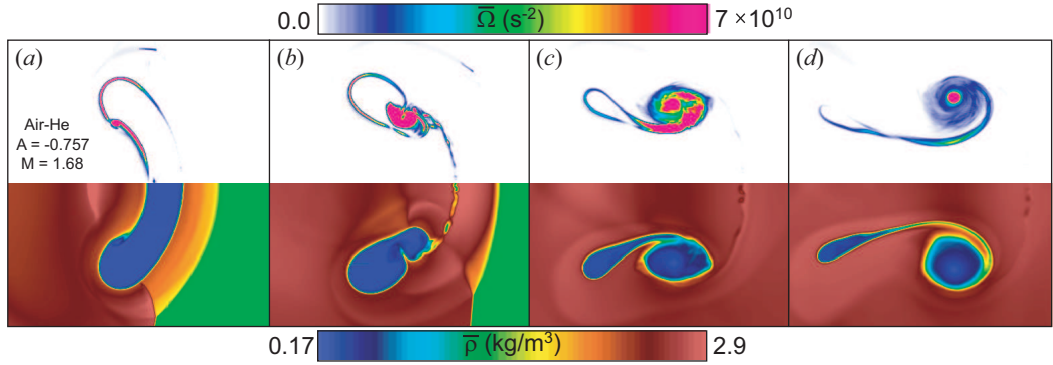


Figure 46: Azimuthally averaged enstrophy (top) and density (bottom) fields for the air-He,  $M = 1.68$  scenario. Dimensionless times  $tu'_1/R$  are (a) 1.0, (b) 2.0, (c) 4.0, and (d) 6.0. Incident shock wave propagation is left-to-right.

### 5.1.5 Mean and fluctuating flowfields

The averaging scheme just described effectively carries out a Reynolds decomposition on the simulated flowfield, separating each variable  $\Phi$  into mean  $\bar{\Phi}$  and fluctuating  $\tilde{\Phi}$  components by simple spatial averages. Favre averages [31] would be more appropriate for the compressible flows considered here, if the computational resources were available to perform such averaging operations efficiently and robustly on large datasets with nonuniform, adaptive grids. In Favre averaging, the expression in Eq. 5.7 would be replaced with a density-weighted average as  $\overline{\Phi\rho}/\overline{\rho}$ , which simplifies the equations of motion for compressible turbulent flow. A density-weighted averaging scheme thus requires two averages to be taken at every  $(r,y)$  location rather than just one, involving more than one variable from the dataset. Since the direction in which averages are taken (the  $\theta$ -direction) is not grid-aligned, this becomes a nontrivial task, particularly in the case of very large datasets.

For the present study, therefore, we follow the approach of Kuhl (1996) [53] and use

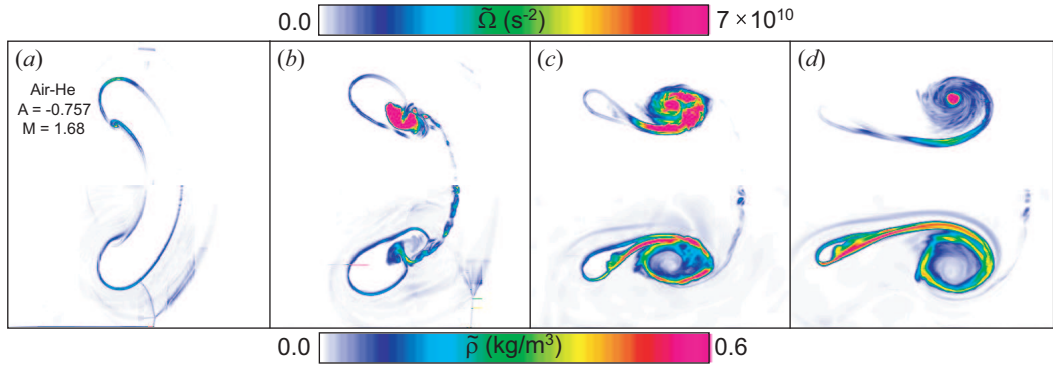


Figure 47: R.m.s. fluctuating enstrophy (top) and density (bottom) fields for the air-He,  $M = 1.68$  scenario. Dimensionless times  $tu'_1/R$  are (a) 1.0, (b) 2.0, (c) 4.0, and (d) 6.0. Incident shock wave propagation is left-to-right.

Reynolds averages in the  $\theta$ -direction. This averaging scheme is used to isolate the mean and fluctuating components of a number of variables in the flowfields, including the density, bubble-fluid volume fraction, pressure, velocity magnitude, specific kinetic energy, and enstrophy. Shown in Figs. 46-53 are the two-dimensional mean and fluctuating fields from four representative parameter study scenarios, for the density  $\rho$  and the enstrophy  $\Omega$ , where the enstrophy is defined as  $\Omega = \boldsymbol{\omega} \cdot \boldsymbol{\omega} = ||\boldsymbol{\omega}||^2$ . (Note that these are the same four scenarios shown in Figs. 23-26.)

In these plots, we examine the mean fields  $\bar{\Omega}(r, y, t)$  and  $\bar{\rho}(r, y, t)$ , and the fluctuating fields  $\tilde{\Omega}(r, y, t)$  and  $\tilde{\rho}(r, y, t)$ . In each case, we see that the regions of greatest non-axisymmetric fluctuations in the density field correspond generally to the regions of greatest shear and interface stretching, where the two fluids intermingle most actively. In the enstrophy fields, however, the regions of large non-axisymmetric fluctuations are generally co-located with regions of large mean enstrophy. Further, although the fluctuations in the density are generally on the order of one-fifth the magnitude of the

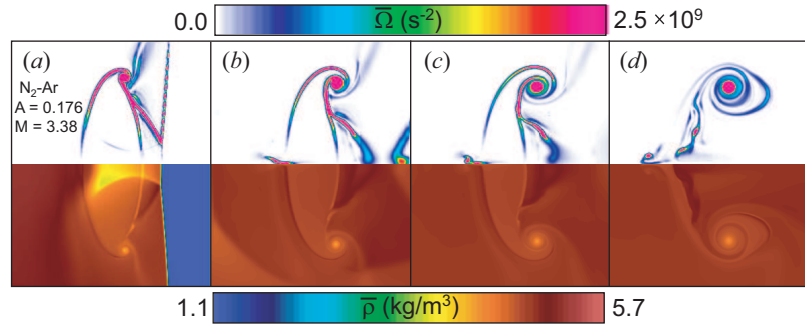


Figure 48: Azimuthally averaged enstrophy (top) and density (bottom) fields for the N<sub>2</sub>-Ar,  $M=3.38$  scenario. Dimensionless times  $tu'_1/R$  are (a) 2.0, (b) 4.1, (c) 5.9, and (d) 15.0. Incident shock wave propagation is left-to-right.

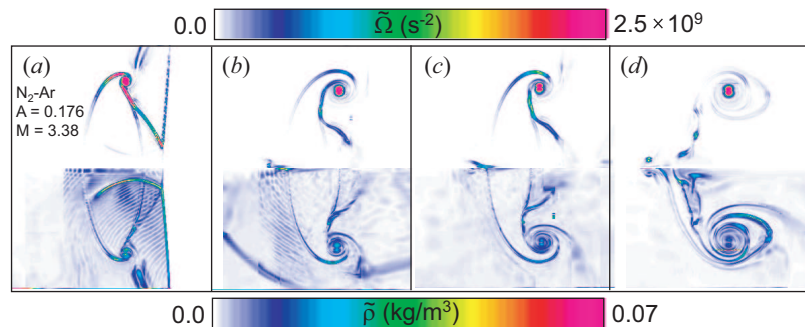


Figure 49: R.m.s. fluctuating enstrophy (top) and density (bottom) fields for the N<sub>2</sub>-Ar,  $M=3.38$  scenario. Dimensionless times  $tu'_1/R$  are (a) 2.0, (b) 4.1, (c) 5.9, and (d) 15.0. Incident shock wave propagation is left-to-right.

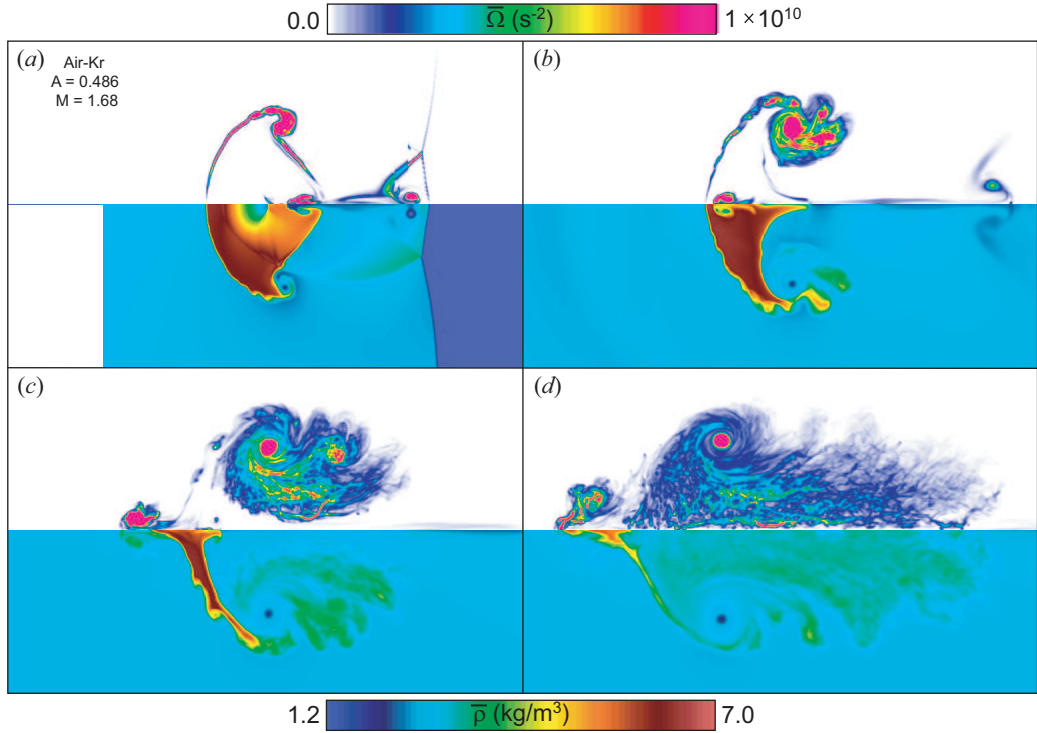


Figure 50: Azimuthally averaged enstrophy (top) and density (bottom) fields for the air-Kr,  $M = 1.68$  scenario. Dimensionless times  $tu'_1/R$  are (a) 2.0, (b) 4.1, (c) 8.0, and (d) 15.0. Incident shock wave propagation is left-to-right.

local mean field or smaller, enstrophy fluctuations appear to have magnitudes at some times that are themselves equal to or greater than the local mean enstrophy ( $\tilde{\Omega} \approx \bar{\Omega}$ ).

We also note in Figs. 46-53 that as we increase the Atwood number, the complexity of structures that appear in the mean and fluctuating enstrophy fields dramatically increases. In fact, we observe a transition from large-scale coherent structures at low and negative  $A$  to fine-scale complex structures at high  $A$ . In the last frame in each of Figs. 46-49, the mean enstrophy is strongly peaked in the vortex core, and the strongest fluctuations appear there as well, with very little activity in the enstrophy fields outside this small region. In Figs. 50-53, however, examining the last frame in each case, we

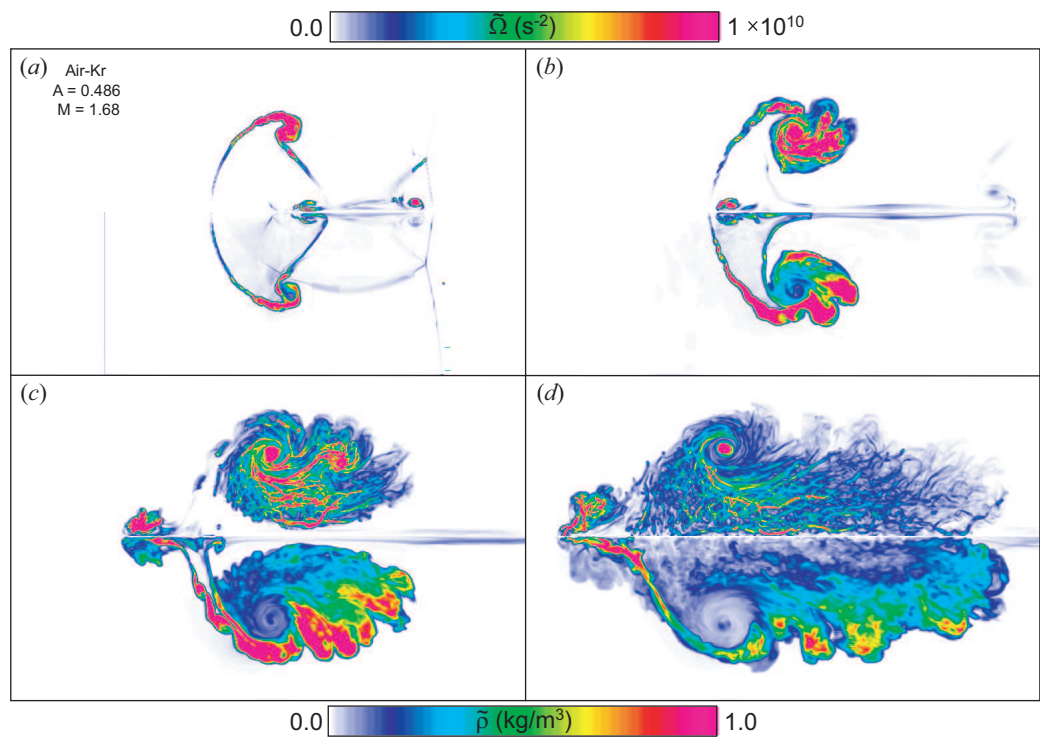


Figure 51: R.m.s. fluctuating enstrophy (top) and density (bottom) fields for the air-Kr,  $M = 1.68$  scenario. Dimensionless times  $tu'_1/R$  are (a) 2.0, (b) 4.1, (c) 8.0, and (d) 15.0. Incident shock wave propagation is left-to-right.

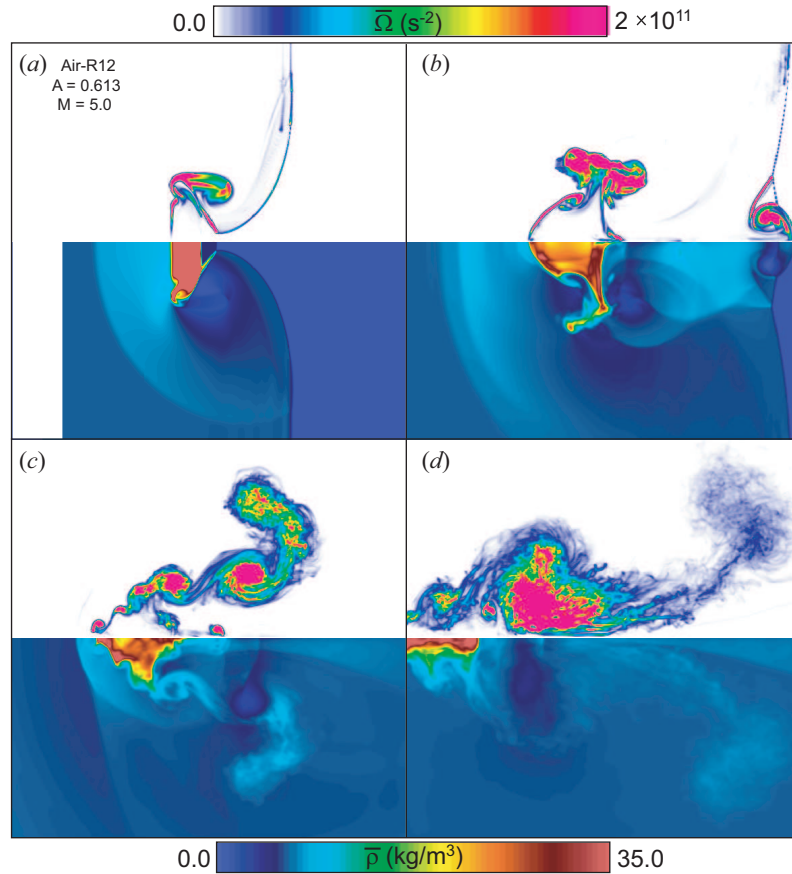


Figure 52: Azimuthally averaged enstrophy (top) and density (bottom) fields for the air-R12,  $M = 5$  scenario. Dimensionless times  $tu'_1/R$  are (a) 2.0, (b) 4.0, (c) 7.9, and (d) 14.9. Incident shock wave propagation is left-to-right.

see that a highly complex enstrophy field develops, and although it is also strongly peaked in the vortex core, a very large region of strong, disordered, filamentary enstrophy fluctuations also appears as a long plume trailing the vortex ring.

A similar transition is apparent in the density fields. For  $A < 0.2$  (air-helium and nitrogen-argon, Figs. 47 and 49), the strongest density fluctuations are localized and confined mainly to the interface in regions that are under severe stretching or straining. For  $A > 0.2$ , however (air-krypton and air-R12, Figs. 51 and 53), significant density

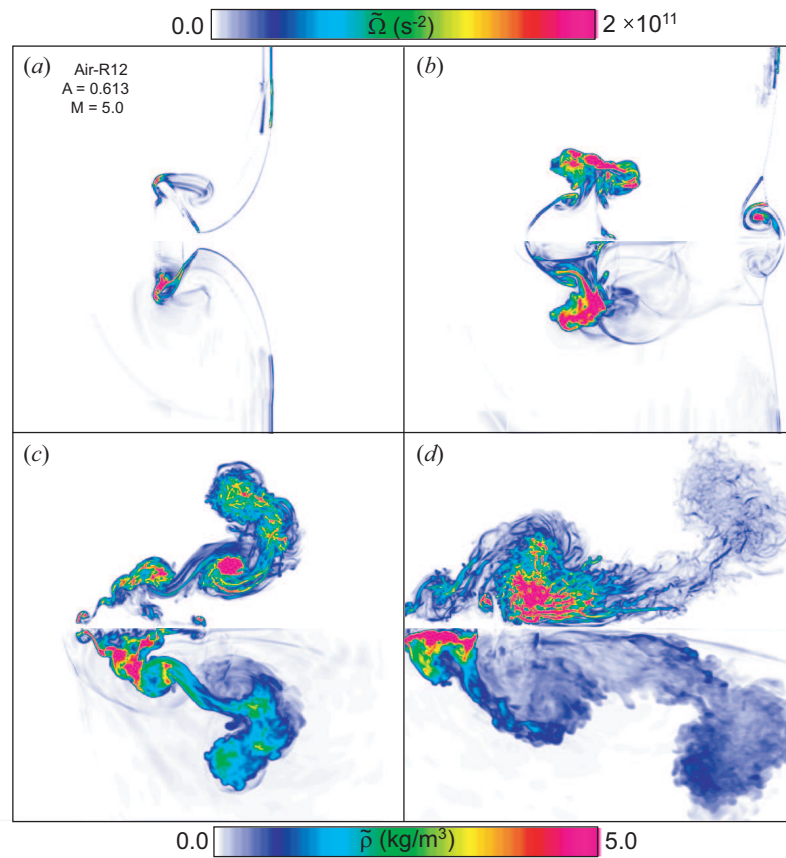


Figure 53: R.m.s. fluctuating enstrophy (top) and density (bottom) fields for the air-R12,  $M = 5$  scenario. Dimensionless times  $tu'_1/R$  are (a) 2.0, (b) 4.0, (c) 7.9, and (d) 14.9. Incident shock wave propagation is left-to-right.

fluctuations appear in a large volume within the downstream plume. This transition from order to disorder, and from highly localized to diffuse and broadly distributed turbulent and non-axisymmetric effects, is a manifestation of the “weak” mixing transition discussed in Sec. 5.1.3, due to the increased  $Re$  in these cases with higher initial bubble-to-ambient density contrast. It is also interesting to note that the filamentary structures appearing in the late-time, high- $A$  enstrophy fields here have also been observed in three-dimensional MILES simulations for decaying supersonic turbulence [83] and transition to turbulence in free square and rectangular jets [33].

The fluctuations in enstrophy and density seen in Figs. 46-53 reach a visible peak in intensity shortly after shock passage. At this time, fluctuations in both of the two variables are concentrated on the interface in the immediate region of baroclinic vorticity deposition. After this peak, the region where non-axisymmetric and turbulent fluctuations are significant gradually expands and increases in complexity, while the magnitude of the fluctuation simultaneously gradually decreases. Thus we see that turbulent effects in these flowfields are inherently transient, maintained only by the input of energy by the passage of the incident shock wave and secondary waves. Although the turbulent effects thus begin to decay very shortly after shock passage, their decay is slowed in the  $A > 0.2$  cases by the appearance of secondary shock waves resulting from strong shock diffraction and focusing. These waves are visible as curved, expanding fronts in the fluctuating density fields in Fig. 51(a) and 53(b). These waves are curved and pass over regions of the interface that have been strongly deformed, so that the associated baroclinic vorticity generation introduces further complexity to the vorticity field that is not present in the air-helium and air-nitrogen cases, as can be seen in subsequent frames in these two figures. Thus, although turbulent effects are inherently transient

in these flows, the baroclinic mechanism driving their development has a very different time history for different gas combinations, due to complex nonlinear-acoustic effects, so that in some cases, turbulent effects are much more intense and longer-lived.

As an aside, some unintended numerical artifacts are visible in the enstrophy fields in Figs. 52(a) and 53(a). A small region of vortical activity just behind the shock front (well outside the bubble region) is visible. This arises because of the unintended de-refinement of this portion of the shock wave for one to two timesteps during the simulation. Such effects can be avoided by tuning AMR settings in the code, but since this region does not interact with the bubble, and because of the inevitable increase in computational cost associated with lower refinement thresholds, such measures are forgone here.

### 5.1.6 Turbulence intensity

As way of directly measuring the overall strength of non-axisymmetric and turbulent effects illustrated in Figs 46-53, we compute trends in the volume-averaged r.m.s. fluctuation from the azimuthal mean,  $\langle \check{\Phi}(t) \rangle$ , in the bubble-fluid region. These measurements are performed for the density field  $\rho(x, y, z, t)$ , and the enstrophy field  $\Omega(x, y, z, t) = ||\boldsymbol{\omega}(x, y, z, t)||^2$ , using the expression in Eq. 5.10. (Because of the large size of the datasets here, however, the bin spacing for this operation is increased to  $\Delta/0.8$ , so that the measurements could be performed robustly. All other measurements shown in this chapter use a bin spacing equal to  $\Delta$ .) The r.m.s. fluctuation is then normalized by an appropriate scaling factor  $\Phi_0$ . For the density fluctuations, we use the bubble-fluid density obtained from the one-dimensional gasdynamics analysis,  $\rho_2''$ . For the enstrophy fluctuations, we use an enstrophy scale  $\Omega_0$  based on the vorticity at the boundary between shocked bubble fluid and shocked ambient fluid in the simulations:

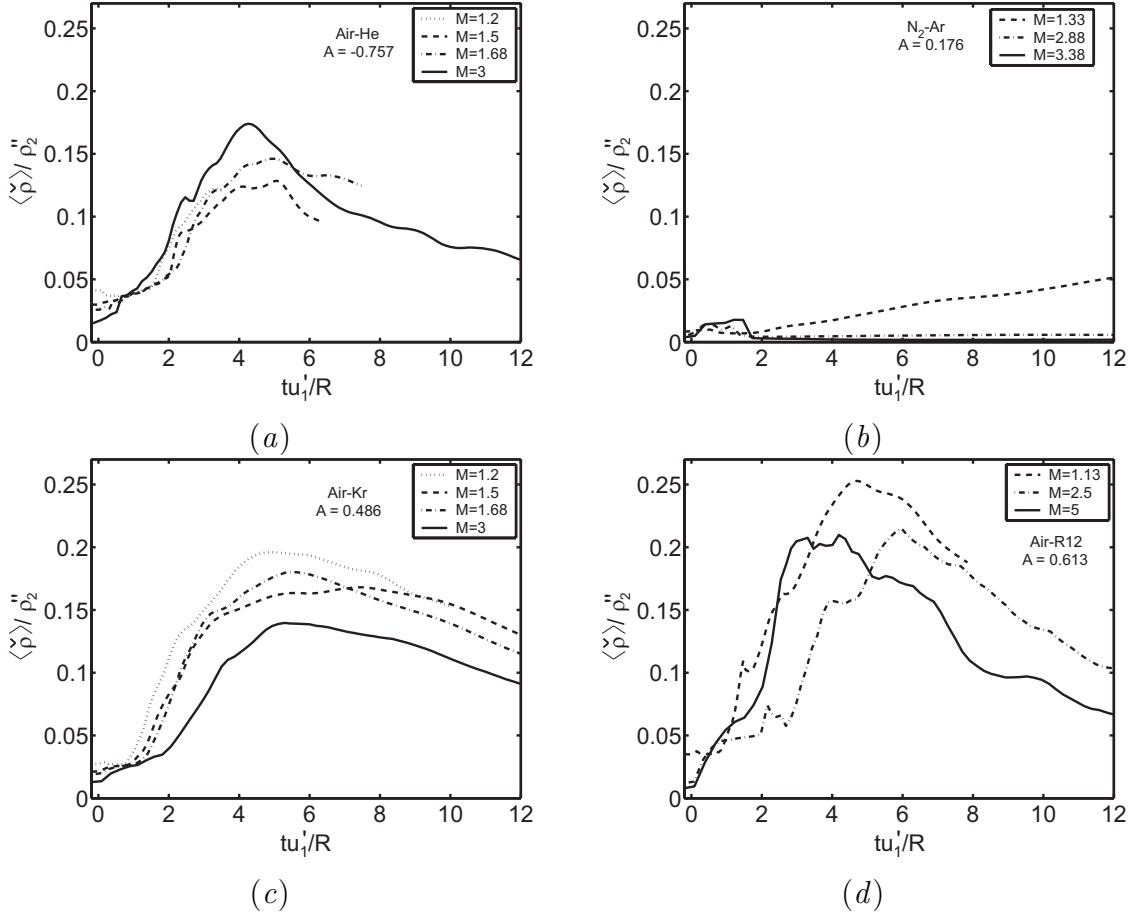


Figure 54: Trends in the volume-averaged r.m.s. density fluctuation from the azimuthal mean obtained using Eq. 5.10, normalized by the one-dimensional gasdynamics bubble-fluid density  $\rho_2''$ : (a) air-He, (b) N<sub>2</sub>-Ar, (c) air-Kr, (d) air-R12.

$$\Omega_0 = \left( \frac{u'_2 - u'_1}{\Delta} \right)^2. \quad (5.13)$$

where  $\Delta$  is the mesh spacing on the highest AMR level.

The normalized trends in the r.m.s. fluctuation intensities for density and enstrophy for all 14 scenarios are shown in Figs. 54-55. We make several observations from the

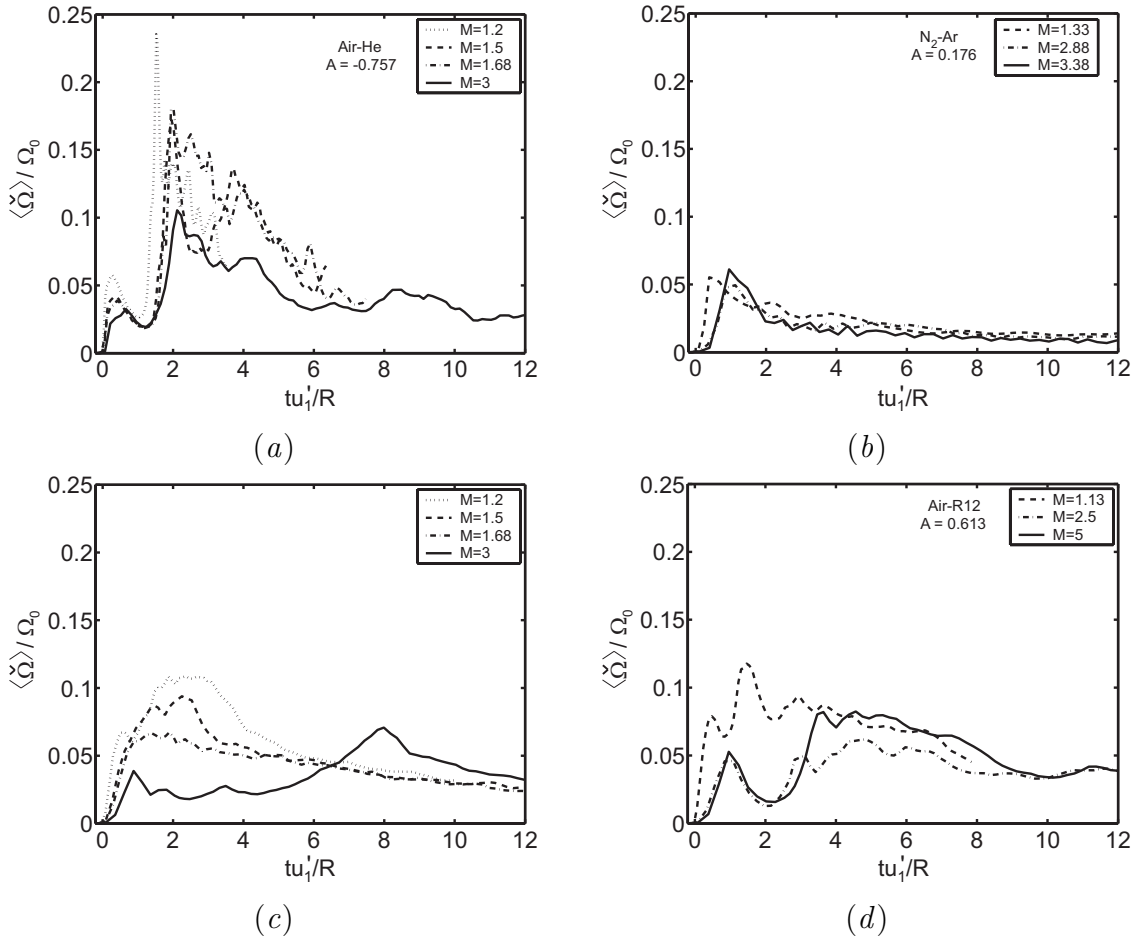


Figure 55: Trends in the volume-averaged r.m.s. enstrophy fluctuation from the azimuthal mean obtained using Eq. 5.10, normalized by the estimated enstrophy scale  $\Omega_0$  from Eq. 5.13: (a) air-He, (b)  $N_2\text{-Ar}$ , (c) air-Kr, (d) air-R12.

trends shown here. First, it should be noted that these trends are plotted on the dimensionless timescale  $tu'_1/R$ , where  $u'_1$  is the post-shock ambient flow speed. This timescale provides the best collapse of the data shown, which was not found with timescalings based on either the incident or transmitted shock wave speed. Therefore, although other timescales are known to be more appropriate for other aspects of shock-bubble interaction flowfields (as discussed in Sec. 4.1), this timescale will be used henceforward for the various time-dependent turbulence diagnostics that are applied here.

From these trends in the intensity of r.m.s. density and enstrophy fluctuations, we note that in general, the magnitude of the fluctuations increases dramatically during the initial transient phase associated with the passage of the initial shock wave and secondary waves over the bubble-fluid region. For density, fluctuations from the azimuthal mean pass through a maximum at approximately  $tu'_1/R = 5$ , then gradually decay to pre-shock levels. (The exception to this is the nitrogen-argon,  $M = 1.33$  case, which shows an unexplained, anomalous linear increase in density fluctuation intensity even at very late times.) For enstrophy, the peak generally occurs slightly earlier, at approximately  $tu'_1/R = 2$ , and the decay after the peak is less monotonic than in the density. This indicates the influence of secondary baroclinic sources of vorticity.

In comparing the relative intensity of fluctuations for different Mach numbers and gas combinations, we note that the strength of density fluctuations correlates well with the magnitude of the Atwood number. The air-R12 and air-helium cases show the strongest density fluctuations, while the nitrogen-argon cases show the weakest. Further, the temporal duration of non-axisymmetric density fluctuations is notably greater for all of the cases with  $|A| > 0.2$  than for the nitrogen-argon scenarios. We observe a similar though weaker correlation with  $A$  in the enstrophy fluctuations in Fig. 55. Enstrophy

fluctuations for  $|A| < 0.2$  are weaker and shorter-lived than for  $|A| > 0.2$ . The strongest enstrophy fluctuations are found in the air-helium scenarios, which also have the highest Atwood number magnitude.

As for the variation in intensities of turbulent fluctuation with the Mach number, we see that, except in a few notable cases, the evolution of the intensities  $\langle \check{\rho} \rangle$  and  $\langle \check{\Omega} \rangle$  is very roughly self-similar with respect to the Mach number, to within a factor of about 2, under the normalizations using  $\rho_2''$  and  $\Omega_0$  and the timescaling based on  $u_1'$ . This indicates that, although the Atwood-number dependence has a very complex and nonlinear character, and is itself time-dependent even on a dimensionless timescale, the Mach-number dependence may be expressed in the form of a simple scaling factor, for most of the cases here.

As a more general observation, in Figs. 54-55, we note that the maximum intensity of non-axisymmetric fluctuations from the azimuthal mean, as a ratio of the selected scaling factor, is generally on the order of 0.05 to 0.2. This indicates that non-axisymmetric fluctuations are significant, but do not dominate the flowfield. Thus, we may expect axisymmetric coherent structures to remain present in the flowfield despite the development of turbulence-like features, and we may expect noticeably more intense turbulence-like features for  $|A| > 0.2$  than for  $|A| < 0.2$ , based on these data.

Qualitatively, however, what we have observed in the mean and fluctuating fields shown in Sec. 5.1.5 is that intense turbulence-like effects are absent for the  $A < 0$  scenarios, even though the measured intensity of fluctuations is large. This suggests that the apparent transition, based on qualitative analysis of the simulated flowfields, is  $A = 0.2$ , not  $|A| = 0.2$ . The experimental data discussed in Sec. 2.3.2 and in Refs. [87] and [88] also show a notable lack of strong turbulence-like features for the air-helium case,

even at high  $M$ . Instead of fine-scale, disordered motion, we observe the development of long-lived vortex rings. Thus, we speculate that the divergent nature of shock refraction for  $A < 0$  precludes the development of the same complex vortical features that appear for  $A > 0.2$ , and that turbulent effects may be expected to be inherently weaker in divergent geometry.

One further discrepancy between the volume-averaged trends in turbulence intensity and the mean and fluctuating fields shown in the previous section is in the magnitude of the enstrophy fluctuations. In Fig. 55, the normalized enstrophy fluctuation  $\bar{\Omega}/\Omega_0$  reaches values no higher than 0.25. In Figs. 46-53, however, we observe enstrophy fluctuations that are as great or greater in magnitude than the local mean enstrophy. This reflects the ambiguity in the choice of the normalizing enstrophy scale  $\Omega_0$ . Here we have chosen an enstrophy scale based on the greatest possible velocity gradient that can be predicted from one-dimensional gasdynamics. Although this provides a consistent basis on which to compare trends in the enstrophy from different gas combinations and shock wave strengths, it clearly minimizes the apparent strength of the enstrophy fluctuations.

### 5.1.7 Radial and axial fluctuation profiles

From the fluctuating density and enstrophy fields shown in Figs. 47, 49, 51, and 53, we extract radial and axial profiles of fluctuations from the azimuthal mean. This is done by performing an additional averaging operation on the two-dimensional, azimuthally averaged fields  $\tilde{\Phi}(r, y)$ , in the radial or axial direction. The data are thus reduced to one-dimensional radial profiles of axially averaged fluctuations  $\bar{\tilde{\Phi}}(r)$ , or axial profiles of

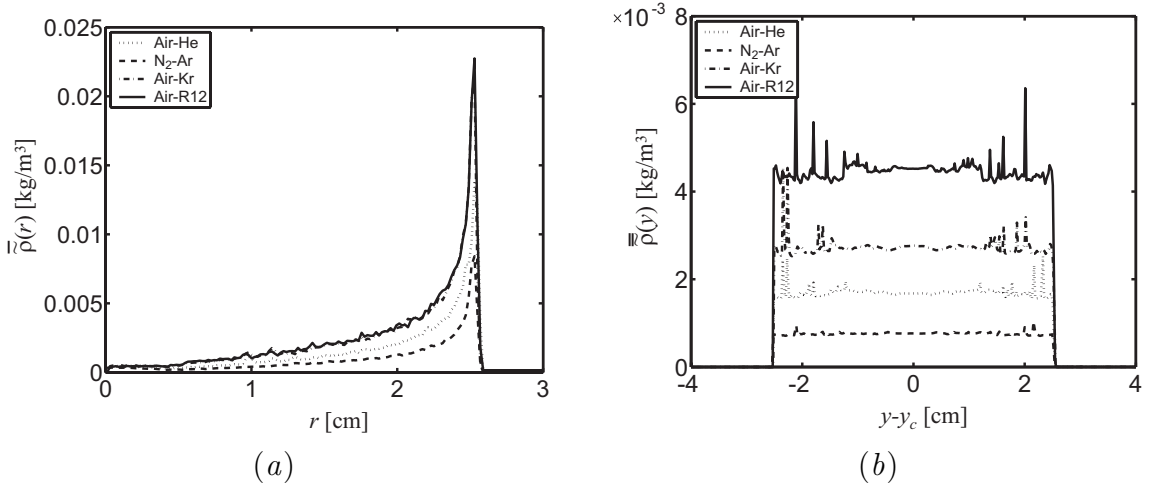


Figure 56: Radial (a) and axial (b) profiles of density fluctuations relative to the azimuthal mean in the initial condition ( $t=0$ ), for each of the four gas combinations, obtained using Eqs. 5.11 and 5.12.

radially averaged fluctuations  $\bar{\Phi}(y)$ . (Note that the double-bar notation merely distinguishes radial averaging from axial averaging, and does not denote nested averages.) These reductions are performed using the averaging expressions in Eqs. 5.11 and 5.12, within a box whose dimensions  $L_y, L_r$  are determined by the maximum axial and radial extents of the bubble-fluid region over all time. (An overall view of the data reduction procedure is shown in Fig. 45.)

In order to characterize the density perturbation associated with the interfacial transition layer in the initial condition, which is the seed for all of the observed post-shock development of non-axisymmetric and turbulent effects, we extract from the initial condition the radial and axial profiles of density fluctuations with respect to the azimuthal mean, and plot them in Fig. 56. We see in Fig. 56(a) that for the radial direction, the strength of the density perturbation is strongly peaked at the limb of the bubble, while it tends to zero on-axis. This reflects an inherent feature of the azimuthal averaging

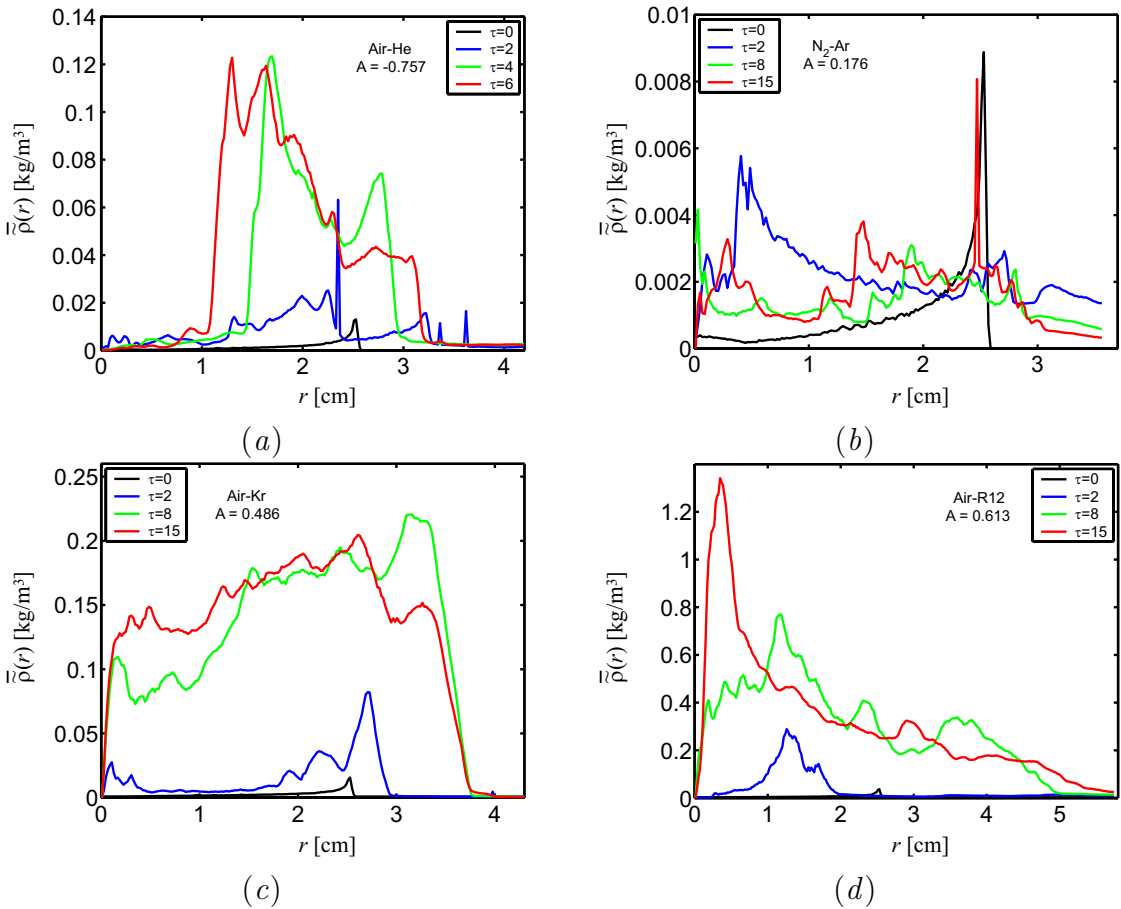


Figure 57: Profiles in  $r$  of the  $y$ -averaged r.m.s. fluctuations in density from the azimuthal mean, computed using Eq. 5.11: (a) air-He,  $M=1.68$ ; (b) N<sub>2</sub>-Ar,  $M=3.38$ ; (c) air-Kr,  $M=1.68$ ; (d) air-R12,  $M=5$ . Note that  $\tau = tu'_1/R$  here.

scheme: since the number of samples in the azimuthal direction tends to unity as  $r \rightarrow 0$  for these quarter-symmetry simulations, then also  $\tilde{\Phi}(r, y) \rightarrow 0$  as  $r \rightarrow 0$ . This should not be interpreted as an indication of the absence of turbulent effects near the axis, but only as a property of the present simulations and of this particular type of diagnostic for turbulent effects.

The axial profiles in Fig. 56(b) provide a clearer picture of the strength of the initial density perturbation. Here we see that the perturbation to the density field due to the

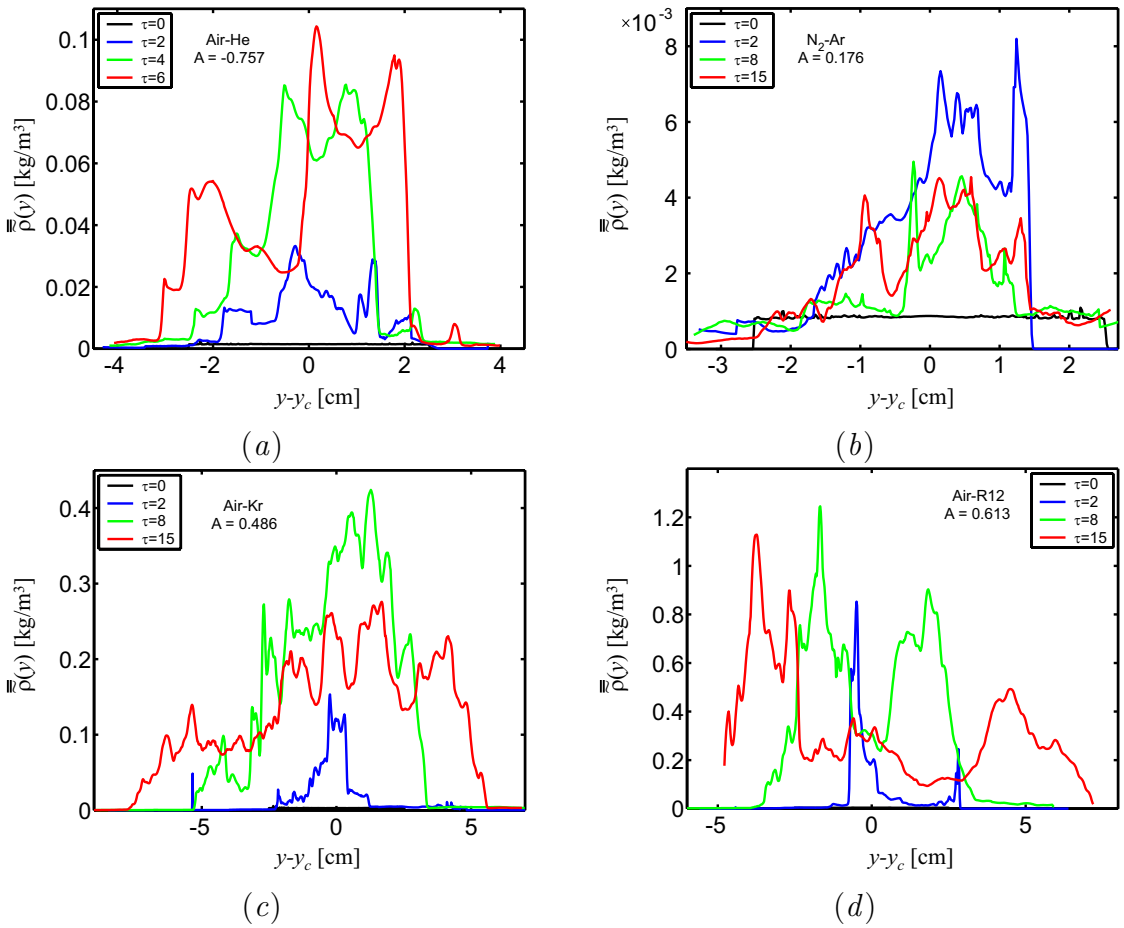


Figure 58: Profiles in  $y$  of the  $r$ -averaged r.m.s. fluctuations in density from the azimuthal mean, computed using Eq. 5.12: (a) air-He,  $M=1.68$ ; (b) N<sub>2</sub>-Ar,  $M=3.38$ ; (c) air-Kr,  $M=1.68$ ; (d) air-R12,  $M=5$ . Note that  $\tau = tu'_1/R$  here.

interfacial transition layer on the surface of the bubble gives a nearly uniformly distributed density perturbation whose magnitude is on the order of 1/1000 of the ambient density. We can also see that the magnitude of the initial density fluctuation is greatest for the air-R12 scenario and least for the nitrogen-argon scenario.

Radial and axial profiles of fluctuations in a number of variables have been extracted for every scenario as a part of the present study. Here, we show representative plots of the radial and axial fluctuation profiles of density ( $\rho$ ) and enstrophy ( $\Omega$ ), for the four scenarios whose evolution is depicted in Figs. 23-26 and in Figs. 46-53. Profiles are shown for a series of fixed dimensionless times  $\tau$  for each scenario, where  $\tau$  here is given by  $\tau = tu'_1/R$ , and  $u'_1$  is the post-shock ambient flow speed (see Table 3). Axial profiles are plotted on a re-centered spatial scale  $y - y_c$ , where  $y_c$  is the  $y$ -component of the centroid of the bubble-fluid region.

Radial and axial profiles of density fluctuations for these four representative scenarios are shown in Figs. 57 and 58. Although the Mach number is not uniform across these four representative scenarios, the rough similarity across Mach numbers at fixed  $A$  of trends in  $\langle \tilde{\rho} \rangle$  shown in Fig. 54 suggests that we may consider these plots, loosely, as representative of behavior at other Mach numbers for the same gas combination. We note, again, that fluctuations tend to zero for  $r \rightarrow 0$ , by construction. The fluctuation profiles and their evolution in time are highly Atwood-number dependent, as we can see in these plots. Even though the Mach number is very high ( $M = 3.38$ ) in the nitrogen-argon scenario shown in Figs. 57(b) and 58(b), the strength of density fluctuations is consistently lower than all of the other scenarios shown, both in terms of their physical magnitude and in terms of their relative magnitude with respect to the initial perturbation. The increase in the magnitude of density fluctuations is most dramatic in the air-R12 cases shown

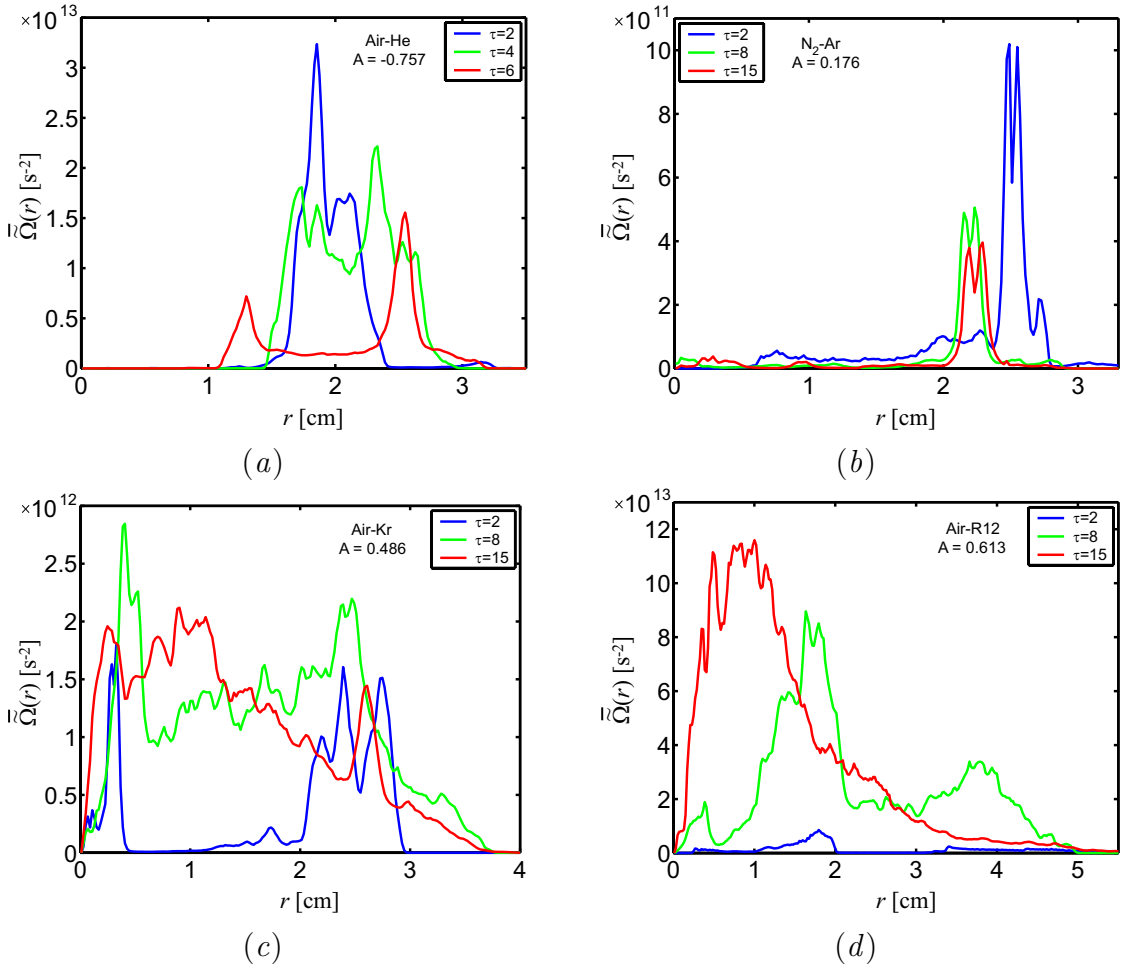


Figure 59: Profiles in  $r$  of the  $y$ -averaged r.m.s. fluctuations in enstrophy from the azimuthal mean, computed using Eq. 5.11: (a) air-He,  $M=1.68$ ; (b)  $N_2$ -Ar,  $M=3.38$ ; (c) air-Kr,  $M=1.68$ ; (d) air-R12,  $M=5$ . Note that  $\tau = tu'_1/R$  here.

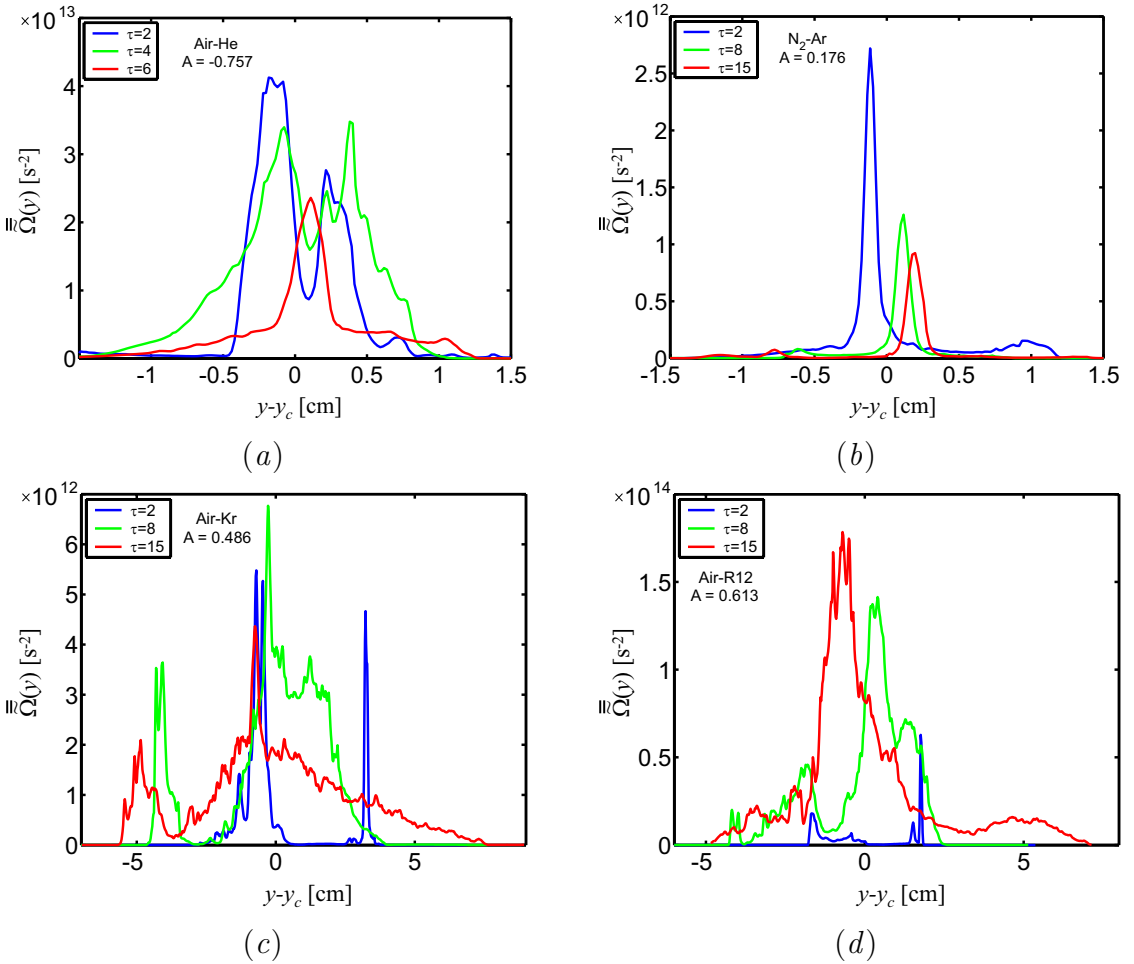


Figure 60: Profiles in  $y$  of the  $r$ -averaged r.m.s. fluctuations in enstrophy from the azimuthal mean, computed using Eq. 5.12: (a) air-He,  $M=1.68$ ; (b)  $N_2$ -Ar,  $M=3.38$ ; (c) air-Kr,  $M=1.68$ ; (d) air-R12,  $M=5$ . Note that  $\tau = tu'_1/R$  here.

in Figs. 57(*d*) and 58(*d*). Also noticeable is the greater extent to which the fluctuating region is spread in the axial direction for the high-*A* scenarios.

Radial and axial profiles of enstrophy fluctuations are shown in Figs. 59 and 60. In Fig. 59, we observe a clear difference between the air-helium and nitrogen-argon ( $A < 0.2$ ) scenarios, and the air-krypton and air-R12 ( $A > 0.2$ ) scenarios. In the former, large fluctuations in the enstrophy remain confined to regions near the outer radius (“limb”) of the bubble, as seen in Fig. 59(*a-b*), even at late times. This indicates the formation of a stable, long-lived vortex ring; although Widnall-type [108] fluctuations appear in the vortex ring, their growth and spread is suppressed. In the latter, high-*A* cases, however, shown in Fig. 59(*c-d*), enstrophy fluctuations appear on-axis at early time due to the formation of upstream and downstream axial jets, and enstrophy fluctuations spread to fill the entire radial extent of the bubble region by  $tu'_1/R = 8$ . This indicates that at high *A*, bending-mode instabilities in the vortex ring are too strong to be suppressed, so that a complex field of disordered vortex filaments fills the bubble region at late times, as seen visibly in Figs. 51(*d*) and 53(*d*).

A similar effect is seen in the axial profiles of enstrophy fluctuations shown in Fig. 60. For  $A < 0.2$ , enstrophy fluctuations remain confined to a relatively small region, concentrated around the primary vortex ring location. Furthermore, as time proceeds, this region actually contracts, as the vortex ring stabilizes after the departure of the shock wave from the bubble region. At higher Atwood numbers, in the air-krypton and air-R12 scenarios, the region of complex non-axisymmetric vortical features extends over a much larger region in the streamwise direction, which continues to grow in time, rather than contracting, long after the passage of the initial shock wave. Thus, we conclude that there are fundamental differences in the underlying vorticity dynamics for shock-bubble

interactions in these two regions of the parameter space.

### 5.1.8 Fluctuation power spectra

As a further means of characterizing the distribution of non-axisymmetric effects among the different scales present in the simulated flowfields, the radial and axial profiles in fluctuating quantities shown in Figs. 57-60 are Fourier-transformed to generate power spectra for non-axisymmetric fluctuations. An even extension is first applied to the profiles  $\tilde{\Phi}(r, t)$  and  $\tilde{\Phi}(y, t)$  to make them periodic. Then power spectra then are computed as

$$\breve{\tilde{\Phi}}(k_r, t) = \left[ \frac{1}{2\pi} \int_{-\infty}^{\infty} \tilde{\Phi}(r, t) e^{-ik_r r} dr \right]^2 \quad (5.14)$$

and

$$\breve{\tilde{\Phi}}(k_y, t) = \left[ \frac{1}{2\pi} \int_{-\infty}^{\infty} \tilde{\Phi}(y, t) e^{-ik_y y} dy \right]^2. \quad (5.15)$$

In practice,  $\breve{\tilde{\Phi}}(k_r, t)$  and  $\breve{\tilde{\Phi}}(k_y, t)$  are obtained using a fast Fourier transform, which yields complex coefficients for the Fourier series representation of the profiles  $\tilde{\Phi}$  and  $\tilde{\Phi}$ . The moduli of these coefficients constitute the coefficients for the discrete cosine series representation of  $\tilde{\Phi}$  and  $\tilde{\Phi}$ , which can be squared and plotted against the wavenumber  $k_r$  or  $k_y$  to produce power spectra for fluctuations in the variable  $\Phi$ .

In the present study, however, we have found that directly plotting these coefficients yields a noisy spectrum from which little meaningful information can be obtained. Therefore, a four-element averaging filter is applied to the power spectra  $\breve{\tilde{\Phi}}(k_r, t)$  and  $\breve{\tilde{\Phi}}(k_y, t)$ , to produce a smoother spectrum (the smoothed spectrum has one element for every four

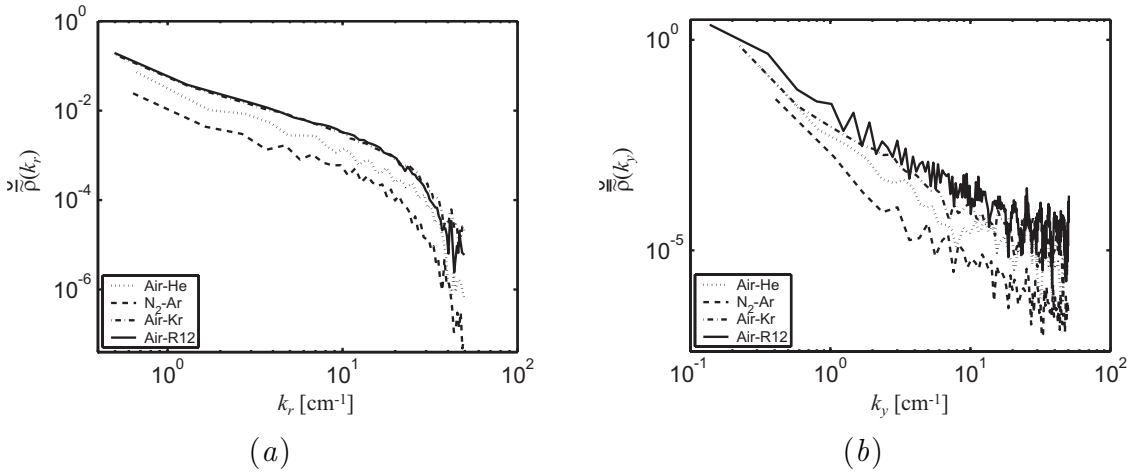


Figure 61: Power spectra in the radial and axial wavenumbers for r.m.s. fluctuations in density from the azimuthal mean in the initial condition ( $t=0$ ), computed using Eqs. 5.14 and 5.15.

elements in the original spectrum).

The smoothed density fluctuation power spectra  $\tilde{\rho}(k_r, t)$  and  $\tilde{\rho}(k_y, t)$  for the initial condition used in these simulations for each gas combination are shown in Fig. 61. In these plots, we see that the interface definition used for these simulations (see Sec. 3.1.5) results in the presence of significant spectral content across the full range of wavenumbers in the density fluctuation power spectra. The radial and axial spectra differ strongly in their curvature because of the strong peak in the radial profile of density fluctuations at the limb of the bubble, which introduces a bulge in the radial spectrum in Fig. 61(a) around  $k_r = 10 \text{ cm}^{-1}$ .

Smoothed radial and axial power spectra for fluctuations in density ( $\tilde{\rho}$ ) are shown, for the four representative scenarios considered above, in Figs. 62 and 63, including spectra from each of a series of dimensionless times in each scenario, labeled by  $\tau = tu'_1/R$ . A line indicating the Kolmogorov  $k^{-5/3}$  scaling is included in each plot for reference, although

it is not clear whether power spectra for density fluctuations should follow such a scaling in the context of shock-bubble interactions. In each of these sets of spectra we note that fluctuations in the density are intensified across all wavenumbers during shock passage, by at least an order of magnitude in all but the nitrogen-argon scenario. But in most cases, the immediate intensification between  $\tau = 0$  and  $\tau = 2$  appears strongest at the larger scales (smaller  $k$ ). Further, as time progresses, the high-wavenumber content of the spectra generally diminishes in magnitude relative to the low-wavenumber region, particularly in the axial spectra in Fig. 63. This corresponds to the gradual decay of strong density gradients in the flow as the fluids mix under the influence of strong shear and vortical effects.

The density fluctuation spectra generally do not follow  $k^{-5/3}$  scaling; instead, the density fluctuation spectra fall off with increasing wavenumber faster than  $k^{-5/3}$  in most cases. The spectra are remarkably similar across the different Atwood numbers, except for the overall magnitude of the spectra, and for the factor by which the fluctuation spectra increase after shock passage, which is strongly sensitive to  $A$ . Overall, however, we note that the axial power spectra generally appear more consistent in their shape, and exhibit fewer irregularities than the radial spectra, indicating that the  $r$ -direction is a more useful direction for averaging, and the  $y$ -direction for generating power spectra.

Similarly, smoothed radial and axial power spectra for fluctuations in enstrophy ( $\tilde{\Omega}$ ) are shown in Figs. 64 and 65 for the same four scenarios. Here we see much stronger differences in the spectral shapes between the various gas combinations. For the nitrogen-argon scenario, and, to a lesser extent, the air-helium scenario, distinctive peaks and bulges are visible in the enstrophy-fluctuation spectra. These features do not appear as strongly in the air-krypton and air-R12 spectra, which generally have a smoother

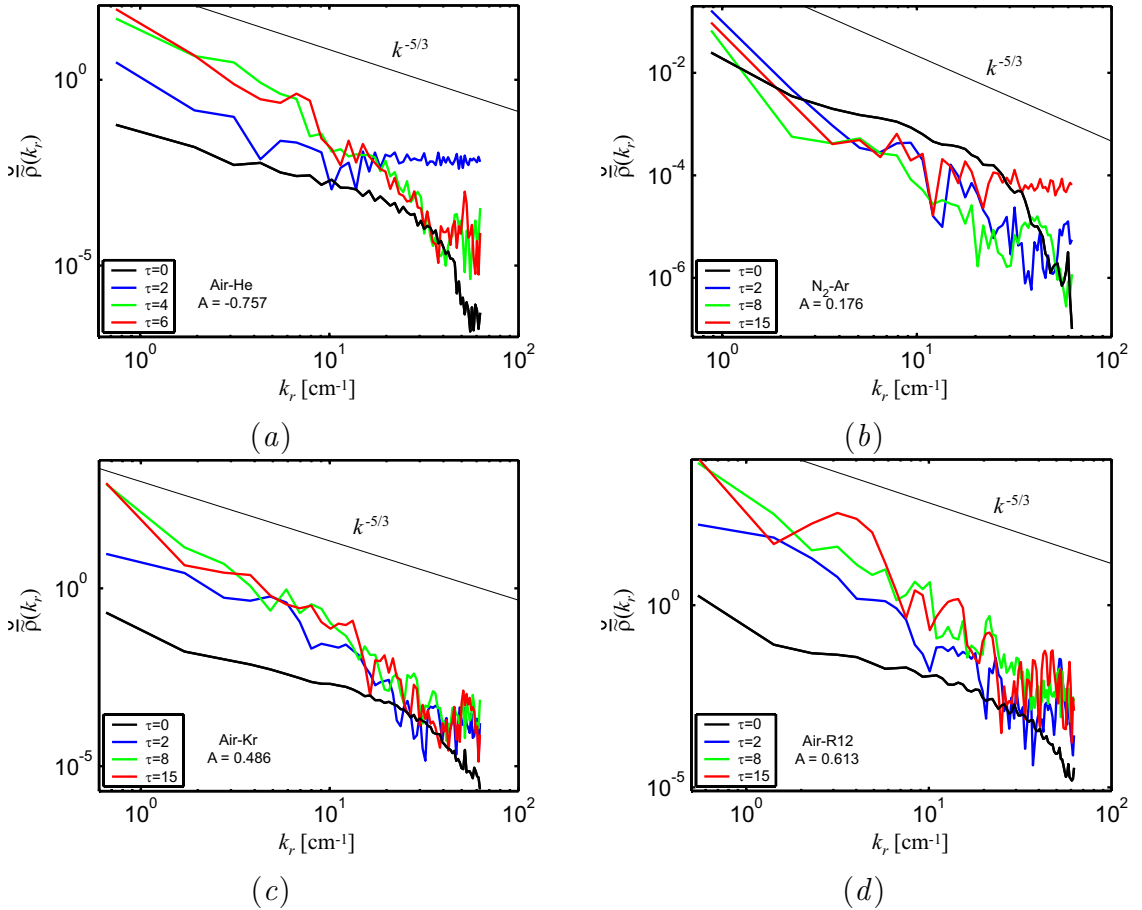


Figure 62: Power spectra in the radial wavenumber for r.m.s. fluctuations in density from the azimuthal mean, computed using Eq. 5.14: (a) air-He,  $M=1.68$ ; (b) N<sub>2</sub>-Ar,  $M=3.38$ ; (c) air-Kr,  $M=1.68$ ; (d) air-R12,  $M=5$ . Note that  $\tau = tu'_1/R$  here.

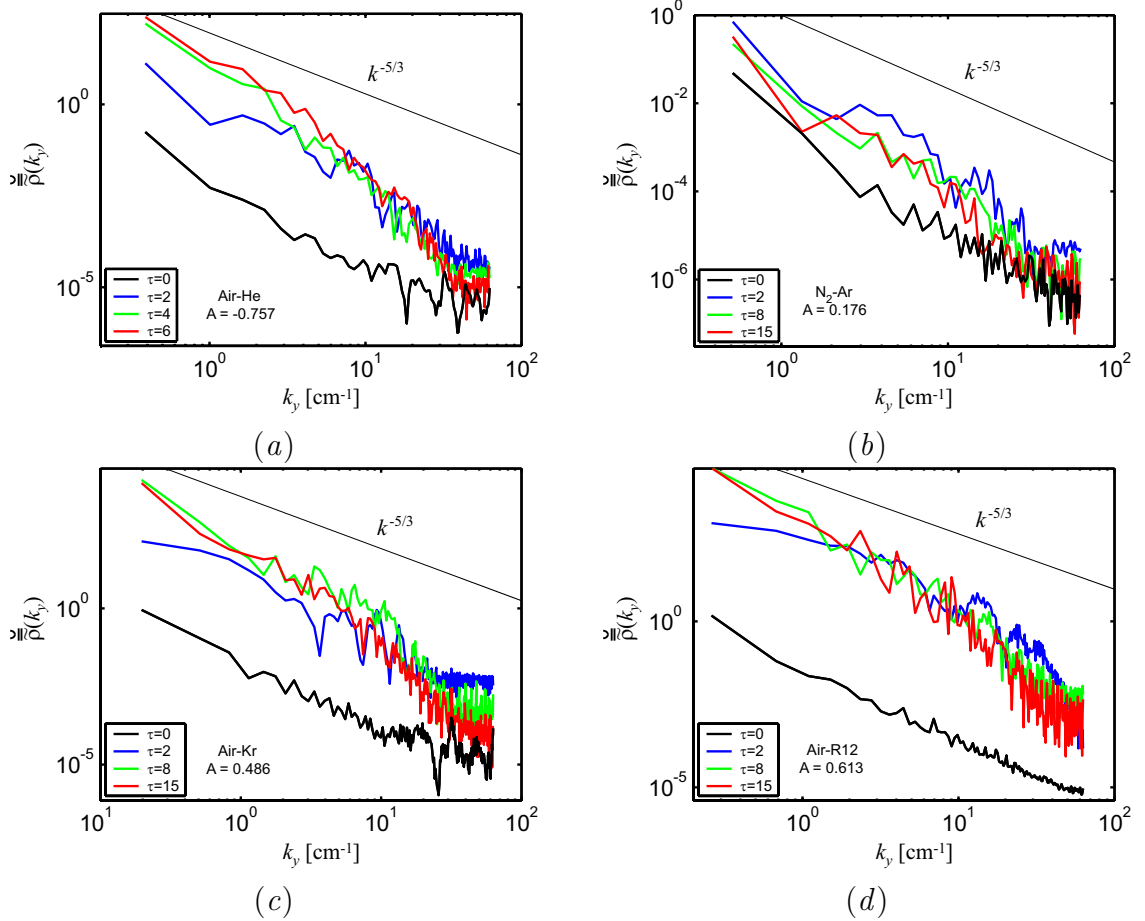


Figure 63: Power spectra in the axial wavenumber for r.m.s. fluctuations in density from the azimuthal mean, computed using Eq. 5.15: (a) air-He,  $M=1.68$ ; (b) N<sub>2</sub>-Ar,  $M=3.38$ ; (c) air-Kr,  $M=1.68$ ; (d) air-R12,  $M=5$ . Note that  $\tau = tu'_1/R$  here.

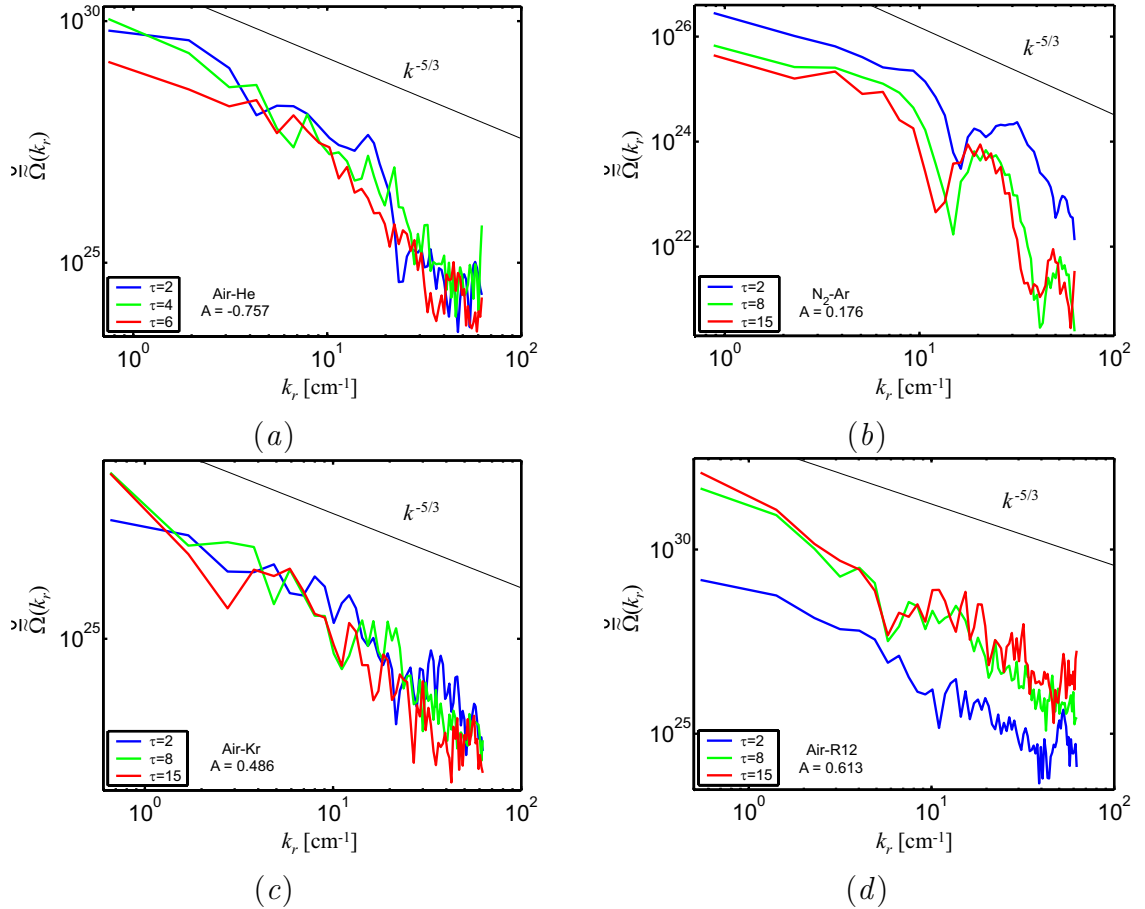


Figure 64: Power spectra in the radial wavenumber for r.m.s. fluctuations in enstrophy from the azimuthal mean, computed using Eq. 5.14: (a) air-He,  $M=1.68$ ; (b) N<sub>2</sub>-Ar,  $M=3.38$ ; (c) air-Kr,  $M=1.68$ ; (d) air-R12,  $M=5$ . Note that  $\tau = tu'_1/R$  here.

shape. This difference is a manifestation of the presence of long-lived, stable vortical structures in the air-helium and nitrogen-krypton scenarios, discussed in Sec. 5.1.7. Because of strong secondary shock and rarefaction wave patterns passing through the bubble region at intermediate times, and because of the strength of non-axisymmetric vortex-bending mechanisms, such coherent structures give way to disordered motion and complex mixing regions in the high- $A$  scenarios, leading to a smoother spectrum of enstrophy fluctuations in those cases.

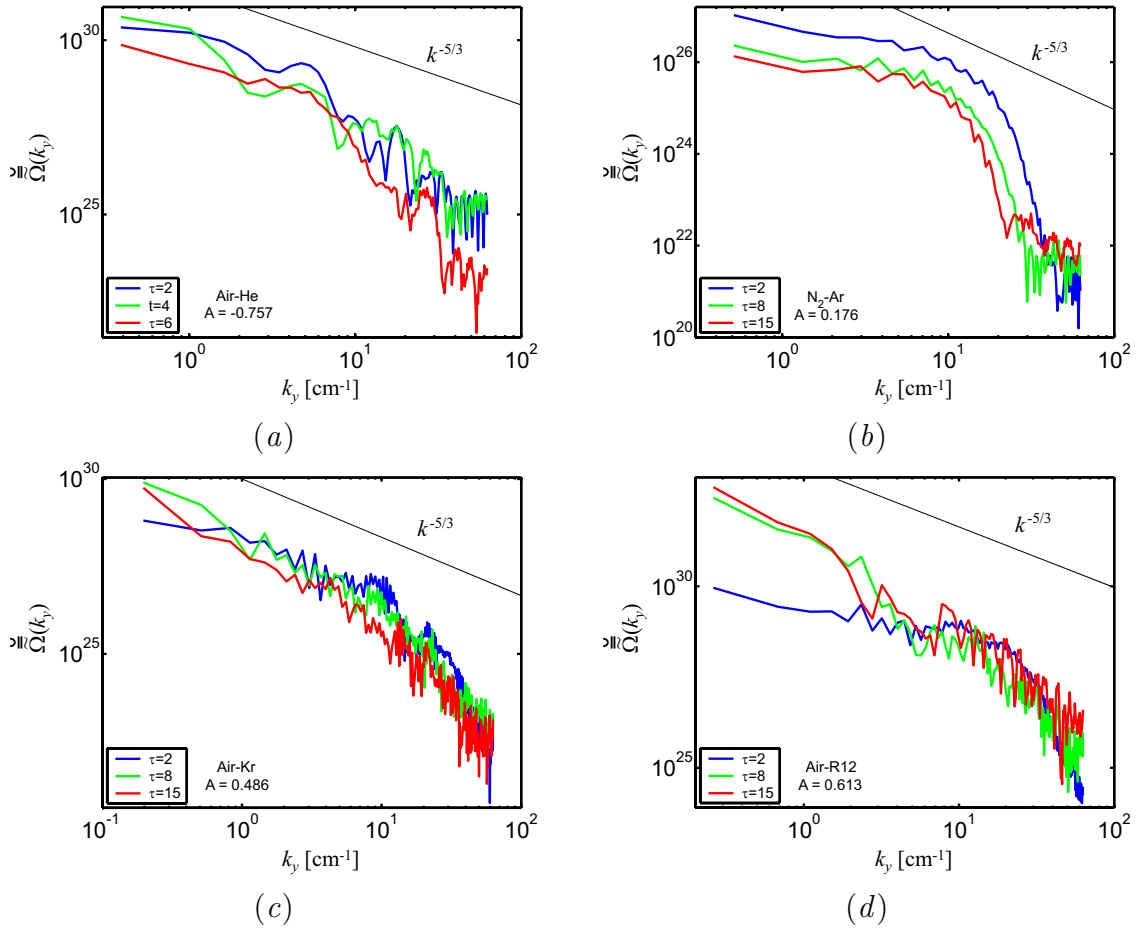


Figure 65: Power spectra in the axial wavenumber for r.m.s. fluctuations in enstrophy from the azimuthal mean, computed using Eq. 5.15: (a) air-He,  $M=1.68$ ; (b)  $N_2$ -Ar,  $M=3.38$ ; (c) air-Kr,  $M=1.68$ ; (d) air-R12,  $M=5$ . Note that  $\tau = tu'_1/R$  here.

In comparison to the density-fluctuation power spectra, the enstrophy-fluctuation spectra show a stronger tendency to follow the  $k^{-5/3}$  scaling. This is only true at the largest scales in the flow, however (smallest  $k$ ). At the smaller scales, the enstrophy fluctuation spectra, like the density fluctuation spectra, fall off with increasing  $k$  faster than  $k^{-5/3}$ . Further, in the nitrogen-argon scenario, the confinement of enstrophy fluctuations to a very small region in the core of the primary vortex ring results in an irregular, bulging spectral shape unlike those seen for the other gas combinations.

## 5.2 Mixing

Closely related to the non-axisymmetric and turbulent effects that develop in shock-bubble interactions is the mixing of the bubble fluid into the ambient medium. This is an inherently multi-scale process, with interface deformation on the largest scales causing the mutual interpenetration of the two fluid regions, eddies at the intermediate scales driving further intermingling, and, on the very smallest scales, the multifluid capturing scheme allowing cells containing fluid mixtures to appear on the interface. On all but the smallest scales, this process is driven by shock-induced vortical motion. The passage of the initial shock wave over the bubble, along with all of the subsequent secondary reflected, refracted and diffracted waves, leaves a complex field of vortex lines distributed throughout the flow. This vortical field initiates vigorous mixing and the growth of multi-scaled turbulent fluctuations in the flow, just described. At the smallest scales, however, it is the VOF multifluid capturing algorithm (see Sec. 2.1.5) that allows single-fluid cells to become mixture cells. In the MILES/ILES approach adopted in the numerical method used here (see Sec. 5.1.2), no explicit modeling is introduced for such

dissipative effects at the smaller scales, and we rely on the inherent numerical dissipation to capture mixing on the smallest scales. We therefore note, as have Latini *et al.* (2007) [57] and Schilling *et al.* (2007) [100], that caution must therefore be used in interpreting the results of these simulations in terms of “mixing.”

In any two-component flow involving two fluids that are initially segregated, the process of mixing involves two distinct processes: interpenetration and interdiffusion [23]. In the first, by mechanical means, the interface between the two fluids is strained, or the fluid regions are broken up into smaller bodies. This process does not change the local composition of the fluid at any point from its original pure state and thus cannot produce a uniform, homogeneous mixture, even with continuous mechanical driving. However, it increases the area of contact between the fluids. This enhances the effects of the other process, which may operate simultaneously, in which molecular diffusion acts irreversibly at the contact surface to neutralize differences of concentration between the neighboring regions. Interdiffusion thus produces a transition region where the fluid locally has a nonzero concentration of both fluids and may therefore be considered to be mixed on the molecular level.

In the present inviscid MILES simulations, only the mechanically-driven interpenetration process is simulated explicitly, as dissipative mechanisms operating on the molecular scales are neither resolved by the mesh nor explicitly modeled in the algorithm. However, we note that (1) the “effective viscous diffusion” in MILES and ILES simulations can be regarded as a surrogate for molecular interdiffusion [39, 57, 100], and (2) the interdiffusion process operates on contact surfaces whose topology is determined by mechanical effects that *are* resolved in the simulations. Therefore, we proceed with a brief discussion of mixing observed in these simulations by measuring three quantities

from the simulation datasets: (1) the overall intensity of fluctuations of the volume fraction  $f$  from the azimuthal mean, (2) the total volume of the mixture region, and (3) the “molecular mixing fraction” of Youngs (1991) [111]. The first is a measure of the action of the interpenetration process; the second and third characterize the local interdiffusion process. It should be noted that the discussion here is brief and in some ways incomplete.

### 5.2.1 Fluctuation intensity

The overall intensity of local fluctuations  $\tilde{f}(r, y)$  from the azimuthal mean bubble-fluid volume fraction is characterized here by using the azimuthal averaging scheme described in Sec. 5.1.4 (Eq. 5.7) to compute  $\tilde{f}(r, y)$ , and then using the expressions in Eqs. 5.8-5.10 to obtain the total volume-averaged fluctuation in the bubble fluid,  $\langle \tilde{f}(t) \rangle$ . This can be regarded as a measure of the total magnitude of the deformation of the interface in the azimuthal direction.

Plots of the quantity  $\hat{\tilde{f}}(t)$  for each of the 14 scenarios on the dimensionless timescale  $tu'_1/R$  are shown in Fig. 66. These plots indicate that the total azimuthal deformation of the interface reaches a maximum in all but the nitrogen-argon scenarios at approximately  $tu'_1/R = 4$ . The initial growth in the fluctuations is due the shock-induced instability of the interface, and the intensity of fluctuations decays after the maximum because of the relaxation of concentration gradients across the interface due to mixing. Several anomalous features appear in these plots, however. First, the fluctuations increase nearly linearly at later times in the nitrogen-argon simulations in Fig. 66(b), and the rate of increase is inversely proportional to the Mach number. This is most likely due to the fact that the post-shock Atwood number at the interface *decreases* with increasing Mach

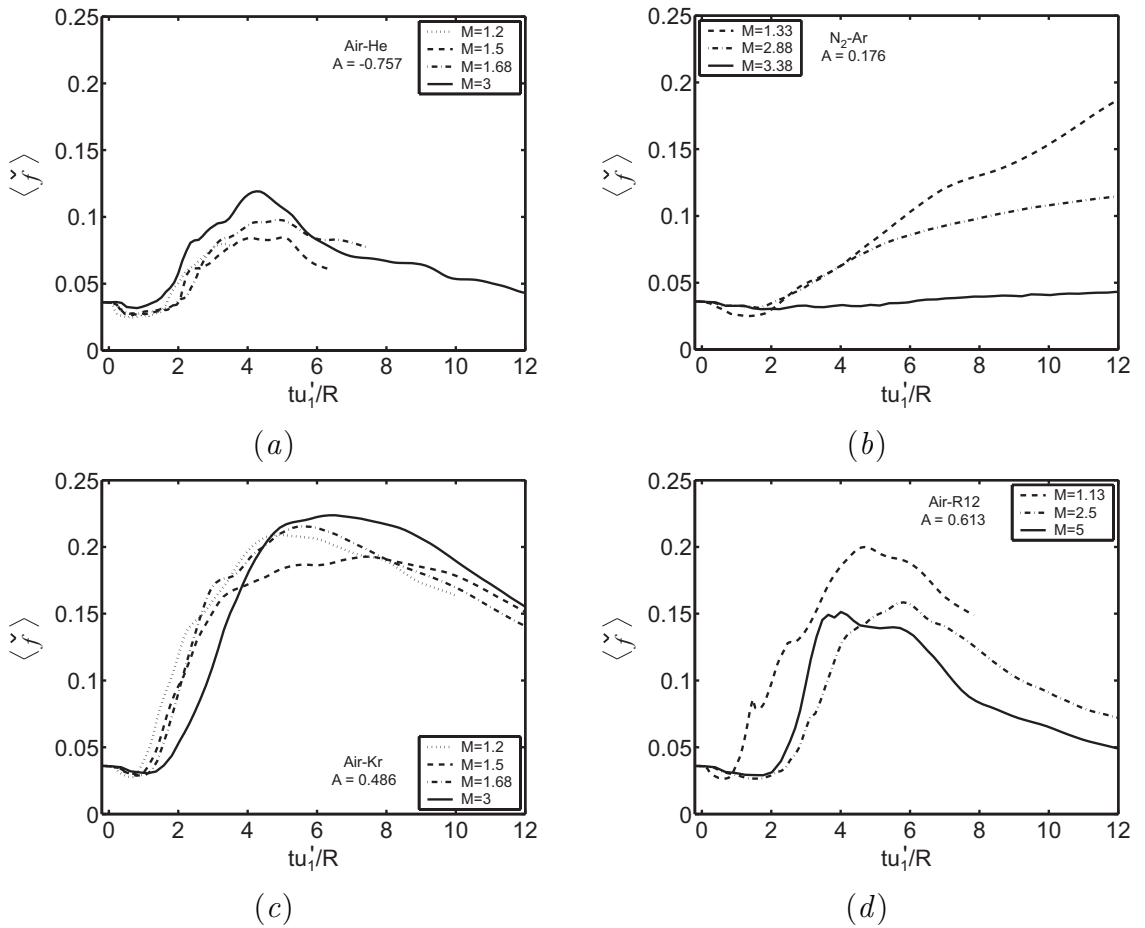


Figure 66: Trends in the volume-averaged r.m.s. fluctuation from the azimuthal mean of the bubble-fluid volume fraction  $f$ , obtained using Eq. 5.3: (a) air-He, (b)  $N_2$ -Ar, (c) air-Kr, (d) air-R12.

number for the nitrogen-argon gas combination, due to the large  $\gamma$  of argon. The very large magnitude of  $\bar{f}$  at late times, particularly in the  $M = 1.33$  cases is unexplained, however. It is also unclear why the largest values of  $\bar{f}$  are found in the air-krypton simulations rather than in the air-R12 simulations.

Although this provides a useful measure of fluctuations from the azimuthal mean, the interface deforms in the other two directions as well. Thus, the diagnostic presented in Fig. 66 is perhaps not ideal for characterizing the interpenetration and interface deformation process described above. We speculate that a diagnostic based on the time evolution of the total area of the  $f = 0.5$  isosurface might provide a more meaningful characterization of the extent to which the interface has been deformed, and the magnitude of the area upon which interdiffusion may operate.

### 5.2.2 Mean ambient-fluid volume fraction

A simple and effective diagnostic for the extent of mixing under the action of the interdiffusion process is to compute the mean volume fraction of *ambient* fluid in the bubble-fluid region  $B$ , where  $B$  includes all cells with  $f > 0$ . As the bubble is deformed by the initial shock wave and the secondary waves that interact with it, strong velocity shear and other effects draw ambient fluid into the bubble-fluid region, and the multi-fluid capturing scheme allows the two fluids to mix. Thus, the volume fraction of fluid 1 increases and the volume fraction of fluid 2 decreases within the body of region  $B$ , and the region  $B$  grows in size.

We define a “mixedness” quantity  $\zeta$  which is equivalent to the mean volume fraction of ambient fluid in the bubble-fluid region:

$$\zeta \equiv \frac{\int_B [1 - f(x, y, z, t)] d\mathcal{V}}{\int_B d\mathcal{V}} = 1 - \frac{\int_B f(x, y, z, t) d\mathcal{V}}{\int_B d\mathcal{V}}. \quad (5.16)$$

This quantity characterizes the extent to which the two fluids may be considered to have mixed on the smallest scales. At time zero, for perfectly segregated fluids,  $\zeta = 0$  by construction. The asymptotic behavior of  $\zeta$  for  $t \rightarrow \infty$  depends on the configuration of the fluid regions. For mixing under interdiffusion of two fluid regions of equal segregated volume  $\mathcal{V}_1 = \mathcal{V}_2$ , we expect  $\zeta \rightarrow \frac{1}{2}$  for  $t \rightarrow \infty$ . However, for the case where the segregated fluid regions are configured such that  $\mathcal{V}_1 \gg \mathcal{V}_2$ , we expect  $\zeta \rightarrow 1$  as  $t \rightarrow \infty$ . (Recall that  $f$  appearing in Eq. 5.16 is the volume fraction of fluid 2.) That is, if fluid 2 is embedded in an effectively infinite volume of fluid 1, as in the case of shock-bubble interactions, then as the mixture tends toward homogeneity, the concentration of fluid 2 tends to zero in the mixture and the concentration of fluid 1 tends to unity.

It is important to note, therefore, that  $\zeta$  provides a normalized measure of the maximum amount of product that would be obtained in a reaction between fluids 1 and 2 if the reaction were limited by the amount of “lean” reactant, fluid 2 (the bubble fluid), and the two fluids were homogeneously mixed. Values near unity correspond to complete mixing. Hence, the interpretation of the quantity  $\zeta$  is identical to that of the normalized “maximum product,”  $P_m(t)/h$  of Cook and Dimotakis (2001) [19], where the stoichiometric-mixture mole fraction  $X_s$  is taken to be zero rather than  $\frac{1}{2}$ . (The quantity  $P_m(t)$  also appears as a measure of mixing for Richtmyer-Meshkov instabilities in Latini *et al.* (2007) [57] and in Schilling *et al.* (2007) [100].) It is also important to note, however, that two-dimensional mesh-sensitivity studies show that the quantity  $\zeta$  is highly nonconvergent, and decreases in magnitude at fixed time with decreasing grid

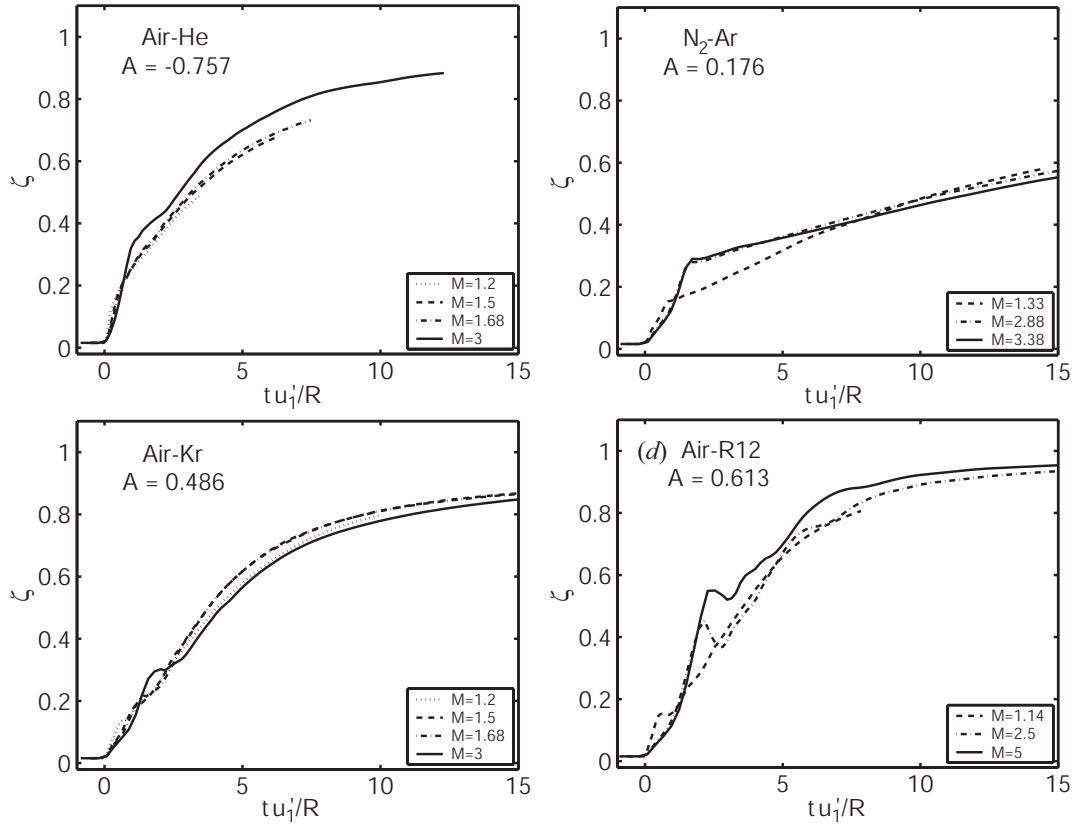


Figure 67: Time-dependent mean ambient-fluid volume fraction  $\zeta(t)$ , obtained from three-dimensional simulations using Eq. 5.16 as representation of the extent of mixing, plotted on the dimensionless timescale  $tu'_1/R$ : (a) Air-He, (b) N<sub>2</sub>-Ar, (c) Air-Kr and (d) Air-R12.

spacing.

The time-dependent “mixedness”  $\zeta$  is computed for the 14 scenarios here, and plotted in Fig. 67. Since the mixing behavior is largely driven by velocity gradients in the post-shock flow, these trends are plotted on a dimensionless timescale based on  $u'_1$  rather than  $W^*$ . The data plotted in Fig. 67 on this timescale collapse nearly to a single self-similar trend for each gas combination. The mixing behavior, computed in this way, is thus shown to depend strongly on the Atwood number, though the Mach number

dependence is generally removed by the timescaling. Other timescales, based on shock wave speeds  $\tilde{W}$  or  $W^*$ , for example, do not produce the collapse seen with the  $u'_1$ -based timescale for the mixing data. For the quantity  $\zeta$ ,  $u'_1$  is appropriate as a characteristic speed because the rate of mixing is dependent directly on the shear rate experienced by the interface, and, thus, on the post-shock flow speed  $u'_1$ . However, as in the mean-density trends from Sec. 4.1.1, the collapse is only successful within each gas pairing, and fails when  $A$  is varied. This is due to the nonlinear dependence of the shock scattering patterns on the initial density contrast.

As for the late-time extent of mixing, we can see from Fig. 67 that the relative magnitude of  $\zeta$  for  $tu'_1/R > 10$  grows consistently with the magnitude of  $A$ . For the nitrogen-argon scenarios, the mean ambient-fluid volume fraction in the mixing region reaches a value of only about 0.6 at late times. In the higher- $A$  cases,  $\zeta$  reaches much greater values at late times: 0.8 and higher for the air-krypton cases, and 0.9 or higher for the air-R12 cases. The intensity of mixing in these scenarios is due not so much to the strength of the shock wave as to the greatly increased complexity and intensity of scattered shock waves and rarefaction waves at high  $A$ . These scattered waves also introduce non-monotonic deviations to the trends in  $\zeta$ , particularly for the air-R12 cases. These are due to the gradient-steepening effects of the transit of secondary shock waves across the mixing region, which introduce a “demixing” effect also noted in the reshock phase of Richtmyer-Meshkov instabilities by Latini *et al.* (2007) [57]. These non-monotonic deviations associated with secondary-wave-induced demixing pose further obstacles to the scaling of mixing behavior across varying  $A$ .

In the two high- $M$  air-R12 scenarios ( $M = 2.5, 5.0$ ), the intensity of shock refraction and vorticity generation in the shock-bubble interaction leads to the development of a

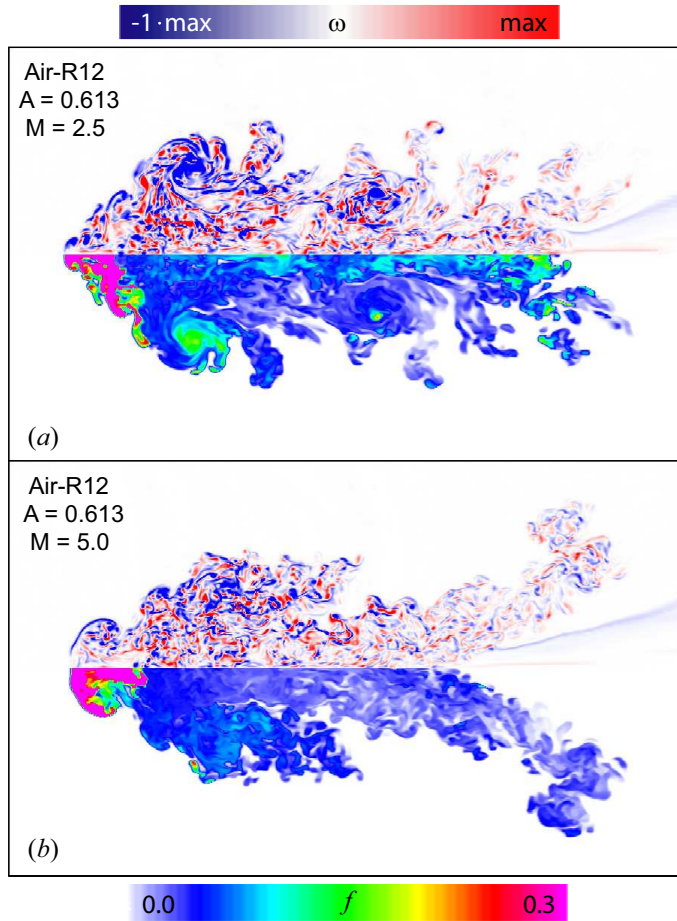


Figure 68: Vorticity magnitude (upper) and R12 volume fraction (lower) fields for the air-R12 scenario, at  $t = 25R/W_i$ , illustrating the turbulence-like flowfield generated in the shock-bubble interaction at late times. (a)  $M = 2.5$ , (b)  $M = 5.0$ . Incident shock wave propagation is from left to right.

very large region of highly intense mixing. In this region, which is a long swath trailing downstream from the main bubble volume, the bubble fluid becomes diluted to  $f < 0.1$  at very late times. Hansen *et al.* (2007) [43] describe this behavior, observed also in experiments, as a “mass-stripping” process. This behavior is distinctive for these two cases, in which, as can be seen in Fig. 26(e-f), the bubble is subjected to very strongly focused shock waves and a series of secondary waves, and is ultimately reduced to a complex plume characterized by a large range of length scales, a complex and disorderly vorticity field and very strong mixing. The volume fraction and vorticity fields from these two cases at  $t = 25R/W_i$  are shown in Fig. 68, which clearly illustrate the high level of mixing, and indicate that the flowfields for these scenarios possess characteristics that can be described in terms of turbulence. We can assume that similar distinctive, turbulent behavior will be observed in shock-bubble interactions when shock strengths and density contrasts are significantly large.

### 5.2.3 Molecular mixing fraction profile

An alternative diagnostic for the extent of mixing is the “molecular mixing fraction” profile  $\theta_Y$  of Youngs (1991) [111]. This quantity is defined as

$$\theta_Y(y) \equiv \frac{\langle f(1-f) \rangle_{xz,B}}{\langle f \rangle_{xz,B} \langle (1-f) \rangle_{xz,B}}, \quad (5.17)$$

where bracketed quantities  $\langle \Phi \rangle_{xz,B}$  here denote averages over the  $x$ - $z$  plane, within the bubble-fluid region  $B$ , for a fixed  $y$ -location. Youngs (1991) [111] used this quantity to characterize the axial time-dependent molecular-mixing pattern in three-dimensional simulations for Rayleigh-Taylor instabilities. Since the Rayleigh-Taylor mixing layer in his simulations spanned the transverse width of the computational domain, but the

mixing region in the current shock-bubble-interaction simulations does not, the spanwise averages denoted by angle brackets here include only the bubble-fluid region  $B$  where  $f > 0$ . (Otherwise, the magnitude of this quantity would depend on the simulation domain width.)

The quantity  $\theta_Y(y)$  characterizes the approach of an inhomogeneous mixture to a homogeneous state. Since this can only be accomplished by a diffusive process, this quantity, like  $\zeta$ , captures the “interdiffusion” aspect of the mixing process. Further, we note that  $\theta_Y(y) = 0$  for any  $x$ - $z$  plane where fluid concentrations are everywhere zero or unity, even if the interface between the two fluids has complex topology and is deformed such that it transects the plane. The minimum and maximum fluid concentration in the plane must be nonzero and non-unity in order for nonzero values of  $\theta_Y$  to appear in the profile  $\theta_Y(y)$ . Physically, the quantity  $\langle f \rangle_{xz,B} \langle (1-f) \rangle_{xz,B}$  is proportional to the reaction rate between the two fluids if they were homogeneously mixed in the  $x$ - $z$  plane, while  $\langle f(1-f) \rangle_{xz,B}$  is proportional to the true reaction rate for the inhomogeneous mixture. Therefore,  $\theta_Y(y)$  is a profile in  $y$  of the extent of interdiffusive mixing; large values of  $\theta_Y$  correspond to thorough mixing, and outside of the mixing region,  $\theta_Y$  is undefined.

The “molecular” or interdiffusive mixing fraction profile is computed using Eq. 5.17 for a series of fixed times in each of the four representative scenarios discussed above in Sec. 5.1, and plotted in Fig. 69 on a spatial scale centered on the bubble-region centroid  $y_c$ . The profiles plotted in black indicate the initial mixing profile, which is nonzero due to the interfacial transition layer on the bubble surface. In the post-shock profiles, labeled by dimensionless time  $\tau = tu'_1/R$ , we see that the mixing region is compressed axially by the shock wave (particularly at the high Mach numbers), and that mixing subsequently proceeds inward from the boundaries of the mixing region. For the high- $A$

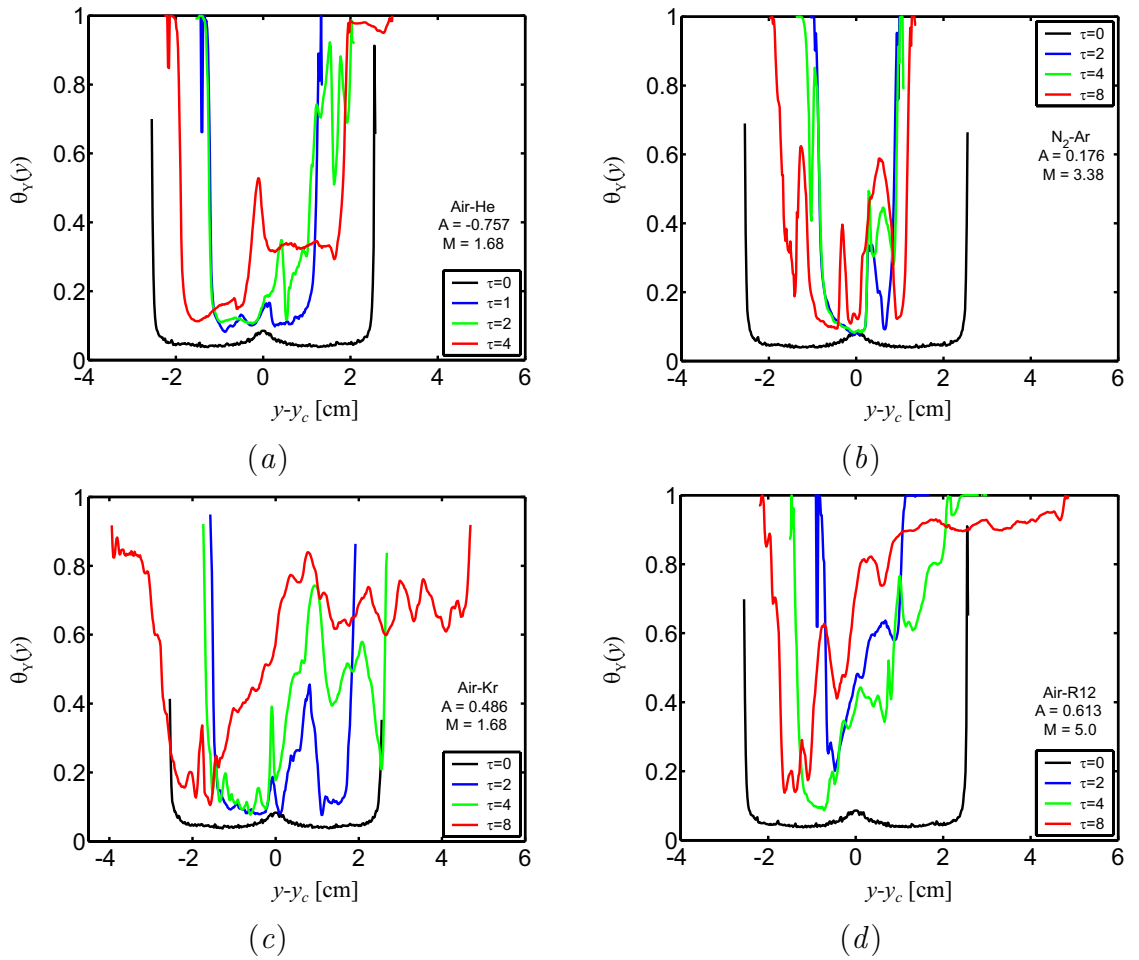


Figure 69: “Molecular” or interdiffusive mixing fraction profiles computed using Eq. 5.17 for (a) air-He,  $M=1.68$ ; (b) N<sub>2</sub>-Ar,  $M=3.38$ ; (c) air-Kr,  $M=1.68$ ; (d) air-R12,  $M=5$ . Note that  $\tau = tu'_1/R$  here.

cases, the mixing region spreads significantly at later times.

The location of the primary vortex ring in the mixing region (visible in the two-dimensional plots in Figs. 46-53) generally lies near the central location  $y - y_c = 0$ , except in the air-helium case, where it is located slightly downstream. Thus, we see that strong interdiffusive mixing is generally associated with the primary vortex ring. In the high- $A$  scenarios (air-krypton and air-R12) in Fig. 69(*c-d*), we also note that the disordered, turbulent plume trailing downstream behind the primary vortex ring at later times is very well-mixed in the interdiffusive (“molecular”) sense. In terms of the magnitudes of  $\theta_Y$ , it is evident from these plots that the intensity of interdiffusive mixing is greatest at large positive Atwood numbers, and appears to be diminished both at small positive Atwood numbers and at negative Atwood numbers. Although the corresponding data at other Mach numbers for these gas combinations are not shown here, the mixing behavior is much less sensitive to the Mach number (after it has been removed using the dimensionless timescale) than it is to the Atwood number, as suggested by the data in Fig. 67.

Overall, the discussion of mixing here is only a preliminary analysis. A number of other diagnostics for mixing are needed, including the integrated molecular mixing fraction  $\Theta$  of Youngs (1991) [111]; the metrics  $P_t$  and  $\Xi$  of Cook and Dimotakis (2001) [19]; and a metric for the total surface area of the interface. (Further information on these mixing metrics, and examples of their use in characterizing Richtmyer-Meshkov mixing can be found in Refs. [57] and [100].) These quantities are omitted here and left for future work.

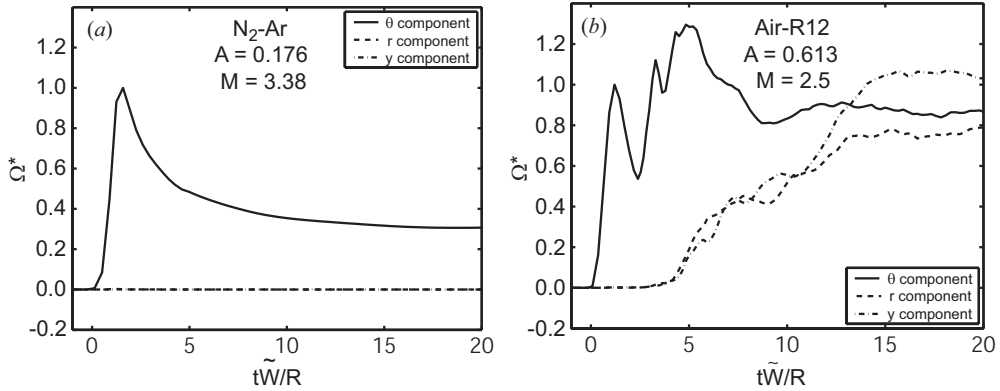


Figure 70: Time-dependent enstrophy associated with axisymmetric ( $\theta$ -) and non-axisymmetric ( $r$ - and  $y$ -) components of the vorticity, plotted on a dimensionless timescale based on the “effective” shock wave speed  $\tilde{W}$ : (a)  $\text{N}_2\text{-Ar}$ ,  $M = 3.38$ , (b) air-R12,  $M = 2.5$ .

### 5.3 Departure from Axisymmetry

As a final note on the development of turbulent and non-axisymmetric features in these simulations, we note that these features arise because of complex shock refraction patterns and vorticity dynamics which strongly amplify initial small-scale non-axisymmetric features at high Atwood numbers. The significance of this behavior – which is captured numerically only in three-dimensional simulations – can be characterized by measuring the enstrophy associated with non-axisymmetric components of the vorticity. In a two-dimensional axisymmetric simulation (such as those shown in Secs. 2.3.3 and 2.3.4), the vorticity can only have a  $\theta$ -component. When axisymmetry is relaxed, the vorticity may develop nonzero components in the  $y$ - (axial) and  $r$ - (radial) directions. This growth in the non-axisymmetric ( $y$ - and  $r$ -) directions is particularly strong and has significant consequences for the flowfield development when  $A > 0.2$ , such that the initial density contrast is significant enough to develop complex secondary shock waves.

The enstrophy associated with each component of the vorticity is therefore measured here by evaluating the integral

$$\Omega_a \equiv \int_B (\boldsymbol{\omega} \cdot \hat{a})^2 dV, \quad (5.18)$$

where  $\hat{a} \in \{\hat{r}, \hat{\theta}, \hat{y}\}$ . The integral is taken only over the bubble-fluid region. Trends in  $\Omega$  are normalized by the value of  $\Omega_\theta$  at the first critical point (local maximum), and plotted as  $\Omega^*$  for two sample cases in Fig. 70. For  $A = 0.176$ , as seen in Fig. 70(a), the departure from axisymmetry is imperceptible, due to the weakness of secondary shock and rarefaction waves generated in this case. From the data shown in Fig. 70(b) for  $A = 0.613$ , however, it is clear that non-axisymmetric effects are quite significant in the later stages of the flowfield development, even though the Mach number is lower in this case. Although the  $\theta$ -component dominates at early times during the initial shock transit, and the  $r$ - and  $y$ -components are zero at that time, the departure from axisymmetry grows dramatically during the intermediate and later stages of the evolution. At late times, the  $r$ - and  $y$ - components are on the same order of magnitude as the azimuthal component. This pronounced growth in the non-axisymmetric components of the vorticity accounts for the qualitative differences observed between the results of the three dimensional air-R12 simulations shown in Figs. 26 and 68, and the results of the two-dimensional simulations shown in Fig. 20. A more complete characterization of these effects for shock-bubble interactions will require the continued development and application of three-dimensional statistical diagnostics for mean and fluctuating quantities, coherent structures and mechanisms of transport and decay of turbulent features. Such efforts have been underway [114], and it is anticipated that in the future, turbulence measurements from simulations for shock-bubble interactions will take advantage of the

averaging schemes and measurement techniques presented here.

# Chapter 6

## Analysis of Film Effects

In typical shock-tube experiments for shock-bubble interactions, cylindrical or spherical bubbles are formed by inflating a soap film or nitrocellulose membrane. A membraneless interface can be created in the case of cylindrical bubbles using a circular laminar jet [49], and some work has been done using spherical bubbles of burned gas inside an expanding flame front [68]. However, the majority of existing mechanical shock tube data for shock-bubble interactions were generated using a liquid soap film layer to confine the bubble gas in the initial condition. Thus, a fundamental concern in the comparison of experimental and numerical results for the interaction of a shock wave with a spherical bubble is the influence of this material on the development of the flowfield: does it strengthen or weaken nonlinear-acoustic effects, and does it significantly alter the deposition of vorticity on the bubble surface, or the post-shock vorticity dynamics?

### 6.1 Modeled Film Material

In order to address these issues, 12 out of the 14 simulations described in Sec. 3.1.6 and listed in Table 3 are repeated, with the addition of a coarse model for the soap film material implemented in the initial condition. These include scenarios 1-3, 5-10, and 11-14 (the  $M = 3$  air-krypton and air-helium cases were excluded). Soap film material is included in the simulations by introducing a third fluid, confined within a thin spherical

cladding around the bubble in the initial condition.

This fluid is modeled only by gross approximation here. First, many of the properties of the fluid are neglected, including, most importantly, its viscosity and its surface tension. This is done in order to preserve the simplicity of the Eulerian simulation, although it is conceivable that such effects could be included in a much more costly simulation with a more complex and less robust numerical method. By neglecting these properties, we lose the ability to simulate the process by which the film material is atomized during shock passage.

Second, the fluid is given a reduced density in the initial condition in order to account for the fact that the true thickness of the film layer cannot be resolved in these simulations. In experiments, based on the appearance of visible interference fringes on the surface of the film layer, we estimate that the thickness of the layer must be on the order of the wavelength of visible light ( $10^{-7}$  m). The simulation grid spacing exceeds this thickness by three orders of magnitude. Therefore, the film layer is regarded as a subgrid feature with a radial thickness  $\delta R_f = 100 \mu\text{m}$ . The spherical cladding is created by querying each cell in the initial condition touching the region between the surfaces  $\|\mathbf{r} - \mathbf{r}_c\| = R$  and  $\|\mathbf{r} - \mathbf{r}_c\| = R + \delta R_f$  for the fraction of its volume that lies inside the region. This is the film-fluid volume fraction assigned to each of these cells. The initial density of the film fluid (fluid 3) is given as

$$\rho_f = \frac{3m_f}{4\pi [(R + \delta R_f)^3 - R^3]}, \quad (6.1)$$

where  $m_f$  is the true total mass of liquid soap film material for a  $R = 2.54\text{-cm}$  bubble. For the current simulations, this density is approximately  $\rho_f = 0.01 \text{ g/cm}^3$ . After shock wave impact, the density of the fluid in the simulation evolves according to a gamma-law

equation of state.

Using this coarse model, a thin cladding of very dense material is added to the bubble surface, whose total mass is approximately equal to the total mass of soap film material present in shock tube experiments. The setup of the simulations is otherwise identical to the setup described in Sec. 3.1.6. This model allows the inertial effects of the film material to be identified and approximated in these simulations, although dynamical effects such as film material breakup and entrainment clearly cannot be captured. We proceed with the simulations aware of the limitations of this approach.

## 6.2 Flow Visualizations

Results from the simulations including film material for four representative scenarios are shown in Figs. 71-74. In the first frame in each of these figures, the film material can be seen as a very thin layer on the bubble surface. By comparison with the filmless simulations shown in Figs. 23-26, we note that nearly all of the features of the flowfield that were observed in the filmless simulations are replicated here with only very subtle changes. We observe the development of an irregular shock refraction pattern in the air-helium,  $M = 1.68$  simulation results in Fig. 71, and of diffracted and focused shock wave patterns in the air-krypton,  $M = 1.68$  and air-R12,  $M = 5$  cases in Figs. 73 and 74. We also note the emergence of a supersonic Winkler-Group [109] supersonic vortex ring (see Fig. 3(d) and Sec. 1.3.3) in these two cases (Figs. 73c and 74c), as well as a region of complex, disordered vortical motion at late times in these cases, downstream from the primary vortex ring, as was observed in the filmless simulations.

Some subtle differences are visible as well. In the air-helium,  $M = 1.68$  scenario,

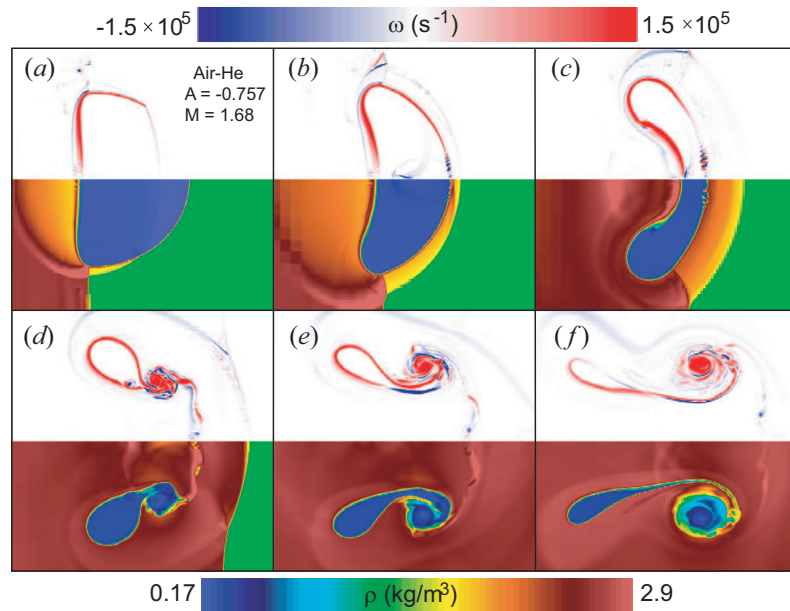


Figure 71: Density (bottom) and vorticity magnitude (top) on the  $\theta = \pi/6$  plane for the  $M = 1.68$  air-He scenario ( $A = -0.757$ ) with modeled film material: (a)  $\tau = 1.4$ , (b)  $\tau = 2.6$ , (c)  $\tau = 4.8$ , (d)  $\tau = 10.0$ , (e)  $\tau = 14.9$ , (f)  $\tau = 24.9$ . The density color palette is shown at bottom, and vorticity is plotted on a symmetric color palette centered on white, shown at top. Note that  $\tau = tW_t/R$  here. Incident shock wave propagation is left-to-right. The corresponding filmless scenario is shown in Fig. 23.

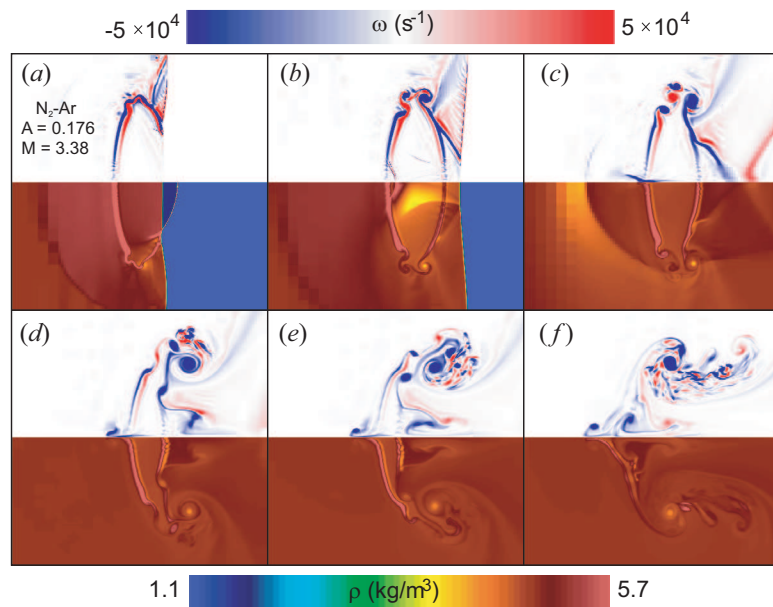


Figure 72: Density (bottom) and vorticity magnitude (top) on the  $\theta = \pi/6$  plane for the  $M = 3.38$   $N_2\text{-Ar}$  scenario ( $A=0.176$ ) with modeled film material: (a)  $\tau = 1.5$ , (b)  $\tau = 2.5$ , (c)  $\tau = 4.9$ , (d)  $\tau = 10.0$ , (e)  $\tau = 15.0$ , (f)  $\tau = 24.9$ . The density color palette is shown at bottom, and vorticity is plotted on a symmetric color palette centered on white, shown at top. Note that  $\tau = tW_i/R$  here. Incident shock wave propagation is left-to-right. The corresponding filmless scenario is shown in Fig. 24.

we note the development of Richtmyer-Meshkov-type structures near the downstream pole of the bubble in Fig. 71(*b-c*), which are not seen in the filmless case. This can be attributed to the higher effective Atwood number associated with the film material. We also note that an upstream reflected shock wave precedes the reflected rarefaction wave arising at the upstream bubble pole in Fig. 71(*a*), due to the reversed sign of the change in acoustic impedance due to the film material. (The appearance of reflected shock waves due to film material for helium bubbles in air can also be seen in figures 7 and 8 of Haas and Sturtevant (1987) [42].) The structure and evolution of the upstream and downstream jets appearing on the bubble poles in the air-krypton case in Fig. 73 also show subtle differences relative to the filmless case, but the magnitude of these effects is relatively insignificant.

Dramatic differences are evident, however, in the nitrogen-argon,  $M = 3.38$  simulation results shown in Fig. 72, relative to the filmless case shown in Fig. 24. The vorticity deposited on the interface by the baroclinic mechanism in Fig. 72 is visibly much greater in magnitude than that seen in the filmless case in Fig. 24. Further, the number of vortical features appearing in the flowfield after shock passage is dramatically increased, and the primary vortex ring is no longer the singular, dominant feature in the vorticity field at late times. Also noticeable is the appearance of numerous regions of opposite-signed vorticity not seen in the filmless case, and, at late times, the development of regions where the vorticity field exhibits features similar to the disordered, turbulence-like motion found in the high- $A$  scenarios at late times. These features of the vorticity field give rise also to a strongly altered interface deformation pattern, particularly at late times, where the shocked bubble region is axially longer and geometrically more complex than in the filmless scenarios. Although results from the  $M = 1.33$  and  $M = 2.88$  simulations

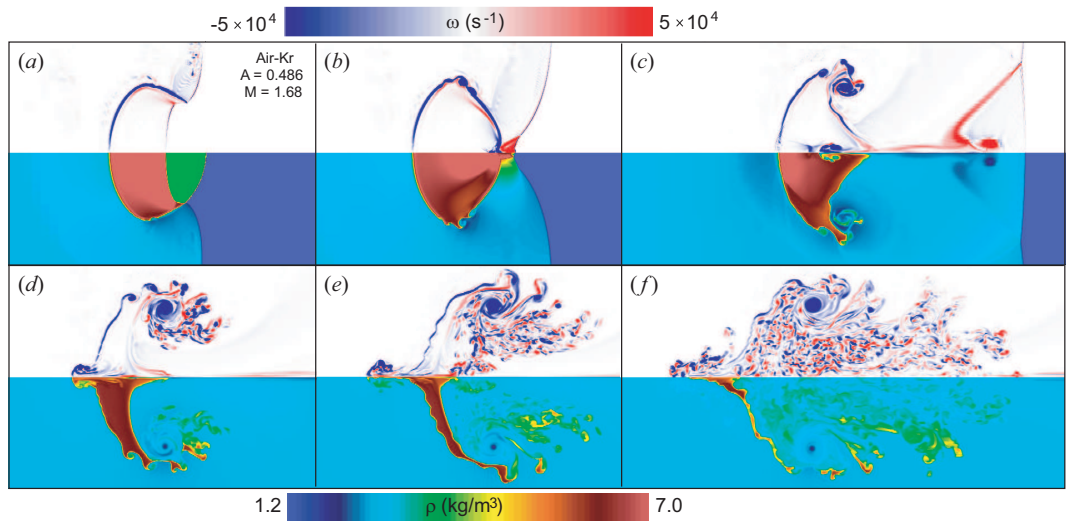


Figure 73: Density (bottom) and vorticity magnitude (top) on the  $\theta = \pi/6$  plane for the  $M = 1.68$  air-Kr scenario ( $A=0.486$ ) with modeled film material: (a)  $\tau = 1.6$ , (b)  $\tau = 2.6$ , (c)  $\tau = 5.0$ , (d)  $\tau = 10.0$ , (e)  $\tau = 14.8$ , (f)  $\tau = 24.9$ . The density color palette is shown at bottom, and vorticity is plotted on a symmetric color palette centered on white, shown at top. Note that  $\tau = tW_i/R$  here. Incident shock wave propagation is left-to-right. The corresponding filmless scenario is shown in Fig. 25.

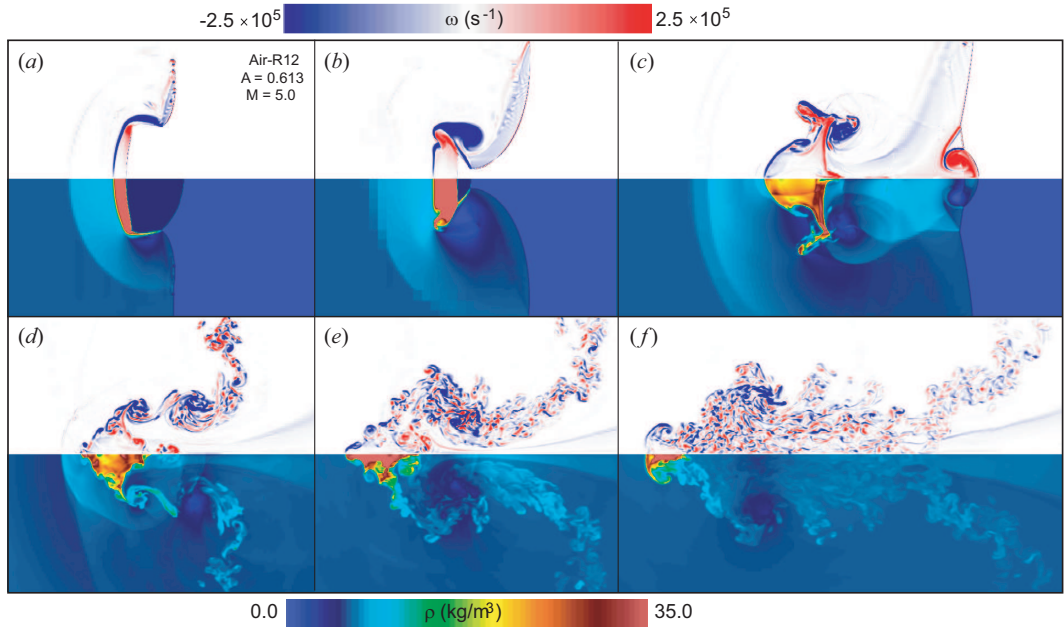


Figure 74: Density (bottom) and vorticity magnitude (top) on the  $\theta = \pi/6$  plane for the  $M = 5.0$  air-R12 scenario ( $A=0.613$ ) with modeled film material: (a)  $\tau = 1.5$ , (b)  $\tau = 2.5$ , (c)  $\tau = 5.0$ , (d)  $\tau = 9.9$ , (e)  $\tau = 15.0$ , (f)  $\tau = 25.0$ . The density color palette is shown at bottom, and vorticity is plotted on a symmetric color palette centered on white, shown at top. Note that  $\tau = tW_i/R$  here. Incident shock wave propagation is left-to-right. The corresponding filmless scenario is shown in Fig. 26.

for the nitrogen-argon gas combination are not shown here, the differences are similarly dramatic, particularly in the evolution of vorticity field. These observations from the simulated flowfields suggest that film effects are significant only for low Atwood number magnitude,  $|A| < 0.2$ .

### 6.3 Mean Bubble-Fluid Density

To verify that the presence of the modeled film material (fluid 3) does not significantly alter the shock-induced compression of the bubble-interior fluid (fluid 2), we have extracted the time-dependent normalized mean density  $\rho^*$  of the bubble fluid (fluid 2) from these simulations, using the same expression employed in the analysis in Sec. 4.1.1,

$$\rho^*(t) = \frac{\langle \rho(t) \rangle - \rho_2}{\rho''_2 - \rho_2}, \quad (6.2)$$

where  $\rho''_2$  is the density from the one-dimensional gasdynamics analysis, for a gas slab after the passage of the initial shock wave and one internally reflected wave. Under this normalization,  $\langle \rho(0) \rangle = 0$  by construction, and  $\langle \rho(t) \rangle \rightarrow 1$  represents the one-dimensional-gasdynamics limit.

The time-dependent mean bubble-fluid density is plotted with this one-dimensional-gasdynamics normalization on the dimensionless timescale  $tW^*/R$  for each of the 12 simulations with modeled film material in Fig. 75. ( $W^*$ , defined in Eq. 3.5, is the incident or transmitted shock wave, whichever is greater.) In these plots, by comparison to the data shown in Fig. 28, we see that the compression history of the bubble fluid is effectively unchanged by the introduction of modeled film material into the simulation. The bubble-fluid density at late times still approaches a value very near to that predicted by the one-dimensional gasdynamics model. This indicates that although the film-material layer strongly influences the vorticity-generation process in shock-bubble interactions in the low- $A$  (nitrogen-argon) case, the shock-compression process is unaltered, in spite of the enhanced acoustic impedance mismatch at the interface.

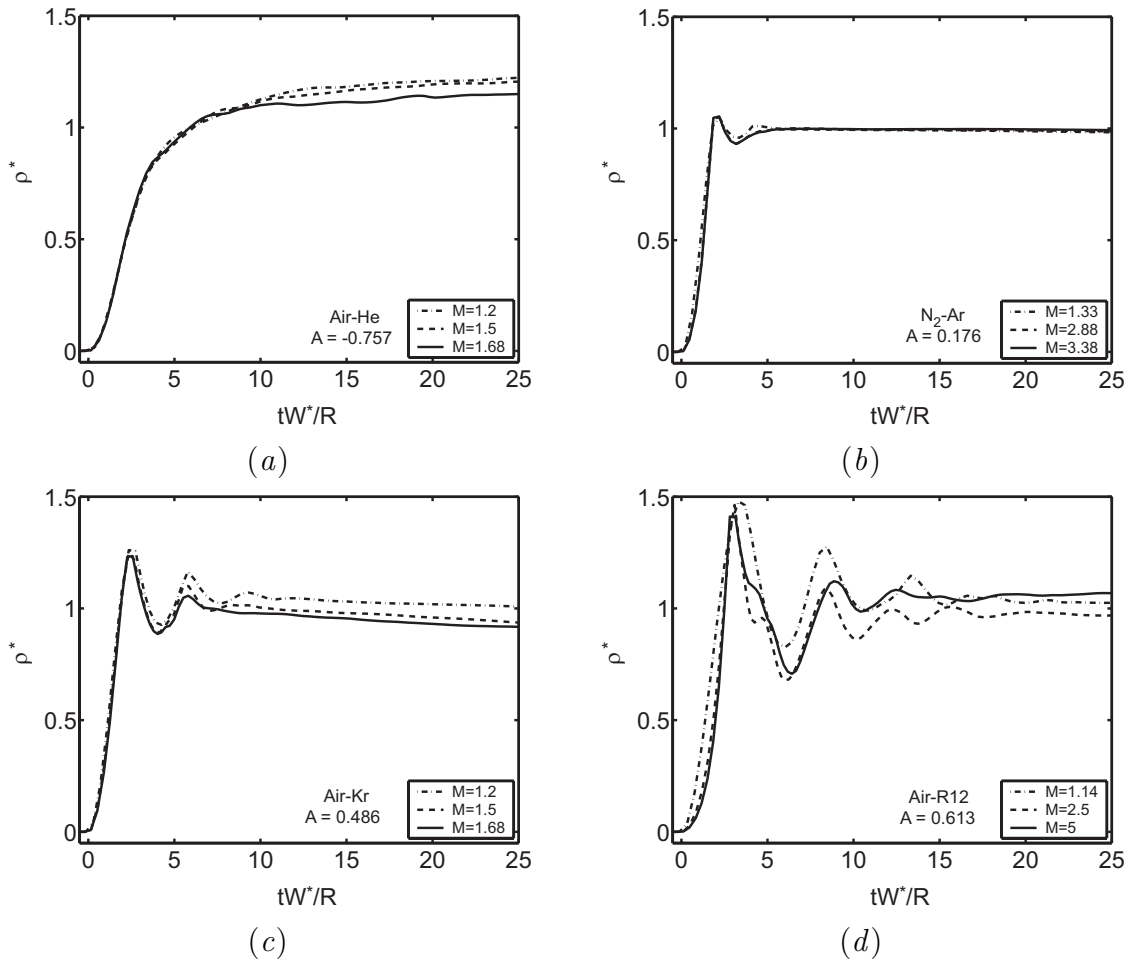


Figure 75: Plots over dimensionless time of the mean bubble fluid density obtained from three-dimensional simulations with modeled film material, normalized to the density obtained from the one-dimensional gasdynamics model, using Eq. 6.2: (a) Air-He, (b) N<sub>2</sub>-Ar, (c) Air-Kr and (d) Air-R12.

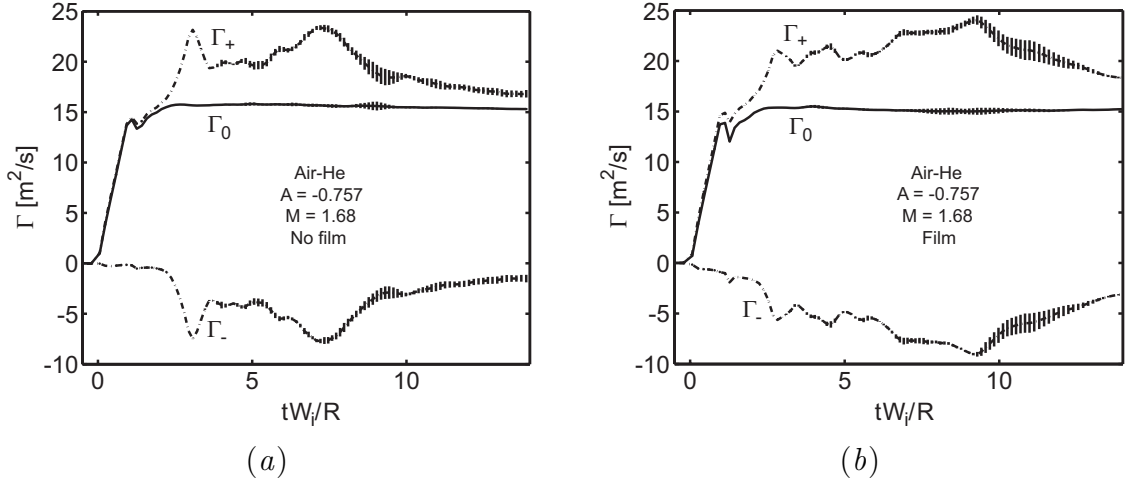


Figure 76: Decomposed circulation  $\Gamma_*$  versus time, for air-He,  $M = 1.68$ , (a) without and (b) with modeled soap film material. Vertical bars indicate r.m.s. azimuthal fluctuations  $\tilde{\Gamma}_*$ .

## 6.4 Circulation

As a measure of the vorticity generation process, the total circulation in the flowfield, and its components, are measured for four representative scenarios, for comparison to the results of the filmless scenarios. These data are extracted from the simulations by evaluating the integral

$$\Gamma = \int_S \boldsymbol{\omega} \cdot dA, \quad (6.3)$$

over a slice plane  $S$  perpendicular to  $\hat{\theta}$ , and averaging the data over 48 slice planes to obtain trends in the positive, negative, and total mean circulation  $\bar{\Gamma}$  and r.m.s. fluctuations  $\tilde{\Gamma}$ , as described in Sec. 4.2.5. Only cells within the bubble-fluid region are included in the integral.

The decomposed, azimuthally-averaged circulation trends and fluctuations extracted

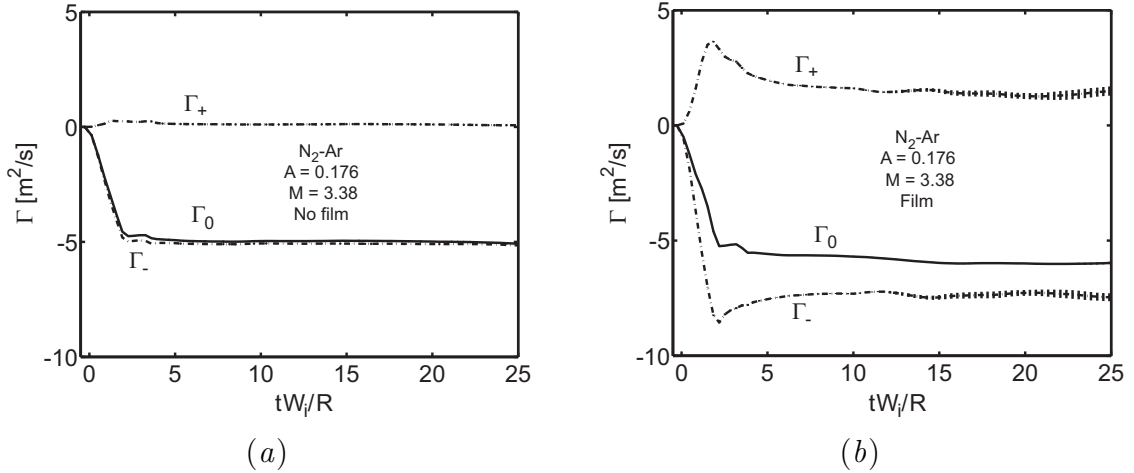


Figure 77: Decomposed circulation  $\Gamma_*$  versus time, for  $N_2\text{-Ar}$ ,  $M = 3.38$ , (a) without and (b) with modeled soap film material. Vertical bars indicate r.m.s. azimuthal fluctuations  $\tilde{\Gamma}_*$ .

from the simulations with and without film for several representative scenarios are shown in Figs. 76-79. In these plots, we see that for  $|A| > 0.2$ , the change in the evolution of both the mean and fluctuating circulation due to the introduction of modeled film material into the simulation is generally subtle and insignificant. For  $|A| > 0.2$ , the trends in the total (net) circulation  $\bar{\Gamma}_0$  are nearly identical with and without modeled soap film, and the components of the circulation  $\bar{\Gamma}_+$  and  $\bar{\Gamma}_-$  exhibit only minor changes. Although the Atwood number  $A_f$  associated with the film-ambient interface ( $A_f = 0.785$  for ambient air) is higher than the bubble-ambient Atwood number, the film layer is so tenuous that very little total angular momentum is generated there, compared to the angular momentum generated by baroclinic torque associated with the bubble-ambient density difference. Thus, the additional effect due to the film material is insignificant for these cases.

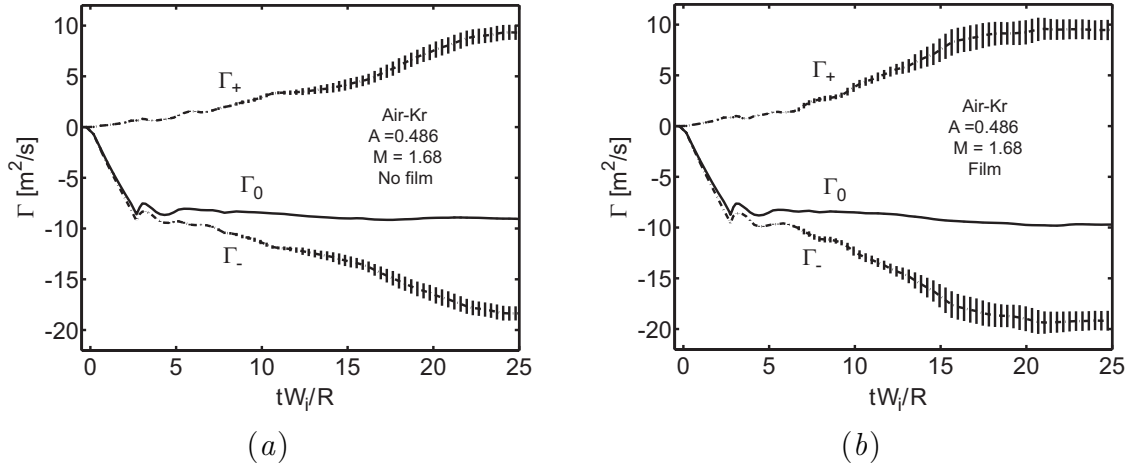


Figure 78: Decomposed circulation  $\Gamma_*$  versus time, for air-Kr,  $M = 1.68$ , (a) without and (b) with modeled soap film material. Vertical bars indicate r.m.s. azimuthal fluctuations  $\tilde{\Gamma}_*$ .

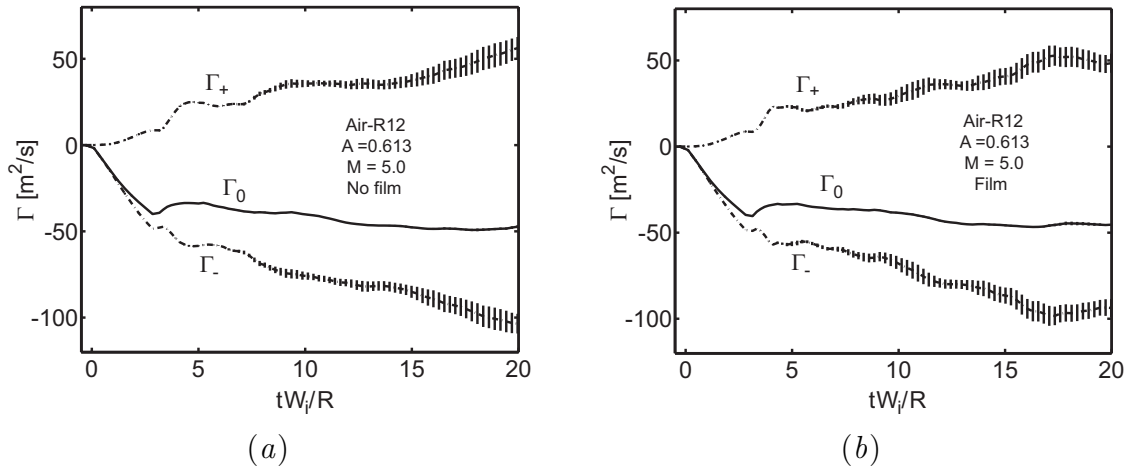


Figure 79: Decomposed circulation  $\Gamma_*$  versus time, for air-R12,  $M = 5$ , (a) without and (b) with modeled soap film material. Vertical bars indicate r.m.s. azimuthal fluctuations  $\tilde{\Gamma}_*$ .

However, in the low-Atwood-number nitrogen-argon scenario, the trends in the components of the circulation are dramatically altered by the introduction of film material into the simulation, as shown in Fig. 77. For the simulation without film material,  $\Gamma_+ \approx 0$  and  $\Gamma_- \approx \Gamma_0$  for the duration of the simulation. But in the case where modeled film material is included, the positive and negative components both pass through a pronounced maximum at shock passage and remain relatively large until late times. This behavior can be observed visibly as the appearance of opposite-signed vorticity in the plots shown in Fig. 72. Further, the total circulation at  $tW_i/R$  is increased from  $-5 \text{ m}^2/\text{s}$  to  $-5.8 \text{ m}^2$ . Finally, we also note that  $\tilde{\Gamma}_+ = \tilde{\Gamma}_- = 0$  for the filmless case, while significant fluctuations appear in the simulation with film material included. Thus, the presence of the film material in the low- $A$  case results in significant intensification and regularization of the vorticity field. This is due to the relative weakness of baroclinic vorticity generation associated with the bubble-ambient density difference in the low- $A$  case, which allows the effects of the film-ambient density difference to become much more prominent. It is speculated that these effects may play a significant role in generating the complex vortical features observed in low- $A$  shock-bubble interactions by Ranjan *et al.* (2005) [86].

In summary, on the basis of these simulations, we conclude that film effects may be expected to play a significant role in shock-bubble interactions with  $|A| < 0.2$ , but only in terms of the vortical effects introduced into the flowfield. The bulk compression of the bubble is unaltered, though the vorticity field evolution and decomposed circulation trends are dramatically different. These effects are absent in the simulations for  $|A| > 0.2$ . It is important to note, however, that these results cannot be generalized, since the film material is included here at a reduced density, due to the limited spatial resolution

of the simulations. At the true liquid density of the film material, it is possible that noticeable film effects might arise even for  $|A| > 0.2$ .

# Chapter 7

## Discussion and Conclusion

The parameter study described in this dissertation includes novel approaches to several aspects of the shock-bubble interaction problem. Most generally, this work constitutes the first parameter study for shock-bubble interactions that incorporates a three-dimensional numerical treatment, and it is the first that simultaneously encompasses positive and negative Atwood numbers. Further, in order to exploit fully the three-dimensionality of the simulation results, azimuthal averaging is implemented and used to generate turbulence statistics of the type measured in many studies for Rayleigh-Taylor and Richtmyer-Meshkov mixing layers [111, 57, 100]. Finally, the first attempt is made to quantify the effects associated with liquid soap film material in shock-bubble interactions by including a coarse model for this material in a series of simulations.

The most important outcomes of the parameter study presented here (and in Ref. [74]) can be summarized as follows. First, we have found that the phenomenology of shock-bubble interactions is fundamentally altered by changes in the Atwood number, because of the strongly variable shock refraction patterns that develop in the bubble at different density contrasts. Second, the appearance of strong non-axisymmetric and turbulent effects and enhanced mixing behavior for  $A > 0.2$  has been documented thoroughly and linked to inherently three-dimensional mechanisms. Third, despite the complex couplings and nonlinear scalings introduced to the flowfield by these multi-dimensional

effects, we find that several important aspects of the flowfield, at late times, finally approach a state that can be accurately predicted using a simple one-dimensional gas-dynamics model; this model can also be used to generate dimensionless timescales on which temporal trends for varying  $M$  collapse. Although the analysis that yields these conclusions is in many ways incomplete and limited in scope, and despite the limitations posed by a purely numerical approach, these outcomes provide valuable insight into the underlying physics of these flows, as described below.

## 7.1 Complex Shock Refraction and Non-Similarity

The simulation results shown here indicate that the shock-bubble interaction is effectively a *different problem* for each gas combination. As the Atwood number changes, and the acoustic impedance mismatch at the interface increases in magnitude or changes sign, the refraction undergone by the primary shock wave, and the pattern of secondary shock and rarefaction waves generated during and after its passage over the bubble varies dramatically. Therefore, the shock-compression and baroclinic-driving histories to which the bubble is subjected vary strongly in intensity, complexity, and duration as the Atwood number is changed. This is a manifestation of the underlying nonlinearity of the problem: discontinuities propagate in the solution due to the nonlinear advection terms in the governing equations. The interaction of these discontinuities with surfaces of acoustic impedance mismatch results in the generation of additional discontinuities, which subsequently propagate throughout the flow, and re-accelerate the fluid.

These effects can be observed visibly in the flow visualizations provided throughout the preceding chapters, including Figs. 18, 20, and 23-27. The origin of these shock

refraction patterns is also depicted schematically for convergent and divergent geometry in Fig. 3. They can be seen most clearly in the fluctuating density and enstrophy plots of Figs. 47, 49, 51, and 53. In Figs. 51(a) and 53(b), curved secondary shock waves associated with shock diffraction and focusing are seen propagating in the radial direction, interacting with the interface that has already been strongly deformed by the initial shock wave. The intensity and complexity of these secondary waves diminishes with decreasing  $|A|$ , and they completely change in character for  $A < 0$ .

These changes are observed quantitatively in the trends of normalized mean bubble fluid density in Fig. 28. The increased intensity of secondary shock and rarefaction waves with increased Atwood number leads to increased amplitude of oscillations in  $\rho^*$  after the passage of the initial shock wave. However, no oscillations at all are observed in the divergent-geometry ( $A < 0$ ) cases, other than at  $M = 3$ . Thus, although these trends show similarity under varying  $M$ , this similarity holds only for fixed  $A$ , because of the variation in shock refraction patterns. Thus we see that altered shock refraction patterns preclude the successful application of any simple linear scaling arguments for variable Atwood number.

These intense shock refraction patterns also lead to the development of localization effects in the flowfield. In convergent geometry at high  $A$ , refraction leads to shock focusing and the associated dramatic pressure pulse at the downstream bubble pole. In divergent geometry, irregular refraction leads to the appearance of triple points and slip surfaces in the flowfield that seed the development of long-lived secondary vortex rings. Thus, a shock wave that spans the width of the domain can become a source of highly local effects due to strong refraction.

## 7.2 Non-Axisymmetric Effects, Turbulence, and Mixing

In the present simulations, the growth of non-axisymmetric features in the flowfield is made possible by mechanisms of vorticity dynamics that are absent in two-dimensional simulations. In particular, the vortex stretching term in the vorticity transport equation (see Eq. 1.7, derived in Appendix B) allows for transport of vorticity in the direction of the vorticity vector  $\omega$ . This is a necessary but not sufficient condition for the appearance of Widnall-type azimuthal vortex ring instabilities [108], and, eventually, the development of a fully three-dimensional vorticity field. The other necessary condition is the presence of a non-axisymmetric perturbation to the flowfield in the initial condition as a seed for this development. This is introduced here by the projection of the curved bubble surface onto the rectangular computational mesh, with the smoothing technique described in Sec. 3.1.5. This provides a full spectrum of modes in the initial condition, as shown in Fig. 61, which may be regarded as a surrogate for the small-amplitude, short-wavelength perturbations existing in experimental initial conditions due to thermal noise, vibrations, nonuniformities in bubble film thickness, and the process of film breakup during shock passage.

The post-shock growth of these azimuthal perturbations is characterized here using an azimuthal averaging scheme and Reynolds decomposition, which yields fluctuating quantities that can be analyzed in terms of turbulence. Trends in the overall volume-averaged magnitude of these fluctuations in the density (Fig. 54) and enstrophy (Fig. 55) fields show that such fluctuations grow to be as large as 25% of the predicted mean-field magnitude, in cases with  $|A| > 0.2$ . For  $|A| < 0.2$  (the nitrogen-argon scenarios),

these fluctuations appear to be suppressed. In the  $|A| > 0.2$  cases, we also qualitatively observe, in the mean and fluctuating flowfield plots in Figs. 46-53, the development of turbulence-like features including regions of complex and strongly disordered motion, close-packed small-scale filamentary structures in the vorticity fields, and well-developed mixing regions. But these features also do not appear in the  $|A| < 0.2$  scenarios. These observations together suggest that turbulent effects are quite significant in shock-bubble-interaction flowfields for  $|A| > 0.2$ .

The mixing behavior of the flowfields suggests a similar conclusion. The data shown in Fig. 67 indicate that mixing, measured in terms of the mean volume fraction  $\zeta$  of ambient fluid in the bubble-fluid region, proceeds noticeably more quickly in all three gas combinations with  $|A| > 0.2$  than otherwise. Strong differences between the molecular mixing profiles for  $|A| > 0$  and  $|A| < 0$  are also seen in Fig. 69, with much larger values of  $\theta_Y$  seen at the higher Atwood numbers at later times. Thus, we speculate that “weak” mixing transition of the type described by Miles *et al.* (2005) [72] occurs near  $A = 0.2$ , which corresponds to grid-scale Reynolds number  $Re_\Delta = 3000$  or physical Reynolds number  $Re_\nu = 10^6$  (see Table 7).

### 7.3 Modeling and Timescaling Arguments Based on One-Dimensional Gasdynamics

Despite the development of these complex nonlinear and three-dimensional effects in shock-bubble interactions, the present simulations show that certain aspects of the flowfield can be modeled with very good accuracy using a simple model based on one-dimensional gasdynamics. In this model, described in Sec. 1.2.2 and in Appendix B,

the bubble is treated as a slab embedded in a one-dimensional medium. The laws of gasdynamics upon which the Rankine-Hugoniot conditions are based can be used to track the state of each gas region in the system through the passage of the initial shock wave and a series of secondary transmitted and reflected shock and rarefaction waves. The mean density, internal energy, and mean streamwise velocity of the bubble fluid are both found to equilibrate to values very near those predicted using this one-dimensional-gasdynamics analysis, after a transient period associated with the passage of the initial shock wave and any secondary shock and rarefaction waves. These results are shown in Figs. 28, 29, and 30, respectively.

The one-dimensional-gasdynamics analysis also proves very useful for constructing an approximation to the circulation in the flowfield at shock passage, as shown in Secs. 4.2.4–4.2.5 and in Fig. 40. Other analytical models for the circulation are provided by integrating the baroclinic torque through the passage of the shock wave over the bubble, or by taking the asymptotically-motivated approach of Samtaney and Zabusky (1994) [99]. Of these three different types of approaches, the one-dimensional-gasdynamics-based model, and the model of Samtaney and Zabusky give the most reliable prediction across the parameter space, except for  $A < 0$ , where only the one-dimensional-gasdynamics model predicts the circulation obtained from simulations consistently with good accuracy.

Finally, from the one-dimensional gasdynamics analysis, we obtain characteristic velocity scales based on shock wave speeds or post-shock flow speeds, from which dimensionless timescales may be constructed that collapse the temporal trends in various extracted quantities for variable  $M$  onto nearly self-similar curves. However, we find that no single velocity scale can collapse the trends in all of the different types of extracted quantities, but that different velocity scales are appropriate for different aspects

of the shocked-bubble evolution. In particular, we find that trends in most quantities associated with turbulence-like features (*e.g.*, the volume-averaged density and enstrophy fluctuations) or mixing tend to scale with the post-shock ambient flow speed,  $u'_1$ . Meanwhile, timescales in the circulation trends, particularly during the initial shock transit, are set by the speed with which the leading shock wave reaches the downstream pole of the bubble and initiates the deposition of opposite-signed vorticity. This “effective” wave speed is given in Eq. 4.18. Trends in the bulk compression and acceleration of the bubble fluid, shown in Figs. 28 and 30, scale with the incident and transmitted shock wave speeds,  $W_i$  and  $W_t$ . Overall, therefore, we find that the one-dimensional-gasdynamics analysis provides a very useful tool for describing many different aspects of shock-bubble interaction flowfields.

## 7.4 Significance and Application

In light of these conclusions gained from the computational parameter study described in this dissertation, a number of comments might be made with relevance to the larger class of shock-accelerated inhomogeneous flows, and to the various applications where these flows are found. First, we note that the observation regarding the equilibration of the density and velocity of the bubble fluid to the value predicted from one-dimensional gasdynamics has consequences for the design of various components of inertial fusion devices. Essentially, this suggests that inhomogeneities should *not* be expected to alter the propagation of shock waves significantly, if the shock wave is allowed to move more than 10-15 radii downstream. By this time, the flow conditions in the bubble region have returned to the state predicted by one-dimensional gasdynamics, so we expect

the same to be true of the shock wave, aside from the presence of features such as the Winkler-Group vortex. Therefore, we expect that ICF target designs incorporating wetted-foam ablators should allow the ablation-driven shock wave to be transmitted to the fuel with minimal disturbance associated with the voids, if a sufficient recovery distance is included. This conclusion is also reached by Collins *et al.* (2005) [18] on the basis of two-dimensional simulations. On the other hand, this result suggests that foams and bubbly liquids will perform poorly as shock-mitigation devices in inertial fusion environments, since the flow may be assumed to equilibrate to the pressure predicted by a one-dimensional analysis shortly after shock wave passage.

The strong localization effects observed in these simulations also imply significant consequences for many environments where shock-accelerated inhomogeneous flows are found. At high Atwood numbers, we have observed that shock diffraction and focusing leads to very intense, highly localized pressure pulses, leading to the subsequent formation of high-speed axial jets. Such localization effects could have significant consequences in environments such as shock wave lithotripsy, where bubble-generated jets are used to fracture kidney stones, and in explosives, where shock waves propagate in inhomogeneous media to initiate detonation, and localization effects can alter the detonation process significantly.

## 7.5 Limitations and Future Work

Before generalizing the insights gained from these simulations, however, it is important to recognize the limitations of the present study, and the points where future work could improve upon what has been done. Among the limitations of the present work is, first

of all, the nonconvergence of the solution. As discussed in Sec. 2.2, as the mesh spacing is decreased, the solution develops increasingly fine-scale structures, particularly in the case where the initial condition contains very well-defined density interfaces. This is a fundamental property of Eulerian simulations for shock-contact interactions, since these problems, when formulated as initial value problems, are ill-posed [97]. Thus, to some extent, the features of the solution on the smallest scales cannot always be trusted, since these features are highly mesh-sensitive. Since the turbulence features described in Chapter 5 exist on these small scales, it is particularly difficult to generalize these results. In the future, a more thorough mesh-sensitivity study is needed, and perhaps a more rigorous characterization of the convergence properties of the various quantities computed from these datasets.

The general applicability of the turbulence characterization included here in Chapter 5 is also limited by several other observations. Most significantly, for these variable-density flows, Favre averaging is much more appropriate for generating mean fields, but was not used here because of the unavailability of resources to implement a more complex averaging scheme. It is anticipated that in the future, such a scheme could be created and implemented for these datasets. Further, it is observed that non-axisymmetric and turbulent features develop in these simulations from an initial seed that is essentially provided by the mesh. Although the post-shock development of the flowfield greatly alters the spectral distribution of fluctuations, the mesh spacing sets the cutoff wavelength for Kelvin-Helmholtz instability development on the interface, thus further increasing the mesh-sensitivity of the simulation. Also, as described in Sec. 1.2, a number of effects are neglected here which are nevertheless important in environments where shock-bubble interactions are found, including phase changes, molecular dissociation, and radiative

energy transfer.

Finally, a significant limitation to the applicability of the present work is the lack of direct comparison to experimental results, which has been removed from the scope of this study. Such comparison is crucial to the development of a meaningful interpretation of numerical results, but has been left for future work.

## 7.6 Conclusion

In shock-bubble interactions within a parameter space accessible to mechanical shock tubes, the simulation results generated as part of this study show that a very broad range of phenomenologies is possible with only a change of a few  $\text{kg}/\text{m}^3$  in the density of the bubble gas. These phenomenologies extend from the formation of a single, dominant vortex ring at low Atwood number magnitude, to the development of complex regions of disordered vortical motion and turbulent mixing at high Atwood number. The evolution of the flowfield is so distinct in each case that we conclude the shock-bubble interaction constitutes a unique problem at each Atwood number. Further, we find that three-dimensional vorticity dynamics and complex secondary vorticity generation introduce strong three-dimensional and turbulent motion into the flowfield for  $|A| > 0.2$ , which do not appear at lower Atwood number magnitudes. Yet, despite this strong variability in the observable effects, we find that time-dependent trends in the underlying integral features of the flowfield, such as the mean density, internal energy, and velocity of the bubble fluid, still often roughly scale according to the simplest laws of gasdynamics. We also find that the shocked-bubble flowfield tends to equilibrate at late times to a state that is, in many cases, predicted by these laws. It is hoped that the ever-expanding

database of experimental and numerical data on shock-bubble interactions and shock-accelerated inhomogeneous flows in general will continue to yield confirmation that such simple approaches provide effective and accurate models for such complex systems, and provide further insight into the nature and implications of their more complex features.

# Appendix A

## One-Dimensional Gasdynamics

### Analysis for a Shocked Gas Slab

The pressure, density, velocity, and other state variables for the gases involved in the one-dimensional interaction of a shock wave with a discrete gas slab can be computed by solving a system of equations based on the shock jump conditions given in Eqs. 1.1-1.3 and the dynamic and kinematic matching conditions given in Eqs. 1.5-1.6. We construct this system by writing down these relations for each interaction of a shock or rarefaction wave with an interface, up to a certain number of reflections in the slab.

Here we consider only the first two reflections, so that three interactions in total are included: (1) the impact of the incident shock wave on the upstream slab surface, (2) the impact of the transmitted shock wave on the downstream interior slab surface, and (3) the impact of the internally reflected shock or rarefaction wave on the upstream interior slab surface. The sequence of waves interacting with the slab surfaces can be seen more clearly in the  $x$ - $t$  plots shown in Fig. 80.

As discussed in Sec. 1.2.1, the following notation is used to distinguish the fluids, their states, and each of the shock and rarefaction waves. Subscripts 1, 2, and 3 refer to the upstream-ambient, slab, and downstream-ambient fluids, respectively. Primed quantities indicate regions of the flow that have interacted with one shock or rarefaction wave;

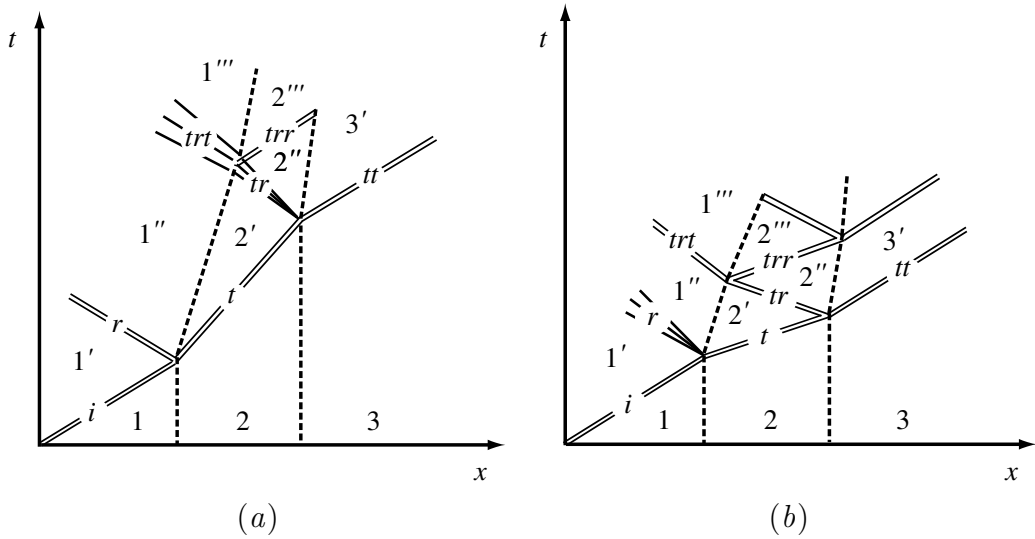


Figure 80: Schematic diagram of 1D shock transmission and reflection in a one-dimensional gas slab: (a) convergent geometry; (b) divergent geometry. Solid double lines indicate shock waves, dashed lines indicate fluid interfaces, and triple diverging solid lines indicate rarefaction waves.

double-primed quantities indicate interaction with two waves, and so on. Subscripts on shock wave speeds  $W$  or Mach numbers  $M$  indicate the wave in consideration: subscript  $i$  represents the incident shock wave;  $r$  the reflected wave;  $t$  the transmitted wave;  $tr$  a wave that was first transmitted across the slab, then reflected at the downstream surface.

We assume the following quantities are known: the gas constants  $\mathfrak{R}_1$  and  $\mathfrak{R}_2$  and ratios of specific heats  $\gamma_1$  and  $\gamma_2$  for the two gases, and the initial temperature  $T_1 = T_2$  and pressure  $p_1 = p_2$  in the system. The initial velocity in the unshocked medium is assumed to be zero everywhere:  $u_1 = u_2 = u_3 = 0$ . We set all of the initial state variables for fluid 3 equal to the state variables for fluid 1, as well, since both represent the ambient medium in which the slab is embedded.

We also assume that the gases in the system are calorically perfect ( $e$  and  $h$  both vary proportionally with  $T$ ). Explicit expressions for the initial sound speeds in the

system are then written as

$$c_1 = c_3 = \sqrt{\gamma_1 \mathfrak{R}_1 T_1} \quad (\text{A.1})$$

$$c_2 = \sqrt{\gamma_2 \mathfrak{R}_2 T_2}, \quad (\text{A.2})$$

and for the densities as

$$\rho_1 = \rho_3 = \frac{p_1}{\mathfrak{R}_1 T_1} \quad (\text{A.3})$$

$$\rho_2 = \frac{p_2}{\mathfrak{R}_2 T_2}. \quad (\text{A.4})$$

In the first interaction, the incident shock wave ( $i$ ) impacts the upstream surface of the slab, generating a reflected wave ( $r$ ) and a transmitted wave ( $t$ ). To find the post-shock state of fluid 1 behind the  $i$  wave, we perform a series of algebraic manipulations on Eqs. 1.1-1.1, taking advantage of Eqs. A.1-A.4, to yield

$$p'_1 = p_1 \left[ 1 + 2 \left( \frac{\gamma_1}{\gamma_1 + 1} \right) (M_i^2 - 1) \right] \quad (\text{A.5})$$

$$S_i = \frac{p'_1}{p_1} \quad (\text{A.6})$$

$$u'_1 = -u_1 + \frac{c_1}{\gamma_1} (S_i - 1) \left[ \frac{\frac{2\gamma_1}{\gamma_1 + 1}}{S_i + \frac{\gamma_1 - 1}{\gamma_1 + 1}} \right]^{1/2} \quad (\text{A.7})$$

$$\rho'_1 = \rho_1 \left[ \frac{1 + \frac{\gamma_1 + 1}{\gamma_1 - 1} S_i}{\frac{\gamma_1 + 1}{\gamma_1 - 1} + S_i} \right] \quad (\text{A.8})$$

$$T'_1 = T_1 S_i \left[ \frac{\frac{\gamma_1 + 1}{\gamma_1 - 1} + S_i}{1 + \frac{\gamma_1 + 1}{\gamma_1 - 1} S_i} \right] \quad (\text{A.9})$$

$$c'_1 = \sqrt{\gamma_1 \Re_1 T'_1}, \quad (\text{A.10})$$

where  $M_i = W_i/c_1$ . (These manipulations are described in detail by Anderson (2003) in Section 3.6 of Ref. [1].) Up to this point, all quantities in the system can be computed explicitly, because the pressure ratio  $S_i$  is known. However, after adding the expressions that follow – for the subsequent reflection/transmission event at the upstream slab surface – the system must be solved iteratively, because  $S_t$  and  $S_r$  are not known.

For the  $t$  wave, we apply the same manipulations to write,

$$p'_2 = p_2 S_t \quad (\text{A.11})$$

$$u'_2 = -u_2 + \frac{c_2}{\gamma_2} (S_t - 1) \left[ \frac{\frac{2\gamma_2}{\gamma_2 + 1}}{S_t + \frac{\gamma_2 - 1}{\gamma_2 + 1}} \right]^{1/2} \quad (\text{A.12})$$

$$\rho'_2 = \rho_2 \left[ \frac{1 + \frac{\gamma_2 + 1}{\gamma_2 - 1} S_t}{\frac{\gamma_2 + 1}{\gamma_2 - 1} + S_t} \right] \quad (\text{A.13})$$

$$T'_2 = T_2 S_t \left[ \frac{\frac{\gamma_2 + 1}{\gamma_2 - 1} + S_t}{1 + \frac{\gamma_2 + 1}{\gamma_2 - 1} S_t} \right] \quad (\text{A.14})$$

$$c'_2 = \sqrt{\gamma_2 \Re_2 T'_2}. \quad (\text{A.15})$$

For the  $r$  wave, we write,

$$p''_1 = p'_1 S_r \quad (\text{A.16})$$

$$u_1'' = u_1' - \frac{c_1'}{\gamma_1} (S_r - 1) \left[ \frac{\frac{2\gamma_1}{\gamma_1 + 1}}{S_r + \frac{\gamma_1 - 1}{\gamma_1 + 1}} \right]^{1/2} \quad (\text{A.17})$$

$$\rho_1'' = \rho_1' \left[ \frac{1 + \frac{\gamma_1 + 1}{\gamma_1 - 1} S_r}{\frac{\gamma_1 + 1}{\gamma_1 - 1} + S_r} \right] \quad (\text{A.18})$$

$$T_1'' = T_1' S_r \left[ \frac{\frac{\gamma_1 + 1}{\gamma_1 - 1} + S_r}{1 + \frac{\gamma_1 + 1}{\gamma_1 - 1} S_r} \right] \quad (\text{A.19})$$

$$c_1'' = \sqrt{\gamma_1 \mathfrak{R}_1 T_1''}. \quad (\text{A.20})$$

Finally, we apply the kinematic and dynamic matching conditions from Eqs. 1.5 and 1.6:

$$u_2' = u_2'' \quad (\text{A.21})$$

$$p_2' = p_2''. \quad (\text{A.22})$$

This closes the system for the first interaction. In the next interaction, the transmitted shock wave ( $t$ ) impacts the interior downstream surface of the slab, generating an internally reflected wave ( $tr$ ) and a transmitted wave ( $tt$ ). A similar system is constructed to obtain the properties behind the  $tr$  and  $tt$  waves. For the  $tt$  wave, we write,

$$p_3' = p_3 S_{tt} \quad (\text{A.23})$$

$$u_3' = -u_3 + \frac{c_3}{\gamma_1} (S_{tt} - 1) \left[ \frac{\frac{2\gamma_1}{\gamma_1 + 1}}{S_{tt} + \frac{\gamma_1 - 1}{\gamma_1 + 1}} \right]^{1/2} \quad (\text{A.24})$$

$$\rho'_3 = \rho_3 \left[ \frac{1 + \frac{\gamma_1 + 1}{\gamma_1 - 1} S_{tt}}{\frac{\gamma_1 + 1}{\gamma_1 - 1} + S_{tt}} \right] \quad (\text{A.25})$$

$$T'_3 = T_3 S_{tt} \left[ \frac{\frac{\gamma_1 + 1}{\gamma_1 - 1} + S_{tt}}{1 + \frac{\gamma_1 + 1}{\gamma_1 - 1} S_{tt}} \right] \quad (\text{A.26})$$

$$c'_3 = \sqrt{\gamma_1 \mathfrak{R}_1 T'_3}. \quad (\text{A.27})$$

For the *tr* wave, we write,

$$p''_2 = p'_2 S_{tr} \quad (\text{A.28})$$

$$u''_2 = u'_2 - \frac{c'_2}{\gamma_2} (S_{tr} - 1) \left[ \frac{\frac{2\gamma_2}{\gamma_2 + 1}}{S_{tr} + \frac{\gamma_2 - 1}{\gamma_2 + 1}} \right]^{1/2} \quad (\text{A.29})$$

$$\rho''_2 = \rho'_2 \left[ \frac{1 + \frac{\gamma_2 + 1}{\gamma_2 - 1} S_{tr}}{\frac{\gamma_2 + 1}{\gamma_2 - 1} + S_{tr}} \right] \quad (\text{A.30})$$

$$T''_2 = T'_2 S_{tr} \left[ \frac{\frac{\gamma_2 + 1}{\gamma_2 - 1} + S_{tr}}{1 + \frac{\gamma_2 + 1}{\gamma_2 - 1} S_{tr}} \right] \quad (\text{A.31})$$

$$c''_2 = \sqrt{\gamma_2 \mathfrak{R}_2 T''_2}. \quad (\text{A.32})$$

Then we apply the kinematic and dynamic matching conditions:

$$u'_3 = u''_2 \quad (\text{A.33})$$

$$p'_3 = p''_2. \quad (\text{A.34})$$

This closes the system through the second interaction. In the third interaction, the transmitted-and-reflected shock (*tr*) impacts the interior upstream surface of the slab,

generating an internally reflected wave (*trr*) and a transmitted wave (*trt*). A third set of equations is constructed to obtain the properties behind the *trt* and *trr* waves. For the *trt* wave, we write,

$$p_1''' = p_1'' S_{trt} \quad (\text{A.35})$$

$$u_1''' = u_1'' - \frac{c_1''}{\gamma_1} (S_{trt} - 1) \left[ \frac{\frac{2\gamma_1}{\gamma_1 + 1}}{S_{trt} + \frac{\gamma_1 - 1}{\gamma_1 + 1}} \right]^{1/2} \quad (\text{A.36})$$

$$\rho_1''' = \rho_1'' \left[ \frac{1 + \frac{\gamma_1 + 1}{\gamma_1 - 1} S_{trt}}{\frac{\gamma_1 + 1}{\gamma_1 - 1} + S_{trt}} \right] \quad (\text{A.37})$$

$$T_1''' = T_1'' S_{trt} \left[ \frac{\frac{\gamma_1 + 1}{\gamma_1 - 1} + S_{trt}}{1 + \frac{\gamma_1 + 1}{\gamma_1 - 1} S_{trt}} \right] \quad (\text{A.38})$$

$$c_1''' = \sqrt{\gamma_1 \Re_1 T_1'''}. \quad (\text{A.39})$$

For the *trr* wave, we write,

$$p_2''' = p_2'' S_{trr} \quad (\text{A.40})$$

$$u_2''' = -u_2'' + \frac{c_2''}{\gamma_2} (S_{trr} - 1) \left[ \frac{\frac{2\gamma_2}{\gamma_2 + 1}}{S_{trr} + \frac{\gamma_2 - 1}{\gamma_2 + 1}} \right]^{1/2} \quad (\text{A.41})$$

$$\rho_2''' = \rho_2'' \left[ \frac{1 + \frac{\gamma_2 + 1}{\gamma_2 - 1} S_{trr}}{\frac{\gamma_2 + 1}{\gamma_2 - 1} + S_{trr}} \right] \quad (\text{A.42})$$

$$T_2''' = T_2'' S_{trr} \left[ \frac{\frac{\gamma_2 + 1}{\gamma_2 - 1} + S_{trr}}{1 + \frac{\gamma_2 + 1}{\gamma_2 - 1} S_{trr}} \right] \quad (\text{A.43})$$

$$c_2''' = \sqrt{\gamma_2 \Re_2 T_2'''}. \quad (\text{A.44})$$

Then we once again apply the kinematic and dynamic matching conditions:

$$u_2''' = u_1''' \quad (\text{A.45})$$

$$p_2''' = p_1''' \quad (\text{A.46})$$

Note that in each equation for the post-shock flow velocity (Eqs. A.7, A.12, A.17, A.24, A.29, A.36, and A.41), the sign of the first term (the pre-shock velocity) is positive if the wave in consideration is moving in the  $-x$  direction, and negative if the wave is moving in the  $+x$  direction, since the fluid moves toward the wave, in a reference frame fixed to the wave. The second term has the opposite sign as the first term, since the impulse to the fluid is always in the same direction as the motion of the wave.

At this point, the system is closed through the third interaction. Although this procedure could be extended to any desired number of interactions, the appearance of rarefaction waves in the system makes this approach less useful for large numbers of interactions, since the dimension of the slab then becomes important. The system at this point may be solved using standard iterative techniques, and, for our purposes, this yields a complete picture of the flowfield.

# Appendix B

## Derivation of Compressible Vorticity Transport Equation

A transport equation for the vorticity  $\boldsymbol{\omega} \equiv \nabla \times \mathbf{U}$  in compressible flows can be obtained by taking the curl of the compressible momentum equation:

$$\frac{\partial \mathbf{U}}{\partial t} + (\mathbf{U} \cdot \nabla) \mathbf{U} = -\frac{1}{\rho} \nabla p + \nu \nabla^2 \mathbf{U}. \quad (\text{B.1})$$

### B.1 Vector Identities

To proceed, we will make use of several vector identities. First, for the gradient of a dot product, we have

$$\nabla(\mathbf{A} \cdot \mathbf{B}) = (\mathbf{B} \cdot \nabla) \mathbf{A} + (\mathbf{A} \cdot \nabla) \mathbf{B} + \mathbf{B} \times (\nabla \times \mathbf{A}) + \mathbf{A} \times (\nabla \times \mathbf{B}). \quad (\text{B.2})$$

Setting  $\mathbf{A} = \mathbf{B} = \mathbf{U}$ , we find

$$\nabla(\mathbf{U} \cdot \mathbf{U}) = 2(\mathbf{U} \cdot \nabla) \mathbf{U} + 2\mathbf{U} \times (\nabla \times \mathbf{U}). \quad (\text{B.3})$$

Rearranging to isolate the convective term, we obtain the identity

$$(\mathbf{U} \cdot \nabla) \mathbf{U} = \frac{1}{2} \nabla |\mathbf{U}|^2 - \mathbf{U} \times (\nabla \times \mathbf{U}). \quad (\text{B.4})$$

For the curl of a cross product, we can write,

$$\nabla \times (\mathbf{A} \times \mathbf{B}) = (\mathbf{B} \cdot \nabla) \mathbf{A} - (\mathbf{A} \cdot \nabla) \mathbf{B} + \mathbf{A} (\nabla \cdot \mathbf{B}) - \mathbf{B} (\nabla \cdot \mathbf{A}). \quad (\text{B.5})$$

Two other vector identities we will need include “curl grad = 0,”

$$\nabla \times \nabla A = 0, \quad (\text{B.6})$$

where  $A$  is a scalar field, and “div curl = 0,”

$$\nabla \cdot (\nabla \times \mathbf{A}) = 0. \quad (\text{B.7})$$

## B.2 Viscous Term

In reference to the viscous term in Eq. B.1, it should be noted that  $\nabla^2$  operating on a vector, by convention, indicates a vector, *e.g.*  $\nabla^2 \mathbf{U} = (\nabla^2 u, \nabla^2 v, \nabla^2 w,)$  in Cartesian coordinates. This vector Laplacian operator can also be written using the identity

$$\nabla^2 \mathbf{A} = \nabla (\nabla \cdot \mathbf{A}) - \nabla \times (\nabla \times \mathbf{A}). \quad (\text{B.8})$$

In view of the fact that we need to take the curl of Eq. B.1, it is useful to prove that a curl operating on a vector Laplacian is equal to a vector Laplacian operating on a curl:

$$\nabla \times (\nabla^2 \mathbf{A}) = \nabla \times [\nabla (\nabla \cdot \mathbf{A}) - \nabla \times (\nabla \times \mathbf{A})]. \quad (\text{B.9})$$

Recalling that  $\operatorname{curl} \operatorname{grad} = 0$ , we can drop the first term in brackets, yielding

$$\nabla \times (\nabla^2 \mathbf{A}) = -\nabla \times [\nabla \times (\nabla \times \mathbf{A})]. \quad (\text{B.10})$$

Setting  $\mathbf{C} = \nabla \times \mathbf{A}$ , we rewrite this as

$$\nabla \times (\nabla^2 \mathbf{A}) = -\nabla \times [\nabla \times \mathbf{C}]. \quad (\text{B.11})$$

We note that the definition of the vector Laplacian in Eq. B.8 can be rewritten as

$$\nabla \times (\nabla \times \mathbf{C}) = \nabla (\nabla \cdot \mathbf{C}) - \nabla^2 \mathbf{C}. \quad (\text{B.12})$$

Substituting Eq. B.12 into Eq. B.11, we obtain

$$\nabla \times (\nabla^2 \mathbf{A}) = \nabla^2 \mathbf{C} - \nabla (\nabla \cdot \mathbf{C}). \quad (\text{B.13})$$

Substituting  $\mathbf{C} = \nabla \times \mathbf{A}$ ,

$$\nabla \times (\nabla^2 \mathbf{A}) = \nabla^2 (\nabla \times \mathbf{A}) - \nabla [\nabla \cdot (\nabla \times \mathbf{A})]. \quad (\text{B.14})$$

Recalling that  $\operatorname{div} \operatorname{curl} = 0$ , we eliminate the second term on the right, leaving

$$\nabla \times (\nabla^2 \mathbf{A}) = \nabla^2 (\nabla \times \mathbf{A}). \quad (\text{B.15})$$

Thus, the operator “curl Laplacian” is equivalent to “Laplacian curl,” and the curl of the viscous term can be written as

$$\nabla \times (\nu \nabla^2 \mathbf{U}) = \nu \nabla^2 (\nabla \times \mathbf{U}) = \nu \nabla^2 \boldsymbol{\omega}. \quad (\text{B.16})$$

### B.3 Derivation

Taking the curl of Eq. B.1, we obtain

$$\frac{\partial \boldsymbol{\omega}}{\partial t} + \nabla \times [(\mathbf{U} \cdot \nabla) \mathbf{U}] = -\nabla \times \left( \frac{\nabla p}{\rho} \right) + \nabla \times (\nu \nabla^2 \mathbf{U}). \quad (\text{B.17})$$

Substituting Eq. B.4 into Eq. B.17 for the convective term,

$$\frac{\partial \boldsymbol{\omega}}{\partial t} + \frac{1}{2} \nabla \times \nabla |\mathbf{U}|^2 - \nabla \times (\mathbf{U} \times \boldsymbol{\omega}) = -\nabla \times \left( \frac{\nabla p}{\rho} \right) + \nu \nabla \times (\nabla^2 \mathbf{U}). \quad (\text{B.18})$$

Noting that  $\operatorname{curl} \operatorname{grad} = 0$ , and making use of Eq. B.16, we eliminate the second term on the left and rewrite the viscous term to obtain

$$\frac{\partial \boldsymbol{\omega}}{\partial t} - \nabla \times (\mathbf{U} \times \boldsymbol{\omega}) = -\nabla \times \left( \frac{\nabla p}{\rho} \right) + \nu \nabla^2 \boldsymbol{\omega}. \quad (\text{B.19})$$

Here, we see that the vorticity equation has three fundamental components, aside from the time dependence: convection/advection, baroclinicity, and diffusion. We can expand the convection/advection term ( $\operatorname{curl} \mathbf{U} \times \boldsymbol{\omega}$ ) using the identity in Eq. B.5:

$$\nabla \times (\mathbf{U} \times \boldsymbol{\omega}) = (\boldsymbol{\omega} \cdot \nabla) \mathbf{U} - (\mathbf{U} \cdot \nabla) \boldsymbol{\omega} + \mathbf{U} (\nabla \cdot \boldsymbol{\omega}) - \boldsymbol{\omega} (\nabla \cdot \mathbf{U}). \quad (\text{B.20})$$

We recall that  $\operatorname{div} \operatorname{curl} = 0$ , and after eliminating the third term on the right, and substituting this expression into Eq. B.19, we find

$$\frac{\partial \boldsymbol{\omega}}{\partial t} - (\boldsymbol{\omega} \cdot \nabla) \mathbf{U} + (\mathbf{U} \cdot \nabla) \boldsymbol{\omega} + \boldsymbol{\omega} (\nabla \cdot \mathbf{U}) = -\nabla \times \left( \frac{\nabla p}{\rho} \right) + \nu \nabla^2 \boldsymbol{\omega}. \quad (\text{B.21})$$

Here we note that the convection/advection term has produced three terms on the left-hand side. One of these is merely the convective part of the total derivative:  $(\mathbf{U} \cdot \nabla)\boldsymbol{\omega}$ . We group this in the total derivative  $D\boldsymbol{\omega}/Dt$ , giving

$$\frac{D\boldsymbol{\omega}}{Dt} - (\boldsymbol{\omega} \cdot \nabla) \mathbf{U} + \boldsymbol{\omega} (\nabla \cdot \mathbf{U}) = -\nabla \times \left( \frac{\nabla p}{\rho} \right) + \nu \nabla^2 \boldsymbol{\omega}. \quad (\text{B.22})$$

## B.4 Baroclinic Source Term

We obtain the usual form of the baroclinic source term from that shown in Eq. B.22 as follows. Using the product rule, we expand the original term as

$$-\nabla \times \left( \frac{\nabla p}{\rho} \right) = - \left[ \nabla \frac{1}{\rho} \times \nabla p + \frac{1}{\rho} (\nabla \times \nabla p) \right]. \quad (\text{B.23})$$

Noting that  $\operatorname{curl} \operatorname{grad} = 0$ , we eliminate the second term in brackets. Then we expand  $\operatorname{grad}(1/\rho)$  using the quotient rule and write

$$-\nabla \times \left( \frac{\nabla p}{\rho} \right) = - \left[ \frac{\rho \nabla(1) - \nabla \rho}{\rho^2} \right] \times \nabla p. \quad (\text{B.24})$$

Since  $\nabla(1) = 0$ , we have the usual form:

$$-\nabla \times \left( \frac{\nabla p}{\rho} \right) = \frac{1}{\rho^2} (\nabla \rho \times \nabla p) \quad (\text{B.25})$$

Substituting Eq. B.25 into Eq. B.22, we obtain the complete, final form of the vorticity equation:

$$\frac{D\boldsymbol{\omega}}{Dt} - (\boldsymbol{\omega} \cdot \nabla) \mathbf{U} + \boldsymbol{\omega} (\nabla \cdot \mathbf{U}) = \frac{1}{\rho^2} (\nabla \rho \times \nabla p) + \nu \nabla^2 \boldsymbol{\omega}. \quad (\text{B.26})$$

# Appendix C

## Input Files

Two input files are read by *Raptor*, named `inputs` and `probin`. The `inputs` file contains parameters that control the calculation, including domain size, boundary conditions, AMR setup, CFL number, *etc.* The `probin` file contains physical parameters and definitions used to set up the initial condition, such as the initial densities and pressures, boundaries between fluid regions, interfacial layer thickness, *etc.* The `inputs` and `probin` files used for the air-R12,  $M = 5$  simulation are printed here for reference.

### C.1 Inputs

```
max_step  = 10000      # maximum timestep

stop_time = 50000.e-06

# ----- INPUTS TO AMR CLASS -----
geometry.coord_sys      = 0 # 0 => cart, 1 => RZ, 2 => Spherical

geometry.prob_lo = 0. -5. 0.
```

```
geometry.prob_hi = 10.16 238.8 10.16

derived.derivevar = log_den pressure xvel yvel zvel vortx vorty vortz

amr.v          = 1

amr.n_cell    = 32 768 32

amr.max_level = 3      # maximum level number allowed
amr.max_level = 0      # maximum level number allowed
amr.max_level = 1      # maximum level number allowed
amr.max_level = 2      # maximum level number allowed

amr.ref_ratio   = 4 4 2 4 2  # refinement ratio

amr.check_int   = 50     # number of timesteps between checkpoints
amr.check_file  = chk    # root name of checkpoint file
amr.plot_file   = plt
amr.plot_int    = 5      # number of timesteps between checkpoints

amr.regrid_int  = 2      # how often to regrid
amr.n_error_buf = 3 3 3 3 3 # number of buffer cells in error est
amr.n_error_buf = 6 6 6 6 6 # number of buffer cells in error est
amr.grid_eff    = 0.7    # what constitutes an efficient grid
```

```
amr.blocking_factor = 1          # block factor in grid generation
amr.grid_log           = grdlog    # name of grid logging file
amr.max_grid_size     = 128
amr.max_grid_size     = 64
amr.max_grid_size     = 32

# ----- INPUTS TO PHYSICS CLASS -----
hyp.dt_cutoff         = 1.e-20  # level 0 timestep below which we halt

hyp.cfl               = 0.2      # cfl number for hyperbolic system
hyp.cfl               = 0.4      # cfl number for hyperbolic system
hyp.cfl               = 0.6      # cfl number for hyperbolic system
hyp.cfl               = 0.8      # cfl number for hyperbolic system

hyp.init_shrink       = 0.05     # scale back initial timestep
hyp.init_shrink       = 0.01     # scale back initial timestep

hyp.change_max        = 1.1      # scale back initial timestep
#hyp.change_min        = 0.8      # scale back initial timestep

#hyp.fixed_dt          = 5.e-12
hyp.sum_interval      = 1          # timesteps between computing mass
```

```
hyp.do_reflux      = 1          # 1 => do refluxing

hyp.do_richardson = 0          # flag for richardson error estimation
hyp.do_special   = 1          # flag for richardson error estimation
hyp.ref_dengrad  = 1

hyp.skip_refined = 0

hyp.do_tracking = 0 # flag for doing multifluid tracking turn off

hyp.do_mf  = 1
hyp.do_mc = 0

hyp.do_real_eos = 0

materials.name    =           mat1  mat2    mat3
materials.id      =           1      2       3
materials.gamma   =           1.143  1.399   1.402
materials.molecular_wt = 120.91 28.967   18.

# for multifluid capturing

hyp.do_hor      = 1
hyp.n_fluids   = 3
```

```
#hyp.do_navier_stokes = 1

hyp.bogus_value = 5.0e+5
hyp.mem_debug = 0
hyp.gravity_x = 0.
hyp.gravity_y = 0.

hyp.num_to_refine = 1
hyp.refine_frac = 1
hyp.regions_to_refine = 1
hyp.refine_region = 1

# ----- PROBLEM DEPENDENT INPUTS
Prob.interp_method = 1

Prob.lo_bc      = 3 2 3
Prob.hi_bc      = 2 2 2

# >>>>>>>>> BC FLAGS <<<<<<<<<<<<
# 0 = Interior          3 = Symmetry
# 1 = Inflow             4 = SlipWall
# 2 = Outflow            5 = NoSlipWall

# multigrid class
```

```
# ----- INPUTS TO MULTIGRID CLASS (NOT USED)

#mg.verbose = 0

smg.useCG = 0

mg.nu_f = 20

smg.eps = 1.0e-3

mg.v = 1

mg.maxiter = 60

mg.maxiter = 100

# turn any of these on to generate run-time timing stats

RunStats.statvar = godunov_box rich_error_est spec_error_est

#RunStats.statvar = rich_error_est

#RunStats.statvar = spec_error_est

# select form of FAB output: default is IEEE

#      ASCII (this is very slow)

#      NATIVE (native binary form on machine)

#      IEEE (default, this is portable)

fab.format = NATIVE

# select single or double precision of FAB output data

#      default is whatever precision code is compiled with.
```

```

fab.precision = DOUBLE      # output in FLOAT or DOUBLE

# -----
# -----      CONTOUR PLOTTING ONLY AVAILABLE IN 2-D      -----
# -----
# uncomment the next line to set a default level for contour plotting
# contour.level = 1

#
# These variables control interactive contour plotting on UNIX systems
# file_name = root name of postscript file (appended with ".ps")
# var_name  = name of thermodynamic variable to plot
# device    = 1 => XWINDOW, 2 = POSTSCRIPT, 3 = both
# freq      = intervals between plots (-1 = off)
# n_cont    = number of contour lines per plot
# sho_grd   = 0 => don't show grid placement, 1 => show grid placement
#           2 => show grid placement and overlay velocity vector plot
# win_siz   = number of pixels in max window direction
#
#       file_name  var_name   device   freq  n_cont  sho_grd win_siz
#       -----  -----  -----  -----  -----  -----  -----
contour.verbose = 0

contour.plot = frac1      frac1      1      -3      20      1      400
contour.plot = den        density     1      -10     20      1      400
contour.plot = yvel       yvel       1      -50     20      1      400

```

```

contour.plot = xvel      xvel          1     -10    20      1     400
contour.plot = xmom      xmom          1     -5     20      1     400
contour.plot = ymom      ymom          1    -100    20      1     400
contour.plot = eden      eden          1     -5     20      1     400
contour.plot = pressure  pressure      1    -10     2      1     400
contour.plot = mvort     mvort         1     -5     20      1     400

xgraph.verbose = 1

xgraph.graph = den      density       100   -1
xgraph.graph = xvel     xvel          100   -1
xgraph.graph = pres     pressure      100   -1
xgraph.graph = frac1   frac1         100   -1
xgraph.graph = rhof1   rhof1         100   -1
xgraph.graph = rhof2   rhof2         100   -1
#xgraph.graph = ieng    ieng          10    -1

```

## C.2 Probin

&fortin

```

rhoref2 = 1.205e-03
vref2   = 0.0
pref2   = 1.013e+06

```

rhoref1 = 5.028e-03

vref1 = 0.0

pref1 = 1.013e+06

rshock = 6.033e-03

ushock = 1.373e+05

pshock = 2.937e+07

sloc = -3.0

radius = 2.54

xcloud = 0.0

zcloud = 0.0

ycloud = 2.501

xcloud2 = 0.0

zcloud2 = 0.0

ycloud2 = -100000.161

radius2 = 0.1

width = 0.0

width2 = 0.05

```
cutoff = 90.

amp = 0.95
amp = 4.0
amp = 100.0
amp = 1.0
amp = 0.1

difmag = 0.0
difmag = 0.1
iorder = 1
iorder = 6
iorder = 2
iorder = 4
smallp = 1.d-06
small = 1.d-06
smallu = 1.d-06
smallr = 1.d-10
smallc = 1.d-06
smallvf = 1.d-8
vfcutoff = 1.d-7

do_bigdiv = 1
```

```
epsm = 1.d-14
eps = 1.d-12
itermax = 100

niter = 1
t_rel = 1.0
fraclim = 0.95
fracmax = 0.0
fracmax = 1.0
do_impl_relax = 1

ref_mat_inter = 1
use_rich = 0

richerr = 1.0
bubgrad = 1.0

do_cloud_shock = 1
do_multi_mode = 1
/
```

# Bibliography

- [1] J. D. Anderson, *Modern Compressible Flow with Historical Perspective*, 3rd ed., McGraw-Hill, New York, 2003.
- [2] S. P. S. Arya and J. C. Wyngaard, *Effect of baroclinicity on wind profiles and the geostrophic drag law for the convective planetary boundary layer*, J. Atmospheric Sciences **32** (1975), 767–778.
- [3] A. Bagabir and D. Drikakis, *Mach number effects on shock-bubble interaction*, Shock Waves **11** (2001), 209–218.
- [4] G. J. Ball and R. A. East, *Shock and blast attenuation by aqueous foam barriers: influence of barrier geometry*, Shock Waves **9** (1999), 37–47.
- [5] R. M. Baltrusaitis, M. L. Gittings, R. P. Weaver, R. F. Benjamin, and J. M. Budzinski, *Simulations of shock-generated instabilities*, journal =, (1996).
- [6] J. B. Bell, M. J. Berger, J. S. Saltzman, and M. Welcome, *Three dimensional adaptive mesh refinement for hyperbolic conservation laws*, SIAM J. Sci. Comp. **15** (1994), 127–138.
- [7] J. B. Bell, P. Colella, and J. A. Trangenstein, *Higher order godunov methods for general systems of hyperbolic conservation laws*, J. Comput. Phys. **82** (1989), no. 2, 362–397.
- [8] M. Berger and P. Colella, *Local adaptive mesh refinement for shock hydrodynamics*, J. Comput. Phys. **82** (1989), no. 1, 64–84.

- [9] M. Berger and J. Oliger, *Adaptive mesh refinement for hyperbolic partial differential equations*, J. Comput. Phys. **53** (1984), 484–512.
- [10] J. P. Boris, F. F. Grinstein, E. S. Oran, and R. J. Kolbe, *New insights into large eddy simulation*, Fluid Dyn. Res. **10** (1992), no. 199–228.
- [11] W. Cabot, *Comparison of two- and three-dimensional simulations of miscible Rayleigh-Taylor instability*, Phys. Fluids **18** (2006), no. 045101.
- [12] P. Colella, *A direct Eulerian MUSCL scheme for gas dynamics*, SIAM J. Sci. Stat. Comput. **6** (1985), no. 1, 104–117.
- [13] P. Colella and H. M. Glaz, *Efficient solution algorithms for the Riemann problem for real gases*, J. Comput. Phys. **59** (1985), no. 2, 264–289.
- [14] P. Colella, H. M. Glaz, and R. E. Ferguson, *Multifluid algorithms for Eulerian finite difference methods*, Unpublished, 1996.
- [15] P. Colella and P. Woodward, *The piecewise parabolic method (PPM) for gas-dynamical simulations*, J. Comput. Phys. **54** (1984), 174–201.
- [16] A. J. Coleman and J. E. Saunders, *A review of the physical properties and biological effects of the high-amplitude acoustic fields used in extracorporeal lithotripsy*, Ultrasonics **31** (1993), no. 2, 75–89.
- [17] B. D. Collins and J. W. Jacobs, *PLIF flow visualization and measurements of the Richtmyer-Meshkov instability of an air/SF<sub>6</sub> interface*, J. Fluid Mech. **464** (2002), 113–136.

- [18] T. J. B. Collins, A. Poludnenko, A. Cunningham, and A. Frank, *Shock propagation in deuterium-tritium-saturated foam*, Phys. Plasmas **12** (2005), no. 062705.
- [19] A. W. Cook and P. E. Dimotakis, *Transition stages of Rayleigh-Taylor instability between miscible fluids*, J. Fluid Mech. **443** (2001), 69–99.
- [20] N. Cowperthwaite, *The interaction of a plane shock and a dense spherical inhomogeneity*, Physica D **37** (1989), 264–269.
- [21] L. A. Crum, *Cavitation microjets as a contributory mechanism for renal calculi disintegration in ESWL*, J. Urology **140** (1988), 1587–1590.
- [22] W. Y. Crutchfield and M. L. Welcome, *Object-oriented implementations of adaptive mesh refinement algorithms*, Sci. Prog. **2** (1993), 145–156.
- [23] P. V. Danckwerts, *The definition and measurement of some characteristics of mixtures*, Appl. Sci. Res. **A 3** (1952), 279–296.
- [24] B. A. Davy and D. T. Blackstock, *Measurements of the refraction and diffraction of a short N wave by a gas-filled soap bubble*, J. Acoust. Soc. Am. **49** (1971), no. 3, 732–737.
- [25] C. F. Delale, S. Nas, and G. Tryggvason, *Direct numerical simulations of shock propagation in bubbly liquids*, Phys. Fluids **17** (2005), no. 121705.
- [26] M. Delius, F. Ueberle, and W. Eisenmenger, *Extracorporeal shock waves act by shock wave-gas bubble interaction*, Ultrasound in Med. and Biol. **24** (1998), no. 7, 1055–1059.

- [27] P. E. Dimotakis, *The mixing transition in turbulent flows*, J. Fluid Mech. **409** (2000), 69–98.
- [28] D. Drikakis, *Advances in turbulent flow computations using high-resolution methods*, Prog. Aerosp. Sci. **39** (2003), 405–424.
- [29] D. Drikakis, F. Grinstein, and D. Youngs, *On the computation of instabilities and symmetry-breaking in fluid mechanics*, Prog. Aerosp. Sci. **41** (2005), 609–641.
- [30] W. Eisenmenger, *The mechanisms of stone fragmentation in ESWL*, Ultrasound in Med. and Biol. **27** (2001), no. 5, 683–693.
- [31] A. Favre, *Equations des gaz turbulents compressibles. I. formes générales*, J. Mèch **4** (1965), no. 361–390.
- [32] J. E. Field, *The physics of liquid impact, shock wave interactions with cavities, and the implications to shock wave lithotripsy*, Phys. Med. Biol. **36** (1991), 1475–1484.
- [33] C. Fureby and F. F. Grinstein, *Large eddy simulation of high-Reynolds-number free and wall-bounded flows*, J. Comput. Phys. **181** (2002), 68–97.
- [34] J. Giordano and Y. Burtschell, *Richtmyer-Meshkov instability induced by shock-bubble interaction: numerical and analytical studies with experimental validation*, Phys. Fluids **18** (2006), no. 036102.
- [35] S. Gordon and B. J. McBride, *Computer program for computation of complex chemical equilibrium compositions, rocket performance, incident and reflected shocks, and Chapman-Jouguet detonations*, Spec. Publ. SP-273, Lewis Research Center, NASA, 1976.

- [36] J. A. Greenough, V. Beckner, R. B. Pember, W. Y. Crutchfield, J. B. Bell, and P. Colella, *An adaptive multifluid interface-capturing method for compressible flow in complex geometries*, AIAA paper 95-1718, 1995.
- [37] J. A. Greenough, B. de Supinski, R. K. Yates, C. A. Rendleman, D. Skinner, V. E. Beckner, M. Lijewski, and J. B. Bell, *Performance of a block structured hierarchical adaptive mesh refinement code on the 64k node IBM BlueGene/L computer*, LBNL Report LBNL-57500, Lawrence Berkeley National Laboratory, Berkeley, CA, April 2005.
- [38] J. A. Greenough and W. J. Rider, *A quantitative comparison of numerical methods for the compressible Euler equations: fifth-order WENO and piecewise-linear Godunov*, J. Comput. Phys. **196** (2004), 259–281.
- [39] F. F. Grinstein and R. H. Guirguis, *Effective viscosity in the simulation of spatially evolving shear flows with monotonic FCT models*, J. Comput. Phys. **101** (1992), 165–175.
- [40] F. F. Grinstein, L. G. Margolin, and W. J. Rider, *Implicit Large Eddy Simulation: Computing Turbulent Fluid Dynamics*, Cambridge University Press, Cambridge, U. K., 2007.
- [41] J. F. Haas, *Interaction of weak shock waves and discrete gas inhomogeneities*, Ph.D. thesis, California Institute of Technology, 1984.
- [42] J.-F. Haas and B. Sturtevant, *Interaction of weak shock waves with cylindrical and spherical inhomogeneities*, J. Fluid Mech. **181** (1987), 41–76.

- [43] J. F. Hansen, H. F. Robey, R. I. Klein, and A. R. Miles, *Experiment on the mass-stripping of an interstellar cloud in a high Mach number post-shock flow*, Phys. Plasmas **14** (2007), no. 056505.
- [44] S. Heinz and E. Churazov, *Heating the bubbly gas of galaxy clusters with weak shocks and sound waves*, Ap. J. **634** (2005), L141–L144.
- [45] L. F. Henderson, *The refraction of a plane shock wave at a gas interface*, J. Fluid Mech. **26** (1966), 607–637.
- [46] ———, *On the refraction of shock waves*, J. Fluid Mech. **198** (1989), 365–386.
- [47] L. F. Henderson, P. Colella, and E. G. Puckett, *On the refraction of shock waves at a slow-fast gas interface*, J. Fluid Mech. **224** (1991), 1–27.
- [48] U. Hwang, K. A. Flanagan, and R. Petre, *CHANDRA X-ray observation of a mature cloud-shock interaction in the bright eastern knot region of Puppis A*, Ap. J. **635** (2005), 355–364.
- [49] J. W. Jacobs, *The dynamics of shock accelerated light and heavy gas cylinders*, Phys. Fluids A **5** (1993), no. 9, 2239–2247.
- [50] A. R. Jamaluddin, G. J. Ball, and T. J. Leighton, *Free-Lagrange simulations of shock/bubble interaction in shock wave lithotripsy*, Shock Waves: Proceedings of the 24th International Symposium on Shock Waves (Z. L. Jiang, ed.), 2005.
- [51] R. I. Klein, K. S. Budil, T. S. Perry, and D. R. Bach, *The interaction of supernova remnants with interstellar clouds: experiments on the NOVA laser*, Ap. J. **583** (2003), 245–259.

- [52] R. I. Klein, C. F. McKee, and P. Colella, *On the hydrodynamic interaction of shock waves with interstellar clouds. I. Nonradiative shocks in small clouds*, Ap. J. **420** (1994), 213–236.
- [53] A. L. Kuhl, *Spherical mixing layers in explosions*, Dynamics of Exothermicity (J. R. Bowen, ed.), Gordon and Breach Publishers, Amsterdam, 1996, pp. 291–320.
- [54] H. Lamb, *Hydrodynamics*, Dover, New York, 1945.
- [55] L. D. Landau and E. M. Lifshitz, *Fluid Mechanics*, 2nd ed., Elsevier, Oxford, 1987.
- [56] A. Lapidus, *A detached shock calculation by second-order finite differences*, J. Comput. Phys. **2** (1967), 154–177.
- [57] M. Latini, O. Schilling, and W. S. Don, *Effects of WENO flux reconstruction order and spatial resolution on reshocked two-dimensional Richtmyer-Meshkov instability*, J. Comput. Phys. **221** (2006), 805–836.
- [58] M. Latini, O. Schilling, and W. S. Don, *High-resolution simulations and modeling of reshocked single-mode Richtmyer-Meshkov instability: Comparison to experimental data and to amplitude growth model predictions*, Phys. Fluids **19** (2007), no. 024104.
- [59] G. Layes, *Etude expérimentale de l'interaction d'une onde de choc avec une bulle de gaz*, Ph.D. thesis, Université de Provence (Aix-Marseille I), 2005.
- [60] G. Layes, G. Jourdan, and L. Houas, *Distortion of a spherical gaseous interface accelerated by a plane shock wave*, Phys. Rev. Lett. **91** (2003), no. 17.

- [61] ———, *Experimental investigation of the shock wave interaction with a spherical gas inhomogeneity*, Phys. Fluids **17** (2005), no. 028103.
- [62] G. Layes and O. LeMétayer, *Quantitative numerical and experimental studies of the shock accelerated heterogeneous bubbles motion*, Phys. Fluids **19** (2007), no. 042105.
- [63] K. Levy, O. Sadot, A. Rikanati, D. Kartoon, Y. Srebro, A. Yosef-Hai, G. Ben-Dor, and D. Shvarts, *Scaling in the shock-bubble interaction*, Laser and Particle Beams **21** (2003), 335–339.
- [64] H. W. Liepmann and A. Roshko, *Elements of Gasdynamics*, John Wiley & Sons Inc., New York, NY, 1957.
- [65] J. Lindl, *Development of the indirect-drive approach to inertial confinement fusion and the target physics basis for ignition and gain*, Phys. Plasmas **2** (1995), no. 11, 3933–4024.
- [66] B. Lipkens and D. T. Blackstock, *Model experiment to study sonic boom propagation through turbulence. Part I: general results*, J. Acoust. Soc. Am. **103** (1998), no. 1, 148–158.
- [67] F. E. Marble, E. E. Zukoski, J. Jacobs, G. Hendricks, and I. Waitz, *Shock enhancement and control of hypersonic mixing and combustion*, 26th AIAA, SAE, ASME, and ASEE Joint Propulsion Conference, Orlando, FL, July 16-18, 1990.
- [68] G. H. Markstein, *A shock tube study of the flame front-pressure wave interaction*, 6th International Symposium on Combustion (New York), Reinhold, 1957, pp. 387–398.

- [69] A. Marquina and P. Mulet, *A flux-split algorithm applied to conservative models for multicomponent compressible flows*, J. Comput. Phys. **185** (2003), 120–138.
- [70] B. D. May and D. E. Kelley, *Effect of baroclinicity on double-diffusive interleaving*, J. Physical Oceanography **27** (1997), 1997–2008.
- [71] E. E. Meshkov, *Instability of a shock wave accelerated interface between two gases*, NASA Tech. Trans. NASA TT F-13074, 1970.
- [72] A. R. Miles, B. Blue, M. J. Edwards, J. A. Greenough, J. F. Hansen, H. F. Robey, R. P. Drake, C. Kuranz, and D. R. Leibbrandt, *Transition to turbulence and effect of initial conditions on three-dimensional compressible mixing in planar blast-wave-driven systems*, Phys. Plasmas **12** (2005), no. 056317.
- [73] G. H. Miller and E. G. Puckett, *A higher-order Godunov method for multiple condensed phases*, J. Comput. Phys. **128** (1996), 134–164.
- [74] J. H. J. Niederhaus, J. A. Greenough, J. G. Oakley, D. Ranjan, M. H. Anderson, and R. Bonazza, *A computational parameter study for the three-dimensional shock-bubble interaction*, J. Fluid Mech. (2007), accepted for publication.
- [75] J. G. Oakley, *Circulation model for compressible flow: line integral of velocity formulation*, unpublished, 2006.
- [76] R. L. Panton, *Incompressible Flow*, John Wiley and Sons, New York, NY, 1984.
- [77] R. B. Pember, J. A. Greenough, and P. Colella, *An adaptive, higher-order Godunov method for gas dynamics in three-dimensional orthogonal curvilinear coordinates*,

- Tech. Report UCRL-JC-123351, Lawrence Livermore National Laboratory, Livermore, CA, February 1996.
- [78] G. Peng, N. J. Zabusky, and S. Zhang, *Vortex-accelerated secondary baroclinic vorticity deposition and late-intermediate time dynamics of a two-dimensional Richtmyer-Meshkov interface*, Phys. Fluids **15** (2003), no. 12, 3730–3744.
- [79] J. M. Picone and J. P. Boris, *Vorticity generation by shock propagation through bubbles in a gas*, J. Fluid Mech. **189** (1988), 23–51.
- [80] J. M. Picone, E. S. Oran, J. P. Boris, and T. R. Young Jr., *Theory of voriticity generation by shock wave and flame interactions*, Dynamics of Shock Waves, Explosions, and Detonations (J. R. Bowen, N. Manson, A. K. Oppenheim, and R. I. Soloukhin, eds.), Progress in Astronautics and Aeronautics, vol. 94, AIAA, New York, NY, 1985, pp. 429–448.
- [81] A. D. Pierce and D. J. Maglieri, *Effect of atmospheric irregularities on sonic-boom propagation*, J. Acoust. Soc. Am. **51** (1972), no. 2, 702–721.
- [82] S. B. Pope, *Turbulent Flows*, Cambridge University Press, Cambridge, UK, 2000.
- [83] D. H. Porter, A. Pouquet, and P. R. Woodward, *Kolmogorov-like spectra in decaying three-dimensional supersonic flows*, Phys. Fluids **6** (1994), no. 6, 2133–2142.
- [84] J. J. Quirk and S. Karni, *On the dynamics of a shock-bubble interaction*, J. Fluid Mech. **318** (1996), 129–163.
- [85] P. Ramaprabhu and M. J. Andrews, *Experimental investigation of Rayleigh-Taylor mixing at small Atwood numbers*, J. Fluid Mech. **502** (2004), 233–271.

- [86] D. Ranjan, M. Anderson, J. Oakley, and R. Bonazza, *Experimental investigation of a strongly shocked gas bubble*, Phys. Rev. Lett. **94** (2005), no. 184507.
- [87] D. Ranjan, J. Niederhaus, B. Motl, M. Anderson, J. Oakley, and R. Bonazza, *Experimental investigation of primary and secondary features in high-Mach-number shock-bubble interaction*, Phys. Rev. Lett. **98** (2007), no. 024502.
- [88] D. Ranjan, J. H. J. Niederhaus, J. G. Oakley, M. H. Anderson, R. Bonazza, and J. A. Greenough, *Shock-bubble interactions: features of divergent shock-refraction geometry observed in experiments and simulations*, (2007), In review.
- [89] J. Ray, R. Samtaney, and N. J. Zabusky, *Shock interactions with heavy gaseous elliptic cylinders: Two leeward-side shock competition modes and a heuristic model for interfacial circulation deposition at early times*, Phys. Fluids **12** (2000), no. 3, 707–716.
- [90] C. A. Rendleman, V. E. Beckner, M. Lijewski, W. Y. Crutchfield, and J. B. Bell, *Parallelization of structured, hierarchical adaptive mesh refinement algorithms*, Computing and Visualization in Science **3** (1998), 147–157.
- [91] C. S. Reynolds, S. Heinz, and M. C. Begelman, *Shocks and sonic booms in the intracluster medium: X-ray shells and radio galaxies*, Ap. J. **549** (2001), L179–L182.
- [92] R. D. Richtmyer, *Taylor instability in shock acceleration of compressible fluids*, Commun. Pure Appl. Math. **13** (1960), 297–319.
- [93] H. F. Robey, T. S. Perry, R. I. Klein, J. O. Kane, J. A. Greenough, and T. R.

- Boehly, *Experimental investigation of the three-dimensional interaction of a strong shock with a spherical density inhomogeneity*, Phys. Rev. Lett. **89** (2002), no. 8.
- [94] G. Rudinger, *Shock wave and flame interactions*, Combustions and Propulsion: Third AGARD Colloquium (New York, NY) (M. W. Thring, ed.), Pergamon, 1958, pp. 153–182.
- [95] G. Rudinger and L. M. Somers, *Behavior of small regions of different gases carried in accelerated gas flows*, J. Fluid Mech. **7** (1960), 161–176.
- [96] D. Ryutov, R. P. Drake, J. Kane, E. Liang, B. A. Remington, and W. M. Wood-Vasey, *Similarity criteria for the laboratory simulation for supernova hydrodynamics*, Ap. J. **518** (1999), 821–832.
- [97] R. Samtaney and D. I. Pullin, *On initial-value and self-similar solutions of the compressible Euler equations*, Phys. Fluids **8** (1996), no. 10, 2650–2655.
- [98] R. Samtaney, J. Ray, and N. J. Zabusky, *Baroclinic circulation generation on shock accelerated slow/fast gas interfaces*, Phys. Fluids **10** (1998), no. 5, 1217–1230.
- [99] R. Samtaney and N. J. Zabusky, *Circulation deposition on shock-accelerated planar and curved density-stratified interfaces: models and scaling laws*, J. Fluid Mech. **269** (1994), 45–78.
- [100] O. Schilling, M. Latini, and W. S. Don, *Physics of reshock and mixing in single-mode Richtmyer-Meshkov instability*, Phys. Rev. E **76** (2007).
- [101] H. Schlichting and K. Gersten, *Boundary Layer Theory*, Springer-Verlag, New York, NY, 2000.

- [102] J. M. Stone and M. L. Norman, *The three-dimensional interaction of a supernova remnant with an interstellar cloud*, Ap. J. **390** (1992), L17–L19.
- [103] G. Strang, *On the construction and comparison of different schemes*, SIAM J. Numer. Anal. **5** (1968), no. 3, 506–517.
- [104] J. C. Tannehill, D. A. Anderson, and R. H. Pletcher, *Computational Fluid Mechanics and Heat Transfer*, Taylor and Francis, Philadelphia, PA, 1997.
- [105] G. I. Taylor, *Formation of a vortex ring by giving an impulse to a circular disk and then dissolving it away*, J. Appl. Phys. **24** (1953), no. 1.
- [106] P. A. Thompson, *Compressible-Fluid Dynamics*, McGraw-Hill, New York, NY, 1984.
- [107] B. van Leer, *Towards the ultimate conservative difference scheme*, J. Comput. Phys. **32** (1979), 101–136.
- [108] S. E. Widnall, D. B. Bliss, and C. Y. Tsai, *The instability of short waves on a vortex ring*, J. Fluid Mech. **66** (1974), 35–47.
- [109] K.-H. Winkler, J. W. Chalmers, S. W. Hodson, P. R. Woodward, and N. J. Zabusky, *A numerical laboratory*, Physics Today **40** (1987), no. 10, 28–37.
- [110] J. Yang, T. Kubota, and E. E. Zukoski, *A model for characterization of a vortex pair formed by shock passage over a light-gas inhomogeneity*, J. Fluid Mech. **258** (1994), 217–244.
- [111] D. L. Youngs, *Three-dimensional numerical simulations of turbulent mixing by Rayleigh-Taylor instabilities*, Phys. Fluids A **3** (1991), no. 5, 1312–1320.

- [112] N. J. Zabusky, *Vortex paradigm for accelerated inhomogeneous flows: visiometrics for the Rayleigh-Taylor and Richtmyer-Meshkov environments*, Ann. Rev. Fluid Mech. **31** (1999), 495–536.
- [113] N. J. Zabusky and S. M. Zeng, *Shock cavity implosion morphologies and vortical projectile generation in axisymmetric shock-spherical fast/slow bubble interactions*, J. Fluid Mech. **362** (1998), 327–346.
- [114] S. Zhang, G. Peng, and N. J. Zabusky, *Vortex dynamics and baroclinically forced inhomogeneous turbulence for shock-planar heavy curtain interactions*, J. Turbul. **6** (2005), 1–29.